

# THÈSE DE DOCTORAT

Soutenue à Aix-Marseille Université

le 22 avril 2024 par

**Hugo ITENEY**

Modélisation de l'état de surface et de la mécanique des  
nano-objets

**Discipline**

Physique et Sciences de la Matière

**Spécialité**

Matière Condensée et Nanosciences

**École doctorale**

ED 352

**Laboratoire/Partenaires de recherche**

Institut Matériaux Microélectronique Nano-sciences de Provence (IM2NP UMR 7334 CNRS)

**Composition du jury**

- Lars PASTEWKA  
Professeur
- Nicolas COMBE  
Professeur
- Eugen RABKIN  
Professeur
- Marie-Ingrid RICHARD  
Directrice de recherche CEA
- Vladislav YASTREBOV  
Chargé de recherche CNRS
- Thomas CORNELIUS  
Directeur de recherche CNRS
- Olivier THOMAS  
Professeur
- Jonathan AMODEO  
Chargé de recherche CNRS

**Rapporteur**

University of Freiburg

**Rapporteur**

Université Paul Sabatier Toulouse

**Président du jury**

Technion Israel Institute of technology

**Examinateuse**

CEA Grenoble

**Examinateur**

Centre des Matériaux MINES Paris

**Directeur de thèse**

Aix-Marseille Université

**Co-directeur de thèse**

Aix-Marseille Université

**Encadrant de thèse**

Aix-Marseille Université

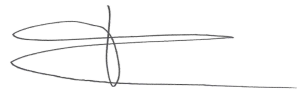


## Affidavit

I, undersigned, Hugo Iteney, hereby declare that the work presented in this manuscript is my own work, carried out under the scientific supervision of Thomas W. Cornelius, Olivier Thomas and Jonathan Amodeo, in accordance with the principles of honesty, integrity and responsibility inherent to the research mission. The research work and the writing of this manuscript have been carried out in compliance with both the french national charter for Research Integrity and the Aix-Marseille University charter on the fight against plagiarism.

This work has not been submitted previously either in this country or in another country in the same or in a similar version to any other examination body.

Done in Marseille, February 26, 2024



This work is licensed under [Creative Commons Attribution-NonCommercial-NoDerivatives 4.0 International Public License](#)

## Liste de publications et participation aux conférences

### Liste des publications et/ou brevets réalisées dans le cadre du projet de thèse:

1. **Hugo Iteney**, Thomas W. Cornelius, Olivier Thomas, Jonathan Amodeo, "Influence of surface roughness on the mechanical response of gold nanoparticle under compression" [under review]
2. **Hugo Iteney**, Javier Antonio Gonzalez Joa, Christophe Le Bourlot, Thomas W. Cornelius, Olivier Thomas, and Jonathan Amodeo. "Pyrough: A Tool to Build 3D Samples with Rough Surfaces for Atomistic and Finite-Element Simulations." Computer Physics Communications 295 (2024): 108958. <https://doi.org/10.1016/j.cpc.2023.108958>
3. **Hugo Iteney**, Thomas W. Cornelius, Olivier Thomas, and Jonathan Amodeo. "Load versus Displacement-Controlled Nanocompression: Insights from Atomistic Simulations." Scripta Materialia 226 (2023): 115245. <https://doi.org/10.1016/j.scriptamat.2022.115245>

### Participation aux conférences et écoles d'été au cours de la période de thèse:

- *Plasticité*, Marseille - France, 2024 [Poster]
- *TMS*, Orlando - USA, 2024 [Oral + Poster]
- *C'Nano*, Poitiers - France, 2023 [Oral]
- *Plasticité*, Lyon - France, 2023 [Oral + Poster]
- *Multiscale Materials Modeling*, Baltimore - USA, 2022 [Oral + Poster]
- *Plasticité*, Toulouse - France, 2022 [Oral]

## **Résumé et mots clés**

Les nano-objets (nanopiliers, nanofils, nanoparticules et films minces) sont particulièrement utilisés dans divers domaines d'application tels que la microélectronique, l'imagerie biomédicale, l'ingénierie ou la catalyse. En comparaison à leurs homologues massifs, ils sont connus pour présenter des propriétés physiques et mécaniques exceptionnelles, liées à leur rapport surface/volume élevé. En effet, tandis que le comportement mécanique des matériaux massifs repose sur la multiplication des dislocations et leur libre parcours moyen, les nano-objets sont rares en défauts, nécessitant la nucléation des dislocations pour initier la déformation plastique. Néanmoins, cette tendance du "smaller is stronger" est caractérisée par une dispersion sévère des données dans les expériences de nanomécanique, qui pourrait être induite par des biais expérimentaux ou même des singularités en surface de l'échantillon (rugosité, couche de passivation, oxyde, etc.), sans parler de l'aspect stochastique du processus de nucléation des dislocations lui-même. L'impact de ces aspects est très peu, voire pas du tout, pris en compte par les méthodologies de modélisation actuelles, ce qui pourrait mener à une description incorrecte des échantillons modélisés et à des protocoles de simulation partiellement erronés, induisant un écart significatif entre modèles et expériences. Cette thèse se concentre sur le développement et l'application de nouvelles méthodologies de conception d'échantillons virtuels et de déformation dans le but de rendre les simulations numériques de nanomécanique plus réalistes, tout en tenant mieux compte des observations expérimentales. Des nano-objets comprenant des rugosités de surface ou une altération chimique, sont conçus et testés à l'aide de simulations de dynamique moléculaire et d'éléments finis. À cette fin, nous avons développé un outil Python en libre accès appelé *Pyrough* qui repose sur la théorie classique de la rugosité pour la conception d'échantillons virtuels en 3D. En utilisant *Pyrough* pour la conception de nanoparticules métalliques rugueuses, nos simulations de nano-compression en dynamique moléculaire montrent que les irrégularités de surface ont un impact majeur sur les propriétés mécaniques et l'évolution des microstructures de dislocations lors de la déformation plastique. Ce résultat est confirmé par une étude statistique et quantitative réalisée sur des centaines d'échantillons d'or et de cuivre. De plus, un protocole original de contrôle en force visant à mieux décrire les essais de compression et d'indentation est introduit en plus de l'approche classique de contrôle en déplacement dans les simulations de dynamique moléculaire. Des sauts de déformation et des "pop-ins" sont désormais observables dans les simulations et l'effondrement abrupt des nanoparticules ou piliers métalliques observé expérimentalement est désormais expliqué. Enfin, la croissance et l'influence d'une couche d'oxyde de surface sur les propriétés mécaniques de nanocristaux sont également étudiées en adéquation avec des expériences TEM *in situ*. En comparaison aux échantillons purs étudiés jusqu'à présent, les simulations confirment la modification des propriétés mécaniques des échantillons oxydés en surface. Cette étude, qui inclut une description plus réaliste des échantillons et du protocole de déformation, apporte un éclairage nouveau dans notre compréhension de la mécanique des nano-objets.

Mots clés: Nanomécanique, Rugosité, Oxydation, Dynamique moléculaire, Modélisation par éléments finis.

## **Abstract and keywords**

Nano-objects (nanopillars, nanowires, nanoparticles and thin films) are widely used in various fields of applications such as micro-electronics, biomedical imaging, engineering as well as catalysis. When compared to their bulk counterparts, they are known to exhibit exceptional physical and mechanical properties related to their high surface/volume ratio. Indeed, while the mechanical behavior of bulk materials relies on managing dislocation multiplication and mean-free path against other defect contents, nano-objects are known to be defect scarce requiring dislocation nucleation to initiate incipient plastic deformation. Nevertheless, this “smaller is stronger” trend is characterized by severe data scattering in nanomechanical experiments, which might be induced by experimental biases or singularities at the surface of the sample (roughness, passivating layer, oxide, etc.), notwithstanding the stochastic aspect of the dislocation nucleation process itself. The impact of these aspects is very little, if not at all, accounted for by current modeling methodologies that might call for improper sample and protocol design at the heart of a significant gap between simulations and experiments. This thesis focuses on the development and application of new sample design and deformation methodologies with the aim of making nanomechanics numerical simulations more realistic while better accounting for experimental observations. Nano-objects with optimized and realistic surfaces, including surface roughness and chemical alteration, are designed and probed using molecular dynamics and finite-element simulations. For this purpose, we developed a numerical and open-source Python tool called *Pyrough* that relies on the classical roughness theory for the design of 3D virtual samples. Relying on *Pyrough* for the design of metal nanoparticles with surface roughness, nanocompression molecular dynamics simulations show that surface irregularities have a major impact on the mechanical properties and dislocation microstructure evolution during plastic deformation, as confirmed by a statistical and quantitative study performed on hundreds of atomistic simulations applied to gold and copper nanoparticles. Furthermore, an original load-control protocol that aims at better describe compression and indentation tests when relying on force monitoring is introduced in addition to the classical displacement-control approach in molecular dynamics simulations. Strain bursts and pop-ins are now observable in simulations and the experimentally-observed abrupt collapse of metal nanoparticles or pillars is now explained. Finally, the growth and the mechanical influence of an oxide layer at the surface of metal nanocrystals is also investigated using reactive force fields, in adequacy with *in situ* TEM experiments. As compared to the pristine samples studied so far, simulations confirm changes in the mechanical properties of surface-oxidized samples. This study that includes a more realistic description of sample and deformation protocol sheds new light on our understanding of the mechanics of nano-objects.

**Keywords:** Nanomechanics, Roughness, Oxidation, Molecular dynamics, Finite-elements modeling

## **Résumé étendu**

Ce chapitre constitue un résumé étendu en français de ma thèse, qui elle, a été rédigée en anglais.

## Introduction

Les progrès récents observés dans divers domaines d'applications comme la médecine, l'électronique et la mécanique sont souvent implicitement liés à l'étude de nano-objets, c'est-à-dire d'échantillons ayant des dimensions de quelques centaines ou dizaines de nanomètres. La caractérisation mécanique des nano-objets, souvent délicate, montre généralement la tendance du paradigme "smaller is stronger" [Uchic et al. 2009; Greer and De Hosson 2011]. Il existe plusieurs méthodes numériques et expérimentales pour étudier les mécanismes de déformation des nano-objets, mais ces approches restent souvent complexes et fastidieuses. Des problèmes intrinsèques ou extrinsèques, tels que le désalignement des échantillons, le mode de contrôle de l'essai, la contamination, la rugosité et l'oxydation, sont fréquemment signalés, contribuant ainsi à une dispersion des données et à l'irréproducibilité des résultats expérimentaux [Williams and Carter 1996; Zaefferer 2011]. Cette variabilité empêche une analyse statistique approfondie et limite ainsi la compréhension des phénomènes étudiés.

D'un autre côté, les méthodes numériques sont souvent utilisées pour aider à interpréter les résultats expérimentaux. Cependant, leur capacité à décrire de manière fidèle les essais de nanomécanique expérimentaux peut être débattue. Jusqu'à présent, la dispersion des valeurs de contrainte critique des nano-objets autour de la tendance globale n'est pas reproduite. Ceci constitue un problème majeur qui empêche la compréhension totale du comportement mécanique des nano-objets et accentue l'écart entre les expériences et les simulations. Un axe d'amélioration possible pour les simulations réside dans la conception des échantillons virtuels. En effet, les nano-objets virtuels sont généralement conçus à l'aide de formes simples et symétriques, telles que des sphères et des cubes parfaits, des cylindres ainsi que des surfaces planes et sans défauts. Ainsi, pour améliorer leur capacité à prédire l'intégrité des nano-objets sous contrainte, les simulations requièrent une conception d'échantillon plus précise et réaliste, basée sur une description détaillée de la topologie de surface incluant la rugosité de surface et l'altération chimique.

Sur la base de ces considérations, une problématique peut être soulevée : est-il possible d'inclure de manière rigoureuse les imperfections réelles dans le monde de la simulation pour reproduire et interpréter la dispersion des données observées expérimentalement ? Ici, nous verrons que la réponse repose sur le développement et l'application de méthodologies et de protocoles de simulation originaux qui tiennent davantage compte de l'architecture de surface et des spécificités expérimentales pour l'étude des propriétés physiques et mécaniques des nano-objets. La rugosité de surface et l'altération chimique seront prises en compte, conduisant à des échan-

tillons plus réalistes, plus proches des observations expérimentales. Une meilleure description des échantillons devrait influencer considérablement les processus de déformation et les réponses mécaniques, comblant ainsi l'écart actuel entre les expériences de nanomécanique et les simulations.

Ce manuscrit est structuré de la manière suivante : une revue bibliographique sur la mécanique aux petites échelles, les principaux biais expérimentaux responsables de la dispersion des données ainsi que les travaux actuels de modélisation atomistique sont d'abord présentés. Ensuite, le deuxième chapitre présente les méthodes utilisées durant ces travaux, notamment les fondements théoriques des simulations atomistiques ainsi que les protocoles et outils employés. Ensuite, les résultats obtenus durant cette thèse sont répartis en quatre chapitres. Le chapitre 3 se concentre sur l'influence du mode de contrôle sur la dynamique des essais mécaniques numériques. Notamment, il présente le développement et l'application d'un protocole original modélisant le contrôle en force des indentateurs. Le chapitre 4 présente le développement de l'outil *Pyrough*, un code Python en accès libre et orienté objet. Il permet de générer des échantillons virtuels 3D présentant des rugosités de surface tels que des films minces, des nanoparticules facettées ou sphériques, et des nanofils cylindriques ou facettés pour des études en éléments-finis ou de simulation atomistique. *Pyrough* est ensuite utilisé dans le chapitre 5 pour générer une centaine de nanoparticules facettées d'or avec différents paramètres de rugosité qui sont testées en compression. La distribution des limites élastiques est comparée à celle des paramètres de rugosité, et un modèle est proposé. Enfin, le chapitre 6 présente une étude de l'influence d'une couche d'oxyde sur la mécanique de nano-objets. Elle combine des observations expérimentales ainsi que des campagnes de simulation atomistique réalisées afin de mieux appréhender le système qui permettrait d'étudier les propriétés mécaniques de nanoparticules réduites et oxydées.

## Chapitre 1 - Etat de l'art

Ces dernières années, l'étude des processus élémentaires de déformation dans les matériaux aux petites échelles est devenue plus fiable, grâce aux progrès des techniques modernes de mécanique à petite échelle telles que la nano-indentation ou les tests de nano-compression *in situ*. Ces tests dont sont extraits les courbes contrainte-déformation montrent des accidents de déformation significatifs, à des valeurs plus élevées de contrainte que pour les échantillons massifs, et lorsque la taille est réduite, ces serrations deviennent plus fréquentes. A l'échelle nanométrique, un tel comportement s'explique principalement par un processus de déformation élémentaire appelé nucléation de dislocations. En effet, tandis que la déformation des matériaux plus massifs repose sur la multiplication des dislocations et de leur libre parcours moyen en tenant compte des défauts internes, les nano-objets contiennent généralement peu ou pas de défauts, ce qui signifie que les dislocations doivent être nucléées (c'est-à-dire créées dans le nanocrystal) pour activer la déformation plastique. Dans ce contexte, les

expériences de micro- et nanomécanique permettent une bonne compréhension des mécanismes fondamentaux de déformation. Cependant, ces expériences souffrent de plusieurs limitations qui entravent une caractérisation fiable. La reproductibilité des expériences est souvent remise en question en raison de biais (extrinsèques ou intrinsèques) expérimentaux, ce qui peut entraîner une dispersion des données. Ces biais sont liés soit à la fiabilité des mesures, à la préparation des échantillons, au protocole, soit aux caractéristiques inhérentes de l'échantillon considéré telles que l'état de surface [Greer and De Hosson 2011; Gerberich et al. 2017; Dehm et al. 2018]. En revanche, les résultats des simulations présentent moins de dispersion par rapport aux expériences, en raison des conditions idéales dans lesquelles les tests sont réalisés et des formes très simplifiées des échantillons. Des travaux ont été entamés pour une meilleure description des échantillons dans les simulations. Notamment, le rôle des marches atomiques en surface a été révélé dans la réduction des performances mécaniques des nano-objets. Cependant, il n'existe actuellement aucune étude numérique exclusivement dédiée à la résistance des nano-objets présentant des surfaces rugueuses. Dans ce travail, nous nous concentrerons sur une meilleure modélisation des biais qui peuvent potentiellement jouer un rôle dans la dispersion des données observée lors des tests mécaniques. En particulier, nous étudions l'influence du mode de contrôle lors de l'essai, ainsi que l'état de surface, dans leur implication sur la résistance et le comportement mécanique des nano-objets.

## Chapitre 2 - Méthodes

Ce chapitre décrit les méthodes utilisées tout au long de ma thèse. Dans les simulations atomistiques, les potentiels interatomiques permettent de modéliser les interactions atomiques en décrivant des paramètres clés du système atomique, tels que le paramètre d'équilibre du réseau, l'énergie de formation des défauts, l'énergie de sublimation, les constantes d'élasticité, etc. Ces potentiels peuvent être basés sur des formulations analytiques simples ou sur des équations inspirées de la mécanique quantique. Dans cette thèse j'utilise des potentiels EAM décrivant les interactions métalliques, et des potentiels de type ReaxFF décrivant les interactions entre atomes métalliques et d'oxygène. De plus, les protocoles de simulation y sont décrits tels que ceux pour la minimisation d'énergie du système, la mise à l'équilibre thermique, les essais mécaniques ou l'oxydation. Enfin, les outils utilisés en support des études de ma thèse sont présentés tels que ATOMSK, OVITO ou Gmsh.

## Chapitre 3 - Nanomécanique contrôlée en force vs. en déplacement

Il n'existe que peu de méthodes permettant d'étudier les propriétés mécaniques à petite échelle. Entre autres, on peut citer la nanoindentation, la micro- et nanocompression ainsi que les essais de traction [Hemker and Sharpe 2007; Legros 2014]. Ces

techniques sont soit contrôlées en force (c'est-à-dire pilotées par des actionneurs qui appliquent des forces) ou contrôlées en déplacement. Les essais contrôlés en force sont facilement discernables des essais contrôlés en déplacement lorsque l'on examine les courbes force-déplacement. Cela est particulièrement vrai lorsque la réponse mécanique atteint le régime de déformation plastique, caractérisé par de grands sauts de déplacement (contrôle en force) ou des chutes de charge soudaines (contrôle en déplacement). Lorsqu'elles sont appliquées à l'étude des nanoparticules sous compression ou à la nanoindentation de films minces, les deux méthodes sont utilisées sans avoir clairement identifié le rôle du mode de contrôle sur la réponse en charge ou sur l'évolution de la forme de l'échantillon [Mordehai et al. 2011a; Han et al. 2015; Issa et al. 2015; Issa et al. 2021]. D'autre part, les simulations atomistiques sont également utilisées pour étudier la mécanique des nano-objets et sont intrinsèquement contrôlées en déplacement, ce qui limite leur utilisation pour discuter des expériences contrôlées en force [Mordehai et al. 2018; Amodeo and Pizzagalli 2021]. Dans ce chapitre, nous développons une approche originale pour réaliser des simulations numériques contrôlées en force. Nous l'utilisons pour discuter des principales différences entre les deux modes de contrôle dans le contexte d'expériences et de simulations récentes réalisées sur des nanoparticules métalliques d'or et d'argent ainsi que sur des films minces de nickel. Alors que les simulations contrôlées en déplacement montrent une plasticité intermittente et des chutes de force, les simulations contrôlées en force sont caractérisées par des sauts de déformation, plus conformes aux observations expérimentales. Une attention particulière est accordée à l'évolution de la microstructure des dislocations en fonction du mode de contrôle. Les résultats montrent des microstructures totalement différentes. Quel que soit le mode de contrôle, le premier événement plastique entraîne un affaiblissement global des nano-objets, c'est-à-dire que l'échantillon est caractérisé par un plus grand nombre de défauts qu'auparavant. Alors que l'affaiblissement de l'échantillon est compensé par la chute de charge dans le cas du contrôle en déplacement, il a des conséquences dramatiques sous le contrôle en force où la force de compression augmente de manière monotone avec le temps : l'échantillon est poussé plus fort tout en étant moins résistant. Par conséquent, les nanoparticules s'effondrent spontanément en une forme de crêpe (nano-compression) et l'indenteur pénètre considérablement au sein du film mince (nano-indentation), en raison de l'avalanche de dislocations. Cette dynamique diffère de celle du contrôle en déplacement qui est caractérisée par des pics intermittents et des chutes de la densité de dislocations. Enfin, l'interprétation d'expériences récentes basées sur des simulations atomistiques sont révisées, y compris le modèle d'enveloppe généralement utilisé pour corrélérer les simulations atomistiques contrôlées en déplacement et les expériences contrôlées en force.

## Chapitre 4 - *Pyrough* : un outil pour construire des échantillons 3D avec des surfaces rugueuses

Les rugosités de surface ont une influence significative sur les caractéristiques mécaniques, physiques et chimiques des matériaux massifs, tout en jouant un rôle crucial aux petites échelles, tel que dans le domaine de la catalyse, où la configuration des surfaces détermine l'efficacité des réactions chimiques. Dans le domaine de la nanomécanique, les aspérités et les creux résultants de la rugosité de surface jouent un rôle majeur en agissant comme des concentrateurs de contrainte [Brochard et al. 2000b; Gouldstone et al. 2001; Mitlin et al. 2005; Navarro et al. 2008; Brochard et al. 2010; Bel Haj Salah et al. 2017]. Les études ont clairement démontré que la morphologie de surface influence de manière significative le comportement des matériaux cristallins, notamment en ce qui concerne le processus de nucléation des dislocations, ce qui souligne l'importance de comprendre et de maîtriser la rugosité de surface dans divers domaines de l'ingénierie des matériaux. Bien que l'optimisation de forme soit récemment apparue comme une première étape vers une conception d'échantillon plus réaliste [Amodeo and Lizoul 2017; Kilymis et al. 2018; Zimmerman et al. 2021], la majorité des simulations numériques atomistiques et macroscopiques se basent sur une conception d'échantillon simplifiée (utilisant par exemple des surfaces planes ou des angles et des bords lisses). Cela empêche l'étude de l'influence des détails de surface et confirme qu'un outil manque pour générer des échantillons virtuels plus réalistes. Dans cette étude, nous décrivons le développement d'un outil numérique libre d'accès appelé *Pyrough*, conçu pour le design d'échantillons virtuels avec des surfaces rugueuses destinés à la modélisation atomistique et aux simulations par éléments finis. La méthode de construction des échantillons est basée sur la théorie classique de la rugosité [Mandelbrot 1985; Jacobs et al. 2017]. *Pyrough* donne à l'utilisateur la possibilité de gérer la rugosité de surface et la distribution des profils de hauteur pour la génération d'objets virtuels rugueux. Contrairement aux solutions existantes dans les domaines de la tribologie et du contact [Multiphysics 1998; Röttger et al. 2022; Lim 2023; Kanafi 2023], *Pyrough* peut servir de pré-processus, pour la génération d'échantillons virtuels rugueux, aux formats d'entrée adaptés aux principaux logiciels de simulation numérique. Dans ce chapitre, nous rappelons d'abord les principaux concepts de la théorie classique de la rugosité et comment générer numériquement des surfaces rugueuses. Ensuite, des détails sur la structure de *Pyrough*, la gestion des fichiers d'entrée/sortie et la génération de surface rugueuse pour plusieurs formes 3D sont fournis. Enfin, des exemples d'applications de *Pyrough* mettant en évidence le rôle de la rugosité de surface sont présentés.

## **Chapitre 5 - Influence des rugosités de surface sur la déformation de nanoparticules d'or en compression**

Bien qu'il soit connu que les surfaces jouent un rôle clé à l'échelle nanoscopique, il devient évident que la caractérisation rigoureuse et l'optimisation des surfaces des nano-objets sont au cœur de la nanomécanique et de l'ingénierie des défauts. Néanmoins, plus l'échantillon est petit, plus il est difficile de le tester mécaniquement. Une conséquence directe de la réduction de taille est une réponse mécanique de plus en plus dispersée en raison à la fois des biais intrinsèques et extrinsèques. En effet, la limite élastique des nano-objets peut varier de plus d'un ordre de grandeur à taille constante, comme le montrent par exemple les références [Sharma et al. 2018; Shahbeyk et al. 2019; Zimmerman et al. 2021]. Dans ce contexte, nous considérons la rugosité de surface comme une source potentiellement majeure de dispersion lors de la mesure de la résistance des nano-objets. Les surfaces des nano-objets métalliques sont souvent rugueuses, avec des marches de surface allant d'une seule couche atomique à plusieurs nanomètres (voir par exemple les références [Iijima 1985; Zhang et al. 2001b; Mordehai et al. 2011b; Kim et al. 2018]). Dans ce chapitre, nous illustrons à quel point la rugosité de surface joue un rôle clé sur la résistance et les processus de déformation élémentaires de nanoparticules métalliques. Nous montrons ici que même la plus faible rugosité impacte considérablement la résistance critique de l'échantillon, pouvant diminuer de près de 80% comparativement à la résistance moyenne des échantillons avec une surface de contact parfaitement plane. Ce résultat apporte des pistes pour expliquer la dispersion des données régulièrement observée dans les expériences à l'échelle nanométrique pour les contraintes critiques. De plus, les nombreuses simulations effectuées confirment que la force critique est parfaitement corrélée avec la morphologie de la surface de contact, c'est-à-dire la fraction d'atomes en contact avec l'indenteur. Un facteur d'échelle de 1 à 2 est introduit pour les régions de contact plus petites où la forme de la première dislocation nucléée passe d'une demi- (îlots isolés) à un quart de boucle (connexion aux bords latéraux). Notre approche statistique a permis de concevoir un modèle de prédiction de la dispersion de la contrainte critique dans le cas d'échantillons à surfaces rugueuses, reposant uniquement sur deux principaux paramètres, à savoir : la caractérisation de la surface supérieure et la résistance idéale du système. Tous deux pouvant être déduits de l'expérience ou de la théorie. De plus, la rugosité de surface s'est révélée être à l'origine de processus de déformation exotiques dans les nanoparticules métalliques d'or, notamment la nucléation et le glissement de dislocations dans des systèmes de glissement inhabituels, ce qui pourrait expliquer des observations expérimentales récentes [Richard et al. 2023].

# **Chapitre 6 - Dynamique de croissance d'une couche d'oxyde sur un film mince métallique et son influence sur la résistance**

L'oxydation des surfaces de métaux et d'alliages métalliques présente un intérêt significatif [Cabrera and Mott 1949; Atkinson 1985] et est cruciale pour diverses applications allant de la microélectronique et la catalyse hétérogène à la protection contre l'usure et la corrosion. De nombreuses études expérimentales se sont concentrées sur la compréhension des processus impliqués dans l'oxydation des métaux. Certains groupes de recherche ont étudié le mécanisme et la cinétique de la croissance des oxydes métalliques [Atkinson et al. 1982; Jeurgens et al. 1999], tandis que d'autres ont exploré la réaction des molécules d' $O_2$  avec les surfaces métalliques [Yamazoe et al. 1979; Kulakarni et al. 1995; Benka and Steinbatz 2003], ainsi que l'adsorption initiale et la diffusion des atomes d'oxygène [Narusawa et al. 1981; Matsumoto et al. 2001; Chevalier et al. 2005]. D'un point de vue mécanique numérique aux petites échelles, seul un nombre limité d'études ont abordé l'influence potentielle d'une couche d'oxyde sur la résistance des nano-objets. Cela représente un manque évident, notamment lorsqu'on considère les observations récentes dans les tests mécaniques qui révèlent la présence d'une couche d'oxyde autour de certaines nanoparticules [Han et al. 2015; Kositski et al. 2016; Sharma et al. 2018; Sharma et al. 2020]. Dans ce chapitre, nous présentons une étude expérimentale préliminaire qui se concentre sur l'oxydation et la réduction de nanoparticules de nickel, réalisée dans le but d'obtenir des informations sur les conditions expérimentales nécessaires aux tests mécaniques et à l'étude de l'impact d'une couche d'oxyde sur la résistance des nano-objets. La cinétique d'oxydation du nickel est quasi instantanée, ce qui en fait un matériau difficile à contrôler lors d'essais non-environnementaux. Pour mieux appréhender le système à étudier dans de telles expériences, nous avons mené une campagne de simulations atomistiques. Le cuivre démontre une cinétique plus lente, ce qui en fait un meilleur candidat. Enfin, des tests virtuels de nano-indentation sont réalisés pour fournir des premiers aperçus de l'influence d'une couche d'oxyde sur la résistance des échantillons métalliques. Les premiers résultats démontrent l'influence accrue de la couche d'oxyde sur les propriétés mécaniques des échantillons métalliques.

## **Conclusion**

Ce manuscrit de thèse repose sur le développement et l'application de méthodes originales visant à permettre une représentation plus précise des essais nanomécaniques dans les simulations. Malgré les données expérimentales très dispersées autour de la tendance globale, il est difficile de distinguer entre les biais intrinsèques et extrinsèques, ce qui empêche la prédiction précise des propriétés mécaniques des nano-objets. Cette limitation n'a pas été rigoureusement abordée par les approches de modélisation existantes, qui négligent souvent l'influence de la géométrie, l'état de

surface de l'échantillon et l'utilisation de protocoles de test adequats. Cela aboutit à une disparité entre les résultats de simulation et les conclusions expérimentales. Notre travail comble cette lacune en prenant en compte les biais expérimentaux dans les simulations, ouvrant ainsi la voie à des études numériques plus réalistes. Nous montrons à quel point le mode de contrôle influence la dynamique des essais mécaniques et les processus de déformations induits dans les nano-objets, où l'avalanche de dislocations explique les formes finales de crêpe ou les "pop-in" observés expérimentalement. Nous démontrons également que la présence de rugosités en surface des échantillons virtuels est responsable de variations allant jusqu'à 80% de la contrainte critique théorique dans les nano-objets. Ces écarts sont en accord qualitatif avec les observations expérimentales qui peuvent montrer jusqu'à un ordre de grandeur de différence entre les contraintes critiques de deux échantillons de même taille. Enfin, la présence d'une couche d'oxyde sur des échantillons métalliques a montré des propriétés mécaniques totalement différentes de celles des échantillons non-oxydés. Ces résultats ouvrent la voie à de futures études telles que la caractérisation expérimentale de profils de rugosité pour leur reproduction et leur influence sur des échantillons virtuels et leurs propriétés mécaniques, l'étude de profils rugueux de plus grande amplitude et leur effet sur les contraintes critiques de nano-objets, ou bien des essais mécaniques expérimentaux sur des échantillons oxydés et non-oxydés.

## **Remerciements**

My deepest gratitude goes first and foremost to *Thomas CORNELIUS*, *Olivier THOMAS* and *Jonathan AMODEO*, my supervisors, for their invaluable guidance, unwavering support, and expertise throughout the completion of this thesis. Your enlightened mentorship, insightful feedback, and availability have profoundly enriched my PhD journey and made it immensely enjoyable. Our discussions and your diverse perspectives have been immense sources of knowledge for me. I am grateful for the trust you placed in me and your constant encouragement to aim for the highest standards. Without your consistent and illuminating instruction, this thesis could not have reached its present form.

I would like to express additional profound appreciation to my supervisor, *Jonathan AMODEO*. I am deeply grateful for every explanation, your clarity, passion, and all the insightful and fruitful hours-long discussions we had. Your support and guidance have been instrumental in my professional and personal growth. Thank you for your mentorship and for consistently pushing me to achieve my best.

I would like to thank the ANR (SASHA), the CNRS and the IM2NP for funding and hosting this PhD thesis.

I would like to thank all the jury members: *Lars PASTEWKA*, *Nicolas COMBE*, *Marie-Ingrid RICHARD*, *Eugen RABKIN* and *Vladislav YASTREBOV*, for having accepted to read and evaluate my PhD work.

I would like to thank *Laurent PIZZAGALLI* and *Pierre BENIGNI* for being part of my PhD management committee, for your follow-up, your advice and your listening skills.

I would like to thank my colleagues from the MNO team: *Lydia ABBASSI*, *Jonathan AMODEO*, *Thomas CORNELIUS*, *Stéphanie ESCOUBAS*, *Thomas FERNANDES*, *Christophe GUICHET*, *Stéphane LABAT*, *Jean-Marc ROUSSEL*, *Soufiane SAIDI*, *Michaël TEXIER*, *Olivier THOMAS*, *Abdelrahman ZAKARIA* for their warm welcome, unwavering support, valuable knowledge exchange, availability, and enlightening discussions.

Thank you *Solène DASSONNEVILLE*, for your kindness, moral support, friendship, constant good mood and all the coffee-breaks we shared.

Thank you *Marc GAILHANOU*, the mood-boosting IT-guy, for your advice, listening skills and all the stimulating conversations we had.

Thank you *Sarah YEHYA*, my coffee-mate, it was great sharing the office with you, good luck on your post-doctoral journey.

I also owe the most sincere gratitude to my friends.

Thank you *Léo*, *Matthieu*, *Maxime*, *Paul*, *Riccardo* and *Stéphan*, my team, for all the great times we had together in Marseille. Thank you for always hearing me complain, for always having my back, for keeping me healthy by sharing tennis, squash, running or gym sessions, for the week-ends we spent together, for the before-parties we had at my apartment and overall for all the great memories that truly enriched my life. It all

began at IMT Mines Albi, led us to Marseille, and I am sure that wherever I will be in the future, I can always rely on your friendship and support.

Thank you *Nicolas*, my "tech lead", for sharing your software engineering and data science skills with me. You were truly part of this project and I look forward to running more with you.

Thank you to all my long-distance childhood friends from Nancy, for your support, for always being there when I got home and for all the great times we had together.

Finally, to my family and my parents, you are my rock, my strength, my inspiration, my everything. Thank you for making *Alice* and I your first priority, for giving us everything and for making our life the best it can be. The education, values and commitment you dedicated to me have shaped my path and made me proud of the man I am today. I dedicate this PhD thesis to you.

# Contents

## Affidavit

<b>Liste de publications et participation aux conférences</b>	I
<b>Résumé et mots clés</b>	II
<b>Abstract and keywords</b>	IV
<b>Résumé étendu</b>	VI
<b>Remerciements</b>	XV
<b>Glossary</b>	5
<b>General introduction</b>	7
<b>1. Literature review</b>	12
1.1. Small scale mechanics . . . . .	13
1.1.1. Smaller is stronger . . . . .	13
1.1.2. Focus on nanomechanics . . . . .	15
1.2. Data scattering and experimental biases . . . . .	22
1.2.1. Strength master plot . . . . .	22
1.2.2. Experimental biases . . . . .	23
1.3. Current state on modeling nanomechanics . . . . .	28
1.3.1. Generalities . . . . .	28
1.3.2. Modeling the mechanics of nanoparticles . . . . .	31
1.3.2.1. Methods . . . . .	31
1.3.2.2. Dislocation nucleation and plasticity in metal nanoparticles . . . . .	31
1.3.2.3. Shape-effect . . . . .	34

1.3.3. Introduction to the modeling of surface alteration . . . . .	35
1.3.3.1. From surface step to atomic-scale roughness . . . . .	35
1.3.3.2. Surface oxidation . . . . .	38
<b>2. Methods</b>	<b>41</b>
2.1. Introduction to atomistic simulations and modeling . . . . .	42
2.1.1. Interatomic potentials . . . . .	42
2.1.1.1. Embedded atomic method . . . . .	42
2.1.1.2. Reactive force field . . . . .	43
2.1.2. Energy minimization using molecular statics . . . . .	48
2.1.3. Molecular dynamics . . . . .	49
2.1.3.1. Thermodynamic ensembles . . . . .	50
2.1.3.2. Boundary conditions . . . . .	52
2.2. Atomistic simulation protocol . . . . .	53
2.2.1. Sample preparation . . . . .	53
2.2.2. Mechanical testing . . . . .	54
2.2.3. Surface oxidation . . . . .	57
2.3. Auxiliary tools and software . . . . .	59
2.3.1. COMSOL . . . . .	59
2.3.2. Gmsh . . . . .	59
2.3.3. Paraview . . . . .	59
2.3.4. <i>Pyrough</i> . . . . .	60
2.3.5. ATOMSK . . . . .	60
2.3.6. Wulffpack . . . . .	60
2.3.7. OVITO . . . . .	61
<b>3. Load vs. displacement controlled nanomechanics</b>	<b>62</b>
3.1. Introduction . . . . .	63
3.2. Load controlled nanocompression modeling . . . . .	64
3.2.1. Methods . . . . .	64
3.2.2. Application to the compression of faceted Au nanoparticles . .	65
3.2.2.1. Mechanical response . . . . .	65
3.2.2.2. Dislocation microstructure . . . . .	67
3.2.2.3. Further developments . . . . .	70
3.2.3. Comparison to the load envelope model . . . . .	72
3.3. Towards nanoindentation modeling . . . . .	73
3.3.1. Methods . . . . .	73
3.3.2. Application to the nanoindentation of Ni thin films . . . . .	76
3.3.3. Benchmarking . . . . .	78
3.4. Conclusion . . . . .	79
<b>4. <i>Pyrough</i> : a tool to build 3D samples with rough surfaces</b>	<b>81</b>
4.1. Introduction . . . . .	82

<b>4.2. Classical roughness modeling . . . . .</b>	<b>83</b>
4.2.1. Current state . . . . .	83
4.2.1.1. Fractal and roughness theory . . . . .	83
4.2.1.2. Statistical descriptors . . . . .	85
4.2.2. Application to contact and friction mechanics . . . . .	86
4.2.3. Rough surface construction using <i>Pyrough</i> . . . . .	88
<b>4.3. Pyrough implementation . . . . .</b>	<b>91</b>
4.3.1. General workflow . . . . .	91
4.3.2. Input file . . . . .	92
4.3.3. <i>In silico</i> roughness design (Sample class) . . . . .	93
4.3.4. Refinement and volumetric 3D mesh . . . . .	98
4.3.5. Atomic position file generation . . . . .	99
4.3.6. Outputs . . . . .	99
<b>4.4. Other examples of application . . . . .</b>	<b>101</b>
4.4.1. Statistically-equivalent surface construction . . . . .	101
4.4.2. Nanoindentation with a roughened spherical tip . . . . .	103
4.4.3. Groovy grain boundary and interface . . . . .	104
4.4.4. Nanowire with rough surface . . . . .	105
<b>4.5. Conclusion . . . . .</b>	<b>106</b>
<b>5. Influence of surface roughness on the deformation of gold nanoparticles in compression . . . . .</b>	<b>108</b>
5.1. Introduction . . . . .	109
5.2. Methods . . . . .	109
5.2.1. Design of nanoparticle with rough surfaces . . . . .	109
5.2.2. Molecular dynamics simulation . . . . .	111
5.3. Results . . . . .	112
5.3.1. Nanoparticle equilibration . . . . .	112
5.3.2. Mechanical response . . . . .	114
5.3.3. Deformation processes . . . . .	116
5.4. Discussion . . . . .	119
5.4.1. Effect of roughness on the strength . . . . .	119
5.4.2. Nucleation model in case of rough surfaces . . . . .	122
5.4.3. Towards multi-layer roughness . . . . .	125
5.5. Conclusion . . . . .	127
<b>6. Surface oxide layer : growth dynamics and influence on nanoin-dentation . . . . .</b>	<b>129</b>
6.1. Introduction . . . . .	130
6.2. Experimental observations of metal nanoparticle oxidation . . . . .	131
6.2.1. Sample preparation and preliminary characterization . . . . .	131
6.2.2. Environmental microscope oxido-reduction of Ni nanoparticles . . . . .	131
6.2.3. Main experimental outcomes . . . . .	133

## *Contents*

6.3. Numerical study of oxide growth on metal at the nanoscale . . . . .	134
6.3.1. Methods . . . . .	134
6.3.2. Oxidation rate and processes . . . . .	135
6.3.3. Oxide structure and re-crystallisation attempts . . . . .	138
6.3.4. Effect of surface roughness . . . . .	141
6.4. Nanoindentation of oxidized nanocrystals . . . . .	143
6.5. Conclusion . . . . .	147
<b>Conclusion and perspectives</b>	<b>149</b>
<b>Bibliography</b>	<b>154</b>
<b>Appendix</b>	<b>190</b>
A. Surface energy calculation . . . . .	190
B. Example of <i>Pyrough's</i> input files . . . . .	191
C. Thermal expansion coefficient computation . . . . .	193
<b>List of Figures</b>	<b>194</b>
<b>List of Tables</b>	<b>204</b>

## **Glossary**

<b>AFM</b> : Atomic force microscope	<b>BC</b> : Boundary condition
<b>BCC</b> : Body-centered cubic	<b>CG</b> : Conjugate gradient
<b>DDD</b> : Discrete dislocation dynamics	<b>DFT</b> : Density functional theory
<b>DXA</b> : Dislocation extraction algorithm	<b>EAM</b> : Embedded atom method
<b>EEM</b> : Electronegativity equalization method	<b>ETEM</b> : Environmental transmission electron microscope
<b>FCC</b> : Face-centered cubic	<b>FEM</b> : Finite-elements modeling
<b>FFT</b> : Fast Fourier transform	<b>FIB</b> : Focused ion beam
<b>FIRE</b> : Fast inertial relaxation engine	<b>GB</b> : Grain boundary
<b>HCP</b> : Hexagonal close packed	<b>HFTN</b> : Hessian-free truncated Newton
<b>LAMMPS</b> : Large-scale atomic/molecular massively parallel simulator	<b>MD</b> : Molecular dynamics
<b>MEAM</b> : Modified embedded atom method	<b>MS</b> : Molecular statics
<b>NEB</b> : Nudged elastic band	<b>NO</b> : Nano-object
<b>NP</b> : Nanoparticle	<b>NW</b> : Nanowire
<b>PBC</b> : Periodic boundary condition	<b>PID</b> : Proportional integral derivative
<b>PRDF</b> : Partial radial distribution function	<b>PSD</b> : Power spectrum density
<b>PTM</b> : Polyhedral template matching	<b>ReaxFF</b> : Reactive force field
<b>SDN</b> : Surface dislocation nucleation	<b>SEM</b> : Scanning electron microscope
<b>SMTB-Q</b> : Second moment tight binding - QEq	<b>STM</b> : Scanning tunneling microscope
<b>SWBC</b> : Shrink-wrapping boundary condition	<b>TEM</b> : Transmission electron microscope

## **General introduction**

Recent advances observed across various technological domains such as medicine, electronics, and mechanics are often implicitly linked to the investigation of nanostructures, characterized by dimensions of the order of a few hundreds or tens of nanometers. Their extensive range of applications is related to the radical changes in their physical properties. In medicine, for instance, nanoparticles (NPs) encapsulated with high chemical absorptive capacities are used for drug delivery [Mohanraj and Chen 2007], as well as for imaging and therapeutic interventions [Paranjpe and Müller-Goymann 2014]. Within information storage technology, nanowires (NWs) are harnessed for their superparamagnetic properties, which include rapid response to external fields coupled with minimal remanence [Lu et al. 2007; Zhang et al. 2010]. In the realms of tribology and mechanics, NPs are employed to optimize lubricant performance [Akbulut 2012; Cui et al. 2020], and in the fabrication of implants [Li et al. 2020b], owing to their exceptional resistance. Additionally, nanocrystals and their improved mechanical characteristics are used to reinforce materials of larger dimensions. At larger scales, NPs serve as fundamental blocks for the construction of nanocrystalline materials, which can be subsequently sintered and compacted to improve the properties of compounds used in devices requiring high mechanical resilience. NWs also serve as reinforcing agents [Elssfah et al. 2007; Shen et al. 2019].

In addition to conventional bulk characterization methods, nano-objects (NOs) can be investigated through mechanical testing, often revealing the so-called "smaller is stronger" trend [Uchic et al. 2009; Greer and De Hosson 2011]. The observed increase in strength of nanocrystals is typically coupled with an increase in ductility. Central to this behavior is an elemental deformation process, that predominantly occurs at the nanoscale, known as dislocation nucleation. While traditional materials engineering focuses on managing dislocation multiplication and their mean-free path with defect contents, NOs generally exhibit few or no defects, which necessitates the nucleation of dislocations within the nanocrystal to enable plastic deformation. Various numerical and experimental methodologies exist to explore the deformation mechanisms of NOs. For instance, nanocompression testing imaged *in situ* via scanning (SEM) or transmission (TEM) electron microscopy represents one of the most prevalent techniques for experimental characterization of NPs. Experimental investigations encompass a range of sizes, typically spanning from a few hundred nanometers down to a few tens of nanometers, and involve low deformation rates ranging from  $10^{-4}$  to approximately  $1\text{ s}^{-1}$ . Despite the advantages of transmission electron microscopy in providing microstructural, defect, and surface characterizations, its application remains a complex and tedious method. Commonly encountered issues include sample misalignment, setup control mode, contamination, surface roughness, and oxidation [Williams and Carter 1996; Zaeferer 2011]. These lead to data scattering deviating from the anticipated trends and hampering the reproducibility of experimental outcomes, which impedes comprehensive statistical analyses.

Given the significance of imperfections [Greer et al. 2013], the process of dislocation nucleation adheres to classical nucleation theory and typically initiates from defective

regions. As surfaces represent primary defective regions of NOs, they serve as sources for the dislocation nucleation mechanism. Hence, while it is widely acknowledged that surfaces at the nanoscale play a key role in functional property applications, it becomes evident that controlling surface morphology could quantitatively impact the mechanical behavior of NOs. Specifically, alterations such as amorphous coatings, oxide layers, and surface roughness can influence the strength of NOs by either affecting the activation energy of the dislocation nucleation process or the type of defects nucleated. However, decorrelating the effects of intrinsic and extrinsic biases in experiments poses a challenge, which hinders the predictive evaluation of the mechanical properties of NOs.

On the other hand, computational methods often provide a support to aid in the interpretation of experimental outcomes. While a variety of simulation techniques in physics and mechanics, such as *ab initio* simulations [Ouyang et al. 2010], dislocation dynamics [Roy et al. 2019], and analytical or finite-element models (FEM) [Cordero et al. 2016], are employed to give insights into the elastic and plastic properties of NOs, molecular dynamics (MD) emerges as the key method due to its ability to describe atomic-scale processes in samples with size comparable to those of the experiment [Komanduri et al. 2001; Amodeo and Pizzagalli 2021]. MD relies on interatomic potentials to compute atomic forces and integrate the dynamics of all atoms within a sample under load. However, due to computational costs, MD is limited in size and simulations are conducted at exceedingly high strain rates ( $\sim 10^8 \text{ s}^{-1}$ ). Yet, the ability of MD to accurately capture the mechanical behavior of experimental NOs remains a subject of debate. Presently, MD simulations are not able to replicate the scattering of strength observed in NOs nanomechanical experiments. This discrepancy presents a significant challenge that impedes a comprehensive understanding of the mechanical properties of NOs and increases the gap between experimental observations and computational simulations. We believe that a large part of the solution lies in the design of samples. Currently, virtual samples are typically fashioned using simplistic and symmetrical shapes, such as perfect spheres, sharp cubes, cylinders, and flawless surfaces. To enhance their predictive capability regarding the integrity of NOs under stress, simulations require more intricate and realistic sample designs, incorporating a detailed description of surface topology, which includes surface roughness and chemical alterations.

Based on these considerations, one can rise the question on the necessity to develop new methods for an accurate protocol and sample description to investigate the influence of extrinsic and intrinsic biases on the strength of NOs. In other words, is it possible to include in a rigorous way real-life imperfections within the simulation world to reproduce and understand the experimentally observed data scattering ?

Here we will see that the answer might rely on the development and application of original nano-by-design modeling methodologies and protocols that better account for surface architecture and experiment specifications when probing physical and

mechanical properties of NOs. Surface roughness and alteration will be accounted leading to more realistic shapes, closer to experimental observations. A better description of samples should strongly influence the deformation processes and mechanical responses, bridging the current gap between nanomechanical experiments and simulations.

The thesis manuscript is organized as follows. In the first chapter, we review the mechanical properties of small-scale objects starting from the micro- down to the nanoscale, including the different deformation mechanisms that come into play. Also, a literature review on the extrinsic and intrinsic biases observed in experiments is made, notably on their influence on the dispersion of data around the global strength trend. From a simulation point of view, we depict the studies that have been performed to date, with a special focus on the lack of accurate samples and protocols description that creates a gap with the experiments. In chapter two, we introduce atomistic simulation theoretical basics and the numerical protocols developed during my PhD to perform mechanical or oxidation tests following sample optimization and thermal equilibration phases. The various interatomic potentials used to describe atomic interactions in this work are presented as well as their relative theoretical background. Additionally, we introduce every side tools employed in the several studies reported in this thesis. In the third chapter, we describe the original algorithm developed to run load-controlled atomistic simulations. Details about the theoretical bricks and the method workflow are given. Several application cases are presented including the load-controlled nanocompression of gold faceted and silver hemispherical NPs, as well as the load-controlled nanoindentation of a nickel thin film, which draw a parallel with experimental observations that were not accurately described by atomistic simulations. A detailed analysis of the deformation mechanisms allows us to explain the differences in the dynamics of both tests depending on the control mode. In chapter four, we present *Pyrough*, a open-access object-oriented Python tool developed with the aim of better representing virtual samples by considering surface roughness. Based on the classical roughness theory, we present the methods and the development of the code that allow to generate 3D samples with surface roughness, for FEM or atomistic simulations. Thanks to an easy usage, the users can monitor the roughness parameters to generate the shapes and height profiles they desire such as rough thin films, faceted and spherical NPs or cylindrical and faceted NWs. A catalog of potential applications of the code are presented as well as all the additional options available. Then, *Pyrough* is used in chapter five as the main tool for the generation of hundreds of rough gold faceted NPs. These samples are tested under compression and the variations of the strength as a function of roughness parameters is presented. Specifically, we show how surface morphology guides the movement of dislocations that nucleate within the sample. Also, a model is proposed to predict the strength distribution of rough NPs by considering the strength of the sample with flat surface and the rough surface morphologies. Finally, in chapter six, we propose an original study on the growth and influence of an oxide layer on the strength of NOs. An initial experimental phase is conducted using an environmental transmission

*General introduction –*

electron microscope (ETEM), where the oxidation and reduction conditions for nickel NPs are proposed. Then, an atomistic simulation study for the comparison of nickel and copper oxide growth kinetics is performed. The oxidized surfaces are also tested under nanoindentation, where different deformation mechanisms are observed as compared to pure crystalline samples.

# 1

## Literature review

In this chapter, we review the literature on micro and nano-scale mechanics with a special focus on the strength and deformation mechanisms of NOS. We introduce the main biases that can induce data scattering when trying to extract statistics from experimental nanomechanical testing campaigns. Finally, we present an overview of the current results in modeling nanomechanics and whether these aforementioned biases are quantified, or not.

## 1.1. Small scale mechanics

### 1.1.1. Smaller is stronger

In recent years, the study of elementary deformation processes at small-scales has become more reliable, thanks to advances in modern experimental techniques such as indentation or *in situ* compression tests. Propelled by advancements in focused ion beam (FIB) technology, the micromachining technique has been increasingly employed for the preparation of small-size specimens derived from bulk materials, specifically tailored for micro and nano-compression tests. Uchic *et al.* pioneered the application of these tests using FIB-milled Ni micro-pillars [Uchic et al. 2004]. They were fabricated through FIB micromilling, with one end remaining seamlessly connected to the substrate that serves as a lower compression plate during the compression test. This methodology avoids micro-manipulation and ensures that the orientation of the pillars matches that of the bulk material [Uchic and Dimiduk 2005; Dimiduk et al. 2005]. SEM images of these samples are shown in Figure 1.1.

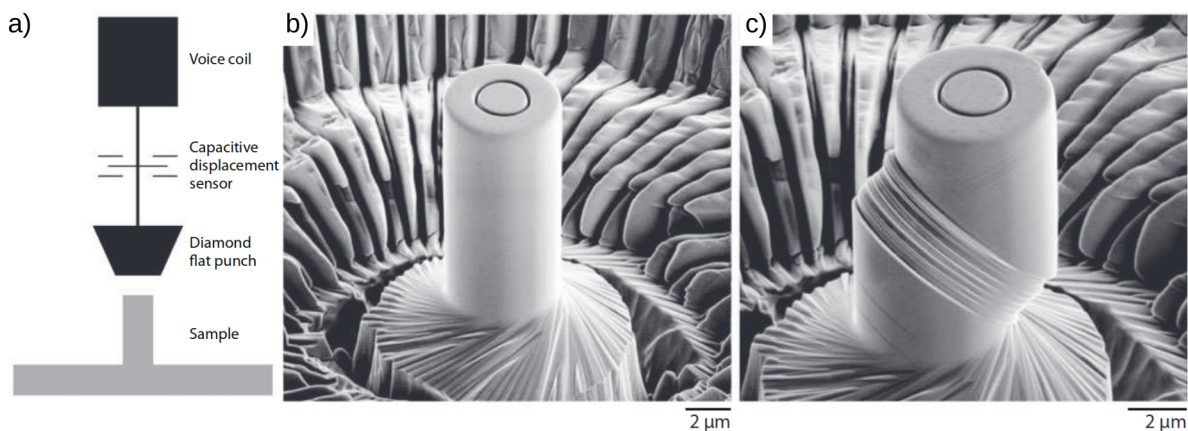


Figure 1.1.: Microcompression of a 5  $\mu\text{m}$  diameter pillar of pure Ni oriented for single slip. a) Schematic of the microcompression test setup. b) SEM image of the FIB-prepared sample. c) SEM image of the same sample after compression test. Adapted from [Dimiduk et al. 2005].

With the use of flat punch indenters, compression tests are performed and stress-strain curves are recorded. Figure 1.2a shows that in the case of a bulk sample, the stress-strain curve exhibits a smooth profile and a low yield strength. In contrast, the reduced-size Ni micropillars reveal noticeable strain bursts, at higher stress, and as the micropillar size is reduced, these bursts become more frequent. Thus, the strength of small single-crystal micropillars depends strongly on their size (the so-called "size-effect"). Since then, numerous research groups have repeated similar experiments on FCC [Greer et al. 2005; Volkert and Lilleodden 2006; Kiener et al. 2006] and more recently on BCC [Kim and Greer 2008; Schneider et al. 2009b] single crystals as well as in any other class of materials [Schuster et al. 2006; Schuster et al. 2008; Volkert et al.

## 1. Literature review – 1.1. Small scale mechanics

2008].

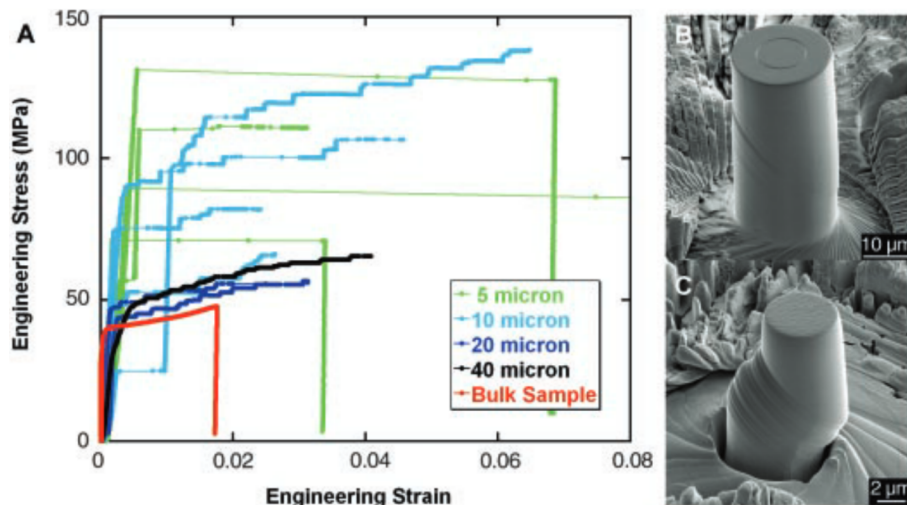


Figure 1.2.: Typical Stress-Strain curves obtained from microcompression testing experiments of pure Ni micropillars at room temperature, from [Uchic et al. 2004]

As most of these experiments revealed that strength becomes much higher as the sample size decreases, a fundamental paradigm emerges : "*Smaller is stronger*".

To explain this size effect at the microscale, several models exist including source exhaustion hardening [Dimiduk et al. 2005; Rao et al. 2008; Norfleet et al. 2008], source truncation [Parthasarathy et al. 2007; Rao et al. 2007], and weakest link theory [Rao et al. 2008; El-Awady et al. 2009]. The source exhaustion hardening process entails the formation of junctions and dipole interactions as the stress increases which results in the shutting-off of scarcely available dislocation<sup>1</sup> sources and the activation of less weak sources at higher stress levels. Following an exhaustion-hardening event, plastic deformation only proceeds when stress increments either release the recently pinned dislocation arms or activate other dislocation segments elsewhere in the material. In the case of source truncation, the conversion of pre-existing double-ended dislocation sources into single-ended sources that intersect and interact with free surfaces establishes a new and shorter characteristic length for dislocation sources, that requires higher stress levels for their activation. Moreover, according to the weakest link theory, the system seeks out the weakest link among the newly formed population of single-arm sources. At a critical stress level, and assuming no strong dislocation interactions, deformation occurs through small and repeated bursts at a constant-stress level driven by single-arm sources repeatedly expanding and interacting with free surfaces. The variation in critical stress depends solely on the location of source pins relative to free surfaces and is independent of the initial Frank-Read source length. These overarching

<sup>1</sup>Dislocations are linear defects responsible of the plastic deformation of crystalline materials.

principles involve representing dislocation source operations discretely and evaluating the impact of sample size on source lengths, thereby affecting their operational strengths. These models encapsulate the commonly observed stochastic signature of experimental results and exhibit either marginal dislocation storage [Dimiduk et al. 2006; Ngan and Ng 2010] or global dislocation loss [Shan et al. 2008; Greer and Nix 2006].

Furthermore, when delving into the nanoscale, new mechanisms justify the even higher strength observed. For instance, the starvation model hypothesizes that mobile dislocations within a NO are more likely to annihilate at a free surface than to interact with each other. Consequently, this phenomenon imposes a shift of the plastic deformation towards a nucleation-controlled regime [Greer et al. 2005; Ng and Ngan 2008; Greer et al. 2008; Brinckmann et al. 2008; Weinberger and Cai 2008; Ng and Ngan 2009].

### 1.1.2. Focus on nanomechanics

Adhering to this approach, Greer and Nix expanded the methodology into the nanoscale regime. In this context, single-crystalline Au nanopillars with diameters below 1  $\mu\text{m}$  achieved remarkable strengths, nearly 50 times higher than in bulk [Greer et al. 2005]. Moreover, numerous research groups have investigated size effects in the plasticity of diverse materials, with a significant emphasis on FCC nanopillars. This exploration has been enhanced through uniaxial tensile experiments, typically conducted within *in situ* mechanical deformation instruments [Kiener et al. 2008; Dehm 2009]. In these studies, uniaxial compression and tension tests were performed on Ni [Dimiduk et al. 2005; Frick et al. 2008], Au [Volkert and Lilleodden 2006; Greer and Nix 2006], Cu [Kiener et al. 2006; Richter et al. 2009], and Al [Ng and Ngan 2008; Ng and Ngan 2009]. Figure 1.3 summarizes the results for the strength of several FCC metal samples tested in compression and tension and illustrates the "*smaller is stronger*" trend.

Beyond single crystalline FCC metals, size effect and mechanical behavior of various systems have been published to date including BCC and HCP metals (W and Ta [Schneider et al. 2009a], Nb [Kim et al. 2009], Mo [Kim and Greer 2009], V [Han et al. 2010], Mg [Lilleodden 2010], Ti [Yu et al. 2010]), shape memory alloys (NiTi [Clark et al. 2010]), metallic glasses [Lee et al. 2007; Lai et al. 2008], Si [Moser et al. 2007; Ye et al. 2012] and ceramics [Korte and Clegg 2009; Camposilvan and Anglada 2016].

In the study conducted by Jennings *et al.*, compression experiments were performed on single-crystalline FCC  $\langle 111 \rangle$ -oriented Cu nanopillars with diameters ranging from 100 to 500 nm, fabricated via lithography with nonzero initial dislocation densities [Jennings et al. 2010]. Such method results in a smaller concentration of dislocations compared to the traditional FIB. Compression was performed at a constant displacement rate of  $2 \text{ nm} \cdot \text{s}^{-1}$  using a flat punch. Figure 1.4a illustrates the stress-strain curves of four samples with different diameters. Notably, a trend of increased strength is observed with decreasing diameter. A log-log plot in Figure 1.4b demonstrates the

## 1. Literature review – 1.1. Small scale mechanics

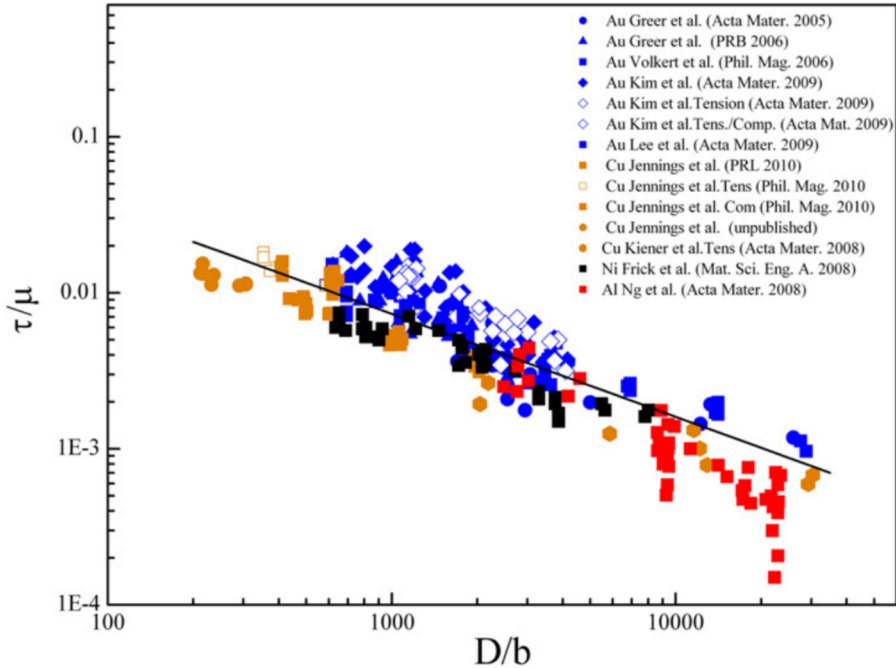


Figure 1.3.: Normalized shear flow stress *vs.* size of several FCC metallic samples, from [Greer and De Hosson 2011].

relationship between the flow stress at 10% strain and the pillar diameter It reveals a power law dependence with a slope of approximately  $-0.63 \pm 0.04$ , consistent with values reported for other metallic pillars. The authors showed that plasticity at the submicron scale is intrinsically linked to microstructure, which in turn defines size effect. In another study focusing on BCC Mo [Kim and Greer 2008], the same research group reported a size-effect in nanopillars with diameter ranging from 200 to 900 nm, compressed at the same constant displacement rate of  $2 \text{ nm.s}^{-1}$ . Figures 1.4c-d present stress-strain curves as well as flow stress and yield strength plotted against pillar diameter, respectively. The slopes of  $-0.44$  and  $-1.07$  indicate that the size effect is more pronounced for the yield strength when compared to the flow stress.

While the observed size effect appears common to both FCC and BCC materials, Brinckmann *et al.* [Brinckmann et al. 2008] explained that fundamentally distinct dislocation motion mechanisms might operate, which explains the different flow stresses observed in Figures 1.4a-c. In FCC crystals, dislocations readily split into ribbons separated by stacking faults, thereby impeding cross-slipping and confining them to glide in {111}-type planes [Duesbery 1998; Brinckmann et al. 2008]. Consequently, in an FCC nanopillar, the proximity of dislocations to the free surface increases their propensity to escape the crystal due to image forces, which leads to dislocation starvation. Conversely, in BCC metals, the screw components of a dislocation loop are not confined to a single glide plane and can move in all three dimensions, whereas the edge counterparts are restricted to their respective glide planes. This allows a single dislocation loop to generate multiple new dislocations and entanglements, owing to

## 1. Literature review – 1.1. Small scale mechanics

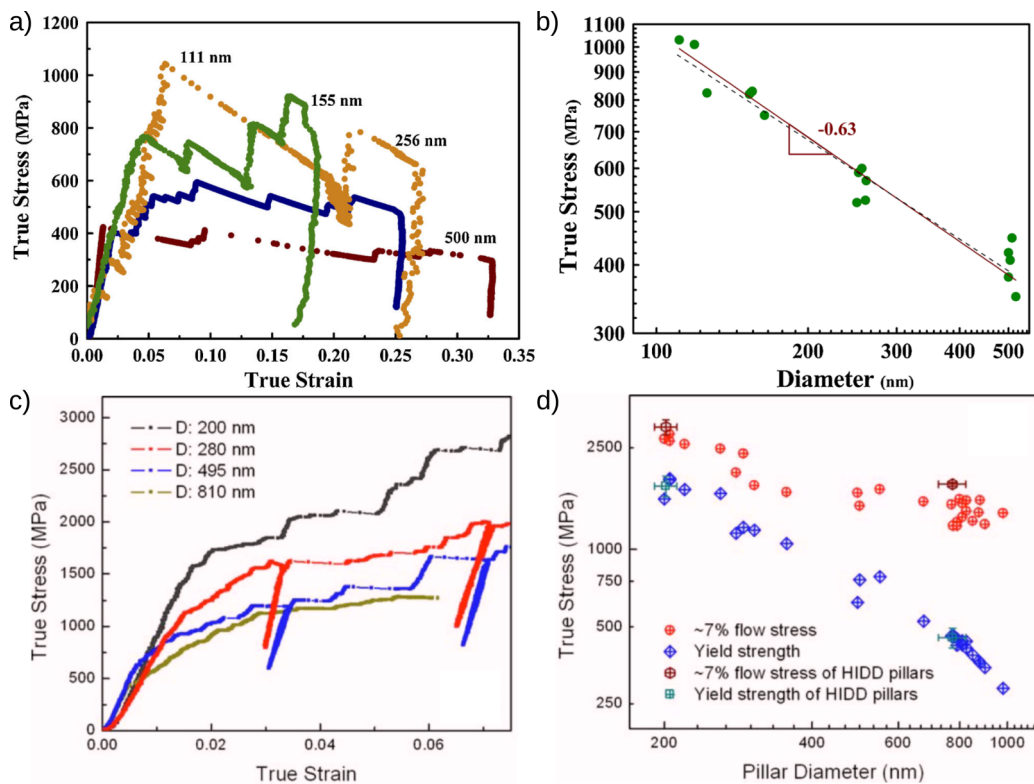


Figure 1.4.: Compression of FCC and BCC metal nanopillars. Stress-Strain curve for a) Cu and c) Mo nanopillars of different diameters showing the “*smaller is stronger*” trend. Yield stress *vs.* pillar diameter for b) Cu and d) Mo with slopes -0.63 and -0.44 respectively. From [Jennings et al. 2010] and [Kim and Greer 2008].

the ability of screw dislocation components to cross-slip between different slip planes [Weinberger and Cai 2012]. Consequently, dislocation segments interact and form Frank-Read sources, which results in an increase in dislocation density with applied stress. The entanglement of these dislocation segments within the pillar contributes to the observed increase in flow stress.

To investigate mechanics at the nanoscale, several research groups conducted NWs testing under tension, bending, or compression [Peng et al. 2012; Roos et al. 2014; Qin et al. 2015; Cheng et al. 2017; Cao et al. 2018; Kim et al. 2018; Cheng et al. 2020; Lam et al. 2020]. Richter *et al.* fabricated high aspect ratio NWs from various FCC metals using a high-temperature molecular beam epitaxy method [Richter et al. 2009]. With this technique, they confirmed the presence of atomically smooth (sometimes with surface steps), faceted surfaces and the absence of pre-existing dislocations via TEM. Mechanical tests were performed on defect-free Cu NWs with diameters ranging from 75 to 300 nm, mounted in a tensile testing setup. Ultrahigh strengths were revealed, the highest ever reported in Cu. The absence of large amounts of plasticity, in contrast to typical behavior observed in pure FCC metals, and the very high strength were

## 1. Literature review – 1.1. Small scale mechanics

ascribed to small sizes and crystalline quality, with surface dislocation nucleation (SDN) presumed as the sole process that governs the deformation. Furthermore, Lee *et al.* reported the transition from dislocation slip to deformation twinning post-SDN [Lee et al. 2014]. Using *in situ* TEM, perfect dislocation nucleation was observed near the sample top and the flat punch in the initial compression stages of Au NWs. These dislocations immediately glided and escaped near the contact region, which resulted in a mushroom-shaped NW top side. Subsequent half loops were detected in regions far from the NW's apex. When the loading direction was reversed, the pre-existing dislocations that formed during compression slipped back. Then, the mechanism predominantly observed was deformation twinning. The force-strain curves for both compression and tension experiments is depicted in Figure 1.5g. Once a twinning region was formed, compressive deformations allowed for detwinning rather than forming partial dislocations.

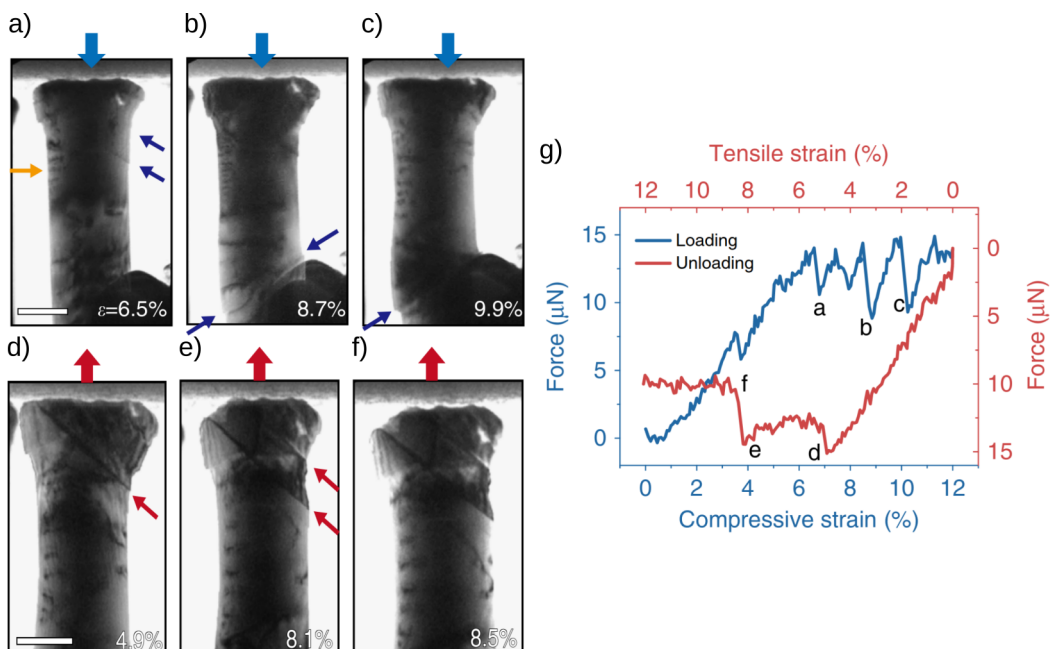


Figure 1.5.: Mechanical test of Au NWs using *in situ* TEM (scale bar of 100 nm). a-c) Images taken after the load drops in the compressive loading. The traces in the lateral surfaces of a dislocation slip mechanism are shown with blue arrows. d-f) Unloading the sample showing the nucleation and extension of nanotwins. g) Recorded force versus strain during the compressive (blue) and subsequent tensile (red) loading. Images from [Lee et al. 2014].

Small-scale mechanics techniques have also been widely used to characterize the mechanical properties of NPs, including faceted or spherical shapes [Mook et al. 2007; Mordehai et al. 2011b; Mordehai et al. 2011a; Han et al. 2015; Sharma et al. 2018; Sharma et al. 2021]. For instance, Mordehai *et al.* studied the size-dependent mechanical behavior of single-crystal Au faceted NPs through a series of experimental

## 1. Literature review – 1.1. Small scale mechanics

nanocompression tests [Mordehai et al. 2011b]. These samples were fabricated via solid-state dewetting on sapphire substrates, which resulted in numerous faceted Au crystals spanning from tens of nanometers to micrometers in size (the smallest ones being defect-free). The stress-strain curves derived from the nanocompression tests are illustrated in Figure 1.6a, while Figure 1.6b displays the NPs before and after deformation. The results confirm the trend of increased strength with decreasing particle size, where dislocation nucleation is the main process for the plastic deformation of defect-free NPs.

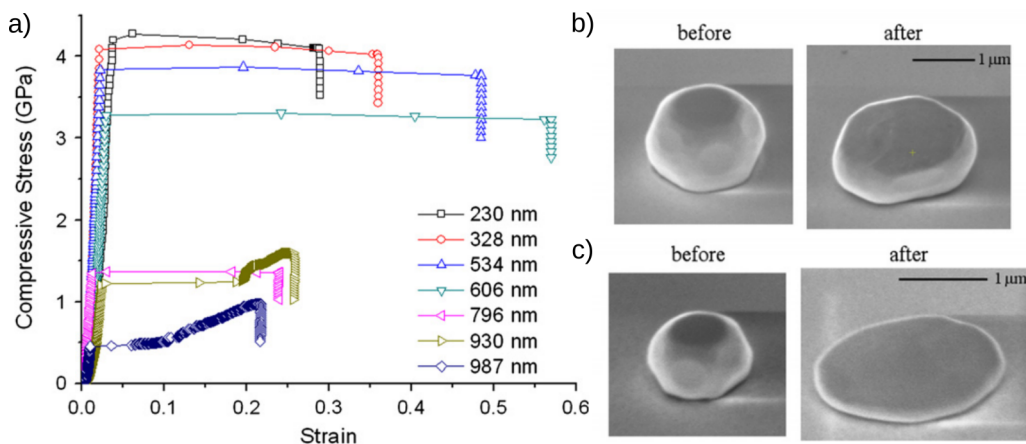


Figure 1.6.: Compression of Au faceted nanoparticles. a) Load–displacement curves and SEM images before/after compression of a b) 800 nm and c) 300 nm top diameter particle, from [Mordehai et al. 2011b].

More recently, Issa *et al.* used *in situ* TEM to compress defect-free ceramic MgO nanocubes [Issa et al. 2015]. The experiments were conducted at a controlled displacement rate of  $2 \text{ nm} \cdot \text{s}^{-1}$  along the [001] direction. Three sizes were investigated: 90 nm, 120 nm, and 140 nm, revealing the well-established trend of increased strength with decreasing size, as depicted in Figure 1.7. Using TEM provided the opportunity to observe the nucleation of dislocations, a process reported to occur at surfaces and edges of the cubes. In parallel, atomistic simulations were performed at room temperature for dislocation-free NPs at smaller sizes, approximately 10 nm. Compression tests were conducted in the [001] direction with a displacement rate equivalent to a strain rate of  $10^8 \text{ s}^{-1}$ . Both experiments and simulations showed that MgO NPs can deform up to extreme strain without cracking. Furthermore, simulations helped to interpret the SDN process happening in the *in situ* experiment (see insets of Figure 1.7). The same research group recently discussed the size-dependent transition from SDN and starvation (for samples smaller than 200 nm) to bulk-like dislocation multiplication (for larger samples) in MgO NPs through *in situ* experiments [Issa et al. 2021].

For multi-components NPs, the significance of interphase boundaries in the nucleation-controlled plasticity regime has also been widely investigated [Conesa-Boj et al. 2014;

## 1. Literature review – 1.1. Small scale mechanics

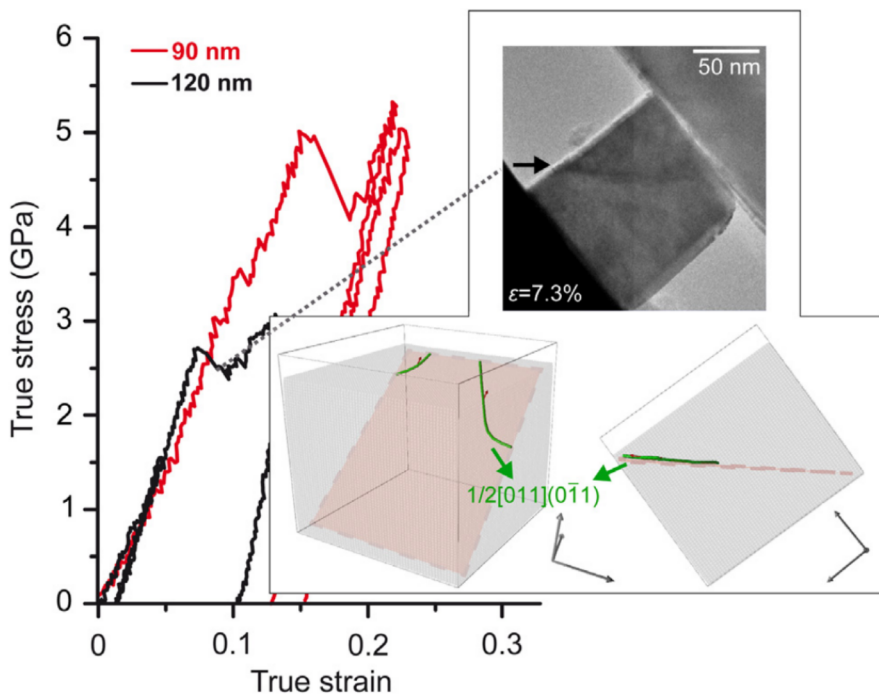


Figure 1.7.: Stress–strain curves for two MgO nanocubes of 90 (red curve) and 120 (black curve) nm edge lengths deformed *in situ* inside the TEM. In the inset: TEM image of a 120 nm sample during compression,  $\varepsilon = 7.3\%$ . The black arrow shows a contrast band corresponding to dislocations that emerge from the surface of the cube. Two numerical simulation snapshots of a 12.6 nm edge length nanocube are also represented. Reconstructed  $1/2\langle 110 \rangle\{110\}$  dislocations are shown in green. From [Issa et al. 2015].

Fleming and Zou 2017; Zhang et al. 2018; Kiliyimis et al. 2018; Shin et al. 2019]. Sharma *et al.* performed nanocompression tests on pristine Ag and Ag-Au core-shell hemispherical NPs to elucidate the role of interphase boundaries [Sharma et al. 2021]. Remarkably, the deformed Ag-Au NPs exhibited no sign of catastrophic plastic flow, which sharply contrasts with the pancake-like shapes observed for compressed single-crystalline Ag particles (see Figure 1.8). In addition, while the load-displacement curves of pristine Ag NPs displayed typical features of plastic deformation controlled by dislocation nucleation, those for the Ag-Au core-shell NPs exhibited a very different behavior (see Figure 1.8e). Here, plasticity initiated at very early stages of deformation, with a notable lack of large singular displacement bursts. This behavior, sometimes referred as "staircase yielding", is associated with the operation of numerous surface or internal dislocation sources, which leads to a more gradual plastic deformation [Corcoran et al. 1997; Bahr et al. 1998]. Thus, the core-shell NPs were found to be weaker than their single-crystalline counterparts, yet their plastic deformation could be better controlled.

To date, Azadehrehanjbar *et al.* have pioneered the investigation of deformation mech-

## 1. Literature review – 1.1. Small scale mechanics

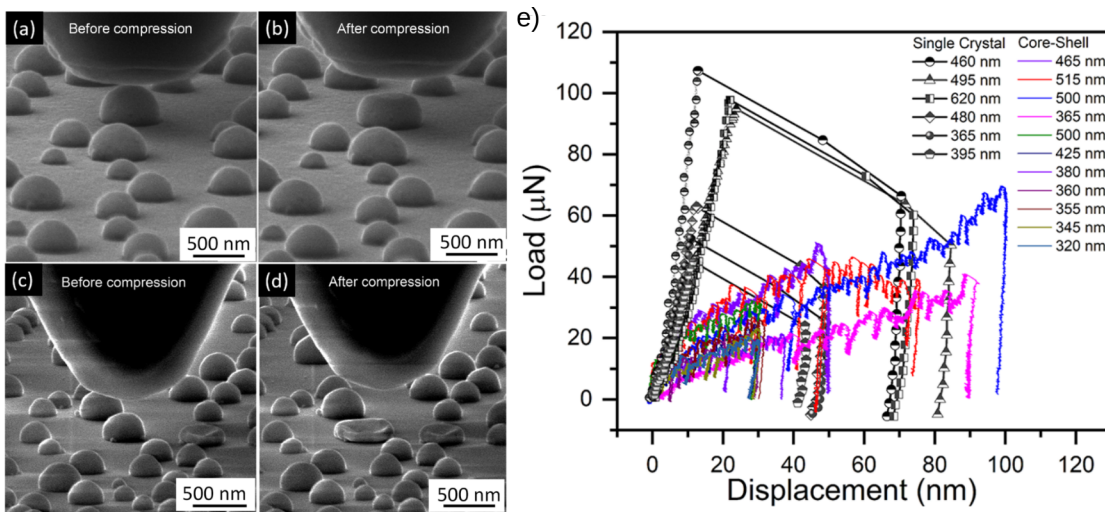


Figure 1.8.: SEM imaging of Ag-Au and Ag NPs compression tests and e) load-displacement curves. a, b) Ag-Au core-shell NPs before and after test. c, d) Single crystalline Ag NPs before and after test. From [Sharma et al. 2021].

anisms for the smallest NPs ever studied in terms of size [Azadehrehanbar et al. 2023]. *In situ* compression tests were performed on Pt NPs with diameters down to 6 nm. At such small-scales, the so-called diffusive plasticity occurs. It is characterized by a homogeneous, liquid-like response to loading, while the NP remains crystalline [Casillas et al. 2013; Sun et al. 2014]. No nucleation of dislocation was observed during testing. Instead, a significant shape alteration occurred at the surfaces near the indenter surface. As the load was applied, the lengths of the {111} surface facets declined, while additional material was added to the {100} facets on the NP's sides. Following compression, the NPs quickly reverted to their original shape, including the surface facets, within a few seconds. A closer examination revealed that the surface was comprised of atomic steps which dynamically changed via a series of atom-hopping events, underscoring that large-scale homogeneous deformation is accommodated by surface atom migration.

In summary, the first part of this literature chapter underscores the prevailing "*smaller is stronger*" trend and the plastic behavior reported in small-scale objects. Notably, the role of dislocations on the plastic deformation mechanisms is highlighted. It is commonly observed that surface nucleation governs plasticity in the smallest defect-free NPs due to the high influence of free surfaces when decreasing size. In this context, micro- and nanomechanical experiments give a good understanding of fundamental deformation mechanisms. However, these experiments suffer from several limitations that hinder reliable characterization. The reproducibility of experiments is often questioned due to inherent thermally activated processes and experimental biases, which can result in data scattering, as depicted in Figure 1.3. In the following

## 1. Literature review – 1.2. Data scattering and experimental biases

section, we will discuss the reliability of experimental data and focus on the factors that possibly influence the deviation from theoretical predictions.

## 1.2. Data scattering and experimental biases

### 1.2.1. Strength master plot

Throughout all experimental tests, the relationship between mechanical properties and a geometrical or microstructural length scale is of interest. Such scaling or size effect, is frequently described by a power-law approach. In the case of FCC materials, the power-law slope typically falls within the range of -0.5 to -1.0 (see Figure 1.9a) and shows no strong variation across different materials [Kraft et al. 2010]. For BCC metals, the strengthening slopes for size dependence span a wide range of values, such as -0.32 for W, -0.42 for Mo or -0.82 for Nb, as shown in Figure 1.9b. In this case, a correlation was shown to exist between this exponent and the residual Peierls barrier at room temperature [Schneider et al. 2009a]. However, while this theoretical estimation is often represented by a linear relationship using a log-log plot, data points do not perfectly align. For instance, in the work of Mordehai *et al.* [Mordehai et al. 2011b], the dependence of the NPs yield stress on their size is described by a power law with an exponent of -0.77, as depicted in Figure 1.9c. But an uncertainty of  $\pm 0.16$  for the exponent is mentioned, which indicates considerable scattering around the mean line. Notably, around the 200 nm mark, results even show a strength difference of an order of magnitude.

Data scattering in terms of strength is evident across various mechanical tests, as shown in Figure 1.9d, where tension and compression are compared [Kraft et al. 2010]. Numerous research groups have undertaken critical examinations of experimental observations to explain this phenomenon [Pharr et al. 2010; Greer and De Hosson 2011; Li et al. 2016a; Gerberich et al. 2017]. Issa *et al.* attempted to explain this dispersion with intrinsic attributes of NPs during the plastic regime [Issa et al. 2021]. They specifically associated the symmetric nature of the scatter around the mean line with the "mild" and "wild" behaviors previously delineated by Weiss *et al.* [Weiss et al. 2015; Zhang et al. 2017]. When the behavior is characterized as "mild," the scatter of the yield point is anticipated to exhibit symmetry around the best fit. Conversely, in the case of "wild" behavior, the scatter should consistently fall on or above the best fit, as higher stresses are required to enable dislocation nucleation. However, despite these observations, no universal law was discerned. In fact, it is revealed that experiments and limited data may contain biases that can significantly influence our understanding of the mechanical properties of NOs.

## 1. Literature review – 1.2. Data scattering and experimental biases

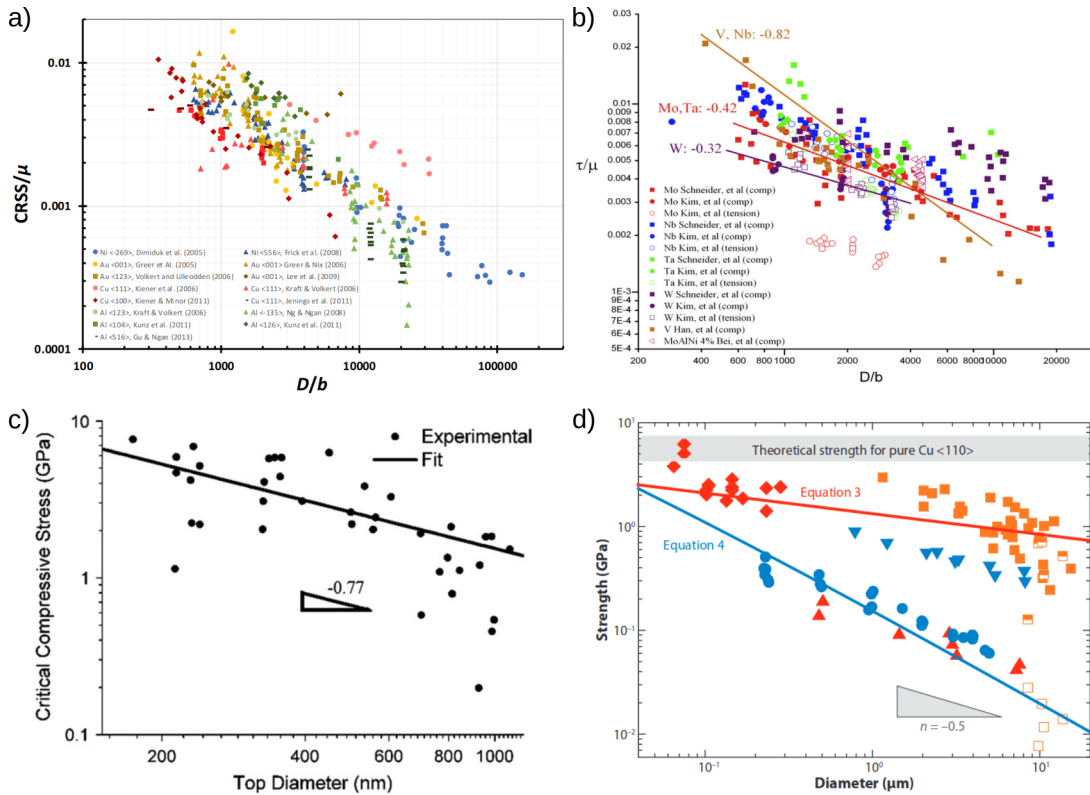


Figure 1.9.: Strength *vs.* size master plot. Review of the nanopillar compressions of a) FCC from ref. [Shahbeyk et al. 2019] and b) BCC from ref. [Greer and De Hosson 2011] metals. Case of nanoparticles compression or whisker tension/compression such as c) Au from ref. [Mordehai et al. 2011b] or d) Cu from ref. [Kraft et al. 2010] (compression in blue and tension in orange), respectively.

### 1.2.2. Experimental biases

Experimental biases are related either to the accuracy and reliability of measurements, sample preparation, protocol (extrinsic) or to inherent characteristics of the sample under consideration such as surface state (intrinsic) [Greer and De Hosson 2011; Gerberich et al. 2017; Dehm et al. 2018].

In sample preparation, notable instances of damage induced by FIB milling include the implantation of Ga within the sample, the formation of point defects, and the development of dislocation-like structures [Kiener et al. 2007]. Particularly in pristine samples, the generation of defects significantly impacts strength as they are favorable sites for the early nucleation of dislocations. This results in a shift from dislocation nucleation in a defect-free volume to heterogeneous dislocation nucleation from surface-near-defects. For example, as depicted in Figure 1.10a, the yield strength of Mo whiskers subjected to  $\text{Ga}^+$  FIB milling decreased from 9 GPa to approximately 1 GPa [Shim et al. 2009]. Also, using an *in situ* TEM nanomechanical testing setup

## 1. Literature review – 1.2. Data scattering and experimental biases

revealed that the electron beam can alter the material being imaged and consequently affect the deformation behavior [Stangebye et al. 2022]. Indeed, the electron beam induces additional thermal activation, thereby accelerating stress-driven, thermally activated plastic deformation and leading to an increase in plastic strain rate.

Under compression, misalignment of the flat punch tip relative to the top surface of the sample results in a distorted stress state, which not only introduces potential errors in the load-displacement curve but also significantly influences the deformation mode of the material under investigation [Zhang et al. 2006]. During the loading process, the misalignment is initially accommodated elastically until plastic deformation occurs. In ductile materials, misalignment is mainly released through plastic deformation at low strains, which results in unique dislocation patterns compared to well-aligned samples. Figure 1.10c shows stress-strain curves of the compression of three differently misaligned Cu micro-pillars as an example [Kirchlechner et al. 2011]. Conversely, brittle materials, characterized by low fracture toughness, often fracture before misalignment is accommodated [Davydok et al. 2016]. This poses challenges in extracting reliable material parameters and measuring theoretical strength in nanomechanical testing. Indeed, perfect alignment remains a theoretical ideal and both the stress-strain curve and post-deformation geometry should be carefully inspected in any case.

Moreover, the machine control - either in force or in displacement [Li et al. 2020a] - and its dynamics can impact the extracted force-displacement data. However, there are only a few studies that investigate their effects [Wu et al. 2009; Hay et al. 2010; Sparks 2017]. Although the basic differences between control modes are observed, such as load drops in displacement control and displacement bursts/pop-ins resulting from load control, the interaction of machine dynamics with the dynamic behavior of materials remains unclear. For instance, it is unclear whether dislocation sources are deactivated during a load drop, while they might continue to operate during a displacement burst, which suggests a material response dependent on the machine used. Figure 1.10b illustrates the very different test dynamics observed using both control modes for the compression of 5  $\mu\text{m}$ -sized single-crystalline Cu pillars [Dehm et al. 2018]. Further theoretical investigation into the deformation mechanisms of NOs in both control modes will be discussed in Chapter 3.

Furthermore, several observations of samples at the nano- and larger scales by *in situ* TEM emphasize surface alterations that could impact experimental measurements. As surfaces constitute the primary defective regions of NOs, they serve as sources for the dislocation nucleation mechanism. Consequently, surface alterations, such as the presence of an amorphous shell, oxide layer, or roughness, might quantitatively influence the mechanics of NOs, such as the activation energy of the SDN process or the types of nucleated defects. In the case of a native oxide layer, extensive studies have focused on the kinetics of oxide growth [Mitchell et al. 1976; Li et al. 1991; O'Reilly et al. 1995; Slezak et al. 1999; Chevalier et al. 2005; López-Beltrán and Mendoza-Galván 2006; Nilius 2009]. However, its influence on deformation mechanisms is often overlooked. Depending on the nature of the oxide, NOs may exhibit

## 1. Literature review – 1.2. Data scattering and experimental biases

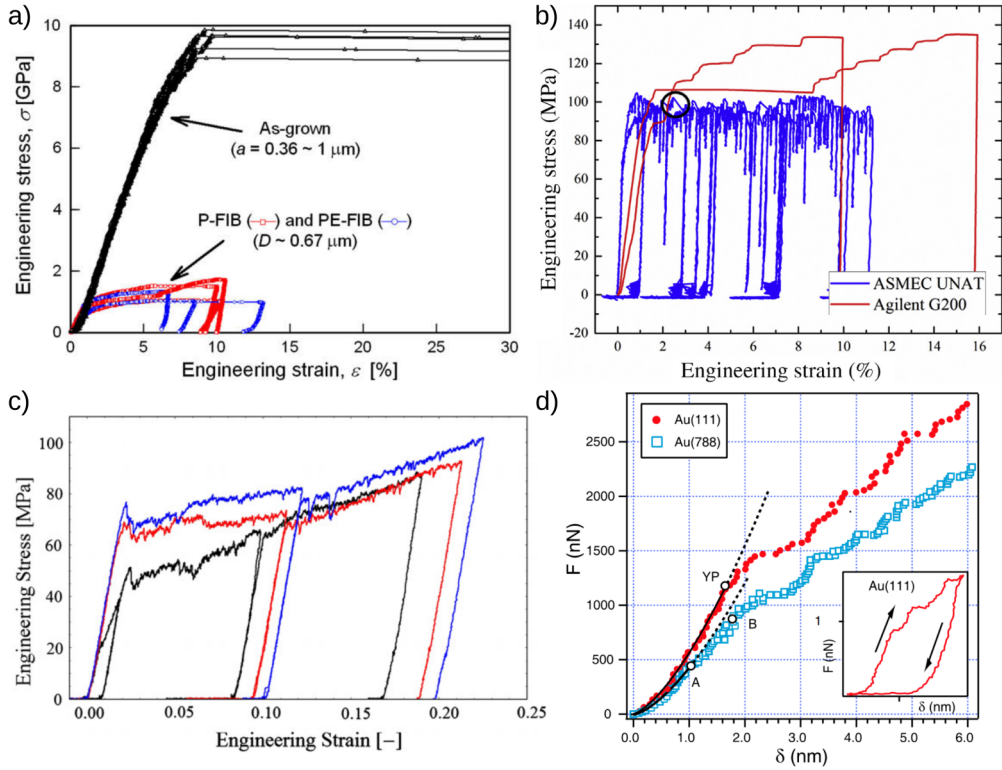


Figure 1.10.: Extrinsic biases affecting the mechanical response of nano-objects. a) Stress–strain curves for as-grown (directionally solidified) and FIB-milled Mo-pillars, from [Shim et al. 2009], b) comparison of load (Agilent G200) and displacement controlled (ASMEC UNAT2) compression tests of  $5 \mu\text{m}$  sized single crystalline Cu pillars, from [Dehm et al. 2018], c) compression of three differently misaligned Cu micro-pillars, from [Kirchlechner et al. 2011], and d) nanoindentation of a gold stepped film (in blue) compared to the case of a (111)-oriented (in red), from [Navarro et al. 2008].

increased ductility with a reduction in yield stress and/or enhanced plastic flow [Syed Asif et al. 2000], or increased brittleness where even flaking of the oxide layer can occur [Morasch and Bahr 2005; Undisz et al. 2009]. Han *et al.* measured the strength of spherical Fe NPs, ranging in size from tens of nanometers to about 500 nm, under compression [Han et al. 2015]. These were synthesized by argon plasma evaporation of an iron target and then passivated in a connecting chamber in an inert gas atmosphere. Their results revealed that the ideal strength of defect-free Fe spherical NPs is nearly achieved. Despite discussing potential biases that might explain data scattering, their observations clearly depict the presence of an oxide overlayer around the NPs, as shown in Figure 1.11a-c. However, this aspect is not mentioned nor taken into account in their study. In addition, the oxide growth process on thin films has been shown to follow an island mode growth [Schmutzler et al. 1992; Rao et al. 1997], as illustrated in Figure 1.11d, which implies that mechanical properties might depend on the state of oxidation in an heterogeneous manner within the sample. For instance, Morasch

### 1. Literature review – 1.2. Data scattering and experimental biases

and Bahr conducted several indentation tests on an Al substrate with a 54 nm thick film [Morasch and Bahr 2005]. The distribution of critical loads is presented in Figure 1.11e and shows clear evidence of data scatter. Thus, the strength of their samples mainly depends on the initial plane-position of the indenter. A deeper focus on the modeling of kinetics of oxide growth at the nano-scale, and its effect on strength is addressed in Chapter 6.

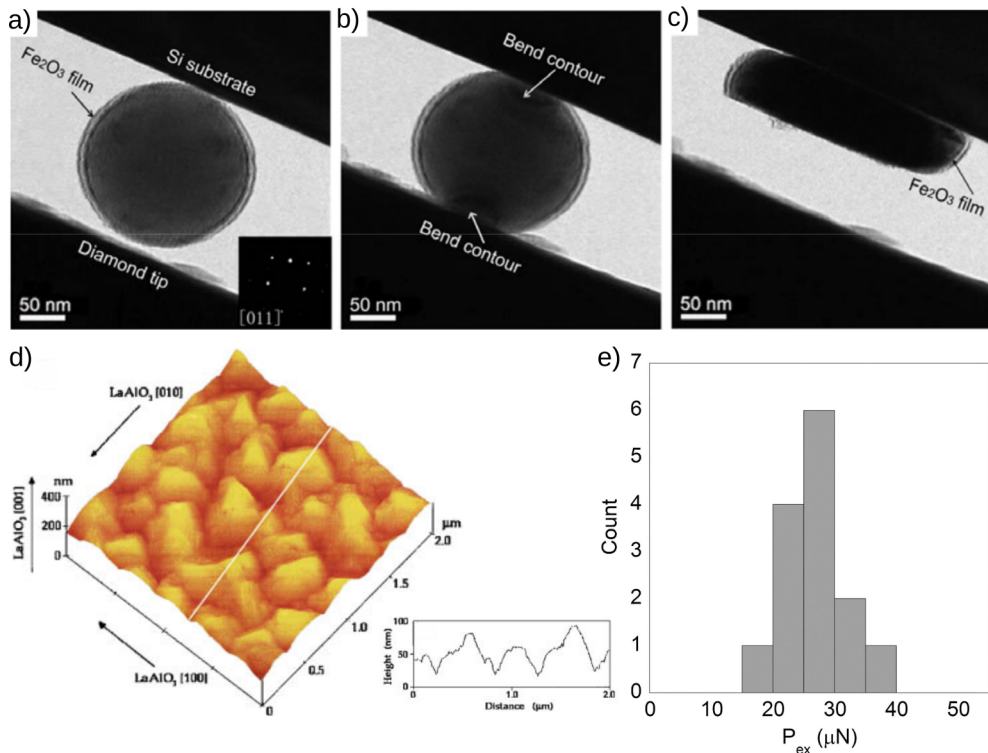


Figure 1.11.: Oxide layer on nano-objects. a-c) Compression of a Fe nanosphere with an oxide overlayer, from [Han et al. 2015], d) STM image of SrRuO<sub>3</sub> thin film showing three-dimensional island growth on LaAlO<sub>3</sub> substrate, from [Rao et al. 1997], and e) histogram of the critical loads for the indentation of an Al substrate with a 54 nm thick oxide film, from [Morasch and Bahr 2005].

Finally, surface roughness represents a potential experimental bias. The visualization of surface irregularities was made possible by advancements in observation techniques such as AFM or Scanning Tunneling Microscope (STM). Surfaces of metal and semiconductor thin films [Arthur 2002; Nahas et al. 2013; Coupeau et al. 2020; Khoroshilov et al. 2022], metal and ceramic NPs [Iijima 1985; Herre et al. 2021] or metal NWs [Zhang et al. 2001b] have been shown to exhibit atomic terraces and imperfect shapes, as shown in Figure 1.12. For instance, the Si(100) surface contains a nearly uniform array of monoatomic terraces that alternate between relatively smooth and relatively rugged regions (Figure 1.12a). Moreover, Coupeau *et al.* recently investigated

## 1. Literature review – 1.2. Data scattering and experimental biases

the influence of atomic steps at the surface of a Ni<sub>3</sub>Al film on the movement of dislocations during compression using STM [Coupeau et al. 2020]. Following successive preparation treatments, the surface was composed of (1̄11) terraces bounded by wavy vicinal steps, as shown in Figure 1.12b. The terraces predominantly lied along one direction and exhibited irregular widths ranging from approximately 5 to 25 nm. The study revealed that slip traces are primarily observed to terminate at the edge of an atomic step (see Figure 1.12b). Consequently, surface irregularities can act as pinning points for dislocations, preventing further slip.

Thus, each sample is uniquely defined by its surface topography that may induce variations of deformation mechanisms and mechanical properties, far from the theoretical strength. For instance, Navarro *et al.* recently studied the influence of surface irregularities on the indentation of Au surfaces [Navarro et al. 2008]. Results show a twice lower yield force for a (788)-oriented stepped surface compared to a flat Au(111) surface, as illustrated in Figure 1.10d, and give a first insight into the effect of surface roughness on the stress distribution inside the samples.

In the case of NOs, some research groups clearly mention the presence of irregularities at the surfaces of the samples : "*a small amount of plastic deformation may occur due to the surface roughness*" [Mordehai et al. 2011a], "*as-fabricated morphology [...] shows some surface roughness*" [Jennings et al. 2010], "*it is expected that all nanocubes have a similar surface roughness*" [Kiani et al. 2019]. Furthermore, experimental observations examples of NOs confirm the presence of surface irregularities or their imperfect shapes, as illustrated in Figure 1.12c-e. For instance, NPs facets are shown to be made of successive atomic steps [Iijima 1985; Chen et al. 2022], and NWs show surface irregularities [Zhang et al. 2001b]. Also, the compression experiments of Landefeld *et al.* [Landefeld et al. 2012] on Ni<sub>3</sub>Al nanocubes clearly exhibits the imperfect shapes of the particles with irregular surfaces and blunt edges (see Figure 1.12d). However, the role of surface roughness is often neglected and no detailed study was performed to date.

In this work, we will consider surface roughness as a potential major source for data scattering when considering the measurement of NOs strength. Here, we study how to model surface roughness and its effect on the strength of samples and underlying deformation mechanisms (see Chapters 4 and 5). This bias reinforces the data scatter and the non-reproducibility of experimental results which are detrimental to in-depth and comprehensive analysis of mechanical properties at small-scales. While it is well-known that contact singularities gradually act as stress concentrators with decreasing size, the influence on the SDN process and overall strength has barely been addressed comprehensively neither experimentally nor in the modeling of small-scale objects. Thus, from a modeling point of view, the problematic of better representing realistic surface alterations and experimental biases arises.

## 1. Literature review – 1.3. Current state on modeling nanomechanics

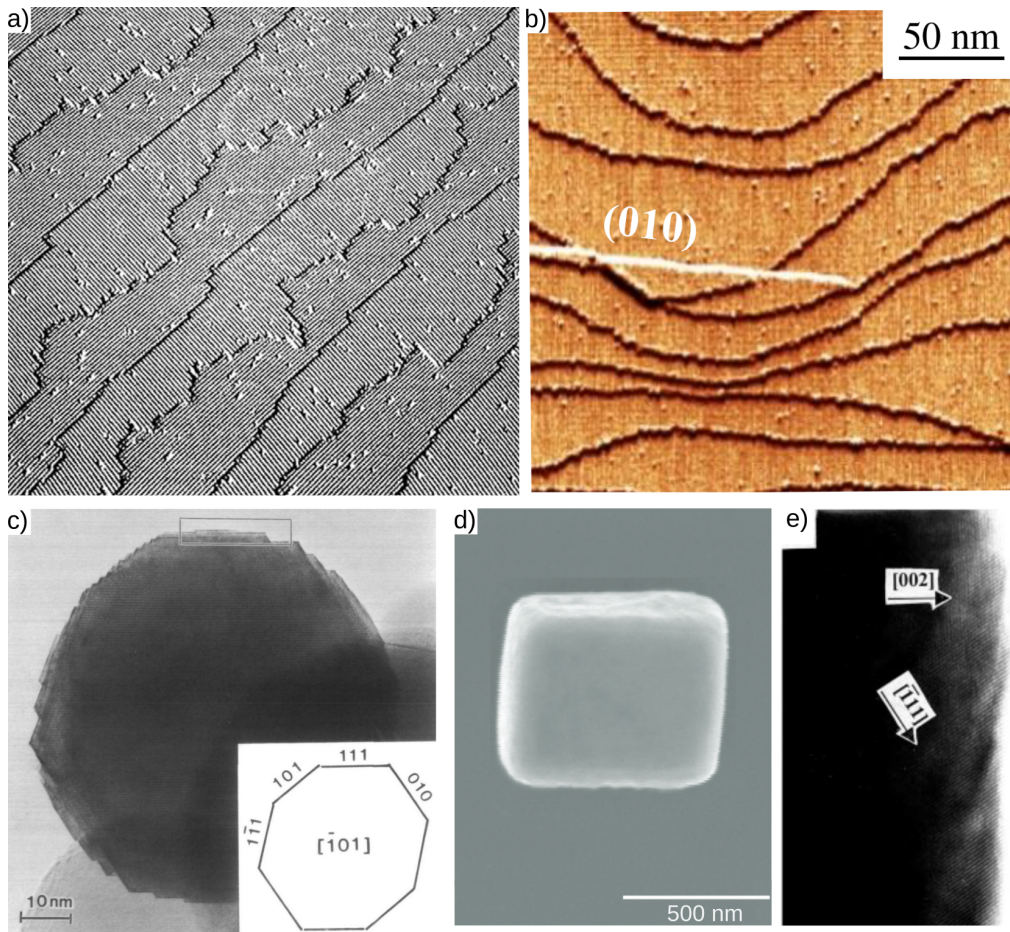


Figure 1.12.: Surface irregularities at small-scales. a) STM 110 nm square image of a Si(100) surface, from [Arthur 2002], b) dislocation interaction with a surface step of Ni<sub>3</sub>Al thin film, from [Coupeau et al. 2020], c) Al<sub>2</sub>O<sub>3</sub> faceted particle, from [Iijima 1985], d) SEM top view of a Ni<sub>3</sub>Al nanocube, from [Landefeld et al. 2012], and e) TEM image of single crystalline Au nanowire, from [Zhang et al. 2001b].

## 1.3. Current state on modeling nanomechanics

### 1.3.1. Generalities

Various computational materials science techniques have already been employed in nanomechanics. They include density functional theory (DFT), MD, molecular statics (MS), discrete dislocation dynamics (DDD), and FEM. While DFT simulations are typically limited to the investigation of small clusters of atoms [Coccoccioni et al. 2005; Cherian et al. 2010; Maioli et al. 2018; Pizzagalli 2020], MS and MD emerge as the most prevalent modeling methods due to their ability to describe atomic-scale elementary deformation processes in virtual samples with sizes comparable to experiments. Further insights into methodological aspects of MS and MD are provided in

### 1. Literature review – 1.3. Current state on modeling nanomechanics

Chapter 2.

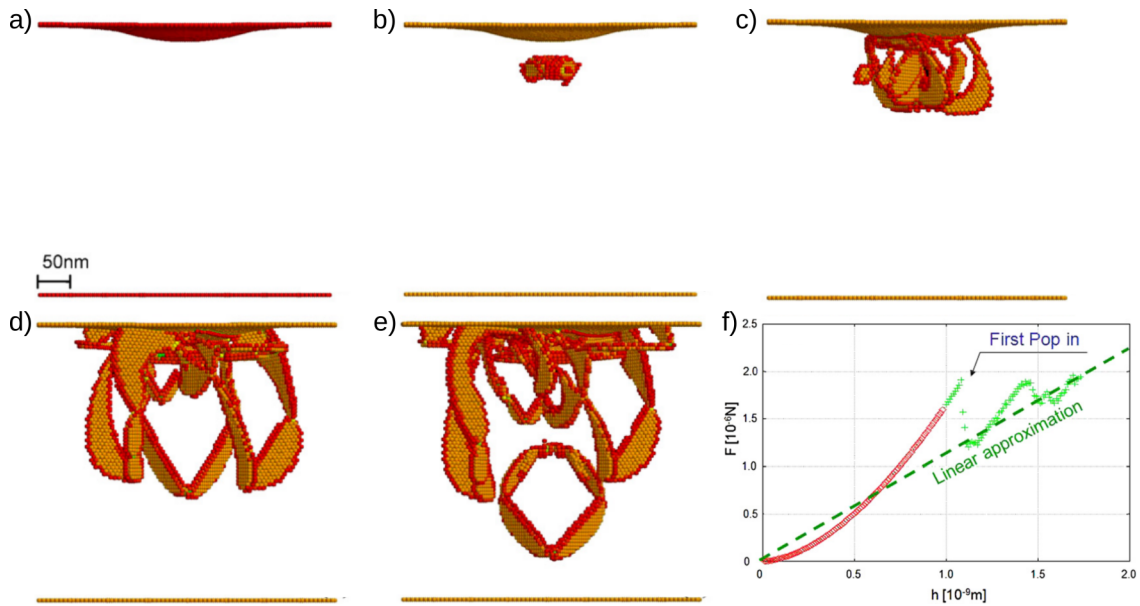


Figure 1.13.: Nanoindentation of a [111]-Ni thin film. a-e) Snapshots of atomic configuration during a plastic event and f) force *vs.* displacement curve. Only the atoms without local FCC environment are shown. From [Chang et al. 2010].

Various MD simulations of thin-film nanoindentation have been conducted to investigate the deformation mechanisms within crystals [Begau et al. 2011; Verkhovtsev et al. 2013; Hu et al. 2015; Yaghoobi and Voyiadjis 2016; Mojumder et al. 2020]. For instance, Chang *et al.* performed quasi-static simulations of nanoindentation along the [111]-direction of a  $224 \times 284 \times 285 \text{ \AA}^3$  Ni crystal, containing approximately 1.5 million atoms [Chang et al. 2010]. They used a spherical indenter with a radius of  $120 \text{ \AA}$ , gradually moved into the crystal in steps of  $0.1 \text{ \AA}$ . As expected, an initial elastic regime was observed, followed by a sudden drop in the indenter force, which corresponds to the nucleation of the first dislocations in the crystal, akin to the experimental pop-in event. Defects emerged a few nanometers below the crystal surface (Figure 1.13b). This structure was highly unstable and evolved into dislocation lines, as depicted in 1.13c, characterized by stacking faults (in orange) bordered by Shockley partial dislocations (in red). The dislocations formed three interstitial prismatic loops (Figure 1.13d), each comprising dislocation segments on two slip systems that shared a common Burgers vector. These loops expanded within the crystal and eventually detached from the surface (Figure 1.13e), after which they move away along their glide cylinder axis-aligned with their Burgers vector. A complex network of dislocations remained near the surface beneath the indenter. Further indentation produced an even more complex network, which regularly emits prismatic loops. These results are later used in my work as a reference for testing original load-controlled algorithms (see Chapter

3).

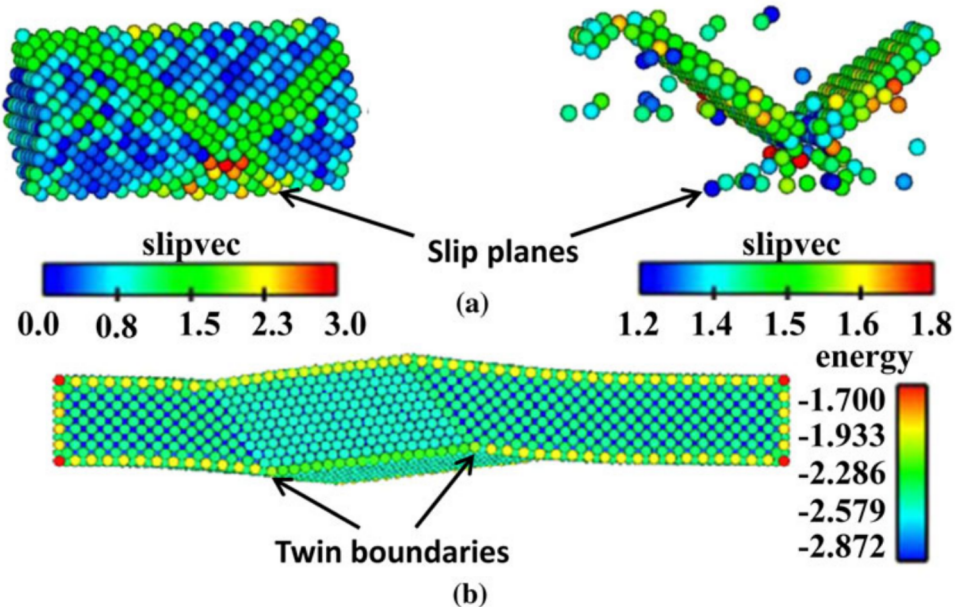


Figure 1.14.: Deformation mechanisms in mechanical testing of nanowires. a) Slip during the yielding of Au nanowire and b) Twinning during deformation of Ag nanowires. From [Lao et al. 2013].

Furthermore, the significant role of free surfaces has been demonstrated in the deformation of NWs through tensile, bending, or compression tests [Hyde et al. 2005; Wu 2006; Diao et al. 2006; Monk and Farkas 2007; Yang et al. 2009; Weinberger and Cai 2012; Weinberger et al. 2012; Lao et al. 2013; Mordehai et al. 2018; Nisany and Mordehai 2022]. Tensile and compression asymmetry in mechanical properties were observed, which is linked to the rearrangement and energetics of surface atoms during dislocation nucleation [Setoodeh et al. 2008; Weinberger and Cai 2012]. Both slip and twinning processes have been observed in the MD simulation of FCC NWs, as shown in Figure 1.14. Twinning initiates with the nucleation of a Shockley partial dislocation and its glide through the NWs, escaping from the opposite side. Consequently, a stacking fault is formed through the cross-section of the NW. The step formed on the surface favors the nucleation of an additional dislocation on an adjacent plane, which splits the stacking fault into two twin boundaries. As this process iterates under tensile loading, the twin boundary propagates, as shown in Figure 1.14b. Liang and Zhou, reported that the competition between partial dislocation slip and twinning is material-dependent through mechanical deformations on Cu, Ni, Au, and Al using MD simulations [Liang and Zhou 2006]. Specifically, for  $\langle 110 \rangle$  axial orientation and  $\{111\}$  side surfaces, Cu and Ni NWs deform by twinning under tensile loading, Al wires deform by full dislocation slip, and Au wires deform by twinning at low temperature (5 K) and by partial dislocation slip at high temperature (200 K). MD studies applied to

## *1. Literature review – 1.3. Current state on modeling nanomechanics*

NWs also reveal the power law relationship between strength and cross-sectional size, consistent with experimental observations.

In this thesis, we particularly focused on the influence of the surface state (roughness, oxidation) on the mechanics of NPs under compression. Thus, an intensive review of major studies on the modeling of NPs nanomechanics is made in the following.

### **1.3.2. Modeling the mechanics of nanoparticles**

#### **1.3.2.1. Methods**

As previously mentioned, nanoindentation and nanocompression are the two primary experimental techniques developed to investigate the mechanical properties of NPs. Both methods use an indenter tip, typically made of materials such as diamond, sapphire, or tungsten carbide. This tip can either indent the top surface of a faceted NP or, after etching, create the so-called "flat punch" shape used for nanocompression experiments. In MD simulations, these experimental tests are often modeled using two main approaches for the design of the indenter and substrate: the "frozen atoms" approach and the "virtual force-field" approach. While both approaches rely on the application of a force-field on the surface and subsurface atoms of the NP, they differ slightly in terms of applied mechanical constraints. In the "frozen atoms" approach, the user designs an indenter, such as a flat punch, a spherical, or a Berkovitch indenter, made out of an infinitely tough, frozen group of atoms. This characteristic is typically achieved in any MD simulation code by canceling the forces acting on these atoms or not accounting for them during time integration. Consequently, the rigid block of atoms creates a tridimensionnal repulsive force-field used to compress the NP. The compression force can then be determined from the atomic interactions between the NP and the frozen block of atoms. In contrast, the "virtual force-field" approach employs an explicit analytical formulation of a directional force-field. This is the method used in this project, with further details provided in Chapter 2. The primary distinction between the two approaches lies in the directional aspect of the force-fields. The "virtual force-field" approach is typically axis-aligned, whereas the use of a rigid block of atoms results in multi-directional as well as additional attractive forces.

#### **1.3.2.2. Dislocation nucleation and plasticity in metal nanoparticles**

Both of these methods have been employed to investigate the mechanical properties and deformation mechanisms of NPs [Wang et al. 2014; Shreiber and Mordehai 2015; Feruz and Mordehai 2016; Yang et al. 2017; Mordehai et al. 2018; Goryaeva et al. 2019; Amodeo and Pizzagalli 2021; Amodeo et al. 2021].

Mordehai *et al.* used the frozen atoms approach in MD simulations to investigate the compression behavior of faceted Au NPs, as depicted in Figure 1.15. This simulation setup aimed to replicate their experimental investigations of Au NPs discussed earlier [Mordehai et al. 2011b]. However, in MD simulations, the NPs exhibit flat surfaces

### 1. Literature review – 1.3. Current state on modeling nanomechanics

and sharp edges and they are typically much smaller in size (ranging from 5 to 25 nm) compared to the experimental ones, due to computational limitations. This constraint in system size is commonly considered in most of MD simulations. The simulations

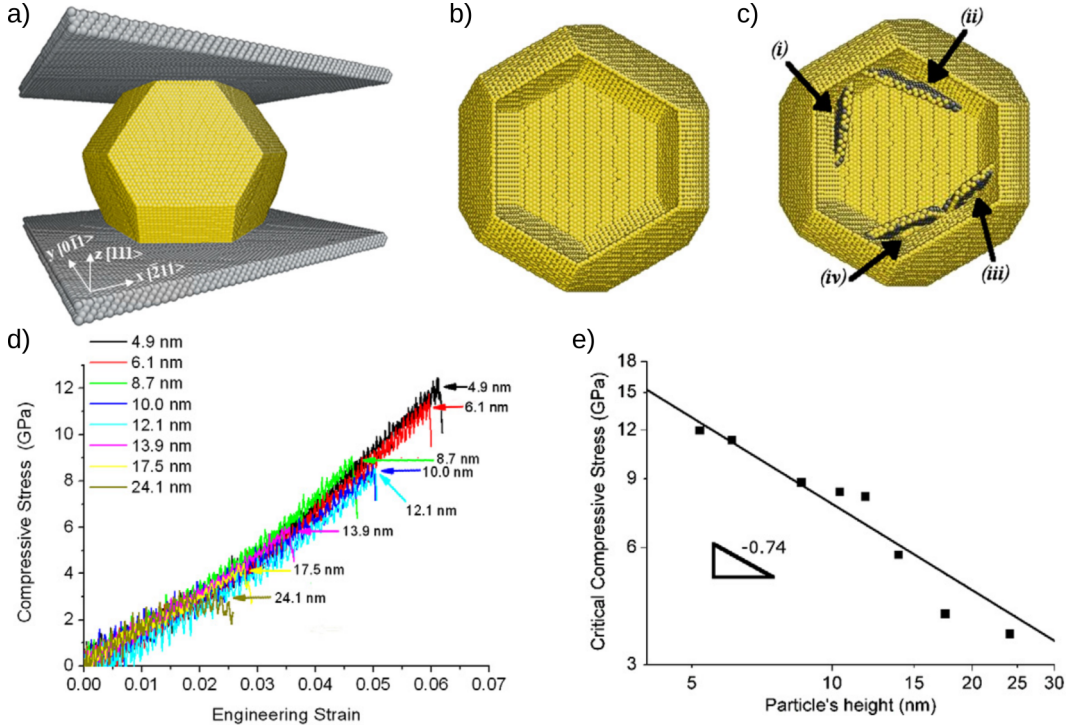


Figure 1.15.: MD compression simulations of faceted Au nanoparticles. a) Simulation setup with frozen atoms for the indents, b-c) dislocation nucleation during the first plastic event, d) stress–strain curves of particles of various heights, terminated at the first dislocation nucleation event, and e) the compressive stress at the point of nucleation of the first dislocation *vs.* particle height. From [Mordehai et al. 2011b].

revealed that pristine particles deform via dislocation nucleation at the upper vertices of the particle due to high stress concentrations, as illustrated in Figure 1.15b-c. The nucleated partial dislocations initially slip in one of the  $\{111\}$  planes with  $1/6 \langle 112 \rangle$  Burger vectors. In all cases, the trailing partial dislocation is nucleated shortly after the leading partial dislocation, which results in the formation of a full, dissociated-dislocation loop with a total Burgers vector along the  $\langle 110 \rangle$  direction, typical of FCC materials. This indicates that the underlying dislocation mechanisms controlling NP deformation are consistent between experiments and simulations.

In contrast, Bian and Wang [Bian and Wang 2013] used the force-field method to investigate the mechanical response of FCC Cu nanospheres under compression, as illustrated in Figure 1.16. No geometric biases were introduced in their study, thus the NPs are perfectly shaped and oriented. During the initial stage of plastic deformation, Shockley partial dislocations nucleate homogeneously from the contact edge and form

### 1. Literature review – 1.3. Current state on modeling nanomechanics

sessile dislocation locks under the indenter, which leads to the formation of pyramid dislocation hillocks, as depicted in Figure 1.16c. The presence of dislocation pyramids restricts the plastic flow of material, thereby dominating the strain hardening in this stage. During further compression (II-III), the load is transmitted through the tip of the microstructure that acts as a stress concentrator to trigger dislocations nucleation, as shown in Figure 1.16c. As compression progresses, partial dislocations nucleate and glide on stacking faults in adjacent {111} planes. Successive emission and migration of such partial dislocations leads to deformation twinning (see inset of Figure 1.16b). The study concludes that dislocation slip dominates initial plastic deformation, while deformation twinning becomes prominent during severe plastic deformation.

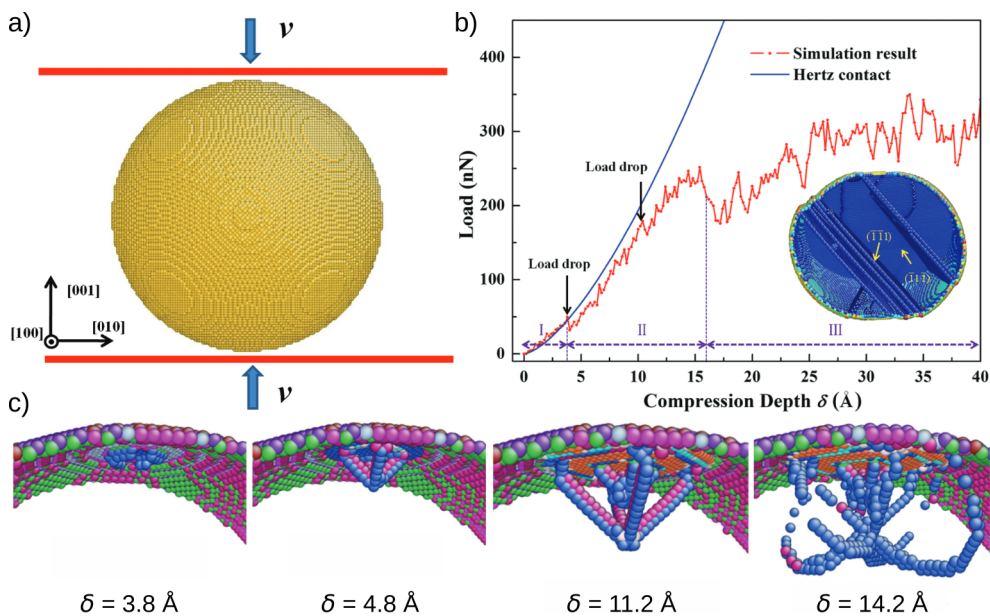


Figure 1.16.: Compression of Cu nanosphere. a) Simulation setup using the force-field approach, b) load-displacement curve with an inset of the particle microstructure at a compression depth of 38.8 Å, and c) the formation and expansion of the pyramid hillocks. From [Bian et al. 2018].

One notable result resumed from the various modeling studies of NP mechanics is the size effect observed on the yield stress across various materials, as depicted in Figure 1.15d. This trend aligns with experimental observations. Figure 1.17 further illustrates the strength of different NPs plotted against size, categorized by material and shape. The materials studied encompass FCC metals, Si, and Mo, with additional data for a BCC metal (Nb), HCP metal (Mg), intermetallic alloy ( $\text{Ni}_3\text{Al}$ ), and covalent alloy (SiC). Across all cases, it is evident that NPs demonstrate significantly higher strength compared to their bulk counterparts. However, simulation results exhibit less scattering compared to experiments due to the ideal conditions in which they are conducted. These simulations reveal that NPs yield through the nucleation of dislocations from the vertices of the faceted NPs, with the size effect attributed to the

## 1. Literature review – 1.3. Current state on modeling nanomechanics

size-dependent buildup of stress gradients at these locations [Mordehai et al. 2018]. A similar explanation was provided for faceted "Wulff-like" Si NPs, which also display a strength-size dependence [Kilimis et al. 2018].

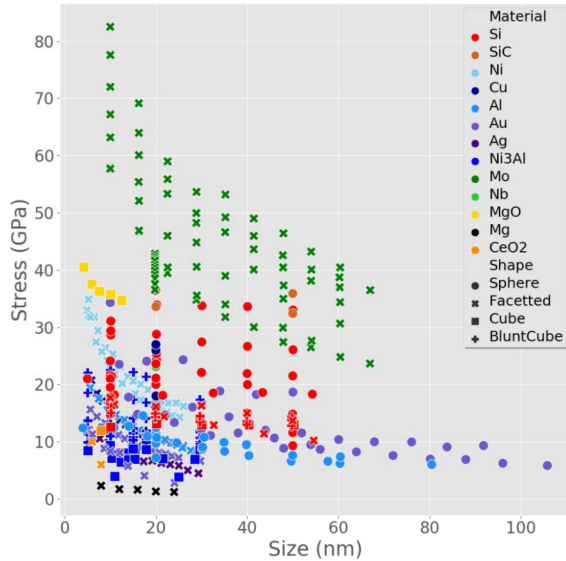


Figure 1.17.: Maximum compressive stress computed during uniaxial compressions, as a function of the size, modeled by MD. Markers and their colors represent the NP shape and materials. From [Amodeo and Pizzagalli 2021].

### 1.3.2.3. Shape-effect

In this context, the question regarding whether virtual samples are designed with sufficient accuracy to quantitatively model surface-based processes and reproduce experimental mechanical conditions arises.

Typically, samples intended for MD nanomechanical tests often lack a high level of detail, as illustrated in Figures 1.15 and 1.16. Virtual NPs and NWs commonly exhibit flat facets bounded by sharp edges and vertices, as observed in previous studies [Mordehai et al. 2011b; Weinberger et al. 2012; Amodeo et al. 2014]. Additionally, nanospheres are often modeled as perfectly and symmetrically shaped [Valentini et al. 2007; Stone and Horstemeyer 2012; Bian and Wang 2013]. This contrasts with various experimental observations that highlight more blunt and rounded shapes (see Figure 1.12 and references [Mordehai et al. 2011b; Stauffer et al. 2012; Wagner et al. 2015]). Consequently, investigations into the shape influence on the mechanical response and the elementary plasticity processes of NOs have gained attention [Lao et al. 2013; Amodeo and Lizoul 2017; Kilimis et al. 2018; Yin et al. 2019; Erbi et al. 2023].

For example, Amodeo and Lizoul designed Ni<sub>3</sub>Al cubic NPs with rounded edges and corners using an algorithm based on a blunting coefficient  $\alpha$  [Amodeo and Lizoul 2017]. The results depicted in Figure 1.18 demonstrate a significant shape effect, where smoothing corners and edges of originally cubic particles leads to an increase

## 1. Literature review – 1.3. Current state on modeling nanomechanics

of the critical yield stress. Hence, the strength of a blunt cube is more than twice that of the perfect one. This underscores the importance of accurately representing the shape of NOs in simulations to faithfully capture their mechanical behavior.

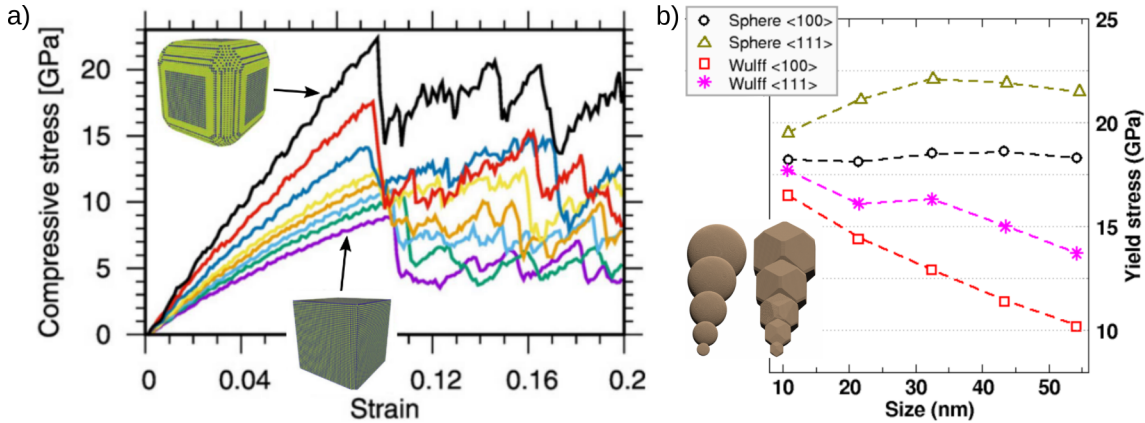


Figure 1.18.: Shape effect on strength. a) Stress-strain curves associated with the compression of Ni<sub>3</sub>Al cubic NPs, with the shape parameter  $\alpha$  increasing from the bottom curve to the top one, from [Amodeo and Lizoul 2017] and b) comparison of yield stresses for spheres and faceted Si NPs of various sizes, from [Kilymis et al. 2018].

The activation of plasticity mechanisms primarily hinges on the location of peak local shear strain and the geometry of the contact surfaces. These characteristics are intimately tied to the shape of NOs. Consequently, various types of dislocations nucleate from the surface, depending on the specific shape of the NOs [Kilymis et al. 2018]. This observed influence of shape may contribute to disparities in yield strength measurements obtained from SEM and *in situ* TEM mechanical tests [Zimmerman et al. 2021]. This emphasizes the crucial need to use models that accurately reflect the geometries of real NOs when aiming to draw meaningful comparisons between computational predictions and experimental outcomes.

### 1.3.3. Introduction to the modeling of surface alteration

#### 1.3.3.1. From surface step to atomic-scale roughness

The first step in the modeling of more realistic NOs shapes is to consider a single surface step and its impact of the strength of the sample. Indeed, the assumption that the presence of surface defects at the atomic level, particularly surface steps, is able to favour the nucleation of dislocations has been investigated and confirmed by several research groups.

Brochard *et al.* studied the process of dislocation nucleation from a straight atomic step on the (100) free surface of a crystalline FCC Al film subjected to an increasing uniaxial tensile stress [Brochard et al. 2000a; Brochard et al. 2001]. They showed that

### 1. Literature review – 1.3. Current state on modeling nanomechanics

the surface step acts as a favoured site for the nucleation of dislocations that glide in the {111} dense planes. The stress level at which glide occurs is  $\sim 1.5 \times$  lower than the theoretical strength of a perfect sample. In addition, further studies demonstrated that in the case of an irregular step, kinks are not necessarily the preferred nucleation site, but seem to be strong anchor points for dislocations, making their motion more difficult along the step [Hirel et al. 2007]. And unlike what would have been thought at first glance, the limit of elasticity is not modified in comparison with straight steps, but the subsequent motion of the formed dislocation is impeded by the kinks. Moreover, recent studies showed that the nucleation process is strongly dependent on the height of the surface step [Brochard et al. 2010]. It can be seen that, for a monoatomic step, the dislocation is always nucleated in the same glide plane : the plane in which the nucleation reduces the step height. But on the other hand, when the step height is increased, a change in the plane where the dislocation nucleates is observed.

The effect of stress directly applied on an atomic surface step was investigated by Zimmerman *et al.* on a thin (111) Au film using nanoindentation with different indent positions relative to the step [Zimmerman et al. 2001]. Results are even more flagrant in this case since, as the indenter center is positioned closer to the surface step during indentation, sample yields at forces that are up to 85% lower than in the case of an indenter far from the step *i.e.* indenting a flat surface.

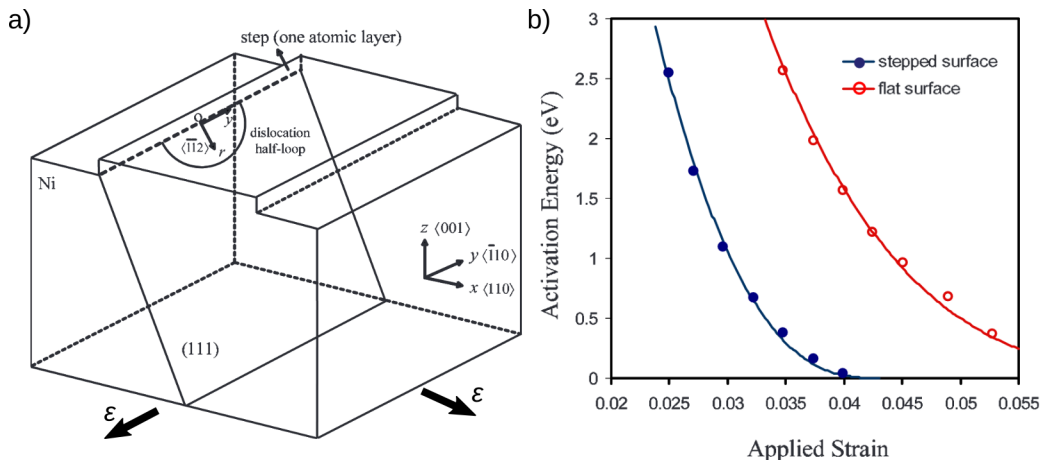


Figure 1.19.: Determination of the activation energy for the nucleation of a dislocation from a surface step. a) Sample subjected to biaxial tension and b) the calculated activation energy as a function of the applied strain for a stepped surface (blue circles) and for a flat surface (red circles). Adapted from [Hara et al. 2009]

These observations were later explained by Hara *et al.* who used the nudged elastic band (NEB) method to determine the minimum energy path and activation energy for the nucleation of dislocation in the case of biaxial tension of a Ni thin film with a stepped surface [Hara et al. 2009]. Their results, presented in Figure 1.19, show that,

### 1. Literature review – 1.3. Current state on modeling nanomechanics

at any given strain, the activation energy for the nucleation of a dislocation from a stepped surface is lower than in the case of a flat surface. They confirm that the step lying on the surface acts as a favorable site for the onset of dislocation nucleation. Thus, it is energetically easier to remove an existing surface defect rather than to create a new one.

One next step in modeling more realistic samples that we chose to investigate, is to implement a series of atomic steps at the surfaces of the NOs, *i.e.* surface roughness. Luan and Robbins revealed that atomic-scale alterations in the arrangement of surface atoms result in significant variations in the width of the contact region and the stress required for plastic yield [Luan and Robbins 2005; Luan and Robbins 2006]. Additionally, Jacobs *et al.* explored the influence of roughness on the adhesion of a nano-scale indenter tip to a flat diamond surface [Jacobs et al. 2013]. They conducted a comparative analysis of adhesion and compression forces during indentation using both perfectly round and roughened carbon tips. To generate rougher indents, 25% of the carbon atoms from the outer 3–5 Å of the tip were randomly removed. As shown in Figure 1.20, simulation results reveal two key findings: the rougher tips exhibit a scatter in force-displacement data, and pull-off forces are approximately 50% lower compared to the perfectly round case. This suggests that adhesion is highly sensitive to atomic-scale roughness. Specifically, work of adhesion values decrease by several orders of magnitude between atomically smooth and the roughest tips. Their work underscores the crucial consideration of atomic-scale roughness when interpreting adhesion and, more broadly, nano-scale contact phenomena.

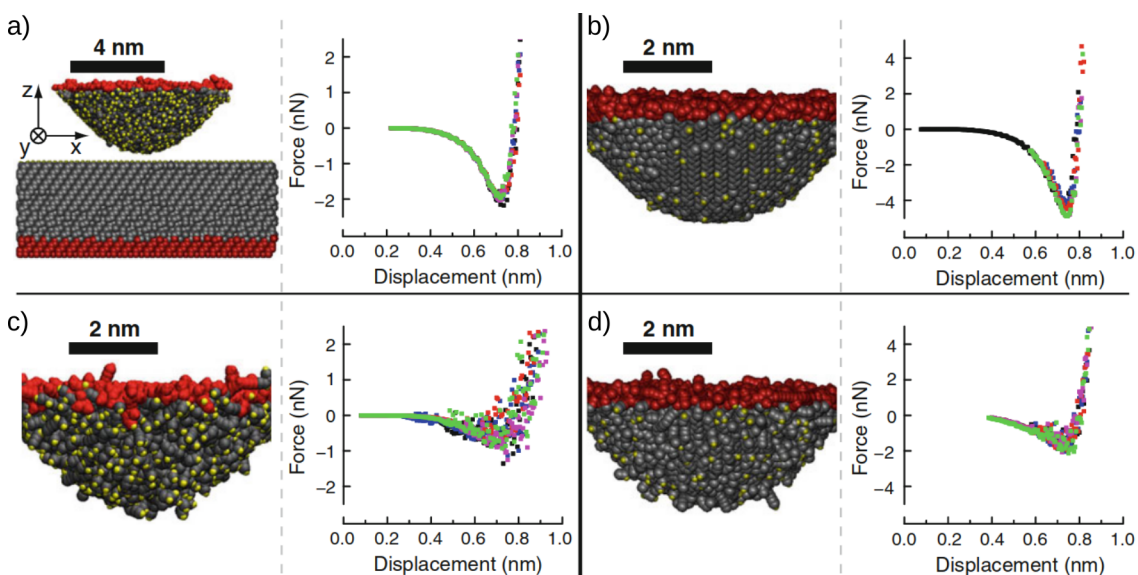


Figure 1.20.: Indentation of diamond substrate with round (a-b) and roughened (c-d) tips. Data points from five tests performed with slightly different contact locations are shown overlapped. From [Jacobs et al. 2013].

However, there is currently a lack of studies that specifically address the strength

## 1. Literature review – 1.3. Current state on modeling nanomechanics

of NOs with rough surfaces. This gap in research represents a potential key factor in the explanation of the observed scattering in mechanical testing data, as illustrated in Figures 1.2 or 1.9, as well as in the understanding of deformation mechanisms. This aspect is further investigated in Chapters 4 and 5.

### 1.3.3.2. Surface oxidation

With the advances in computational techniques, it is now possible to model the charged interactions between metal and oxygen at the atomic scale (see Chapters 2 and 6) and to study the growth of an oxide layer and its mechanical influence.

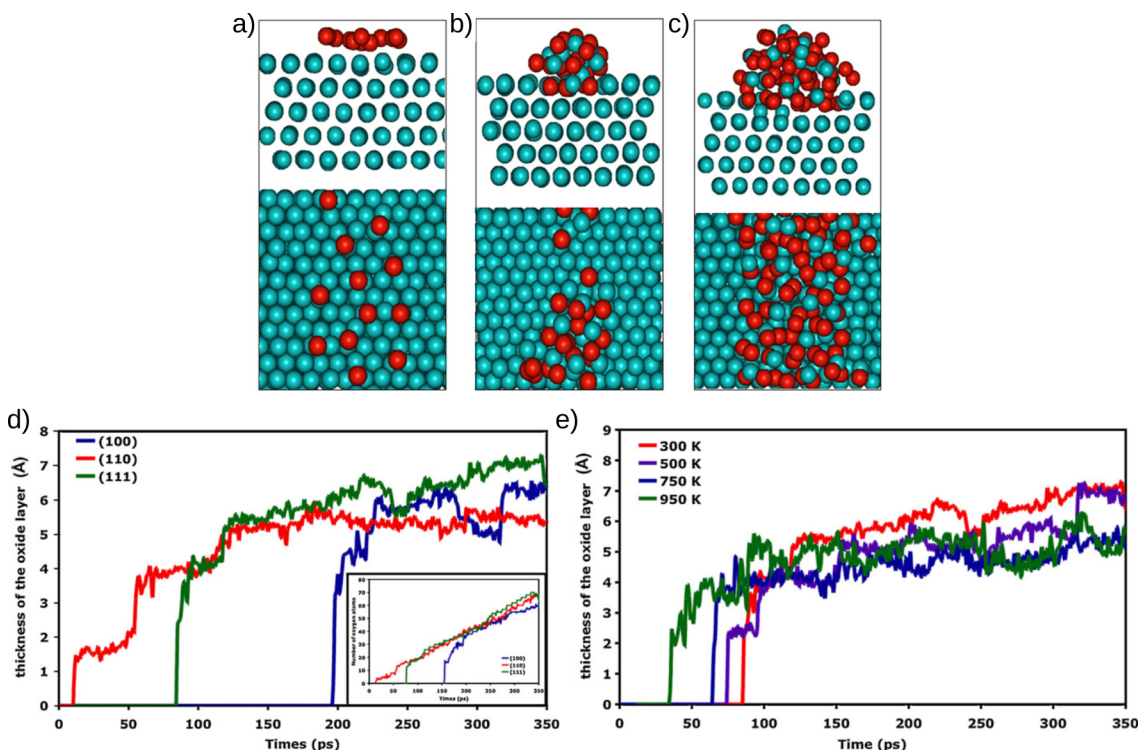


Figure 1.21.: Early-stage of Ni oxidation. a) dissociative chemisorption stage, b) rapid nucleation of nickel oxide island, and c) lateral growth of the oxide island. Oxide thickness as a function of d) the cristallographic orientation and e) the temperature. Adapted from [Garruchet et al. 2010].

The early-stage oxidation of thin films has been investigated by several research groups using MD for Al [Trybula and Korzhavyi 2019; Kim and Choi 2021], Cu [Jeon et al. 2011; Gattinoni and Michaelides 2015], Ni [Garruchet et al. 2010; Sankaranarayanan and Ramanathan 2010] or Fe [Lu et al. 2015]. The main result of these studies is that, as observed experimentally, an island growth mode is observed (see example of Ni in Figure 1.21 a-c and oxidized surface observed experimentally in Figure 1.11). It is composed of three different stages: a dissociative chemisorption stage, the nucleation

### 1. Literature review – 1.3. Current state on modeling nanomechanics

of oxide island and the lateral growth of oxide islands. Results also show that parameters such as crystallographic orientation or temperature have an influence on the kinetics of oxide growth, as shown in Figure 1.21d-e, as well as gas pressure.

Then, only a few studies were applied to the mechanics of NOs with considering oxidized surfaces. Skarlinski and Quesnel simulated the tensile properties of oxide-coated-copper thin films for the first time [Skarlinski and Quesnel 2015]. The oxide layers lowered the yield stress by 30%–40%, and embrittled the material such that yield occurred at much lower strains. They showed that the causes of the embrittlement are restructuring events within the oxide layers which nucleate defects into the inner copper film before yielding.

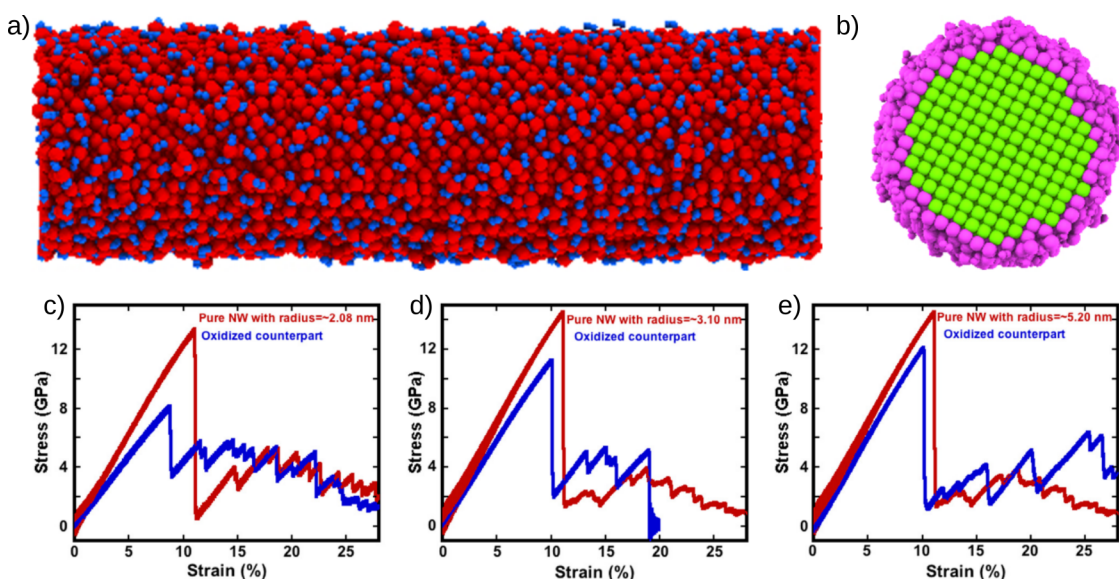


Figure 1.22.: Tensile testing of pre-oxidized Cu NWs. a) Initial structure (red spheres represent Cu atoms, and blue spheres denote O atoms) with b) the amorphous (purple) and FCC (green) lattice structures. Stress-strain curves comparison between the pristine NWs (in red) and their pre-oxidized counterparts (in blue) for the pristine NW radius c) 2.08, d) 3.10, and e) 5.20 nm, respectively. Adapted from [Aral and Islam 2023].

More recently, Aral *et al.* ran a succession of studies on the influence of native oxide layers on the mechanical properties of Cu, Ni and Fe nanowires [Aral et al. 2016; Aral et al. 2018; Aral et al. 2019; Aral and Islam 2023]. The comparison of results between the pristine NWs and their oxidized counterparts confirms that the presence of an oxide shell layer has a crucial role on the onset of plasticity, deformation mechanism and on the related properties of NWs, which results in a global weakening and confirms preliminary experimental observations [Shin et al. 2019]. Their work clarifies that the presence of an oxide shell layer at the free surface accelerates the initiation of defects at the onset of plasticity since the oxidized NWs exhibit lower yield stress and strain.

### *1. Literature review – 1.3. Current state on modeling nanomechanics*

In this work, we focus on better modeling biases that potentially play a role in the data scattering observed in mechanical testing. Especially, we investigate the setup control mode as well as the surface state in their implication on the strength and mechanical behavior of NOs.

#### **Chapter I summary:**

**Three main axis are covered in this literature review chapter to better assess the rest of the PhD manuscript. First, we have introduced micro- and nanomechanics and the high strength of miniaturized systems compared to their bulk counterparts ("smaller is stronger"). Then, we have discussed how experimental biases can affect the strength of NOs including extrinsic and intrinsic effects such as setup control mode or surface alteration. Finally, a review on the current state of the art on nanomechanics modeling highlights the lack of studies that account for potential biases and their influence on the strength of NOs.**

# 2

## Methods

In this chapter, a comprehensive overview of the computational techniques employed in the studies presented in subsequent chapters is provided. We start by providing a brief introduction about atomistic simulations, which includes defining interatomic potentials, describing thermodynamic ensembles, and explaining boundary conditions. Then we describe the protocols to model nanocompression, nanoindentation and surface oxidation, covering sample preparation and the procedure to conduct mechanical tests. Finally, the auxiliary tools used in these studies are introduced.

## 2.1. Introduction to atomistic simulations and modeling

Throughout this work, we use the Large-scale Atomic/Molecular Massively Parallel Simulator (LAMMPS) simulation code [Plimpton 1995; Thompson et al. 2022] to conduct MS and MD simulations. Its full parallelization makes it a good choice for the simulation of moderate-to-large atomistic systems using multiple processors. We focus here on key aspects of these methodologies relevant to the simulation protocols used in the current studies.

### 2.1.1. Interatomic potentials

In atomistic simulations, interatomic potentials enable the modeling of atomic interactions by encompassing key attributes of the atomic system, such as the equilibrium lattice distance, defect formation energy, sublimation energy or constants of elasticity. These potentials can be based either on simple analytical formulations or on intricate quantum-based equations.

In the following two sub-sections, we present the formalism for the two categories of interatomic potentials employed in our studies, namely, the embedded atom method (EAM) [Daw and Baskes 1984] to describe metallic bonds and the Reactive force field (ReaxFF) potential [van Duin et al. 2001] for characterizing interactions between oxygen and metals. Of course, other definitions do exist including the description of covalent [Tersoff 1986; Tersoff 1988] or ionic [Adams and McDonald 1974; Catlow 1977] interactions, as well as alternative formalisms for metallic bonds (MEAM) [Baskes 1992] or charged interactions (SMTB-Q) [Hallil et al. 2006]. Furthermore, recent computational developments gave access to machine learning inter-atomic potentials that improve realism in materials modeling by “learning” electronic-structure data [Zuo et al. 2020; Mishin 2021; Byggmästar et al. 2022]. However their application is out of the scope of this study so they will not be discussed further.

#### 2.1.1.1. Embedded atomic method

The EAM potential is employed to describe the metallic nature of bonding. The underpinning of the EAM potential lies in the analysis of the electron density encompassing each atom, which can be regarded as the aggregate contribution of neighbouring atoms. Consequently, the total energy associated with each atom can be defined as the combination of an embedding energy term  $E_e(\rho_{h,i})$ , representing the electron density of the given atom within the background electron density formed by the surrounding atoms, along with a pairwise core-core repulsion energy term  $\Phi(r_{ij})$  [Foiles et al. 1986]. This results in the approximation of the total energy of the system  $E_{system}$ ,

$$E_{system} = \sum_i E_e(\rho_{h,i}) + \frac{1}{2} \sum_i \sum_{j \neq i} \Phi(r_{ij}) \quad (2.1)$$

## 2. Methods – 2.1. Introduction to atomistic simulations and modeling

where,  $\rho_{h,i}$  is the host electron density of the  $i^{th}$  atom due to the surrounding ones, and  $r_{ij}$  is the distance between atoms  $i$  and  $j$ .

The electron density of atom  $i$  is approximated by the superposition of neighbor atomic densities:

$$\rho_{h,i} = \sum_{j \neq i} \rho_j(r_{ij}) \quad (2.2)$$

where,  $\rho_j(r_{ij})$  is the contribution of the atom  $j$  to the density of atom  $i$ .

The pair-wise interaction between atom  $i$  and  $j$  is defined as:

$$\Phi(r_{ij}) = \frac{q_i q_j}{|r_{ij}|} \quad (2.3)$$

where  $q_i$  is an effective charge associated to atom  $i$ .

Both the embedding function  $E_e$  and the pair repulsive energy  $\Phi$  are typically obtained via an empirical fit of intrinsic material properties which are then uniquely defined by the potential.

The EAM is the most frequently employed technique to compute properties of metals. In this work, we use the EAM potentials proposed by Grochola *et al.* [Grochola et al. 2005], Mishin *et al.* [Mishin et al. 2001], Angelo *et al.* [Angelo et al. 1995] and Zhou *et al.* [Zhou et al. 2004] to respectively study the mechanical properties of Au, Cu, Ni and Ag. The transferability of these potentials to nanomechanics is addressed in several studies in which computed lattice, surface and dislocation properties were shown to accurately reproduce experimental and DFT results [Shinoda et al. 2004; Mordehai et al. 2011b; Rassoulinejad-Mousavi et al. 2016; Sharma et al. 2021].

### 2.1.1.2. Reactive force field

ReaxFF enables to model reactive processes occurring at the interfaces of gas, liquid, and solid phases which is pertinent in contexts of heterogeneous catalysis on metals and oxides or atomic layer deposition [van Duin et al. 2001]. A non-exhaustive overview of ReaxFF applications is presented in Figure 2.1. In the framework of the ReaxFF, both reactive and non-reactive interatomic interactions are defined using a bond-order formalism in combination with descriptions of polarizable charges [Nomura et al. 2008; Senftle et al. 2016]. This enables ReaxFF to provide accurate representations of covalent and electrostatic interactions in a wide variety of materials. The environment-dependent charge distribution is described using the electronegativity equalization method (EEM) [Mortier et al. 1986] and the energy contributions are delineated as follows:

$$E_{\text{system}} = E_{\text{bond}} + E_{\text{over}} + E_{\text{angle}} + E_{\text{tors}} + E_{\text{vdWaals}} + E_{\text{Coulomb}} + E_{\text{spe}} \quad (2.4)$$

Here, we provide a description of each partial energy term introduced in equation 2.4.

- **Bonding energy  $E_{\text{bond}}$**

## 2. Methods – 2.1. Introduction to atomistic simulations and modeling

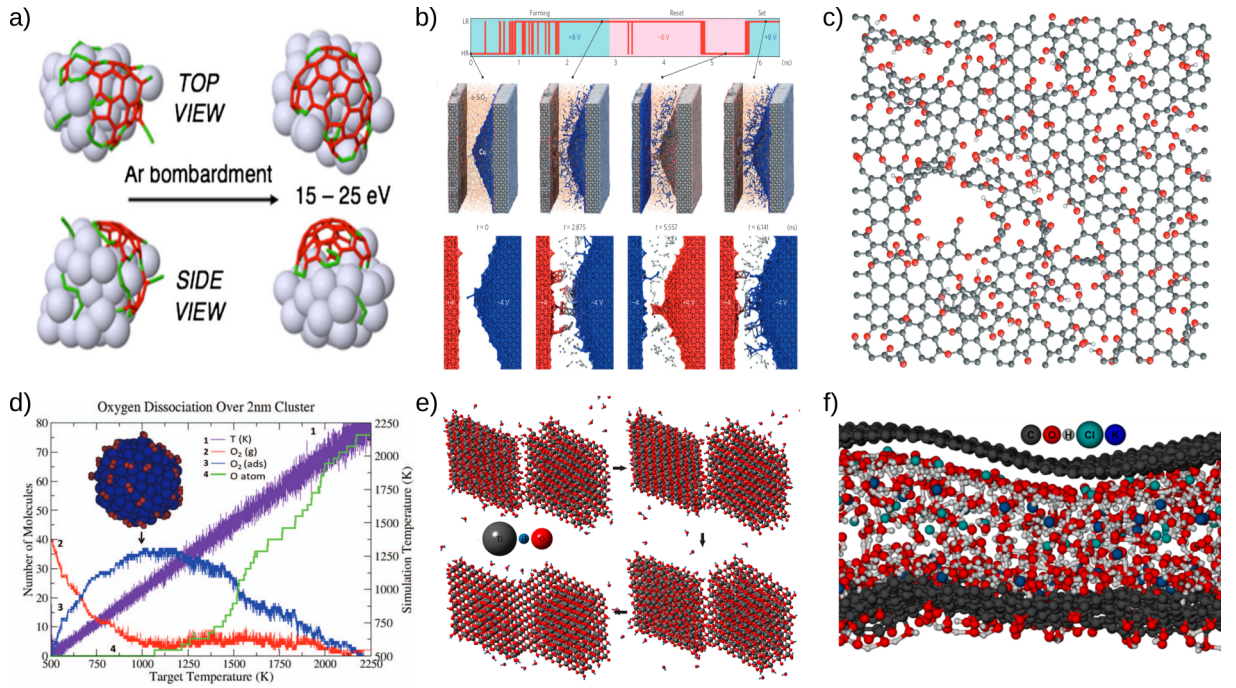


Figure 2.1.: Example of applications of the ReaxFF method. a) Ni-catalysed Carbon nano-tubes growth [Neyts et al. 2013], b) electrometallisation cells [Onofrio et al. 2015], c) reduction of graphene oxide [Bagri et al. 2010], d) Pd surface oxidation [Senftle et al. 2013], e) oriented attachment mechanisms in TiO<sub>2</sub> nanocrystals [Raju et al. 2014], f) capacitive mixing by double layer expansion [Hatzell et al. 2014]. Adapted from [Senftle et al. 2016].

$E_{bond}$  is a continuous function of interatomic distances and quantifies the energy related to bond formation between atoms. A core assumption of ReaxFF is that the bond order  $BO_{ij}$ , which characterizes the type and strength of covalent bonds between a pair of atoms, can be directly determined from the interatomic distance  $r_{ij}$  as outlined in Equation 2.5. In the calculation of the bond orders, it distinguishes between contributions from  $\sigma$ -bonds,  $\pi$ -bonds and  $\pi\pi$ -bonds.

$$BO_{ij} = BO_{ij}^{\sigma} + BO_{ij}^{\pi} + BO_{ij}^{\pi\pi} \\ = \eta_{ij}^{\sigma} \exp \left[ p_{bo1} \left( \frac{r_{ij}}{r_0^{\sigma}} \right)^{p_{bo2}} \right] + \eta_{ij}^{\pi} \exp \left[ p_{bo3} \left( \frac{r_{ij}}{r_0^{\pi}} \right)^{p_{bo4}} \right] + \eta_{ij}^{\pi\pi} \exp \left[ p_{bo5} \left( \frac{r_{ij}}{r_0^{\pi\pi}} \right)^{p_{bo6}} \right] \quad (2.5)$$

where  $r_0^{\sigma}$ ,  $r_0^{\pi}$  and  $r_0^{\pi\pi}$  are the equilibrium bond lengths,  $\eta_{ij}^{\sigma}$ ,  $\eta_{ij}^{\pi}$  and  $\eta_{ij}^{\pi\pi}$  are correction coefficients that rely on the number of bonding electrons defined as  $Val_i$  and  $p_{bo1}, \dots, p_{bo6}$  are fitting parameters.

## 2. Methods – 2.1. Introduction to atomistic simulations and modeling

The bonding energy is then computed by summing on each (i,j) atoms pairs,

$$E_{bond} = \sum_i \sum_j \left[ -D_e^\sigma BO_{ij}^\sigma \exp \left[ p_{be1} \left( 1 - \left( BO_{ij}^\sigma \right)^{p_{be2}} \right) \right] - D_e^\pi BO_{ij}^\pi - D_e^{\pi\pi} BO_{ij}^{\pi\pi} \right] \quad (2.6)$$

where  $D_e^\sigma$ ,  $D_e^\pi$  and  $D_e^{\pi\pi}$  are bond energy parameters and  $p_{be1}$  and  $p_{be2}$  are fitting parameters.

- **Overcoordination  $E_{over}$**

$E_{over}$  is an energy penalty designed to prevent excessive coordination of atoms, in accordance with the atomic valence rule, as shown in Figure 2.2a. When an atom is overcoordinated ( $\Delta_i > 0$ ), Equation 2.7b introduces an energy penalty to the system. The degree of overcoordination  $\Delta_i$  is reduced if the atom contains a lone electron pair that has been dissociated or disrupted.

$$\Delta_i = -Val_i + \sum_j BO_{ij} \quad (2.7a)$$

$$E_{over} = \frac{\sum_j p_{ovun1} D_e^\sigma BO_{ij}}{\Delta_i + Val_i} \left[ \frac{\Delta_i}{1 + \exp(p_{ovun2} \Delta_i)} \right] \quad (2.7b)$$

where  $p_{ovun1}$  and  $p_{ovun2}$  are fitting parameters.

- **Angle energy  $E_{angle}$**

$E_{angle}$  denotes the energy associated with three-body valence angle strain, as shown in Figure 2.2b. Similar to bond terms, it is crucial that the energy contribution from valence angle terms approaches zero as the bond orders within the valence angle approach zero. Equation 2.8 is used to compute the energy contribution from valence angles. The equilibrium angle  $\Theta_0(SBO^\pi)$  for  $\Theta_{ijk}$  relies on the cumulative sum of  $\pi$ -bond orders ( $SBO^\pi$ ) around the central atom  $j$ .

$$E_{angle} = \eta_{ijk} p_{val1} \left[ 1 - \exp \left( -p_{val2} (\Theta_0(SBO^\pi) - \Theta_{ijk})^2 \right) \right] \quad (2.8)$$

where  $\eta_{ijk}$  is a correction coefficient that depends on the bond orders  $BO_{ij}$  and  $BO_{jk}$  and  $p_{val1}$  and  $p_{val2}$  are fitting parameters.

- **Torsion angle  $E_{tors}$**

$E_{tors}$  is the energy associated with four-body torsional angle strain, as shown in Figure 2.2b. As with angle terms, it is imperative to ensure that the energy dependence

## 2. Methods – 2.1. Introduction to atomistic simulations and modeling

of the torsion angle  $\omega_{ijkl}$  properly accounts for  $BO$  values approaching zero and for values greater than 1. This is done by Equation 2.9.

$$E_{tors} = \eta_{ijkl} \sin \Theta_{ijk} \sin \Theta_{jkl} \cdot \left[ \frac{1}{2} V_1 (1 + \cos \omega_{ijkl}) + \frac{1}{2} V_2 \exp \left( p_{tor1} \left( BO_{jk}^{\pi} - 1 + \eta_{jk} \right)^2 \right) (1 - \cos 2\omega_{ijkl}) + \frac{1}{2} V_3 (1 + \cos 3\omega_{ijkl}) \right] \quad (2.9)$$

where  $\eta_{ijkl}$  and  $\eta_{jk}$  are correction coefficients that depend on the bond orders  $BO_{ij}$ ,  $BO_{jk}$ ,  $BO_{kl}$  and the coordination numbers  $\Delta_j$  and  $\Delta_k$ ,  $p_{tor1}$  is a fitting parameter and  $V_1$ ,  $V_2$  and  $V_3$  are torsional rotational barriers.

- **Van der Waals interactions**  $E_{vdWaals}$

$E_{vdWaals}$  is the electrostatic contribution computed between all atoms, regardless of their connectivity and bond-order, as shown in Figure 2.2c. The consideration of van der Waals interactions is achieved using a distance-corrected Morse potential, as outlined in Equations 2.10a and 2.10b. The inclusion of a shielded interaction helps to prevent excessively strong repulsion between bonded atoms and atoms that share a valence angle.

$$E_{vdWaals} = T_{ap} D_{ij} \left[ \exp \left( \alpha_{ij} \left( 1 - \frac{f(r_{ij})}{r_{vdW}} \right) \right) - 2 \exp \left( \frac{1}{2} \alpha_{ij} \left( 1 - \frac{f(r_{ij})}{r_{vdW}} \right) \right) \right] \quad (2.10a)$$

$$f(r_{ij}) = \left[ r_{ij}^{p_{vdW1}} + \left( \frac{1}{\gamma_W} \right)^{p_{vdW1}} \right]^{\frac{1}{p_{vdW1}}} \quad (2.10b)$$

where  $T_{ap}$  is a taper correction [De Vos Burchart et al. 1992],  $r_{vdW}$  is the cutoff distance and  $D_{ij}$ ,  $\alpha_{ij}$ ,  $p_{vdW1}$  and  $\gamma_W$  are fitting parameters.

- **Coulomb interactions**  $E_{Coulomb}$

Similar to the van der Waals interactions, Coulomb interactions are considered between all pairs of atoms, as shown in Figure 2.2d. To account for orbital overlap between atoms at close distances, a shielded Coulomb potential is employed,

$$E_{coulomb} = T_{ap} C \frac{q_i(r_{ij}) q_j(r_{ij})}{\left[ r_{ij}^3 + \left( \frac{1}{\gamma_{ij}} \right)^3 \right]^{\frac{1}{3}}} \quad (2.11)$$

where  $C$  and  $\gamma_{ij}$  are fitting parameters.

Atomic charges  $q_i$  are dynamic variables over time. Following updates to atom coordinates, the EEM subroutine recalculates the charge distribution by minimizing the Coulomb energy while adhering to the charge-neutrality constraint,  $\sum q_i = 0$ . With the use of the Lagrange-multiplier method [Mortier et al. 1986], achieving constrained energy minimization is similar to solve for the electronegativity equalization problem,

$$-\frac{\partial E_{Coulomb}}{\partial q_i} = -\mu \quad (2.12)$$

## 2. Methods – 2.1. Introduction to atomistic simulations and modeling

where  $\mu$  is the electronegativity. The constrained minimization problem is solved using the conjugate gradient (CG) method. Because of the electronegativity equalization condition of Equation 2.12, the force contribution from  $E_{Coulomb}(q_i(r_i), r_i)$  given by,

$$F_{Coulomb} = -\sum_i \frac{\partial E_{Coulomb}}{\partial q_i} \frac{\partial q_i}{\partial r_i} - \frac{\partial E_{Coulomb}}{\partial r_i} = -\mu \frac{\partial}{\partial r_i} \sum_i q_i - \frac{\partial E_{Coulomb}}{\partial r_i} = -\frac{\partial E_{Coulomb}}{\partial r_i} \quad (2.13)$$

does not contain chain-rule terms associated with charges  $q_i$  originally induced by the functional derivative.

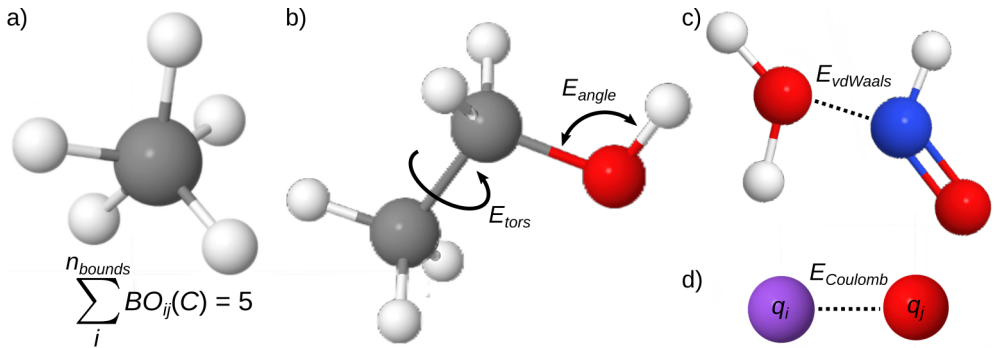


Figure 2.2.: Schematic representation of interatomic interactions including a) overcoordination of a C atom, b) torsion and angle energies, c) van der Waals and d) Coulomb interactions.

- Additional contributions  $E_{spe}$

This energy term  $E_{spe}$  regroups the contributions of system-specific terms. They include terms like  $E_H$  which characterizes the bond-order dependent hydrogen bond interactions in an X-H—Z system (Equation 2.14) or  $E_{C2}$  designed to account for the instability of the C-C triple bond due to terminal radical electrons (Equation 2.15). Additional contributions may be incorporated to describe the total energy of the system, and interested users can find a comprehensive list in ref. [Nomura et al. 2008].

$$E_H = p_{hb1} [1 - \exp(p_{hb2} BO_{XH})] \exp\left(p_{hb3} \left(\frac{r_{hb}^0}{r_{HZ}} + \frac{r_{HZ}}{r_{hb}^0} - 2\right)\right) \sin^8\left(\frac{\Theta_{XHZ}}{2}\right) \quad (2.14)$$

where  $r_{hb}^0$  is the equilibrium hydrogen bond length and  $p_{hb1}$ ,  $p_{hb2}$  and  $p_{hb3}$  are fitting parameters.

$$E_{C2} = k_{C2} (BO_{ij} - \Delta_i - 0.04\Delta_i^4 - 3)^2 \quad (2.15)$$

where  $k_{C2}$  is an energy fitting parameter.

## 2. Methods – 2.1. Introduction to atomistic simulations and modeling

Given the large amount of fitting parameters involved, ReaxFF potentials undergo optimization through a training phase that uses experimental data. This phase iteratively minimizes the sum of squares for each parameter to achieve refinement. In this work, we use the ReaxFF potentials developed by Assowe *et al.* [Assowe et al. 2012] and Zhu *et al.* [Zhu et al. 2020] to study oxidation processes and the influence of a surface-oxide layer on the mechanical properties of Ni and Cu, respectively (see Chapter 6).

### 2.1.2. Energy minimization using molecular statics

MS is a simulation method employed to determine the force-free equilibrium state of a specific atomic configuration by iteratively adjusting their positions to reach a local energy minimum. This state is representative of conditions at absolute zero temperature (0 K) wherein neither time nor atomic velocities are defined. In MS, the potential energy  $E_{pot}$  of a set of atoms is formulated as follows:

$$E_{pot} = E(\vec{r}_1, \vec{r}_2, \dots, \vec{r}_N) \quad (2.16)$$

where,  $\vec{r}_i$  denotes the position of the  $i^{th}$  atom, and  $N$  represents the total number of atoms within the system.

The force  $\vec{F}_i$  acting on the  $i^{th}$  atom can be determined by computing the negative derivative of the potential energy with respect to the displacement of that atom,

$$\vec{F}_i = -\nabla_i E(\vec{r}_1, \vec{r}_2, \dots, \vec{r}_N) \quad (2.17)$$

To achieve a local energy minimum configuration, various optimization methods can be used, including the Polak-Ribiere CG [Polak and Ribiere 1969; Shewchuk 1994], the Hessian-Free Truncated Newton algorithm (HFTN) [Nash 1985; Martens 2010] or the Fast Inertial Relaxation Engine (FIRE) [Bitzek et al. 2006; Guénolé et al. 2020].

In our work, we predominantly use the CG algorithm to conduct geometric optimization. It is an iterative approach designed to solve sparse systems of linear equations. At each CG iteration, the force  $\vec{F}_i$  acting on the  $i^{th}$  atom located at  $\vec{r}_i$  is calculated from the gradient of the system potential energy  $E$  for every atom in the system, as defined in Equation 2.17. Subsequently, the atom is displaced both in the direction of energy reduction and orthogonal to its prior displacement. CG produces new linearly independent search directions at each step aiming to a relaxed configuration within a specified tolerance threshold  $\epsilon$ . This achievement occurs in a relatively modest number of iterations (hundreds of simulation steps in general), particularly when compared to the system's dimensions, as the algorithm progressively enhances approximations toward the precise solution. In the case of the FIRE algorithm, the method entails a damped dynamics approach, using an Euler integration scheme [Tamagnini et al. 2002; Bitzek et al. 2006].

In this work, we perform MS simulations prior to each MD calculation as a sample optimization step to study systems originally in their ground state.

### 2.1.3. Molecular dynamics

MD is the standard method employed to model the time evolution of an atomistic system. This is achieved through the numerical integration of Newton's equations of motion for all individual particle within the system,

$$m_i \frac{d^2 \vec{r}_i}{dt^2} = \vec{F}_i \quad (2.18)$$

where  $m_i$  is the mass of particle  $i$ .

In MD simulations, time is discretized, and the time step  $\delta t$  is typically selected to be as small as a fraction of the fastest atomic vibrations ( $\approx 10^{-15}$  s). In this short time interval, the forces acting on the particles are assumed to be constant. The potential energy  $E_{pot}(\vec{r}_1, \vec{r}_2, \dots, \vec{r}_N)$  of the system is determined from the relative positions of the particles that interact with each other due to the interatomic potential, and is evaluated at each MD step. Provided that the initial state and the total potential energy are known, the trajectory of each particle can be fully described by integrating Equation 2.18. As the  $n$ -body problem typically lacks a closed-form analytical solution, numerical integration is applied by using the finite difference method. Some efficient numerical integrators are available in LAMMPS and in this work, we use the Velocity Verlet algorithm [Swope et al. 1982], based on the original algorithm proposed by Verlet [Verlet 1967]. The position  $\vec{r}_i$  of the  $i^{th}$  particle at  $t + \delta t$  according to the Velocity Verlet algorithm is derived from a Taylor expansion,

$$\begin{cases} \vec{r}_i(t + \delta t) = \vec{r}_i(t) + \frac{d\vec{r}_i(t)}{dt}\delta t + \frac{1}{2!} \frac{d^2\vec{r}_i(t)}{dt^2}\delta t^2 + \frac{1}{3!} \frac{d^3\vec{r}_i(t)}{dt^3}\delta t^3 + \mathcal{O}(\delta t^4) \\ \vec{r}_i(t - \delta t) = \vec{r}_i(t) - \frac{d\vec{r}_i(t)}{dt}\delta t + \frac{1}{2!} \frac{d^2\vec{r}_i(t)}{dt^2}\delta t^2 - \frac{1}{3!} \frac{d^3\vec{r}_i(t)}{dt^3}\delta t^3 + \mathcal{O}(\delta t^4) \end{cases} \quad (2.19)$$

After simplification, the system of equations leads to,

$$\vec{r}_i(t + \delta t) = 2\vec{r}_i(t) - \vec{r}_i(t - \delta t) - \frac{1}{m_i} \vec{\nabla}_i E(\vec{r}_1, \vec{r}_2, \dots, \vec{r}_N) \delta t^2 \quad (2.20)$$

Note that the Verlet algorithm does not use the velocities to compute the new positions. One, however, can derive it from the trajectory, using,

$$\vec{v}_i(t) = \frac{\vec{r}_i(t + \delta t) - \vec{r}_i(t - \delta t)}{2\delta t} + \mathcal{O}(\delta t^2) \quad (2.21)$$

In the contrary to MS, MD is performed at finite-temperature as derived from atomic velocities.

A minimalist outline of a typical MD program is presented in the following and illustrated in Figure 2.3:

## 2. Methods – 2.1. Introduction to atomistic simulations and modeling

- A simulation protocol defines the specific parameters to govern the overall conditions for the system's simulation including initial temperature, initial pressure, target temperature, target pressure, boundary conditions (BCs), number of MD steps, time step  $\delta t$  and other relevant factors.
- The system initialization involves the assignment of initial positions and velocities to the atoms, as well as the provision of all essential system information such as the interatomic potential.
- The simulation is initiated, and for each iteration corresponding to a time step  $\delta t$  :
  - 1) The total potential energy of the system as a function of particle positions is computed.
  - 2) The forces acting on all particles are computed (Equation [2.17](#)).
  - 3) The new positions and velocities of atoms are determined by numerically integrating the equations of motion using Velocity Verlet algorithm (Equation [2.20](#)).
  - 4) Optionally, relevant quantities, such as actual particle positions and velocities, can be stored in suitable data files for subsequent post-processing.
  - 5) If the maximum number of MD steps is reached, the simulation stops; otherwise, the next iteration starts.
  - 6) The total simulated time is incremented by  $\delta t$ .

### 2.1.3.1. Thermodynamic ensembles

MD simulations can be conducted in different thermodynamical conditions, commonly referred as ensembles. They serve as means to extract the thermodynamic properties of a system based on the principles of classical and quantum mechanics. We mainly focus here on the most frequently used ensembles, which are also employed in the underlying studies. The core concept is that different ensembles represent systems with varying degrees of interaction with their surrounding environment. This spectrum ranges from systems that are completely isolated (referred to as the microcanonical ensemble) to entirely open ones (referred to as the grand canonical ensemble). The selection of the ensemble depends on the specific problem being addressed and the conditions under which the simulation is performed.

- **The microcanonical ensemble NVE** describes isolated systems, that can not exchange heat or matter with the outer environment, with constant number of atoms  $N$ , volume  $V$ , and total energy  $E_{tot}$ . The result is a system where the total energy is conserved but fluctuations in potential and kinetic energy ( $E_{tot} = E_k + E_{pot}$ ) are still allowed.

## 2. Methods – 2.1. Introduction to atomistic simulations and modeling

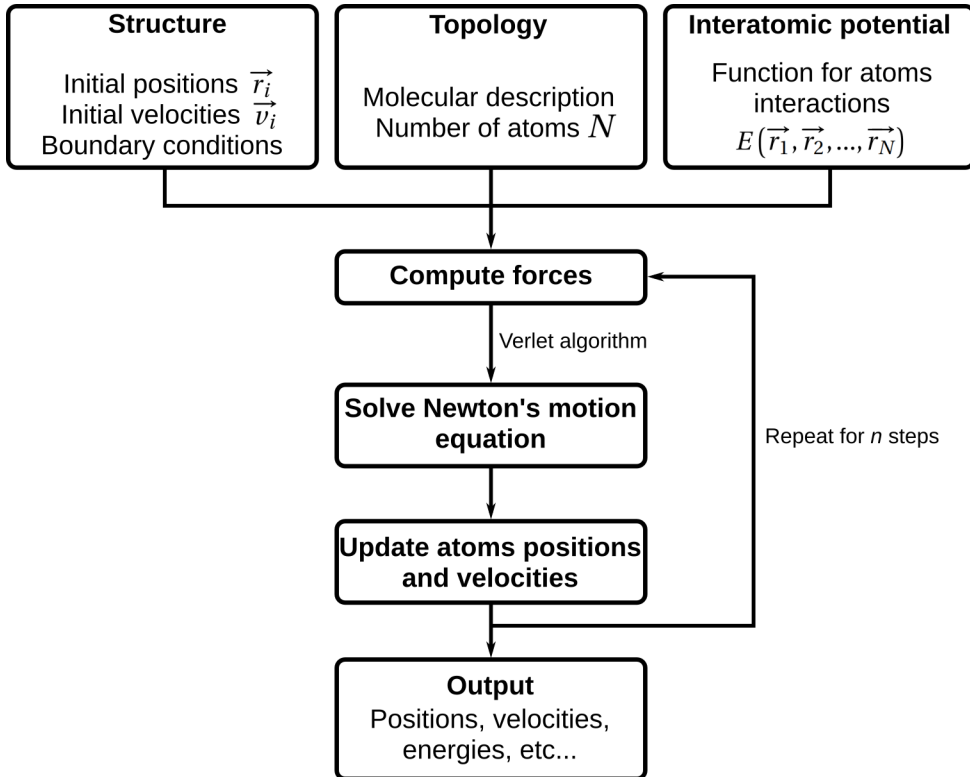


Figure 2.3.: MD workflow including initial parameters such as system's structure and interatomic potential as well as Newton's equations of motion solving and atomic positions update.

- **The canonical ensemble NVT** is an ensemble describing systems at a fixed number of atoms  $N$ , volume  $V$ , and thermodynamic equilibrium temperature  $T$ . The temperature can be controlled using various kinds of thermostats including the Nosé-Hoover thermostat that couples the system to an external heat bath [Nosé 1984; Hoover and Holian 1996]. This method deals with the introduction a fictitious dynamic variable,  $\xi$ , which can be compared to a friction force, influencing the atoms to either slow down or accelerate. It ensures that the temperature converges to the desired target value. In this case, the equations of motions are:

$$\frac{d^2\vec{r}_i}{dt^2} = \frac{1}{m_i} \vec{F}_i - \xi \frac{d\vec{r}_i}{dt} \quad (2.22)$$

$$\frac{d\xi}{dt} = \frac{1}{2Q} \left[ \sum_i m_i \|\vec{v}_i\|^2 - (3N+1) k_B T \right] \quad (2.23)$$

where  $Q$  is an effective mass determining the relaxation of the dynamics of the friction and  $m_i$  and  $\vec{v}_i$  are respectively the mass and the velocity of atom  $i$ .

## 2. Methods – 2.1. Introduction to atomistic simulations and modeling

The kinetic energy  $E_k$  and the temperature  $T$  are derived from the atoms velocities,

$$T = \frac{2}{3} \frac{E_k}{Nk_B} = \frac{1}{3Nk_B} \sum_i m_i \|\vec{v}_i\|^2 \quad (2.24)$$

where  $k_B$  is the Boltzmann's constant.

- **The isobaric isothermal ensemble NPT** where number of atoms  $N$ , pressure  $P$ , and temperature  $T$  are conserved. The unit cell vectors are subject to adjustment, and pressure is controlled by modifying the volume  $V$  as follows,

$$P = \frac{N}{V} k_B T + \frac{1}{3V} \sum_i \vec{r}_i \cdot \vec{F}_i \quad (2.25)$$

Various types of barostats, including the Berendsen [Berendsen et al. 1984] and Nose-Hoover [Nosé 1984] barostats, can be used to control the overall volume of the simulation cell. These barostats can be applied based on a scalar pressure or in relation to orthogonal and tilt directions ( $x, y, z, xy, xz, yz$ ) using a symmetric stress tensor.

A schematic view of these three ensembles is shown in Figure 2.4. Other thermodynamic ensembles exist too, such as the grand canonical ensemble  $\mu$ VT where the number of particles is only fixed on average [Eslami and Müller-Plathe 2007] or NPH where the enthalpy  $H$  is fixed [Andersen 1980] but they are not used in the underlying studies.

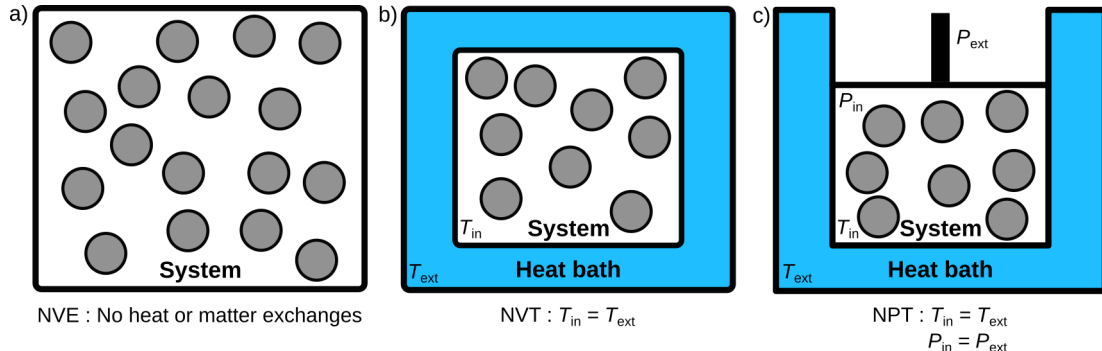


Figure 2.4.: Schematic example of thermodynamic ensembles. a) NVE, b) NVT and c) NPT

### 2.1.3.2. Boundary conditions

In the realm of atomistic simulations, various BCs are employed to simulate and investigate the behavior of nanoscale materials and structures. These BCs play a crucial role in trying to replicate real-world scenarios and determining how atoms interact with the boundaries of the simulation cell. Four primary BCs are mainly used.

## 2. Methods – 2.2. Atomistic simulation protocol

- **Periodic Boundary Conditions (PBC)** are used in MD simulations to mimic the behavior of bulk. It assumes the replication of the simulation cell in all three dimensions, creating a continuous and repeated environment. PBC allows for the study of nanoscale systems as if they were part of an infinitely extended material, eliminating edge effects and enabling the investigation of bulk properties and long-range interactions.
- **Free Boundary Conditions (Free-BC)** lead to no replication of the simulation box, atoms at the boundary are under-coordinated when compared to bulk. Free-BCs are used to model isolated systems and free-surfaces.
- **Fixed Boundary Conditions (Fixed-BC)** are commonly used to investigate a subsystem surrounded by perfect crystal conditions or to avoid rigid displacements. Using these BCs, the motion of atoms within the simulation cell is restricted by the predefined boundaries.
- **Shrink-Wrapping Boundary Condition (SWBC)** is particularly relevant when studying systems with free surfaces that undergo significant deformation or structural changes during simulations. Under this condition, the simulation cell is equivalent to Free-BCs with adaptative simulation cell dimensions to encompass the evolving configuration of the system. This methodology facilitates the investigation of highly deformable systems and the observation of their mechanical responses under diverse conditions, all while upholding computational efficiency.

These BCs will be recalled later in the forthcoming chapters and sections specifically focused on MD nanocompression (SWBC) or nanoindentation (PBC, Free-BC) tests.

## 2.2. Atomistic simulation protocol

For mechanical investigations conducted using MD, our simulation protocols are structured into two or three distinct phases depending on the study. The first phase involves sample preparation, which encompasses energy minimization to achieve the configuration with local minimum energy, followed by a thermal equilibration process. The details of this initial stage vary depending on the specific atomic system being prepared, such as NP or thin film. In the case of surface oxidation, an additional equilibration step is performed where O<sub>2</sub> gas is added above the sample. Subsequently, the equilibrated sample is subjected to nanocompression or nanoindentation. This section provides comprehensive explanations of these protocol stages.

### 2.2.1. Sample preparation

We use ATOMSK [Hirel 2015] (*-create* mode and *-duplicate*, *-select* and *-rmatom* options) for the construction of basic shaped NOs such as half-spheres (see Chapter

## 2. Methods – 2.2. Atomistic simulation protocol

3) or thin films (see Chapter 3 and 6). Faceted NPs are built using the Wulffpack library coupled with ASE (see Chapters 3, 4 and 5). Samples with surface roughness are generated using *Pyrough* (see Chapters 4, 5 and 6) a new tool developed in the context of this PhD. For the energy minimization, we initially employ the CG method with a convergence criterion on the forces experienced by the atoms  $\epsilon_f=10^{-6}$  eV $\text{\AA}^{-1}$ . This corresponds to each atomic force component (*i.e.*,  $f_x$ ,  $f_y$  and  $f_z$ ) lower than  $10^{-6}$  eV $\text{\AA}^{-1}$ . Then, a second minimization step is carried out using the FIRE algorithm and  $\epsilon_f=10^{-8}$  eV $\text{\AA}^{-1}$ . Secondly, the temperature is initialized using the NVE ensemble. The initial temperature is generally set particularly low (a few K). To account for the equipartition theorem, *i.e.* the initial energy spread between  $E_k$  and  $E_{pot}$  during the MD run, it is set twice as large as the target temperature. Finally, we further proceed with the sample equilibration by running one or a few MD runs (including possible temperature ramps) in the NPT or NVT ensemble depending on the context. Note that for rough NPs, the thermal equilibration process conducted in the NVT ensemble is crucial for surface relaxation and is subjected to a detailed investigation (refer to Chapter 5 for more details). For film oxidation, 2D-PBCs are used along the  $xy$  film directions while free-BCs are used in the  $z$ -direction normal to the film where a gas-filled space is introduced. In this latter case, equilibration is performed in the NPT ensemble. More details on thin film equilibration are provided in Chapter 6.

### 2.2.2. Mechanical testing

The equilibrated samples are used as inputs for mechanical testing simulations. We employ the force-field method for the indenter description as described in refs [Issa et al. 2015; Amodeo and Lizoul 2017] to load or indent our virtual samples.

In LAMMPS, a spherical indenter exerts a force of magnitude,

$$f_i = -K(r_i - R)^2 \quad (2.26)$$

on each atom where  $K$  is the specified force constant,  $r_i$  is the distance from the atom to the center of the indenter, and  $R$  is the radius of the indenter. The force is repulsive and  $f_i = 0$  for  $r_i > R$ . This formalism is used in this study to model nanoindentation. To model nanocompression, we use a planar force field described using the same Equation 2.26. However,  $r_i - R$  becomes the distance between atom  $i$  and the indenter position in this latter case. The total force  $F$  exerted by the indenter is then given by,

$$F = \sum_i f_i \quad (2.27)$$

For the compression of NPs, two planar force fields are used as indenter and substrate along the  $z$ -direction. SWBC are used in all directions to accomodate the significant deformations along the  $x$  and  $y$  directions.

For the nanoindentation of thin films, a moving spherical force field is used along the  $z$ -axis to mimick the indenter tip. To maintain the sample, bottommost atoms

## 2. Methods – 2.2. Atomistic simulation protocol

are frozen meaning that velocities (along the  $z$  direction) and forces are equal to zero. The thickness of this frozen atoms layer is greater than the cutoff distance for atomic interactions ensuring that the lowermost row of frozen atoms do not interact with the first non-frozen layer. Particular attention is paid to the  $z$ -dimension as space must be created above the film to accommodate the indenter. An empty volume with a height of at least  $2R$  is created to ensure that the force field does not act on the bottom atoms from the replicated simulation box, induced by PBC. It is important to note that this process necessitates additional minimization steps during sample preparation, as it generates free surfaces.

An illustration of the protocols employed in both scenarios is provided in Figure 2.5.

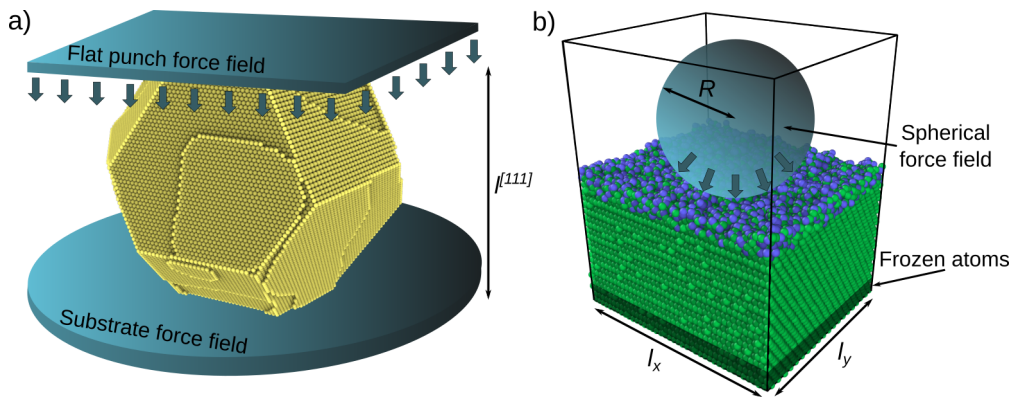


Figure 2.5.: Simulation protocol for MD a) nanocompression of a rough faceted particle and b) nanoindentation of an oxidized thin film. The height variation of the faceted nanoparticle is denoted by  $l^{[111]}$ .

In this work, force field is either displacement or load controlled, depending on the specifics of the study. The load controlled approach was developed in the context of this PhD and is further detailed in Chapter 3. Here the displacement control method is presented, which is also the usual approach used in MD mechanical testing. Relying on an iterative update at a constant displacement rate  $\dot{\Delta}l$ , the position of the indenter  $z_{ind}$  is computed using Equation 2.28.

$$z_{ind}(\dot{\Delta}l, t) = z_{ind}^0 \left( 1 - \frac{\dot{\Delta}l}{z_{ind}^0} t \right) \quad (2.28)$$

where  $z_{ind}^0$  is the initial position of the indenter.

In the case of NPs nanocompression, the engineering strain  $\varepsilon_E$  is defined using the total deformation  $\Delta l$  compared to the initial height of the sample  $l_0$  as specified in Equation 2.29,

$$\varepsilon_E = \frac{\Delta l}{l_0} = \frac{l_0 - l}{l_0} \quad (2.29)$$

where  $l$  is the current height of the sample.

Note that in nanoindentation, displacement refers to the change in the position of

## 2. Methods – 2.2. Atomistic simulation protocol

the indenter relative to its initial position. The engineering stress  $\sigma_E$  is computed as the ratio between the indenter force  $F$  and the initial contact area  $S_0$  (Equation 2.30a). The true stress  $\sigma_T$  is calculated in Equation 2.30b by taking into account the evolution of the contact area  $S$ .

$$\sigma_E = \frac{F}{S_0} \quad (2.30a)$$

$$\sigma_T = \frac{F}{S} \quad (2.30b)$$

where  $F$  is the applied force.

In this thesis, surface areas are calculated using a convex Hull approach [Barber et al. 1996] in the context of load or displacement-controlled nanocompression applied to metal NPs with flat surfaces (see Chapter 3). This method identifies the smallest convex set that encompasses all the atoms under investigation, as shown in Figure 2.6a. The surface is defined as the area of the smallest region that encloses all the atoms, where external atoms are connected by straight lines.

This method was improved in the case of rough surface NPs (see Chapter 5) that require a specific treatment because of its discontinuous nature. Here we use an approach inspired from the work of Goryaeva *et al.* [Goryaeva et al. 2019], where a criterion  $|z_{max} - z_i| < 1 \text{ \AA}$  (with  $z_{max}$  the maximum atoms position) is used to identify the group of atoms that compose the top surface *on-the-fly*. Thus, the contact surface  $S$  is computed as  $S = n_i \cdot s$  where  $s$  is an elementary surface associated to each atom of the top surface ( $s = \frac{a_0^2 \sqrt{3}}{4}$  in the case of (111) surface for instance, where  $a_0$  is the lattice parameter) and  $n_i$  is the total number of atoms contained in the group. This method is used to get rid of outlier results provided by regular convex contour methods to distinct top islets of atoms induced by roughness [Mo et al. 2009], as shown in Figure 2.6b. Note that the definition of contact in case of rough surfaces is still widely debated in the literature (see e.g., ref. [Jacobs and Martini 2017]).

The stress per atom is computed using the Virial theorem,

$$\sigma_{\alpha\beta}^i = -\frac{1}{V_i} \left[ m_i v_\alpha^i v_\beta^i + \frac{1}{2} \sum_j r_\alpha^j f_\beta^{ij} \right] \quad (2.31)$$

where  $v_\alpha^i$  and  $v_\beta^i$  are the velocities of atom  $i$  along  $\alpha$  and  $\beta$  directions,  $m_i$  is the mass,  $r_\alpha^j$  is the position of nearby atom  $j$  along the  $\alpha$  direction and  $f_\beta^{ij}$  is the force exerted by the neighbor atom  $j$  on atom  $i$  along the  $\beta$  direction. The atomic volume  $V_i$  is computed using the VORO++ Voronoi tessellation approach [Rycroft 2009]. The

## 2. Methods – 2.2. Atomistic simulation protocol

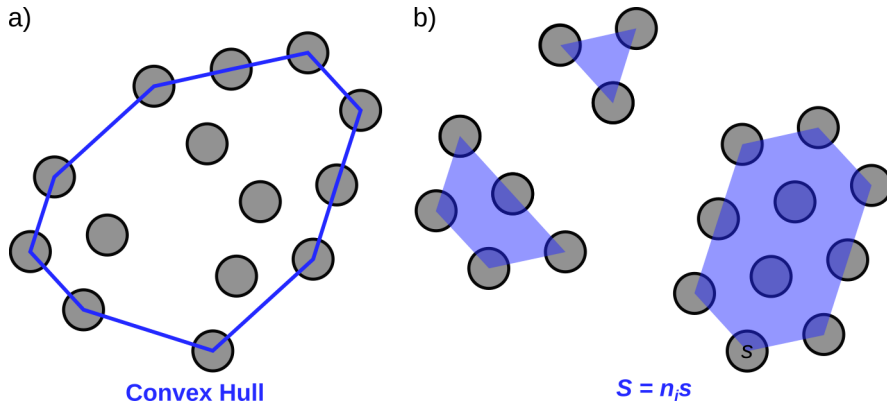


Figure 2.6.: Surface area computation using a) a convex Hull envelope delineating the region enclosed by the blue boundary or b) the number of surface atoms  $n_i$  times an elementary surface  $s$ .

per-atom von Mises stress is computed as,

$$\sigma_M^i = \frac{1}{\sqrt{2}} \left[ \left( \sigma_{xx}^i - \sigma_{yy}^i \right)^2 + \left( \sigma_{yy}^i - \sigma_{zz}^i \right)^2 + \left( \sigma_{zz}^i - \sigma_{xx}^i \right)^2 + 6 \left( (\sigma_{xy}^i)^2 + (\sigma_{xz}^i)^2 + (\sigma_{yz}^i)^2 \right) \right]^{1/2} \quad (2.32)$$

Please note that due to unrealistic calculation of surface atom volume, stress-per atom does not make sense for surface atoms.

### 2.2.3. Surface oxidation

[111]-Ni and [111]-Cu thin films of dimensions  $l_x = 100 \text{ \AA}$ ,  $l_y = 86 \text{ \AA}$ ,  $l_z = 61 \text{ \AA}$  are generated with ATOMSK and prepared following the aforementioned protocol. To model the oxidation process, the simulation box dimension is increased along  $z$ -direction by 120  $\text{\AA}$  which lets room for the  $\text{O}_2$  gas (see Figure 2.7). Charges equilibration is performed every MD step, with a timestep of 0.5 fs.  $\text{O}_2$  molecules with initial velocity  $v_{\text{O}_2}$  are inserted above the thin film, with a 5  $\text{\AA}$  margin to avoid instantaneous interactions. Also, a reflective wall is set at the top of the simulation cell to avoid losing atoms. The number of  $\text{O}_2$  molecules  $n_{\text{O}_2}$  is computed to target a constant concentration  $C_{\text{O}_2}$ ,

$$n_{\text{O}_2} = C_{\text{O}_2} V N_A \quad (2.33)$$

with  $V$  the volume of the gas (*i.e.*, the simulation cell solid excluded) and  $N_A$  the Avogadro number.  $\text{O}_2$  velocities are directed downwards along the  $z$ -direction and their magnitude  $v_{\text{O}_2}$  is adjusted to correspond to the target temperature  $T_{\text{gas}}$ . From Equation 2.24 we get,

$$v_{\text{O}_2} = \sqrt{\frac{3k_B T_{\text{gas}}}{m_{\text{O}_2}}} \quad (2.34)$$

## 2. Methods – 2.2. Atomistic simulation protocol

where  $m_{O_2}$  is the mass of  $O_2$  molecule.

Two regions are defined for the control of the temperature, one for the thin film and another one corresponding to the gas volume. Oxidation simulations are performed in the NVT ensemble for both of these regions using a Nosé-Hoover thermostat with  $T_{gas}$  set equal to  $T_{film}$  the temperature of the thin film. The protocol is presented in Figure 2.7.

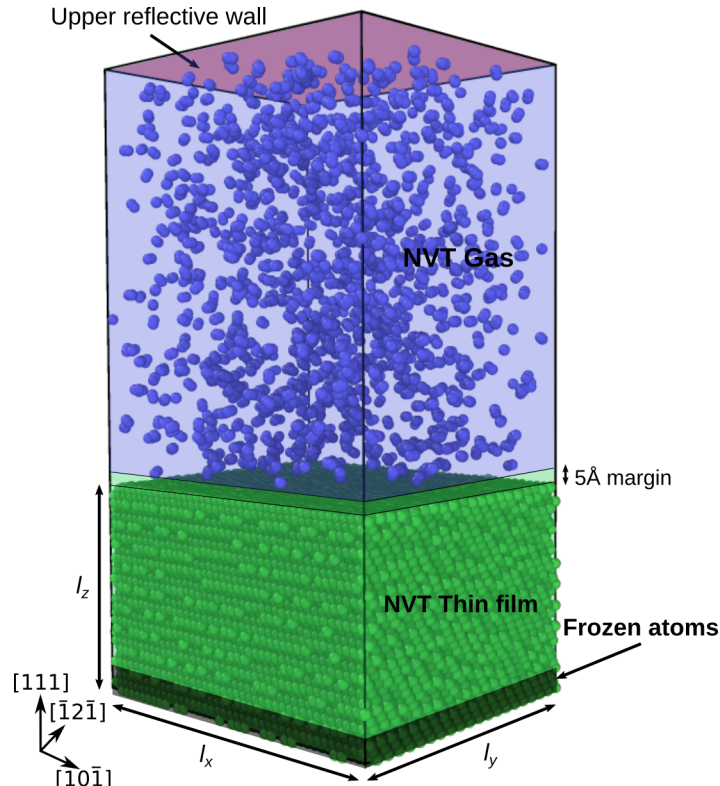


Figure 2.7.: Oxidation simulation protocol. Bottom atoms are frozen while two NVT regions are defined for the thin film and the gas. Upper wall reflects atoms downwards when they come in contact. The 5 Å gap between gas and film corresponds to the high-range interaction cut-off.

To account for the oxygen absorption by the surface and the constant gas concentration, the effective number of  $O_2$  molecules in the gas volume is computed *on-the-fly* during the simulation. Every 1000 steps, new molecules are added randomly and with an initial velocity  $v_{O_2}$  so that the total number of  $O_2$  molecules in the gas region stays equal to  $n_{O_2}$ .

Due to the small number of  $O_2$  molecules and initial velocity conditions, the constant oxygen flux through the thin film top surface can be computed as

$$\Phi_{O_2} = N_A C_{O_2} v_{O_2} \quad (2.35)$$

In this context, the partial pressure of O<sub>2</sub> as computed by the kinetic theory of gases [Hudson 1998; Vannice 2005] is,

$$P_{O_2} = \Phi_{O_2} \sqrt{2\pi m_{O_2} k_B T_{gas}} \quad (2.36)$$

One can note that  $P_{O_2}$  is here overestimated when compared to the perfect gas definition mostly due to the initial atom velocity definition used to reduce CPU costs.

Finally, the mechanical properties of oxidized thin films are investigated using the protocol described in section 2.2.2.

## 2.3. Auxiliary tools and software

### 2.3.1. COMSOL

COMSOL Multiphysics [Multiphysics 1998] is a software platform used for simulation and modeling in the field of engineering and science [Altay et al. 2020; Zahoor et al. 2020; Gumir et al. 2022]. It operates on the basis of finite element analysis and works by dividing the domain into smaller interconnected elements or meshes, and then applying equations to each element to model the behavior of physical systems. It allows users to define and customize their own physics-based models, making it highly versatile and adaptable for a wide range of applications.

In this thesis, we use COMSOL to perform FEM calculations in the case of nanoin-dentation using a rough spherical indenter (see Chapter 4).

### 2.3.2. Gmsh

Gmsh [Geuzaine and Remacle 2009] is an open-source mesh generation software widely used in computational physics, engineering, and mathematics [Wu 2017; Mulligan et al. 2019; Berre et al. 2019]. It operates by defining geometry through a script or graphical interface and subsequently generating high-quality meshes that conform to that geometry. Gmsh employs Delaunay triangulation [Mavriplis 1995] and other meshing algorithms to create complex, unstructured meshes, which are crucial for the accurate simulation of intricate geometries. One of Gmsh's features is its Python API, which allows users to script and automate mesh generation processes to perform repetitive or parameterized simulations.

In this work, we use the Gmsh Python API in *Pyrough* development to generate 3D surface and volumic meshes for the creation of virtual rough samples or to refine a mesh along a defined mathematical field.

### 2.3.3. Paraview

Paraview [Ayachit 2015] is an open-source data visualization and analysis software adapted for multidisciplinary fields such as fluid dynamics, structural mechanics,

and medical imaging [Li et al. 2018; Weishaupt et al. 2019; Svolos et al. 2020]. The software’s graphical user interface enables users to visualize and conduct quantitative analysis on complex phenomena. In this work, we use Paraview to visualize and analyse complex 3D FEM meshes generated in the context of the development of *Pyrough* in Chapter 4.

### 2.3.4. *Pyrough*

*Pyrough* is a versatile Python program that aims at building virtual samples characterized by configurable surface roughness for numerical applications such as atomistic and FEM simulations [Iteney et al. 2024]. The program, that was mainly developed in the context of this PhD work, is open source and relies on the classical roughness theory [Mandelbrot 1985]. Several basic shapes including basic blocks, spheres, grains and wires with surface irregularities are implemented and the object-oriented structure of the program simplifies the implementation of more complex objects. *Pyrough* enables more realistic simulations by improving the virtual sample design. We first present the development of *Pyrough* as well as the theoretical aspects on which it relies (see Chapter 4). It is then used as the tool for the generation of rough samples in the study of surface roughness influence on the mechanical properties of NOs in Chapter 5 or on the oxide growth kinetics in Chapter 6.

### 2.3.5. ATOMSK

ATOMSK is a command-line tool [Hirel 2015] designed for creating and manipulating atomic systems for atomistic simulations. It offers compatibility with various file formats and facilitates the straightforward conversion of atomic configuration files. ATOMSK’s capabilities encompass the creation of perfect crystal supercells and the ability to introduce point and line defects, cracks, planar defects like stacking faults, and deformation or transformation of simulation cells.

Throughout this work, various options provided by ATOMSK are employed to generate atomic systems. For instance, thin films are produced using ATOMSK with the *-duplicate* and *-orient* options to fit with the desired dimensions and orientations. Additionally, the *-rmatom* option, interfaced within *Pyrough*, is used to sculpt a raw 3D atomic box based on an input mesh file, particularly in the context of generating rough atomic samples (as described in Chapter 4).

### 2.3.6. Wulffpack

The Wulffpack library [Rahm and Erhart 2020] is a python library named after the Wulff theory, a fundamental concept in crystallography [Ringe et al. 2011; Barmparis et al. 2015], and is primarily focused on crystal shape prediction. Given a direction-dependent surface energy  $\gamma[\mathbf{n}]$ , the Wulff construction provides the lowest energy shape, based on Wulff theorem [Wulff 1901]. For each direction, a plane at a distance  $\gamma[\mathbf{n}]$  from the origin is created. The Wulff shape is thus the inner set of points such

as  $W = \{\mathbf{x} : \mathbf{x} \cdot \mathbf{n} \leq \gamma[\mathbf{n}] \text{ for all } \mathbf{n}\}$ . WulffPack can construct the regular, single-crystalline Wulff shape as well as decahedra, icosahedra, and particles in contact with a flat surface (the Winterbottom construction). Users can input surface energy data, crystallographic information, and additional parameters to generate detailed predictions of a crystal's morphology.

In this work, gold-faceted NPs are generated using Wulffpack. These are then used to investigate the influence of the control mode on the mechanics of NPs (see Chapter 3) or surface roughness, as interfaced with *Pyrough* (see Chapters 4 and 5), on their mechanical behavior under compression.

### 2.3.7. OVITO

OVITO is a scientific data visualization and analysis software designed for molecular and particle-based simulations, among other applications [Stukowski 2010]. It is developed by OVITO GmbH, a company based in Germany, founded by Stukowski, the original developer of the software. OVITO is built using object-oriented C++ and offers user-friendly control through a straightforward plug-and-play interface or via Python scripts.

In this work, OVITO is used as the primary tool for analyzing the outcomes of MS and MD simulations, creating both 2D and 3D images, and generating simulation movies. Various functions within OVITO are employed to process atomic datasets. For example, the polyhedral template matching (PTM) analysis is used to identify crystalline structures for each atom based on local environment analysis [Larsen et al. 2016]. Additionally, the dislocation extraction algorithm (DXA) is utilized to characterize dislocations and determine their Burgers vectors [Stukowski 2018].

#### Chapter II summary :

**This chapter focuses on the methods used throughout my PhD research program. First, we have introduced atomistic simulation methods (MS and MD) within the LAMMPS framework as well as the various theoretical backgrounds related to the interatomic potentials used to model metallic or reactive interactions. Then, simulation protocols were presented for sample preparation, nanomechanical testing (compression and indentation) and surface oxidation. Finally, companion tools both related to FEM and atomistic simulations were described. They have been used throughout this work to generate samples or analyse simulations outcomes.**

# 3

## **Load vs. displacement controlled nanomechanics**

This chapter refers to the development of an original method for MD load-controlled mechanical tests. Parts of the results were published in ref. [Iteney et al. 2023], where mathematical model for the nanocompression, examples of application and comparison to previous methods and experiments are detailed. Furthermore, we provide here additional contents on the algorithm development and the method is also applied to load-controlled nanoindentation.

## 3.1. Introduction

Only few methods exist to probe mechanical properties at small-scales including nanoindentation (maybe the most common), micro- and nanocompression as well as tensile tests [Hemker and Sharpe 2007; Legros 2014]. These techniques are either load-controlled (*i.e.*, driven by actuators that apply forces) or displacement-controlled. Two kinds of displacement-controlled tests currently exist. On the one hand, the most commonly used mode is the pseudo displacement-controlled mode where a feedback control algorithm such as the proportional integral derivative (PID) is used to monitor displacements via a force actuator setup with more or less precision [Warren et al. 2004]. On the other hand, true displacement-controlled setups drive the displacements of grips or indenters based on the high-stiffness of fast-response piezoelectric actuators. One can notice that true displacement-controlled devices still suffer from the self-compliance of the load cell despite significant improvements in recent years [Dehm et al. 2018]. In small-scale mechanical tests, open-loop force-controlled and pseudo displacement-controlled tests are easily recognizable from intrinsic displacement-controlled ones when looking at the load *vs.* displacement curves. This is particularly true when the mechanical response reaches the plastic deformation regime characterized by large displacement bursts/pop-ins (load-controlled or pseudo displacement-controlled cases) or sudden load drops (true displacement-controlled case). When applied to the study of NPs under compression or to the nanoindentation of thin films, both methods are used without having clearly identified the role of the control mode on the load response or sample shape evolution [Mordehai et al. 2011a; Han et al. 2015; Issa et al. 2015; Issa et al. 2021]. On the other hand, MD simulations are also used to explore the mechanics of NOs [Mordehai et al. 2018; Amodeo and Pizzagalli 2021]. MD allows to identify the elementary deformation processes occurring during mechanical tests (not always observed experimentally) as well as a qualitative evaluation of the yield stress. From a simulation point of view, force-field indenters or frozen boundary atoms are displaced as a function of time to mimic experimental BCs. The MD nanomechanical simulations are therefore inherently displacement-controlled which does not preclude their use to discuss load-controlled experiments. While most collaborative studies do not comment on the control mode mismatch between experiments and MD, an envelope load model is often used to compare MD displacement-controlled simulations and load-controlled experiments and to justify the occurrence of strain bursts or pop-ins [Mordehai et al. 2011a; Feruz and Mordehai 2016; Kositski et al. 2016; Sharma et al. 2021]. Whereas one can argue on the validity of such an approach, a more general question arises about the pros and cons of exclusively using MD displacement-controlled simulations to interpret any type of nanomechanical experiments.

In this chapter, we develop an original approach to run load-controlled MD virtual experiments and use it to discuss the main differences between load- and displacement-controlled tests in the context of recent experiments and simulations performed on metal Au and Ag NPs as well as Ni thin films.

## 3.2. Load controlled nanocompression modeling

### 3.2.1. Methods

In MD nanocompression simulations, the usual displacement-controlled approach relies on changing the indenter position  $z_{ind}$  iteratively at a constant displacement rate  $\Delta l$  as described in Section 2.2.2.

Here, we introduce an original load-controlled simulation setup inspired by the experimental feedback concept built using a Python solver as a feedback loop. Here, the indenter displacement is actuated to adjust the indenter force (and not the other way around). The Python solver is called at time interval  $\Delta t$  by the main MD script to force the match between  $F = \dot{F}t$  with  $\dot{F}$  the user-imposed load rate and  $t$  the simulation time, and the effective indenter force  $F_{ind}$ . The updated indenter position  $z_{ind}(\dot{F}, t)$  is computed solving Equation 3.1.

$$\dot{F}t = F_{ind} \quad (3.1)$$

Note that this feedback approach is extensible to any indenter shape as long as the group of atoms to which the indenter force is applied is properly defined. In the following,  $\Delta t$  is equal to the MD timestep  $\delta t$  ( $\Delta t=\delta t=2$  fs) *i.e.*, we first focus here on comparing ideal load-controlled compression tests with displacement-controlled cases. The quantification of the influence of the machine compliance by using greater  $\Delta t$  is addressed later in section 3.2.2.3.

Thanks to the harmonic force expression for  $F_{ind}$  used in LAMMPS *fix indent* command (Equation 2.27), one obtains a second order polynomial describing the evolution of the flat indenter's position used for nanocompression,

$$z_{ind}^2 - z_{ind} \frac{2}{N} \sum_{i=1}^N z_i + \frac{1}{N} \sum_{i=1}^N z_i^2 - \frac{\dot{F} \cdot t}{KN} = 0 \quad (3.2)$$

where  $N$  is the number of atoms affected by the flat force field *i.e* the number of atoms in the group  $R^N$  defined by  $z_i \geq z_{ind}$  with  $z_i$  the  $z$ -coordinate of the atom.  $K$  is the force field rigidity constant.

Equation 3.2 leads to two possible solutions for which only the lowest polynomial root ensures the monotonous increase of  $F_{ind}$ . Under load-control, the updated position of the indenter is provided by Equation 3.3.

$$z_{ind}(\dot{F}, t) = \frac{1}{N} \sum_{i=1}^N z_i - \frac{1}{N} \sqrt{\left( \sum_{i=1}^N z_i \right)^2 + N \left( \frac{\dot{F} t}{K} - \sum_{i=1}^N z_i^2 \right)} \quad (3.3)$$

The MD protocol for load-controlled nanocompression is shown in Figure 3.1 and can be described in four steps. First, the force-field position is initiated at  $z_{ind}(\dot{F}, 0)$ . Then, the dynamic region  $R^N$  comprising the atoms affected by the force field ( $z_i \geq z_{ind}$ ) is updated. Note that if  $R^N$  is empty (*e.g.* when the indenter is over

the sample), the indenter's position is instantly lowered by a  $0.01 \text{ \AA}$  margin. Following the computation of  $N$ ,  $\sum_{i=1}^N z_i$  and  $\sum_{i=1}^N z_i^2$  from group  $R^N$ , the Python solver is called to compute the new  $z_{ind}(\dot{F}, t)$  position. Finally, the indenter is moved to its new position, a MD run of duration  $\Delta t$  is performed and the dynamic region  $R^N$  is updated.

Note that the call to the Python solver is not strictly necessary. In this case of nanocompression, Equation 3.3 gives an explicit expression of the indenter's position, it can thus directly be implemented in LAMMPS. However, the algorithm is developed in a more global context where, in some cases, the solution is not explicit and the call for the Python solver is crucial (see Section 3.3).

### 3.2.2. Application to the compression of faceted Au nanoparticles

MD simulations for the compression of Au faceted NPs are performed at 10 K using both methods *i.e.* the classical displacement-control and the original load-control algorithm developed in this work. We use the Grochola interatomic potential for Au [Grochola et al. 2005]. Wulff-shaped Au NPs with characteristic heights ranging from 7.52 to 22.56 nm are designed using the Python WulffPack package [Rahm and Erhart 2020] including low-index surface energies  $\gamma_{\{100\}}=1296.5$ ,  $\gamma_{\{110\}}=1531.2$  and  $\gamma_{\{111\}}=1196.4 \text{ mJ.m}^{-2}$  as inputs. The method for the computation of surface energies is detailed in Appendix A. After the design of the NPs using the WulffPack package, the system is equilibrated following the procedure described in Chapter 2 and refs. [Issa et al. 2015; Amodeo and Lizoul 2017].

#### 3.2.2.1. Mechanical response

Figure 3.2 illustrates the mechanical response of a [111]-oriented along  $z$ -direction 14.57 nm Au faceted NP, compressed at various loading rates  $\dot{F}$  ranging from 0.50 to 6.10  $\text{nN.ps}^{-1}$ , which corresponds to an engineering strain rate  $\dot{\epsilon} \sim 10^7 \text{--} 10^8 \text{ s}^{-1}$  computed in the elastic domain, *i.e.* according to the Hooke's law. Note that this strain rate range is typical of usual MD simulations. In addition, a displacement-controlled simulation with  $\dot{l}=0.01 \text{ \AA.ps}^{-1}$  equivalent to  $\dot{\epsilon}=1.03 \cdot 10^8 \text{ s}^{-1}$  is shown. As usual for the latter, two deformation regimes are easily recognizable including a quasi-linear elastic regime up to a yield force  $F_y=689 \text{ nN}$  where a force drop marks the occurrence of plasticity. The compression consists then in a succession of elastic load and force drops. As shown in Figure 3.3, the onset of plasticity is related to SDN and consecutive glide events that reduce the height of the NP along the compression axis and, as a consequence, reduce the force exerted by the indenter during displacement-controlled simulations. In the case of load-control, the force also initially increases linearly following the imposed load-rate during elastic deformation before a rate-dependent load dip occurs, followed by a reload of the indenter force. For the displacement-controlled case, the engineering strain monotonically increases with time as a consequence of the imposed displacement rate whereas a rate-discontinuity is apparent at the load

3. Load vs. displacement controlled nanomechanics – 3.2. Load controlled nanocompression modeling

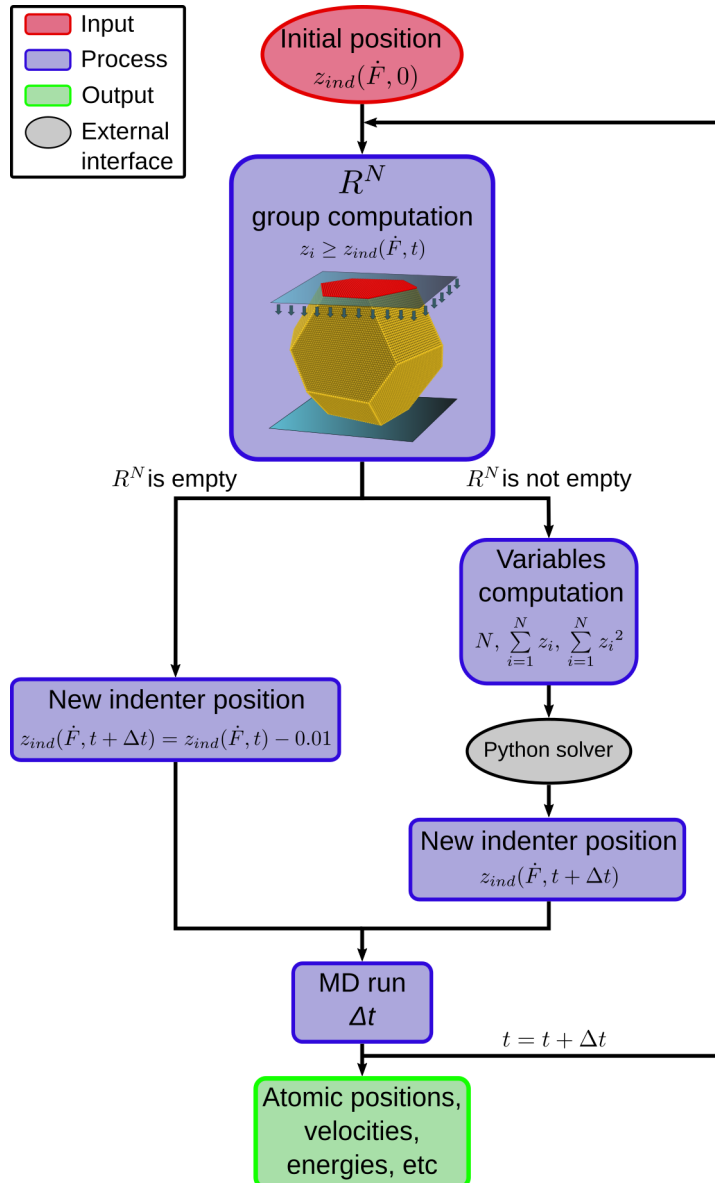


Figure 3.1.: MD load-controlled nanocompression workflow including the computation of group  $R^N$  every  $\Delta t$ , calculation of every atomic variables and the use of a Python feedback loop to solve Equation 3.3.

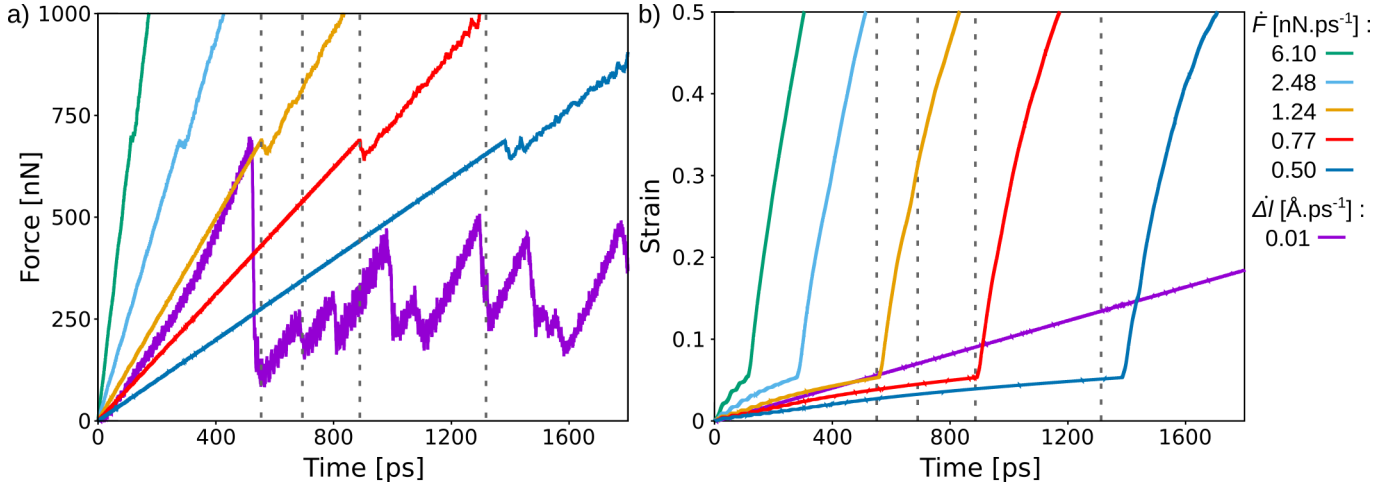


Figure 3.2.: Mechanical response of a 14.57 nm height Au faceted NP under compression using load and displacement-controlled MD simulations. a) Load *vs.* time, b) engineering strain *vs.* time. Black dashed lines refer to time configurations illustrated in Figure 3.3.

dip for force-controlled compression tests. It should be noted here that lowering the imposed displacement rate closer to experimental conditions might also induce strain-rate singularities. Details on critical values and rates before and after the load dip are provided in Table 3.1.

The sample shape and dislocation microstructure for the two simulations  $\dot{F}=1.24$  nN·ps<sup>-1</sup> and  $\dot{\Delta}l=0.01$  Å·ps<sup>-1</sup> are compared in Figure 3.3. For the displacement-controlled simulation, the first SDN event happens at  $t=516$  ps with the nucleation of a  $\frac{1}{6}[1\bar{2}\bar{1}](\bar{1}\bar{1}1)$  Shockley partial dislocation. Then, the kinetics of the SDN process is particularly smooth in this case as dislocations nucleate in an uncorrelated manner. On the other hand, the first plastic event occurs at  $t=555$  ps for the load-controlled compression and is followed by a strain burst made of numerous SDN events clustered in a very short time. These results reproduce and explain the sudden collapse of NPs (the "pancake" shape [Mordehai et al. 2011b]) commonly observed in compression experiments using load-controlled or pseudo displacement-controlled setups (see e.g., refs. [Mordehai et al. 2011b; Han et al. 2015]), in contrast to more gradual shape changes observed in true displacement-controlled compression tests of NPs (see e.g., refs. [Issa et al. 2015; Issa et al. 2021]).

### 3.2.2.2. Dislocation microstructure

Dislocation density  $\rho$  profiles (Figure 3.4a) show (i) load-controlled case: a  $\rho$  burst when the sample yields followed by a drop of the dislocation density by a factor two. Only a slight dependence on the load rate is noticed in the investigated conditions of deformation which is consistent with the constant  $F_y$  behaviour. Finally,  $\rho$  reaches a steady state of about  $1\text{-}3 \cdot 10^{17}$  m<sup>-2</sup>, (ii) displacement-controlled case:  $\rho$  is lower than in load-controlled simulations but continuously increases up to  $4 \cdot 10^{16}$  m<sup>-2</sup>. Unlike

3. Load vs. displacement controlled nanomechanics – 3.2. Load controlled nanocompression modeling

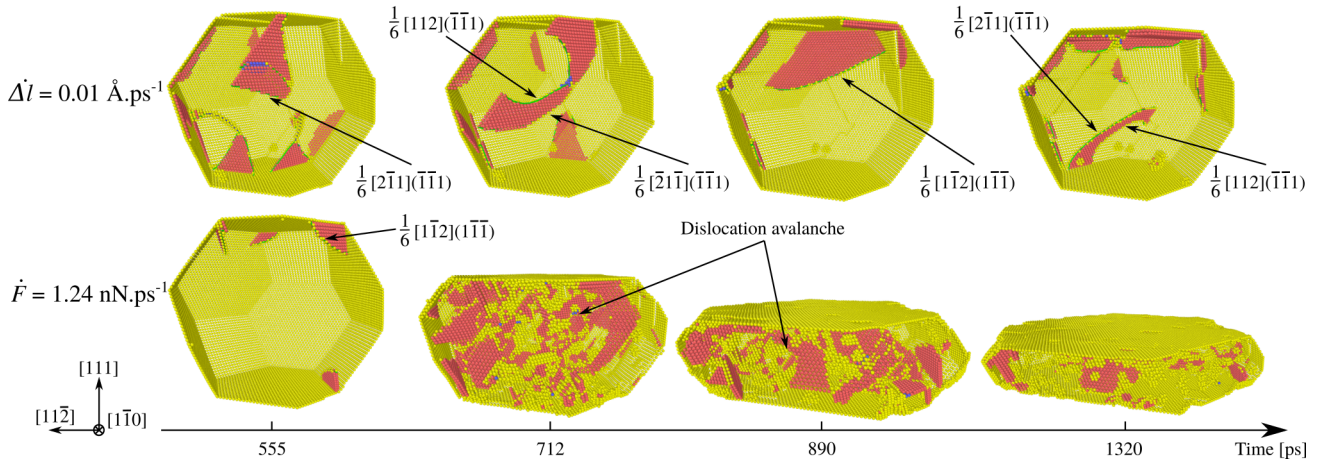


Figure 3.3.: Shape and dislocation microstructure evolution of a 14.57 nm height Au faceted NP under compression using load and displacement-controlled MD simulations. Atoms colored in gold and red, respectively, refer to surfaces and stacking-fault environments. Perfect crystal atoms are removed for the sake of clarity. Shockley partial dislocations are illustrated by green curves.

Table 3.1.: Yield force  $F_y$ , critical stress and time  $\sigma_y$  and  $t_y$  as well as adjusted elastic and plastic strains and load rates ( $\dot{\varepsilon}_e$ ,  $\dot{\varepsilon}_p$ ,  $\dot{F}_e$  and  $\dot{F}_p$ ) computed during MD compression simulations of a 14.57 nm height Au faceted NP using load or displacement-control (respectively labelled  $\dot{F}$  and  $\dot{\Delta}l$ ).

	$\dot{F}$ [nN.ps <sup>-1</sup> ]				$\dot{\Delta}l$ [Å.ps <sup>-1</sup> ]	
	6.10	2.48	1.24	0.77	0.50	0.01
$F_y$ [nN]	698	688	690	689	687	689
$\sigma_y$ [GPa]	8.80	8.67	8.70	8.69	8.66	8.69
$t_y$ [ps]	113	280	555	890	1380	516
$\dot{\varepsilon}_e$ [10 <sup>8</sup> s <sup>-1</sup> ]	4.73	1.89	0.94	0.59	0.38	1.03
$\dot{\varepsilon}_p$ [10 <sup>8</sup> s <sup>-1</sup> ]	27.12	24.88	22.23	24.19	19.53	1.03
$\dot{F}_e$ [nN.ps <sup>-1</sup> ]	6.10	2.48	1.24	0.78	0.50	1.29
$\dot{F}_p$ [nN.ps <sup>-1</sup> ]	6.12	2.51	1.29	0.87	0.59	-

### 3. Load vs. displacement controlled nanomechanics – 3.2. Load controlled nanocompression modeling

load-controlled simulations, significant jumps and drops of  $\rho$  are observed when the displacement is controlled. They characterize discrete dislocation nucleation and exhaustion events as shown in Figure 3.3.

Also, the mean dislocation velocity  $\bar{v}$  is obtained using the Orowan's equation  $\dot{\epsilon} = m\rho b\bar{v}$  where  $m=0.314$  is the maximum Schmid factor for partial dislocation slip systems assuming a compression axis along [111] and a partial dislocation Burgers vector  $b=1.66 \text{ \AA}$  (Figure 3.4b). The first point is that  $\bar{v}$  is lower than the speed of the acoustic wave in Au ( $\sim 3200 \text{ m.s}^{-1}$ ) and, more broadly, does not saturate whatever the control mode [Gurrutxaga-Lerma et al. 2021; Tsuzuki et al. 2009; Marian and Caro 2006; Bryukhanov 2020]. For load-controlled simulations,  $\bar{v}$  is characterized by a peak when the first dislocation nucleates ranging from  $253$  to  $405 \text{ m.s}^{-1}$  and then settles in the  $90$  to  $170 \text{ m.s}^{-1}$  range except for the lowest load-rate  $\dot{F}=0.50 \text{ nN.ps}^{-1}$  that shows a continuous increase of  $\bar{v}$  conditioned by a singular decrease of  $\rho$ . In the displacement-controlled case,  $\bar{v}$  reaches a maximum of  $\sim 180 \text{ m.s}^{-1}$  before it significantly decreases down to a steady-state regime at about  $\sim 70 \text{ m.s}^{-1}$ . Here we note that  $\bar{v}$  is constrained by the strain rate which is about  $25\times$  lower in displacement-controlled than in load-controlled simulations in the plastic deformation regime (see Table 3.1).

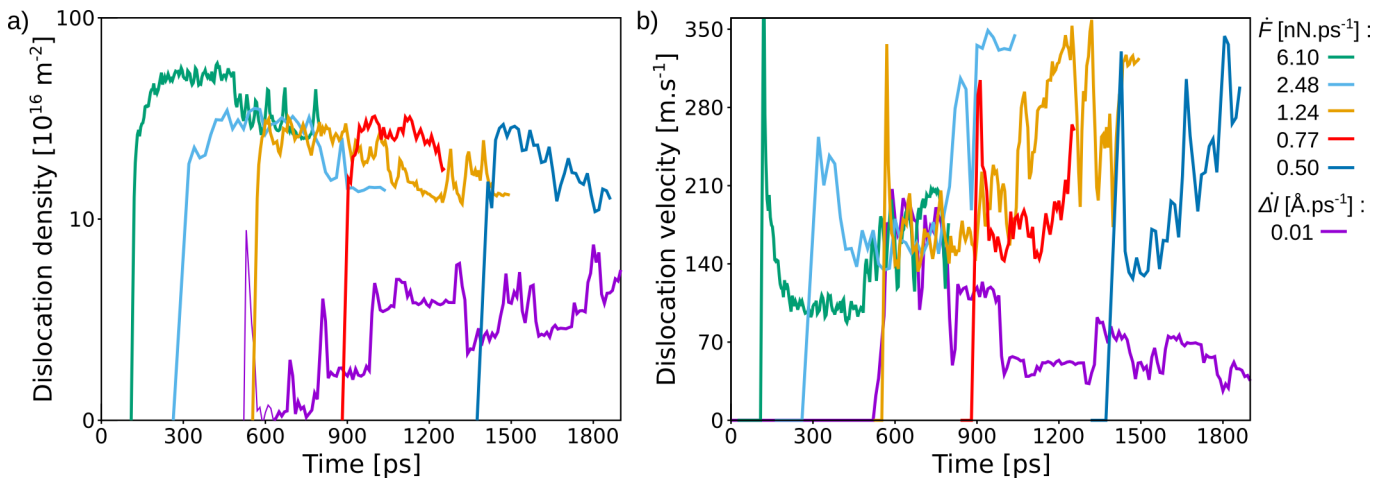


Figure 3.4.: a) Dislocation density and b) average dislocation velocity in a  $14.57 \text{ nm}$  height Au faceted NP under compression using load- or displacement-controlled MD simulations

Whatever the control mode, the first SDN event leads to a global weakening of the NP *i.e.*, the NP is characterized by more numerous defects (surface ledges, dislocations) after the first SDN event than before. Therefore, this softens the energy landscape for the subsequent nucleation events, as confirmed by the lower amplitude of the secondary force peaks in Figure 3.2. While the softening of the sample is offset by the load drop in the displacement-controlled case, it has dramatic consequences under load-control where the compressive force monotonically increases with time: the sample is pushed harder while becoming softer. As a consequence, the NP sponta-

neously collapses into a flat pancake shape due to the burst of dislocations in a very different manner than in the displacement-controlled case that is characterized by intermittent peaks and drops of the dislocation density (Figure 3.4a). The changes in terms of dislocation dynamics between the load- and displacement-controlled setups are confirmed in Figure 3.5 that shows engineering compressive stress *vs.* strain curves for Au faceted NP with size ranging from 7.52 to 22.56 nm, in the same interval than in the original work of Mordehai *et al.* [Mordehai et al. 2011a; Feruz and Mordehai 2016]. As shown in Figure 3.5, the computed yield stress  $\sigma_y$  increases with decreasing size which leads to smaller NPs being stronger than larger ones. These results quantitatively corroborate Mordehai *et al.* original MD results on the yield stress and nucleation processes. However, we show using our load-controlled MD setup that it becomes possible here to catch the sudden strain bursts originally observed in Mordehai *et al.* [Mordehai et al. 2011a] nanocompression experiments but lacking in their displacement-controlled MD simulations.

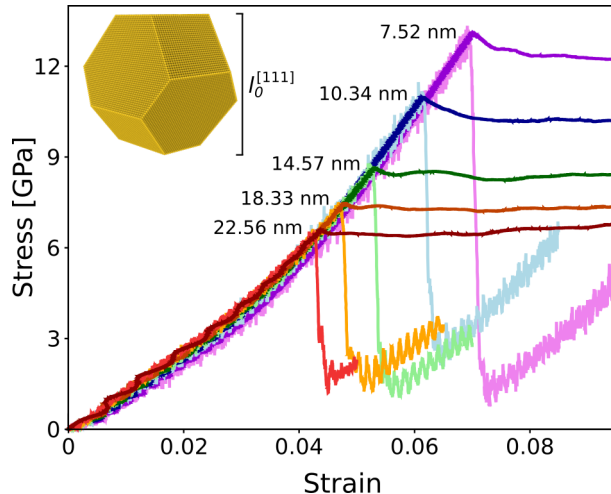


Figure 3.5.: Stress-strain curves for Au faceted NPs of various size  $l_0^{[111]}$  under compression computed using load ( $\dot{F}=0.77 \text{ nN.ps}^{-1}$ , dark-colored curves) and displacement-controlled ( $\dot{\Delta l}=0.01 \text{ \AA.ps}^{-1}$ , light-colored curves) MD simulations.

### 3.2.2.3. Further developments

- **Feedback loop sweep frequency**

In the same way as for a PID controller, the Python feedback loop sweep frequency  $v_f = 1/\Delta t$  affects the mechanical response of the model. While instantaneous looping allows for an accurate and dynamic system response, a too low scanning frequency induces delay responsible for force relaxation, as shown in Figure 3.6a. In this case, load-controlled nanocompression tests were performed on 3 nm height Au faceted

### 3. Load vs. displacement controlled nanomechanics – 3.2. Load controlled nanocompression modeling

NPs and  $\Delta t$  varies from 2 to 100 fs which corresponds to 1 to 50 MD timesteps between two consecutive calls of the Python solver. Similar to the stiffness of a load cell, changing  $\Delta t$  in Equation 3.1 leads to an intermediate response in between the intrinsic displacement-controlled and load-controlled tests. By definition (see Equation 2.26), atoms  $i \in R^N$  are pushed by the indenter meaning that they can eventually go out of group  $R^N$  during the  $\Delta t$  interval. As a consequence, the measured force decreases leading to intermediate regimes presented in Figure 3.6a. To get a strict load-control during mechanical testing it is then advised to use a high sweep frequency, of the order of a MD step. These results corroborate recent experimental developments of high stiffness actuators or highly performing PID aiming for high sweep frequencies [Zhang et al. 2009; Dehm et al. 2018].

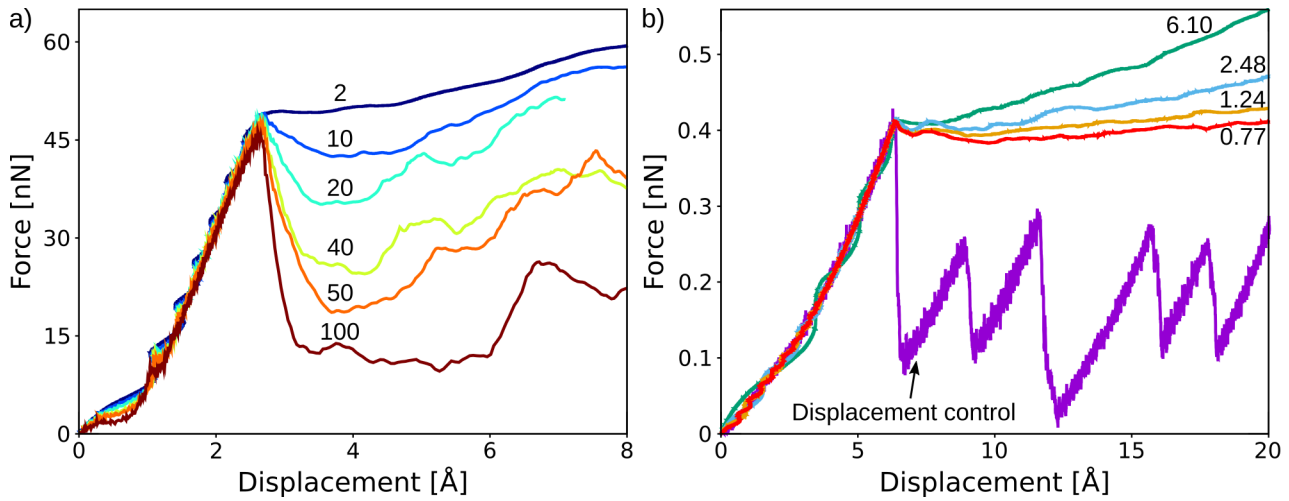


Figure 3.6.: Mechanical response of Au faceted NP under load-controlled MD compression as a function of a) the feedback-loop period  $\Delta t$  in fs and b) the load rate  $\dot{F}$  in  $\text{nN} \cdot \text{ps}^{-1}$ .

- **Load rate influence**

The mechanical response of a 11 nm height Au NP is studied as a function of the load rate  $\dot{F}$ . Figure 3.6b shows force *vs.* displacement curves for load-controlled compression tests using  $\dot{F}$  values presented in Table 3.1. While the yield force remains the same no matter  $\dot{F}$ , as discussed previously, the plastic behavior is clearly impacted by the load rate. At elevated load rates ( $6.10 \text{ nN} \cdot \text{ps}^{-1}$ ), the force exhibits a notable and continuous increase in the plastic regime. It results in a non-zero slope during the displacement burst. On the contrary, a low  $\dot{F}$  reveals a horizontal force *vs.* displacement behavior. This can be explained as follows. At high  $\dot{F}$ , the indenter pushes continuously harder on the NP while it is deforming in order to keep the load rate constant in such a small time interval. Conversely, lower  $\dot{F}$  ensures that the indenter follows the collapse of the NP while not pushing too hard in such a small time interval. Thus, choosing high  $\dot{F}$  may overly stress the particle while it weakens, leading to

a force increase during the displacement burst. These results draw a parallel with the influence of strain-rate in displacement-controlled simulations, that has been discussed in refs. [Zhu et al. 2008; Fu et al. 2017; Long et al. 2018].

### 3.2.3. Comparison to the load envelope model

To compare the mechanical response computed in displacement-controlled MD to those derived from load-controlled or pseudo displacement-controlled experiments, several research groups assume an envelope load model that connects load maxima. To confront this hypothesis to our load-controlled MD protocol, we reproduced the virtual compression experiments of Sharma *et al.* [Sharma et al. 2021] on 20.1 nm Ag hemispheres using both our load-controlled and displacement-controlled protocols. Due to the similar conditions of simulation, our displacement-controlled simulation perfectly reproduces Sharma *et al.* results (Figure 3.7).

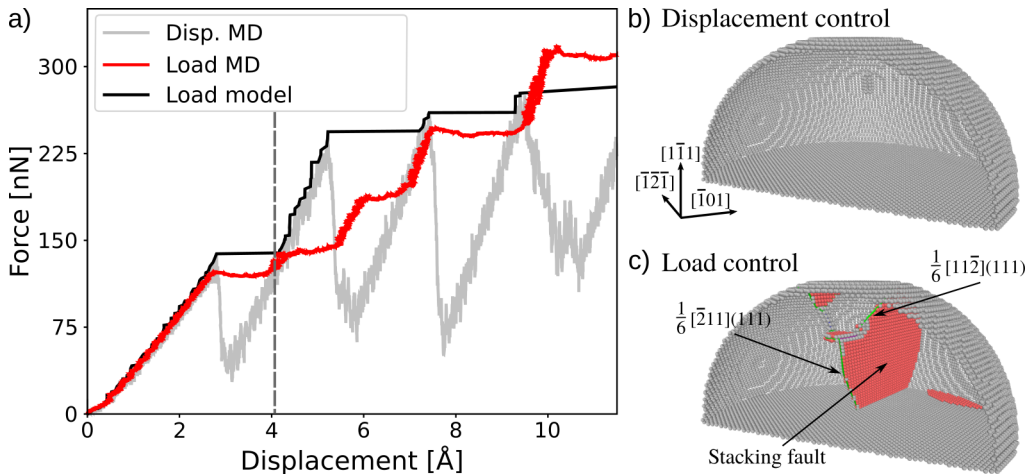


Figure 3.7.: MD nanocompression simulation of a 20.1 nm Ag half-sphere using load and displacement-controlled MD. a) Force *vs.* displacement curves computed using load-controlled MD (Load MD), displacement-control (Disp. MD) and the envelope load model (Load model), b), c) evolution of the dislocation microstructure at displacement  $\delta = 4.04 \text{ \AA}$  for the displacement and load-control cases, respectively.

As for Au NPs, the stress response is characterized at the beginning by an elastic regime that yields at about  $F_y=122 \text{ nN}$  where SDN starts, the rest of the curve being made of classical MD load/unload cycles marked by subsequent nucleation events. The load envelope model connects the first load peak at critical displacement  $\delta_y=2.80 \text{ \AA}$  to the next elastic reload (at displacement  $\delta=4.17 \text{ \AA}$ ), mimicking an experimental burst of deformation. Then, the model follows a classical peak-to-peak behaviour. One can notice that the NP initially strengthens here due to its hemispherical shape that constrains the evolution of the contact area and stress heterogeneities. Load-control simulation results show a similar elastic trend with the first SDN event occurring at

$F_y=122$  nN and  $\delta_y=2.75$  Å. As confirmed by the envelope load model, a displacement jump up to  $\delta=3.96$  Å is observed in the load-controlled simulation, after the first SDN event. However, the MD simulation and the model diverge after  $\delta=4.04$  Å. To interpret this change in the mechanical response, we reveal the atomic structure of both NPs at this stage in Figure 3.7a and b. While the displacement-controlled simulation shows a defect-free sample, the load-controlled simulation exhibits a well-established dislocation microstructure made of Shockley partial dislocations and extended stacking-faults. So, on one hand, an elastic reload up to high-stress is necessary to further plastically deform a defect-free sample via SDN (displacement-controlled case) while, on the other hand, a stress plateau is at the roots of a dislocation microstructure that has to be disorganized to carry on further the deformation (load-controlled case). As in the case of the Au faceted NPs discussed above, the larger amount of defects in the load-controlled case for the same strain level as in the displacement-controlled case is attributed to stress steady-state whereas the displacement-controlled simulation shows load relaxation. We conclude that the envelope load model is not able to quantitatively reproduce a load-controlled test as it does not account explicitly for the dislocation microstructure that drastically evolves during strain bursts.

In the next section, this modeling approach is applied to nanoindentation simulations.

### 3.3. Towards nanoindentation modeling

Nanoindentation testing is widely used in experimental nanomechanics [Gouldstone et al. 2000; Ohmura et al. 2001; Gouldstone et al. 2007]. Most experimental setups were primarily load-controlled and this presents a challenge for making meaningful qualitative comparisons with MD simulations as previously introduced. Here, we introduce an original algorithm for load-controlled MD nanoindentation simulations adopting the same approach as in Section 3.2.

#### 3.3.1. Methods

In the case of a spherical indenter, the  $r_i$  term associated to the indenter force per atom  $K(r_i - R)^2$  is defined as,

$$r_i = \sqrt{(x_i - x_{ind})^2 + (y_i - y_{ind})^2 + (z_i - z_{ind})^2} \quad (3.4)$$

where  $R$  is the indenter's radius. In the contrary to the flat punch case, there is no simple explicit expression for  $z_{ind}$  here. To solve this non-linear equation, we use the Newton-Raphson method [Ypma 1995]. Designed to approximate the roots of real-valued functions, it relies on the iterative refinement of an initial guess to converge towards a more accurate solution. At each iteration  $j$ , the algorithm involves evaluating the function  $f$  and its derivative  $f'$  at the current estimate, and then

### 3. Load vs. displacement controlled nanomechanics – 3.3. Towards nanoindentation modeling

updating the estimate using the Newton-Raphson formula shown in Equation 3.5,

$$z_{ind}^{j+1}(\dot{F}, t) = z_{ind}^j(\dot{F}, t) - \frac{f(z_{ind}^j(\dot{F}, t))}{f'(z_{ind}^j(\dot{F}, t))} \quad (3.5)$$

while  $|z_{ind}^{j+1}(\dot{F}, t) - z_{ind}^j(\dot{F}, t)| > \epsilon$

This iterative process continues until the difference between consecutive estimates falls below a specified tolerance level  $\epsilon$ . This process is shown in Figure 3.8. In our case,  $f$  and  $f'$  functions are given by Equations 3.6a and 3.6b,

$$f(z_{ind}(\dot{F}, t)) = K \sum_{i=1}^N \left[ \sqrt{(x_i - x_{ind})^2 + (y_i - y_{ind})^2 + (z_i - z_{ind}(\dot{F}, t))^2} - R \right]^2 - \dot{F}t \quad (3.6a)$$

$$f'(z_{ind}(\dot{F}, t)) = -2K \sum_{i=1}^N \left[ z_i - z_{ind}(\dot{F}, t) - \frac{R(z_i - z_{ind}(\dot{F}, t))}{\sqrt{(x_i - x_{ind})^2 + (y_i - y_{ind})^2 + (z_i - z_{ind}(\dot{F}, t))^2}} \right] \quad (3.6b)$$

Among the two distinct solutions of Equation 3.4, only one ensures the convergence of the algorithm and to reduce the computational time, we set the initial guess at time  $t$  equal to the last indenter's position  $z_{ind}^0(\dot{F}, t) = z_{ind}(\dot{F}, t - \Delta t)$ . The use of the Python feedback loop consists then in solving the Newton-Raphson formula at each time interval  $\Delta t$ .

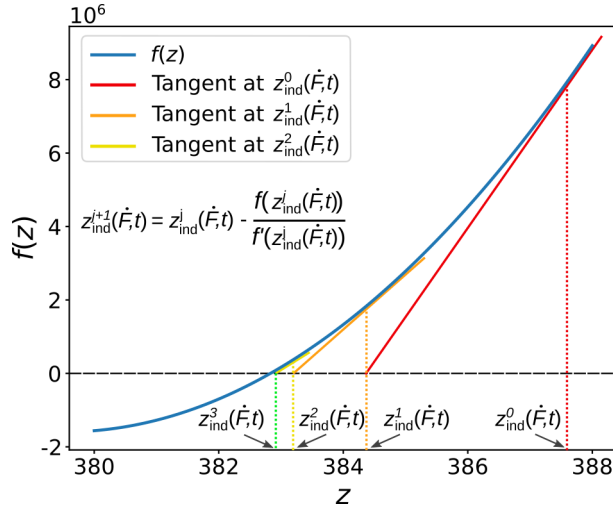


Figure 3.8.: Newton-Raphson iterative algorithm for the solving of non-linear equation and the computation of the indenter's position  $z_{ind}(\dot{F}, t)$  at each time step.

The MD protocol for running load-controlled nanoindentation is presented in Figure 3.9. First the spherical force field position along  $z$ -axis is initiated at  $z_{ind}(\dot{F}, 0)$ . Then, the dynamic region  $R^N$  comprising the atoms affected by the force field ( $r_i < R$ )

### 3. Load vs. displacement controlled nanomechanics – 3.3. Towards nanoindentation modeling

is updated. At this step, every  $x_i$ ,  $y_i$  and  $z_i$  are known as well as  $K$ ,  $R$ ,  $x_{ind}$  and  $y_{ind}$  that are constant during the entire simulation. Subsequently, the Python solver is called to calculate  $z_{ind}(\dot{F}, t)$  using the iterative Equation 3.5. Finally, the indenter is moved to its new position, a MD run is performed for  $\Delta t$  and the dynamic region  $R^N$  is updated.

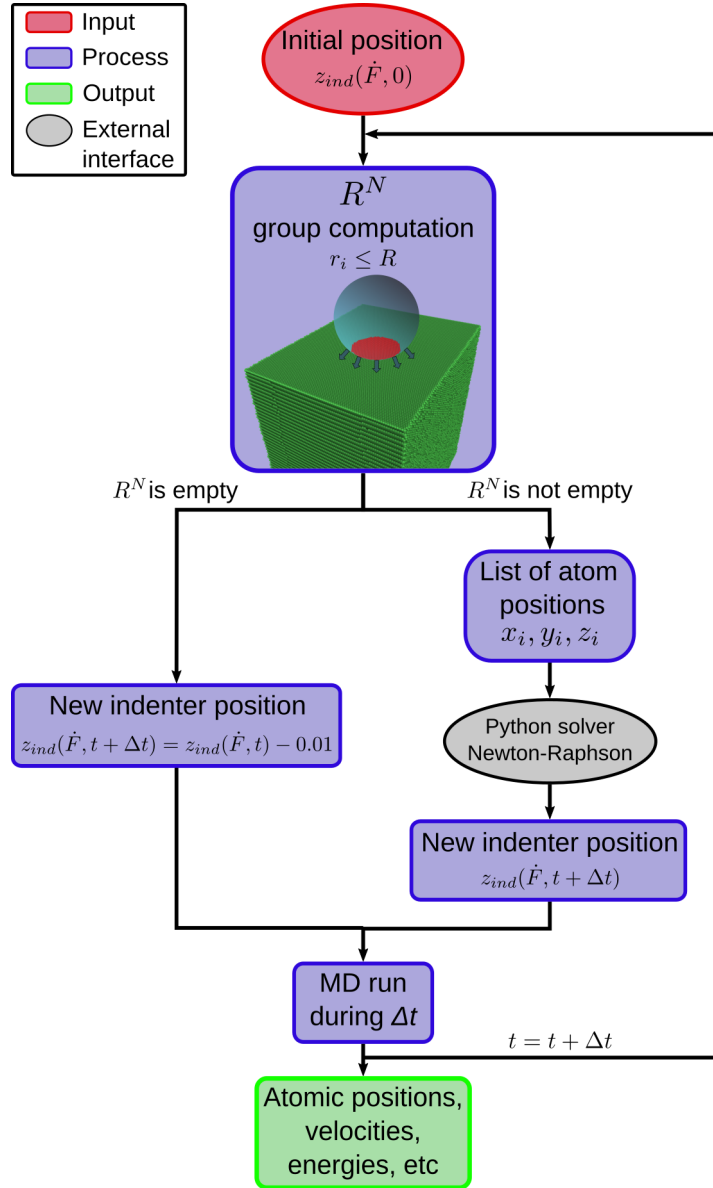


Figure 3.9.: MD Load-controlled nanoindentation workflow including the computation of group  $R^N$  every  $\Delta t$ , listing of every atom  $i \in R^N$  coordinates and the parallel Newton-Raphson feedback loop to solve Equation 3.5.

### 3.3.2. Application to the nanoindentation of Ni thin films

MD simulations for the indentation of a (111)-Ni thin film are performed using a displacement-controlled and a load-controlled spherical indenter. This study is inspired by the work of Chang *et al.* [Chang et al. 2010] where a displacement-controlled spherical indenter is used. We use the same sample dimensions ( $22.4 \times 28.4 \times 28.6 \text{ nm}^3$ ), indent radius (120 Å), interatomic EAM potential [Angelo et al. 1995], PBC along  $x$  and  $y$ -coordinates and Free-BC along  $z$ -axis. Sample design and thermal equilibration are detailed in Chapter 2. The difference here is that we run a dynamic mechanical test at 10 K with a timestep of 1 fs, while Chang *et al.* used a 0 K quasi-static method. Load-control rate is set at  $\dot{F} = 12 \text{ nN.ps}^{-1}$  and displacement rate is  $\dot{\delta}l = 0.01 \text{ \AA.ps}^{-1}$  for the displacement controlled-case.

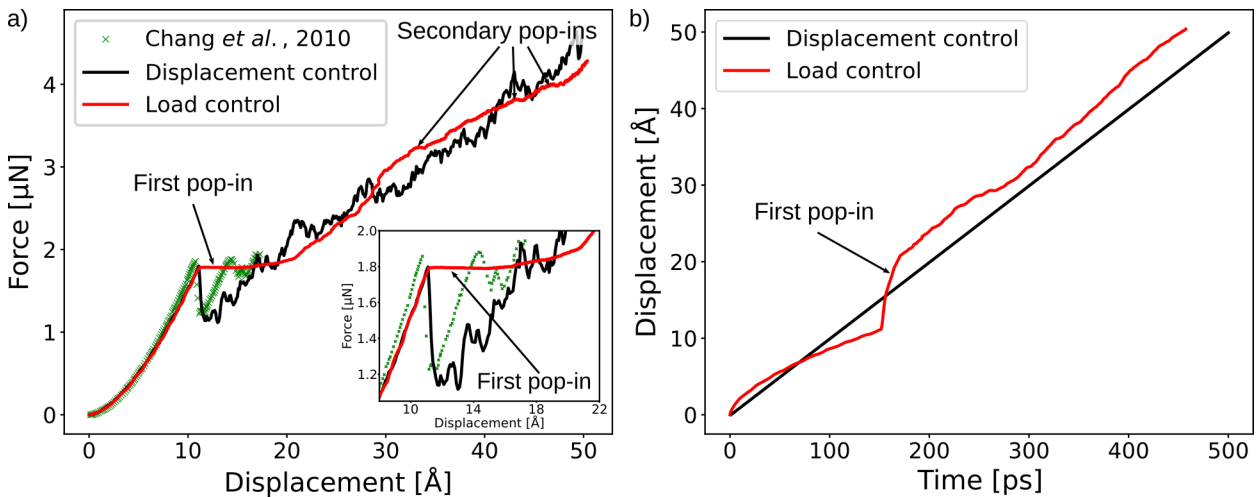


Figure 3.10.: Comparison between displacement-controlled and load-controlled nanoindentation. a) Force *vs.* displacement curves showing the pop-ins and a comparison with data from [Chang et al. 2010]. The inset shows the first pop-in. For better visualisation, markers size is reduced. b) Indenter's displacement *vs.* time denoting the penetration of the indenter inside the sample in the case of a load-controlled MD setup.

Figure 3.10a shows the load *vs.* displacement curve for both cases as well as a comparison to data from [Chang et al. 2010]. Both elastic regimes exhibit similarity, regardless of the control mode, and align with the Hertzian elastic theory [Frank and Lawn 1967; Johnson 1987]. The first plastic events occur at the same force level for both simulations, with  $F_y = 1.80 \mu\text{N}$  at a displacement  $\delta_y = 11.10 \text{ \AA}$ . These values are similar to the results of [Chang et al. 2010] where  $F_y = 1.86 \mu\text{N}$  is reported and translates a faithful reproduction of the simulation protocol (bearing in mind temperature differences). After this point, load *vs.* displacement behaviors diverge. On the one hand, an expected load drop occurs for the displacement-controlled simulation, followed by a load increase with a sequence of elastic reload and subsequent load

drops. The occurrence of the second load drop differs from ref. [Chang et al. 2010], where it happens at  $\delta = 14.34 \text{ \AA}$ , while our simulation shows a load increase until  $\delta = 17.01 \text{ \AA}$ . This discrepancy may be attributed to the dynamic nature of our simulation compared to the protocol used in Chang *et al.*'s work. On the other hand, in the case of a load-controlled indenter, a large pop-in of  $9.72 \text{ \AA}$  amplitude is observed and indicates a significant penetration of the indenter into the sample, as depicted in Figure 3.10b. Then, the force increases and exhibits small secondary pop-ins of several angstroms at  $\delta = 38.90 \text{ \AA}$ ,  $\delta = 42.97 \text{ \AA}$  and  $\delta = 46.30 \text{ \AA}$ . These results qualitatively reproduce the commonly observed pop-in process occurring during the first plastic event in indentation experiments using load-controlled setups and followed by several tighter ones in subsequent plasticity [Gouldstone et al. 2000; Ohmura et al. 2001].

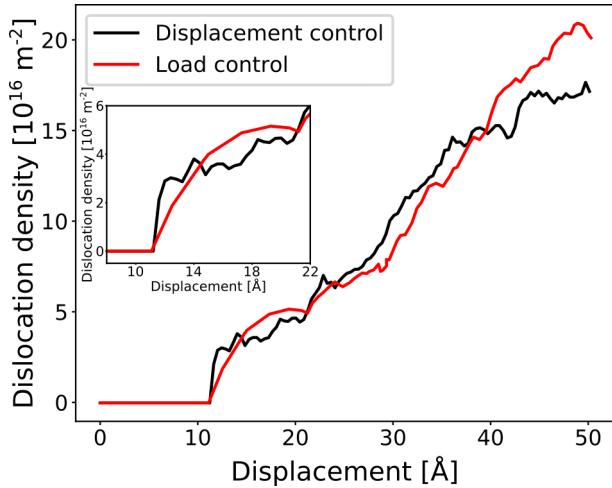


Figure 3.11.: Evolution of the dislocation density as a function of indenter's displacement during Ni thin film nanoindentation by using both control modes. The inset shows the dislocation density burst that occurs at the critical displacement  $\delta_y = 11.10 \text{ \AA}$ .

For a better understanding of the occurrence of pop-ins in load-controlled MD nanoindentation compared to the conventional displacement-controlled case, dislocation densities  $\rho$  are depicted in Figure 3.11. In both scenarios a burst in dislocation density occurs when sample yields, reaching values of approximately  $4.5 \cdot 10^{16} \text{ m}^{-2}$ . Nevertheless, this burst appears to be more abrupt in the case of displacement control, whereas load control exhibits a more gradual increase. One possible explanation might be the differences in term of stress-gradients within the thin film right beneath the indenter. Indeed, in the displacement controlled case, the nucleation of dislocations is concurrent to a load drop *i.e.* a large stress gradient while in the load controlled case the gradient remains constant, by definition. As Miller *et al.* showed in refs. [Miller 2004; Miller and Rodney 2008], high stress gradient zones correspond to the exact location of the dislocation nucleation processes which could explain the sudden burst observed in the displacement control case. Further investigations would be required to confirm this hypothesis. After these bursts, no significant differences are observed

in the  $\rho$  evolution.

In both cases, a complex network of dislocations remains near the surface beneath the indenter and indenting further leads to the formation of a more intricate network, regularly emitting prismatic loops, which has also been observed in previous MD nanoindentation studies too [Chang et al. 2010; Yaghoobi and Voyadjis 2014; Yaghoobi and Voyadjis 2016]. This phenomenon explains the emergence of pop-ins in load-controlled nanoindentation. Similar to the nanocompression case, the sample becomes softer locally as it undergoes increasing forces responsible for the nucleation of numerous dislocations. Since the position of the indenter is not constrained by a displacement rate, it penetrates deeper into the sample to maintain a constant load rate, resulting in the appearance of pop-ins in the force *vs.* displacement curves.

### 3.3.3. Benchmarking

A particular attention is devoted to the cumulative computational time for each nanoindentation protocol, as illustrated in Figure 3.12. The calculations are conducted using the High-Performance Computing (HPC) mesocenter resources (P2CHPD) provided by the Fédération Lyonnaise de Modélisation et Sciences Numériques (FLMSN). The system is composed of 1,675,080 atoms and parallelization is implemented on 160 processors, which corresponds to approximately 10,500 atoms per processor. In the case of displacement-controlled MD simulation, the indenter's position is known at each step which requires no additional processing. Consequently, the computation time exclusively encompasses the execution of MD. The total simulation time for a 50 Å indenter displacement (500,000 MD steps) equals 109,000 seconds, as depicted in Figure 3.12, which is approximately 31 hours. Thus, a single MD step computation lasts approximately 0.1  $\mu$ s per processor and per atom, a common duration for the utilization of EAM potentials (refer to LAMMPS benchmarks documentation or ref. [Plimpton and Hendrickson 1992]). In load-controlled nanoindentation, the cumulative computational time mirrors the displacement-controlled case in the initial simulation steps. However, beyond 150,000 calculation steps, a global increase in cumulative computational time is observed. The cumulative computation time shows here a second order polynomial evolution with a final value of 192,000 seconds, or approximately 53 hours. Here, the indenter's position must be computed with the Python subroutine in additional processing, involving a longer computation time at each simulation step. As the indenter penetrates the sample, it processes an increasing number of atoms within the  $R^N$  group. This accounts for the initial processing time similarity to the displacement-controlled case, as the feedback loop deals with only a small number of atoms, resulting in a Python execution time close to zero. However, in the final steps of the simulation, managing the atom coordinates list and solving Equation 3.5 leads to a Python processing duration of the order of the MD step execution.

Although no specific emphasis was placed on computational performance during the development of both algorithms, it is noteworthy that load-controlled MD

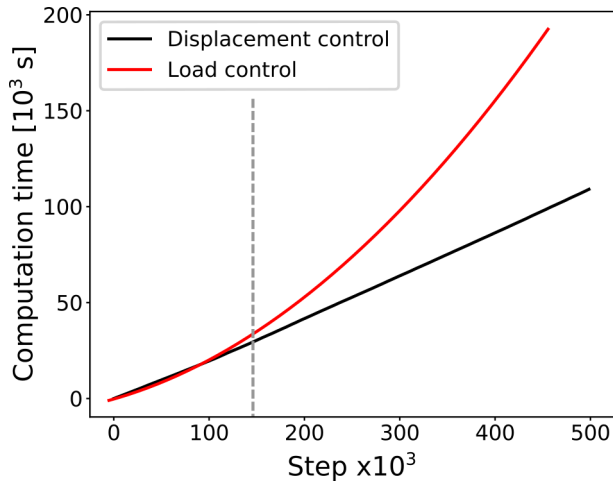


Figure 3.12.: Comparison of cumulative computation time as a function of the MD step for load and displacement-controlled nanoindentation tests. The step corresponding to the pop-in occurrence in the case of load control mode is denoted by the grey vertical dotted line

nanoindentation takes approximately twice as long compared to the conventional displacement-controlled cases. This duration is deemed acceptable in our context. However, there is certainly room for enhancing the efficiency of the Python solver to narrow the computational time gap between the two methods.

### 3.4. Conclusion

Load-controlled MD simulations allow to draw a more comprehensive picture of nanomechanical experiments and simulations. Indeed, at variance with usual displacement-controlled atomistic simulations, load-controlled simulations exhibit strain bursts more akin to those observed in NPs or pillars experiments when compressed inside the microscope [Mordehai et al. 2011b; Greer et al. 2005], as well as pop-ins as depicted by nanoindentation experiments [Gouldstone et al. 2000; Ohmura et al. 2001; Gouldstone et al. 2007]. The origin of these events is now well explained and related to the control mode used : samples are pushed harder while becoming softer. When applied to metal NPs, load-controlled MD simulations provide a clear explanation for the often observed "magic collapse" of samples, which has nothing to do with a nanoscale property of metals but rather relies on the experimental setup used. As a result, load-controlled MD provides an improved basis for better interpretations of nanomechanical experiments.

**Chapter III summary:**

**This chapter focuses on the formulation of a novel algorithm designed for load-controlled MD mechanical testing. It is tailored for nanocompression and nanoindentation tests, wherein the mechanical responses of Au-faceted NPs, Ag half-spheres and Ni thin films are compared to the conventional displacement-controlled MD approach. The simulations now capture the abrupt collapse of NPs and the occurrence of pop-ins, mirroring observations from experimental studies in a more accurate way. Additionnally, a comprehensive benchmark is conducted for both control modes.**

# 4

## ***Pyrough : a tool to build 3D samples with rough surfaces***

This chapter refers to the development of *Pyrough*, a numerical tool for the design of 3D virtual samples with surface roughness. The development of the code is published in ref. [Iteney et al. 2024], where mathematical model, code implementation and examples of application are detailed. Also, additional content on how surface mesh nodes are displaced, the transition from FEM to atomic position files and the development of the surface analysis module is provided.

## 4.1. Introduction

Surface roughness has a fundamental impact on the mechanical, physical and chemical properties of bulk materials with implications in various fields such as *e.g.*, friction [Sedlaček et al. 2009], lubrication [Jeng 1990; Menezes and Kailas 2016], machining [Khorasani et al. 2012] or polishing [Özgünaltay et al. 2003]. It is also known to play a key role at small scales as in the field of catalysis where surface morphology is a key factor for chemical reaction efficiency [Gao et al. 2013; Lin et al. 2018] or in nanomechanical engineering applications where peaks and valleys associated with surface roughness act as stress concentrators which are natural sites for dislocation nucleation [Brochard et al. 2000b; Gouldstone et al. 2001; Mitlin et al. 2005; Navarro et al. 2008; Brochard et al. 2010; Bel Haj Salah et al. 2017]. Indeed, these studies have emphasized the crucial role of surface steps and roughness on the mechanical behavior of crystalline materials and, especially, on the dislocation nucleation process which governs the strength of materials at the nanoscale.

Although shape optimization has recently emerged as a first step towards a more realistic, *in silico*, sample design [Amodeo and Lizoul 2017; Klymis et al. 2018; Zimmerman et al. 2021], several mathematical formulations including linear transformation [Patir 1978], 2D filters [Hu and Tonder 1992] and time series methods [Watson et al. 1979] were already used in the past to consider non-equilibrium *i.e.*, mathematical surface roughness. Furthermore, simple theoretical approaches based on the fractal theory and more common observations of natural surfaces were made to investigate adhesion or friction at the nanoscale shedding light on the influence of surface details in mechanical testing [Mandelbrot 1985; Pastewka and Robbins 2014; Weber et al. 2018]. Despite these approaches, the majority of atomistic and macroscopic numerical simulations usually rely on a simplified sample design (*using e.g.*, flat surfaces, sharp angles and edges) which prevents studying the influence of surface details and confirms that a user-friendly tool is missing to generate more realistic virtual samples.

In this study, we describe the implementation of a numerical and open-source tool called *Pyrough*, that is developed to design virtual samples with rough surfaces for atomistic and FEM simulations, based on the classical roughness theory [Mandelbrot 1985; Jacobs et al. 2017]. *Pyrough* gives the user the ability to manage the surface roughness and height distribution for the generation of rough virtual objects. Unlike existing (often closed-source) solutions in the fields of tribology and contact engineering [Multiphysics 1998; Röttger et al. 2022; Lim 2023; Kanafi 2023], *Pyrough* can serve as a pre-processor for an easy mapping of the generated rough topography for flat and curved samples. In what follows, we first recall the main concepts of the classical roughness theory and how to numerically generate rough surfaces. Then, details on *Pyrough*'s workflow, input/output file management and the implementation of the rough surface generation for several 3D shapes are provided. Finally, examples of *Pyrough*'s applications that emphasize the role of surface roughness are presented.

## 4.2. Classical roughness modeling

### 4.2.1. Current state

#### 4.2.1.1. Fractal and roughness theory

Fractals were first conceptualized by Mandelbrot to describe shapes with disordered and irregular geometries, including natural coastlines [Mandelbrot 1967], natural materials [Turcotte 1997], biological structures [West et al. 1997] and rough surfaces [Brown and Scholz 1985]. A distinctive property of fractals is their independence from the chosen unit of measurement, following a scaling law of the form,

$$M(l) \propto l^{D_f} \quad (4.1)$$

where  $M$  is the length of a line, the area of a surface, or the volume of an object, and  $D_f$  is the fractal dimension, that can be fractional. Equation 4.1 conveys the self-similarity property, which means that the value of  $D_f$  remains constant across a range of length scales denoted by  $l$ . Fractal geometry and self-similarity can reproduce repetitive geometrical processes from the observation of natural objects. One famous illustration is the broccoli romanesco vegetable shown in Figure 4.1. A smaller section of the broccoli looks exactly like the whole broccoli head itself, and this pattern keeps repeating at progressively smaller scales.



Figure 4.1.: Self-similarity and successive magnifications in the broccoli romanesco vegetable, from [Bancaud et al. 2012].

In fact, an examination of a broad-spectrum of natural surfaces such as sea-floor [Mareschal 1989], rock surfaces [Candela et al. 2012; Wong et al. 1986], clouds [Rys and Waldvogel 1986; Marshak et al. 1995], machined or fractured surfaces [Hasegawa et al. 1996; Mandelbrot et al. 1984], reveals an intrinsically multi-scale roughness [Mandelbrot 1982] across spatial dimensions, way more complex than self-similarity. The notion of self-affinity was used first to characterize the Brownian fractional reliefs,

introduced by Mandelbrot and Van Ness [Mandelbrot and Van Ness 1968; Mandelbrot et al. 1984; Mandelbrot 1985]. Unlike self-similar objects, self-affine structures are not statistically invariant through a global dilatation but rather through an affine transformation,

$$\lambda^H h\left(\frac{x}{\lambda}, \frac{y}{\lambda}\right) = h(x, y) \quad (4.2)$$

where  $\lambda$  is a scalar and  $h(x, y)$  is the surface height measured at  $x$  and  $y$  coordinates.  $H$  is the Hurst exponent and takes its values in the  $[0, 1]$  interval. It describes how data are correlated. Specifically, when  $H < 0.5$ , the dataset exhibits anti-persistent correlations, meaning that a height increment is more likely to be succeeded by a decrement. This results in a rougher profile [Mandelbrot 1985]. Conversely, when  $H > 0.5$ , persistent correlations are observed, which leads to smoother profiles. The self-affinity property can also extend to the nano-scale. As shown in Figure 4.2, nano-surfaces exhibit height topography remarkably akin to that observed in natural features such as sea floors or mountains, which underscores the potential of the approach to effectively model nano-scale roughness.

The power spectral density (PSD) of a surface  $S$  is a mathematical tool that decomposes the surface into contributions from different spatial frequencies. Mathematically, the PSD represents the Fourier transform of the autocorrelation function of the signal across a given spectrum of wave vectors [Nayak 1971; Persson et al. 2005; Youngworth et al. 2005; Jacobs et al. 2017]. This allows for the identification of spatial frequencies composing the signal to provide statistical information about the surface topography. It is defined by,

$$C^{2D}(\mathbf{q}) = \frac{1}{(2\pi)^2} \int_S \langle h(\mathbf{x}) h(\mathbf{0}) \rangle e^{-i\mathbf{q} \cdot \mathbf{x}} d\mathbf{x} \quad (4.3)$$

where  $\mathbf{x} = (x, y)$  and  $h(\mathbf{x})$  is the surface height measured from the average surface plane, defined so that  $\langle h \rangle = 0$ . Here  $C^{2D}(\mathbf{q})$  has the  $\text{m}^4$  unit but note that the PSD unit is based on its own definition. Equations 4.2 and 4.3 show that the PSD has a power-law dependence on the spatial frequency in the case of self-affine scaling such as,

$$C^{2D}(\mathbf{q}) \propto \mathbf{q}^{-2-2H} \quad (4.4)$$

where  $H$  is related to the surface fractal dimension  $D_f$  by the relation  $D_f = 3 - H$ . Thus, the maximum achievable wave vector is denoted as  $q_1 = 2\pi/a$  where  $a$  represents a specific atomic distance or lattice constant and the minimum attainable wave vector is expressed as  $q_L = 2\pi/L$ , where  $L$  corresponds to the linear dimensions of the surface. While real rough surfaces may exhibit self-affine characteristics across the entire length scale range spanning from  $a$  to  $L$ , the majority typically demonstrate such behavior within a limited wave vector range  $q_0 < q < q_1$  [Persson 2006]. Figure 4.2a shows the schematic example of a PSD *log-log* graph where the slope for  $q \in [q_0, q_1]$  gives access to  $H$  using Equation 4.4.

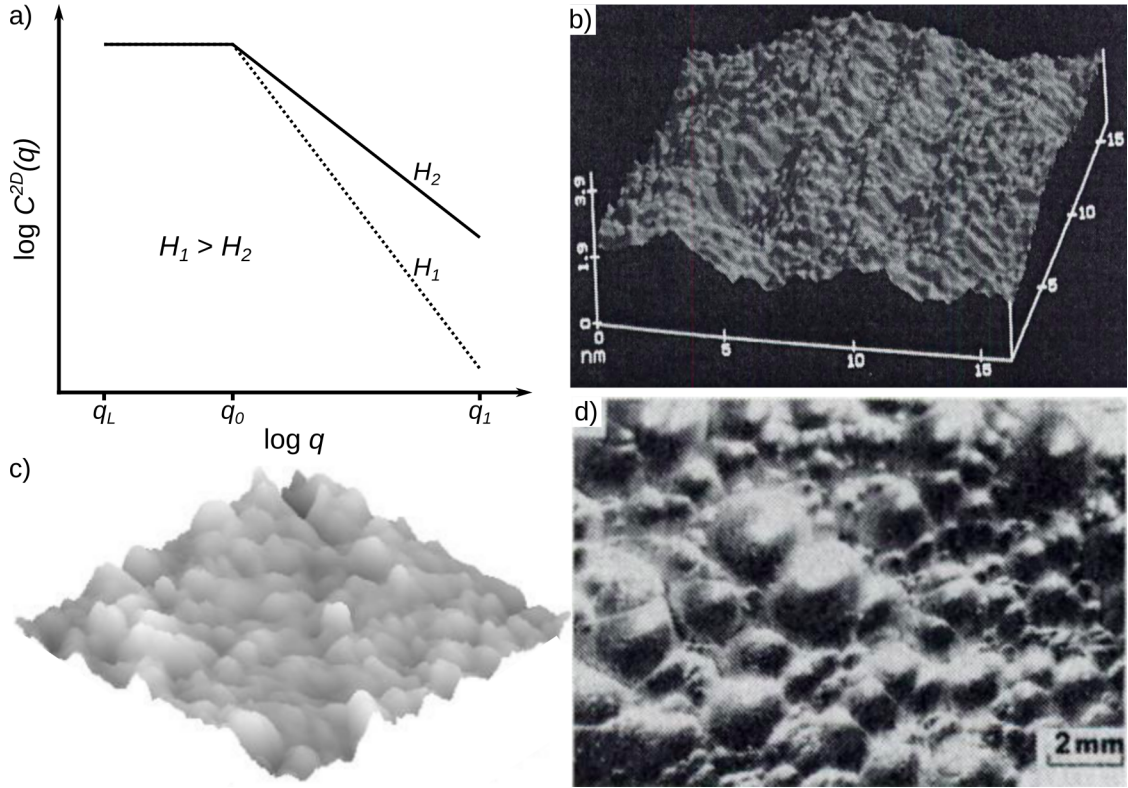


Figure 4.2.: Characterization of rough surfaces. a) PSD of self-affine surfaces characterized by different Hurst exponents  $H_1$  and  $H_2$ , b) STM image of a rough Au substrate, from [Barabási and Stanley 1995], c) AFM topography image of a Au thin film, from [Bonyár 2016], d) optical micrograph of a thick metal film, from [Barabási and Stanley 1995].

#### 4.2.1.2. Statistical descriptors

Among a wide variety of rough surfaces, one characteristic is the Gaussian aspect of the height distribution which implies that surface heights can be normally distributed [Williamson et al. 1969; Nayak 1971]. Statistical analyses allow to characterize every unique discrete height distribution related to its random aspect. Several statistical parameters that vary with the moment  $\mu_v$  of the discrete height distribution  $h$  can be used to define the ID-card of the rough surface,

$$\mu_v = \frac{1}{N_x N_y} \sum_{i,j} h_{i,j}^v \quad (4.5)$$

where  $v$  states for the order of the moment,  $N_x$  and  $N_y$  are the total number of points of the height distribution along  $x$  and  $y$ -axis, respectively, and  $h_{i,j}$  is the height value at point  $(i, j)$ .

The root mean square (*RMS*) or quadratic mean refers to the square root of the second moment  $\mu_2$  [Bakolas 2003; Duparré et al. 2002]. It provides information on

the variability of the heights data set and is calculated using Equation 4.6. Note that the standard deviation  $\sigma$  is equal to the *RMS* in the case of a zero-centered height distribution.

$$RMS = \sigma = \sqrt{\mu_2} = \sqrt{\frac{1}{N_x N_y} \sum_{i,j} h_{i,j}^2} \quad (4.6)$$

Statistical inputs derived from higher moments provide a more complete description of the rough surface. For example, the skewness  $sk$  allows to measure the symmetry of the statistical height distribution [Doane and Seward 2011],

$$sk = \frac{\mu_3}{\mu_2^{3/2}} = \frac{1}{N_x N_y \sigma^3} \sum_{i,j} h_{i,j}^3 \quad (4.7)$$

A symmetrical distribution with evenly distributed height peaks and valleys leads to  $sk$  tending to 0. Last, the kurtosis  $K$  described by Equation 4.8 translates the spiky nature of the height distribution [Ruppert 1987; DeCarlo 1997]. A Gaussian distribution has  $K \sim 3$  whereas lower values correspond to flatter distributions.

$$K = \frac{\mu_4}{\mu_2^2} = \frac{1}{N_x N_y \sigma^4} \sum_{i,j} h_{i,j}^4 \quad (4.8)$$

Another scale-dependent roughness parameter for the measure of heights variations with the size scale is the root mean-square gradient [Röttger et al. 2022],

$$S_{\nabla h} = \left[ \frac{1}{N_x N_y} \sum_{i,j} [(D_x h)_{i,j}^2 + (D_y h)_{i,j}^2] \right]^{1/2} \quad (4.9)$$

where  $(D_x h)_{i,j} = (h_{i+1,j} - h_{i,j})/\Delta x$  states for the local slope between two adjacent height values along  $x$ -axis and same for  $(D_y h)_{i,j} = (h_{i,j+1} - h_{i,j})/\Delta y$  along  $y$ -axis.

### 4.2.2. Application to contact and friction mechanics

In tribology, most of the issues are associated with the concept of static elastic contact. Initially, many predictions in contact mechanics were formulated based on models derived from the Greenwood and Williamson's theory [Greenwood and Williamson 1966]. In this theory, the contact between two solids is treated as the summation of non-interacting, identical spherical asperity contacts. This model was improved by Bush *et al.* [Bush et al. 1975], latter recalled as the BGW model in this work, which incorporates a distribution of paraboloids with varying curvatures. The BGW model relies on the application of the Hertzian contact theory to each summit of the asperities [Hertz 1896].

Recently, Persson *et al.* have adopted an alternative approach [Persson 2001; Persson 2002; Persson et al. 2002]. They state that the PSD is the geometric property that determines the pressure distribution and, consequently, the contact area. In contrast

to the BGW model, which assumes independent contact regions of asperities, Persson's approach acknowledges the presence of surface roughness on various length scales for real surfaces. This recognition holds true even at low nominal contact pressures. They find out that the ratio between the real area of contact  $A$  and the macroscopic projected area  $A_0$  follows an error function given by Equation 4.10a (see Figure 4.3). In addition, when applied to microscopic contact, the asymptotic form for  $A/A_0$  is given by Equation 4.10b.

$$\frac{A}{A_0} = \operatorname{erf} \left( \frac{\sigma_0 \sqrt{2}}{E^* S_{\nabla h}} \right) \quad (4.10a)$$

$$\frac{A}{A_0} = \kappa \frac{\sigma_0}{S_{\nabla h} E^*} \quad (4.10b)$$

where  $\kappa$  is a dimensionless constant of proportionality,  $\sigma_0$  is the mean pressure normal to the interface,  $S_{\nabla h}$  is the root mean-square gradient of the height profile  $h$ , and  $E^* = E/(1 - \nu)$  is the biaxial elastic modulus, where  $E$  is the Young's modulus and  $\nu$  the Poisson ratio. BGW theory predicts  $\kappa = \sqrt{2\pi}$ , while Persson *et al.* give  $\kappa = \sqrt{8/\pi}$ . However, precise calculations for the relative contact area  $A/A_0$  of solids featuring rough surfaces fall midway between the two theoretical predictions [Campana and Muser 2007; Hyun et al. 2004].

Additional insights were provided by Hyun and Robbins [Hyun and Robbins 2007], who emphasized the noteworthy impact of the lower cutoff wave vector  $q_L$  on the response of an elastic rough surface. They showed a change in  $\kappa$  for different  $q_L$  values and highlighted its nonlinear evolution. Later, the notion of representativity was associated with the lower cutoff wavelength in ref. [Yastrebov et al. 2012], in which the authors demonstrated a strong dependence of the proportionality coefficient  $\kappa$  and other relevant quantities on the representativity of the considered surfaces. Figure 4.3a shows the influence of  $q_1/q_L$  ( $k_s/k_L$  in the labels) on the slope  $\kappa$  for the evolution of small contact area fraction as a function of normalized applied pressure.

Sliding friction between a body and a hard solid substrate is also a subject of both fundamental and technological significance, particularly in industries such as automotive and cosmetics [Grosch 1963; Greenwood 1966; Persson 2013]. Persson applied his multiscale contact mechanics theory to formulate a theory of hysteresis friction in viscoelastic materials, which assumes that the energy dissipation resulting from friction is equal to the energy loss due to internal friction in the rubber [Persson 2001]. In this framework, the friction coefficient  $\mu_f$  is computed owing the PSD form of the corresponding surface. Indeed, multiple studies have demonstrated that  $\mu_f$  is affected by surface roughness. Specifically, as the roughness coefficient decreases (indicating an increase in surface irregularity at a small scale), the friction coefficient tends to increase [Heinrich et al. 2000; Palasantzas 2003].

Furthermore, Lorenz *et al.* introduced a semi-empirical model for the friction coefficient at low sliding velocities [Lorenz et al. 2015]. This model incorporates the contribution from the real contact area to friction, calculated based on previously

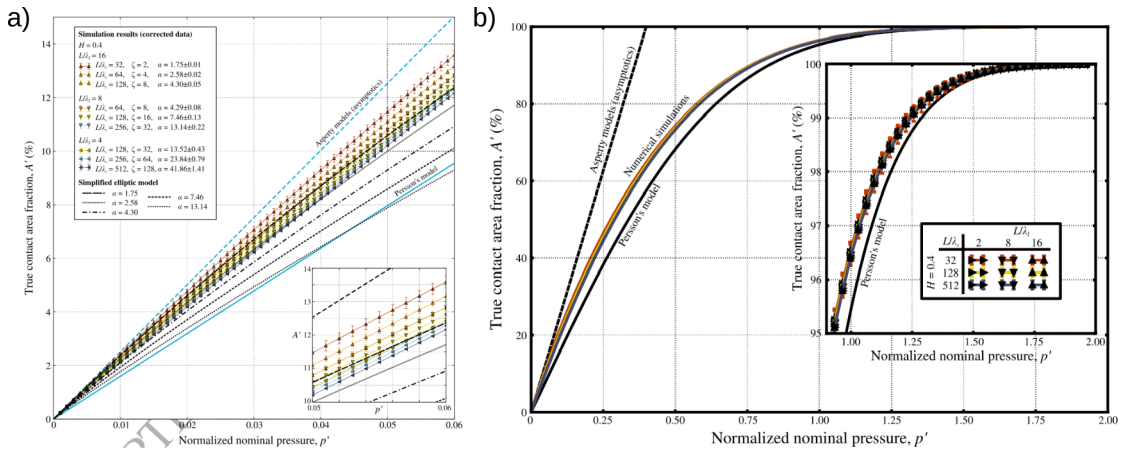


Figure 4.3.: Evolution of contact area fraction for rough surfaces with different  $q_1/q_L$  compared with the prediction of Persson's model (dashed curve) from Equation 4.10a. a) Zoom on microscopic contact and b) entire evolution of contact area fraction. Asymptotics of the BGW theory is given as an indication (black solid line). From [Yastrebov et al. 2017].

mentioned theories. As a result, they proposed that  $\mu_f$  over a broad range of velocities could be determined by combining the semi-empirical model with the hysteresis friction [Emami et al. 2021].

While continuous models developed for both contact and friction mechanics exhibit good accuracy, their validity diminishes at the nanoscale [Rubio et al. 1996; Jacobs and Martini 2017]. Numerous research groups have underscored the critical influence of smallest-scale roughness in recent investigations involving contact and adhesion of nanoscale hard materials or macroscale soft solids [Jacobs et al. 2013; Dalvi et al. 2019]. Additionally, few studies suggested that the bulk friction depends fundamentally on the interatomic interactions more so than any continuum-like contact area [Gao et al. 2004]. This confirms the need to model systems at smaller scales for a more comprehensive understanding of the underlying processes involved in contact and friction mechanics [Jacobs and Martini 2017].

### 4.2.3. Rough surface construction using *Pyrough*

Derived from the PSD definition (Equation 4.3), rough surfaces generated by *Pyrough* rely on the sum (in the real space) of cosine functions where each term of the sum represents the contribution of a spatial frequency. When compared to reciprocal space approaches (see e.g., [Jacobs et al. 2017]), this comes to account for the sole real part of the discrete Fourier transform. In Cartesian coordinates, the mathematical expression of spatial oscillations is given by Equation 4.11,

$$\cos(\mathbf{q} \cdot \mathbf{x} + \phi) = \cos[2\pi(v_x x + v_y y) + \phi] \quad (4.11)$$

where  $v_x$  and  $v_y$  are the spatial frequencies along the  $x$  and  $y$  directions, respectively, and  $\phi$  is the phase.

A discrete set of spatial frequencies  $v_x = a$  and  $v_y = b$  (where  $a$  and  $b$  are integers) is used to rationalize the range of investigated frequencies.  $A$  and  $B$  are defined as the respective high-frequency cutoffs for  $a$  and  $b$  so that  $a \in [-A; A]$  and  $b \in [-B; B]$ . Thus, the shortest wavelengths are  $\lambda_{x,min} = \frac{1}{A}$  and  $\lambda_{y,min} = \frac{1}{B}$  along the  $x$  and  $y$  directions, respectively.  $a$  and  $b$  can be positive or negative to ensure oscillations in both directions. Thus, a rough surface  $h(x, y)$  can be described by a sum of elementary waves as,

$$h(x, y) = \sum_{a=-A}^A \sum_{b=-B}^B \alpha(a, b) \cos[2\pi(ax + by) + \phi] \quad (4.12)$$

where  $\alpha(a, b)$  is the associated amplitude of each elementary wave.

Based on Equation 4.12, two more contributions are made in order to allow *Pyrough* to generate rough surfaces that are randomly perturbed. First, the phase is randomly perturbed using  $\phi = U_{a,b}$  where  $U_{a,b}$  stands for a uniform distribution on an interval of length  $\pi$ . Also, random perturbations and the power law are implemented within  $\alpha(a, b)$ . In *Pyrough*,  $\alpha(a, b)$  is a zero-centered Gaussian distribution defined to get a smooth but random variation in amplitudes without constraining the magnitude *i.e.*,  $\alpha(a, b) = G_{a,b}(a^2 + b^2)^{-(1+\eta)}$  where  $G_{a,b}$  is a scalar randomly extracted from a reduced centered normal distribution for each  $(a, b)$  pair and  $(a^2 + b^2)^{-(1+\eta)}$  expresses the power-law dependency of spatial frequencies, in line with Equation 4.4, with  $\eta$  a normalized roughness parameter. Finally, the construction of a randomly perturbed, rough, periodic surface can be modeled using Equation 4.13 in which  $\eta$  allows to monitor the roughness, as illustrated in Figure 4.4.

$$h(x, y) = C_1 \sum_{a=-A}^A \sum_{b=-B}^B G_{a,b}(a^2 + b^2)^{-(1+\eta)} \cos[2\pi(ax + by) + U_{a,b}] \quad (4.13)$$

where  $C_1$  is a normalization factor introduced to fit the surface heights to the sample dimensions.

It is important to note that this mathematical definition allows for the generation of any type of rough surface, parameterized by  $\eta$ . Specifically, to model self-affine rough surfaces characterized by  $H \in [0; 1]$ , the equivalence between the power laws of Equations 4.4 and 4.13 results in  $\eta = (H - 1)/2$ .

Additional theoretical details about how to model fractal surfaces can be found in ref. [Barnsley et al. 1988]. Note that a similar approach based on scalar spherical harmonics (Equation 4.14) can be used to describe the surface of spherical-shaped objects as done to model particle systems [Feinauer et al. 2015; Wei et al. 2018], brain sections [Ruiz de Miras et al. 2020] or other 3D objects [Mousa et al. 2007].

4. Pyrough : a tool to build 3D samples with rough surfaces – 4.2. Classical roughness modeling

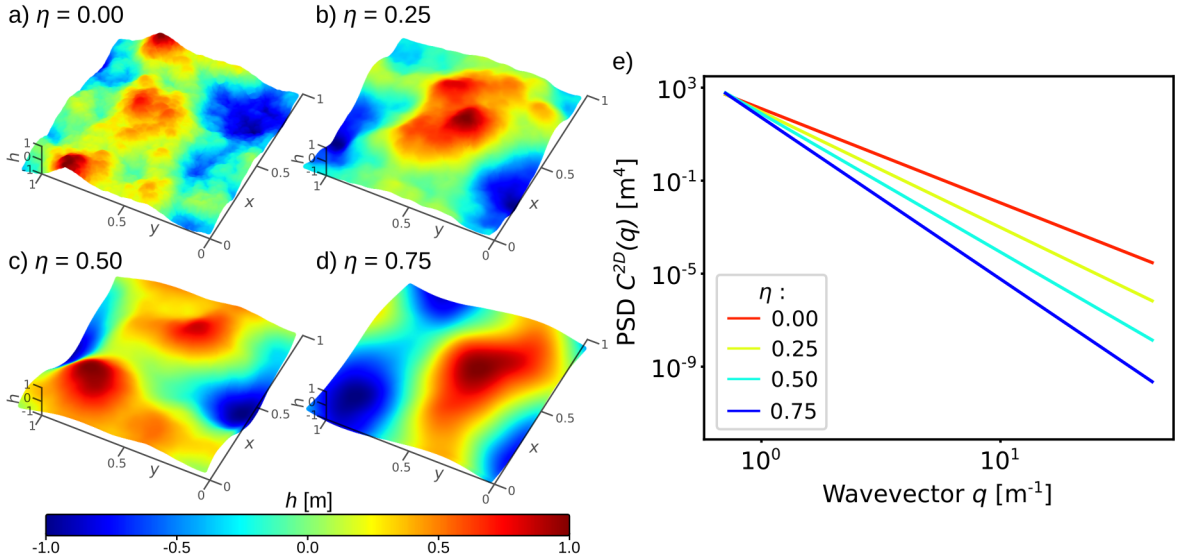


Figure 4.4.: Random rough surfaces modeled using Equation 4.13 for various roughness parameters. a)  $\eta=0.00$ , b)  $\eta=0.25$ , c)  $\eta=0.50$ , d)  $\eta=0.75$ , e) PSD of the various  $h$  profiles computed as  $C^{2D}(\mathbf{q})=\sum_{x,y} h_{\mathbf{q}}(x,y)^2$  with  $h_{\mathbf{q}}(x,y)$  the height matrix corresponding to the wave vector  $\mathbf{q}$ . For all calculations,  $A=50$ ,  $B=50$  and  $h(x,y)$  values are normalized between 1 and -1.

$$r(\theta, \phi) = \sum_{l=0}^{\infty} \sum_{m=-l}^l c_l^m Y_l^m(\theta, \phi) \quad (4.14)$$

where  $r(\theta, \phi)$  is the polar radius of the sphere at coordinates  $\theta \in [0, \pi]$  and  $\phi \in [0, 2\pi]$ ,  $c_l^m$  is the associated spherical harmonic coefficient and  $Y_l^m(\theta, \phi)$  is the spherical harmonic function given by Equation 4.15,

$$Y_l^m(\theta, \phi) = \sqrt{\frac{2l+1}{4\pi} \frac{(m-l)!}{(m+l)!}} P_l^m(\cos\theta) e^{im\phi} \quad (4.15)$$

where  $l$  and  $m$  are the degree and order of the associated Legendre function  $P_l^m(x)$  expressed by,

$$P_l^m(x) = (1-x^2)^{\frac{|m|}{2}} \frac{d^{|m|}}{dx^{|m|}} \left[ \frac{1}{2^l l!} \frac{d^l}{dx^l} (x^2 - 1)^l \right] \quad (4.16)$$

According to Equation 4.14, a spherical harmonic function representing the morphology of a rough sphere is characterized by its number of degrees and orders. Their amplitudes determine the intensity of the morphological characteristics that is expressed by,

$$L_l = \sqrt{\sum_{m=-l}^l |c_l^m|^2} \quad (4.17)$$

Wei *et al.* [Wei et al. 2018] showed that the spherical harmonic descriptor  $D_l$  has a power-law dependence on the spherical harmonic degree  $l$  that scales with the roughness parameter  $\eta$

$$D_l = \frac{L_l}{L_0} \propto l^{-2(2\eta+1)} \quad (4.18)$$

## 4.3. Pyrough implementation

### 4.3.1. General workflow

In a nutshell, *Pyrough* relies on integrating the roughness approach (Equation 4.13 and 4.14) and the statistical analysis tools presented in section 4.2.1.2 to design *in silico* 3D samples with rough surfaces for FEM or atomistic simulations applications. *Pyrough* is written in Python 3 and is developed under the GNU General Public License version 3 or later [GNU 2007]. The code is object-oriented and is easy-to-use or improve even for non-coding users. It is currently available on GitHub : <https://github.com/jamodeo12/Pyrough>, and its online documentation can be found on <https://jamodeo12.github.io/Pyrough>. *Pyrough* is executed using the following command line,

```
python Pyrough.py input.json
```

where *Pyrough.py* is the main python file that calls for the additional classes and functions existing in the *src/* folder during the process and *input.json* is the input file that informs the code about the sample geometry and roughness parameters as well as material and crystal structure. Several examples of *.json* files can be found in the *examples/* repository on GitHub or in Appendix B.

The default workflow of *Pyrough* is presented in Figure 4.5. It can be subdivided into four domains: *Input*, *Process*, *Output* and *External interface*. After the load of the *.json* input file, a pristine mesh is generated based on the shape of the targeted rough sample (*e.g.*, film, wire, sphere, *etc.*) using the *gmsh* library [Geuzaine and Remacle 2009]. This section of the code is summarized as the *Param* class. Then, rough surfaces are generated using Equation 4.13 (or 4.14 in case of spherical samples) according to the roughness parameters contained in the input file. This is implemented in the *Sample* class. At this stage, the full ID-card of the sample containing statistical information such as RMS, kurtosis, *etc.*, is generated as an output. The numerical rough surface is used to displace each surface node of the mesh to generate the main output *i.e.*, an *.stl* mesh file containing the description of the rough samples (nodes, facets, *etc.*). Optionally, the roughened sample mesh can be used as a mould to be filled with atoms, based on the material lattice and crystallographic properties provided in the input file, using an external interface with the open source program ATOMSK [Hirel 2015]. Finally, atomic positions are saved as additional output files using various atomistic formats including *.xyz*, *.lmp*, *.cfg*, *etc.* depending on user's requirements.

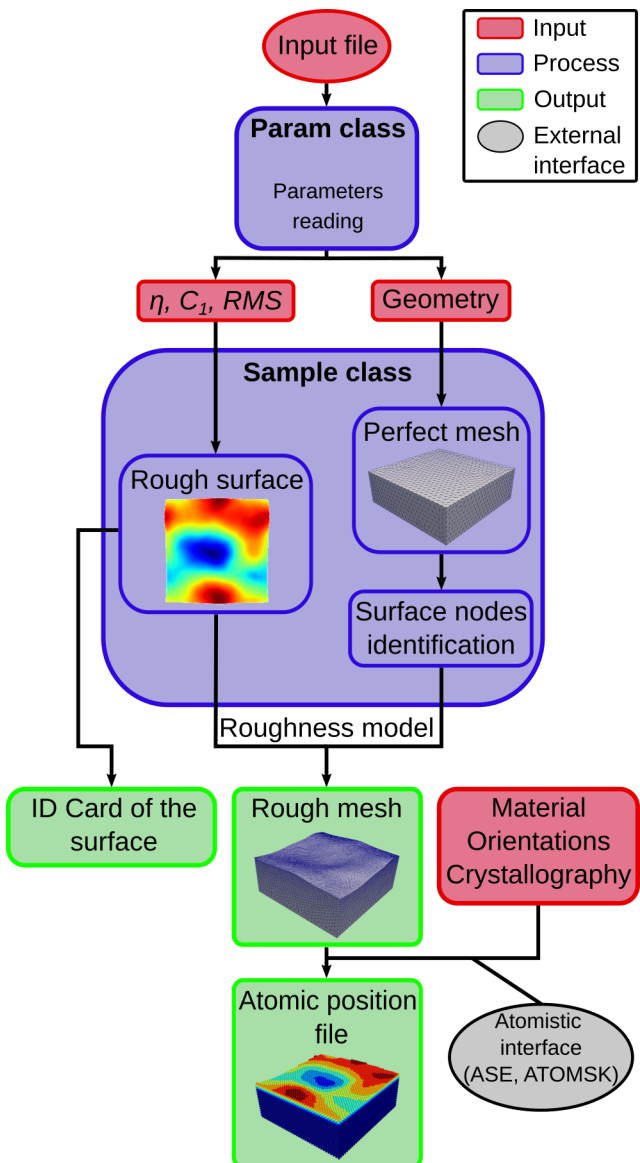


Figure 4.5.: Pyrough default workflow categorized in four domains: *Input*, *Process*, *Output* and *External interface*.

### 4.3.2. Input file

The *.json* input file of *Pyrough* is subdivided into four sections (see Table 4.1) that are processed within the *Param class*. First, the object type section informs the code on the sample shape to design. Each shape is associated to an object keyword in *Pyrough*. Currently, the available shapes are the film (keyword *Box*), cube (*Cube*), circular-based wire (*cWire*), faceted wire (*fWire*), sphere (*Sphere*) and faceted particles (*Wulff*). In addition, the user can easily implement additional shapes and associated keywords thanks to the object-oriented architecture of the code. Additional objects can be derived from aforementioned mother shapes as e.g., the *Grain* object that will be

described later. The second section in Table 4.1 describes the sample dimensions and surface roughness including mesh precision information ( $n_s$  and  $\alpha$ ) and roughness parameters such as  $\eta$ , the normalization factor  $C_1$ , the desired  $RMS$  or the frequency ranges  $A$  and  $B$  used to generate the rough surfaces. The user can control the amplitude of the rough height distribution either by imposing  $C_1$  or the  $RMS$  in the input file.  $n_s$  is the characteristic size of the element before roughening and  $\alpha$  is a scaling factor for mesh refinement in the roughened region (this will be discussed further in a later section). Additional information required for specific cases (e.g., surface energies in case of Wulff-shaped systems) are also provided here. Then, the crystal structure (optional) section provides atomic-scale information on the material such as lattice parameter, crystal structure and crystalline orientation required if building the atomic structure. Finally, a last section relies on the output files generated by *Pyrough*. Associated with the FEM and ATOM parameter lists, several roughened mesh and atomic position files with various formats can be generated by the user including *.stl*, *.msh*, *.inp*, *.obj*, *.vtk*, etc. for FEM and *.xyz*, *.lmp*, *.cfg*, *.POSCAR*, etc. for atomic position files (see Gmsh and ATOMSK documentations for more details on output formats). Empty FEM and/or ATOM lists will not generate output files except the processed *.stl* file.

Note that it is also possible to directly provide a pristine mesh file on which the user wishes to apply surface roughness still using the *.stl* format (particularly useful for users with their own *.stl* mesh). In this latter case, surfaces are identified based on the type of object (*Box*, *cWire*, etc.) chosen by the user.

All the inputs are read and interpreted by the *Param* class, i.e. *Pyrough* generates a *param* object after the input file reading in order to gather all the variables required for further processing. For instance, a simple call to the *param.width* variable is done to access the width of the sample within *Pyrough*. This class is used to distribute variables towards the different internal processes of *Pyrough* what simplifies the implementation of new sample shapes.

### 4.3.3. *In silico* roughness design (Sample class)

After reading the input file, *Pyrough* generates a rough sample following a two-step process. Firstly, a pristine sample with dimensions imposed by the user is generated using the *Sample* class that gathers most of the processes up to the end of *Pyrough* execution. To this aim and for the sake of computational time optimization, *Pyrough* relies on *gmsh* to generate 3D surface meshes out of triangular elements. Depending on the targeted sample shape, the appropriate function is chosen and the mesh nodes as well as corresponding facets are stored respectively in the *vertices* and *faces* variables. Below is an example of the function used for the generation of a sphere, centered at (0,0,0) with a radius of 10 nm.

```
gmsh.initialize()
gmsh.model.add("sphere")
```

#### 4. Pyrough : a tool to build 3D samples with rough surfaces – 4.3. Pyrough implementation

Table 4.1.: Description of *Pyrough*'s input file.

Parameter	Type	Description	Example
<b>Type of object</b>	<i>str</i>	Shape of the sample	<i>Box, cWire, Cube, etc.</i>
<b>Sample and roughness</b>			
<i>radius/length/width/height</i>	<i>float</i>	Sample dimensions (nm×nm×nm)	100, 100, 40
$\eta$	<i>float</i>	Roughness parameter	0.75
<i>RMS</i>	<i>float</i>	Root mean square	1.9
$C_1$	<i>float</i>	Normalization factor	1.2
$A, B$	<i>int</i>	Frequency range	30, 30
$n_S$	<i>int</i>	Mesh elements size (before roughness)	10
$\alpha$	<i>int</i>	Mesh refinement scaling factor $\in [0;1]$ ( <i>optional</i> )	0.33
Raw stl	<i>str</i>	Initial object's mesh ( <i>optional</i> )	<i>mymesh.stl</i>
<i>fWire case :</i>			
$n_f$	<i>int</i>	Number of wire facets	5
<i>Wulff case :</i>			
Surfaces	<i>list</i>	Surface list (Miller indices)	[1,0,0], [1,1,0], [1,1,1]
Energies	<i>list</i>	Surface energies [mJ/m <sup>2</sup> ]	1297, 1531, 1196
$n_{At}$	<i>int</i>	Number of atoms	277389
<b>Crystal structure</b>			
Material	<i>str</i>	Chemical formulation	<i>Au</i>
Lattice parameter	<i>float</i>	Lattice parameter of the crystal [Å]	4.08
Crystal structure	<i>str</i>	Lattice structure of the crystal	<i>fcc</i>
Orientation	<i>list</i>	Orientations along x, y and z-axis	[1,0,0], [0,1,0], [0,0,1]
<b>Output parameters</b>			
<i>ATOM</i>	<i>list</i>	Formats of the output atomic files	[ <i>"lmp", "xyz"</i> ]
<i>FEM</i>	<i>list</i>	Formats of the output FEM files	[ <i>"stl", "msh", "inp"</i> ]

```
gmsh.model.occ.addSphere(0, 0, 0, 10)
gmsh.model.occ.synchronize()
gmsh.option.setNumber("Mesh.MeshSizeMin", ns)
gmsh.option.setNumber("Mesh.MeshSizeMax", ns)
gmsh.model.mesh.generate(3)
node_tags, node_coords, _ = gmsh.model.mesh.getNodes()
element_types, element_tags, element_nodes = \
gmsh.model.mesh.getElements(dim=2)
vertices = node_coords.reshape(-1, 3)
triangle_idx = np.where(element_types == 2)[0][0]
faces = element_nodes[triangle_idx].reshape(-1, 3)-1
gmsh.finalize()
```

While a similar approach is used for several *Pyrough* shape presets, the process is slightly different for faceted systems that rely on the Wulff theory [Wulff 1901; Barm-paris et al. 2015]. In this case, the Wulffpack library [Rahm and Erhart 2020] is used for the generation of facets and nodes, according to the surface and energy parameters provided in the input file (see Table 4.1). Note that using *Pyrough* with the Wulff option requires ASE [Hjorth Larsen et al. 2017] as an additional package. Once the

Wulff-shaped structure is generated, each facet is constructed using the `addLine`, `addCurveLoop` and `addPlaneSurface` functions of the `gmsh` library.

Secondly, *Pyrough* generates roughness displacing mesh surface nodes perpendicularly to the original surface. To this aim, a numerical rough surface  $h(x, y)$  is generated using the roughness model (Equation 4.13 or 4.14) for each facet while surface nodes to be displaced are identified. Depending on the targeted sample shape, various protocols are used to identify surface nodes and apply roughness. In the following, we provide details for the various sample shapes already implemented in *Pyrough*.

- **Film**

The `Box` object can be used to design films *i.e.*, 2D-periodic samples with a single rough surface. `Box` is particularly useful to model *e.g.*, the indentation of rough surfaces or perform contact friction simulations. A cell of dimensions  $length \times width \times height$  and mesh size  $n_S$  is first constructed. In this case, only the top surface is going to be roughened and surface nodes are originally located at the maximum height of the pristine sample mesh. A numerical grid is then generated from the surface nodes with  $x$  and  $y$  coordinates : each grid point refers to a surface node on the original mesh. Because of the periodicity of Equation 4.13 on the  $[0, 1]$  interval, the grid is normalized and the numerical surface roughness function  $h$  is applied to its normalized coordinates, *i.e.* no repetition of the pattern appears along the  $x$  and  $y$  axis. The roughening procedure simply consists in displacing each surface node perpendicularly to the  $(x, y)$  surface (*i.e.*, along the  $z$ -axis) according to  $h(x, y)$ . The generation of a rough film is illustrated in Figure 4.6a.

- **Wire with circular cross-section**

The second type of samples available in *Pyrough* is the `cWire` object (wire with circular cross-section) that can be useful to model rough cylinders in FEM [Somadder and Islam 2018] or NWs for MD applications [Weinberger and Cai 2012; Deb Nath 2014; Byggmästar et al. 2015]. As illustrated in Figure 4.6b, a cylinder of radius  $radius$  and length  $length$  is constructed using the `extrude` function of `gmsh`, *i.e.* we first generate a circle in the  $xy$ -plane centered in  $(0, 0)$  with  $n_S$  points along its circumference that we extrude along the  $z$ -axis with a regular mesh. This allows to consider vertices at the wire surface to be those positioned on the external radius  $r$  of the cylinder. In this case, the idea is to roll a rough surface around the wire in order to apply roughness. To do so, a numerical grid is generated on the  $[0, 1]$  interval in the same way as in the case of a `Box` object except that the number of points along the  $x$ -axis is equal to the number of mesh points dividing the circular base and the number of points along the  $y$ -axis corresponds to the number of layers along the length of the wire. The numerical surface roughness function  $h$  is then applied to the numerical grid normalized on  $[0, 1]$  interval for the sake of periodicity. Thus, each surface node from the wire mesh

#### 4. Pyrough : a tool to build 3D samples with rough surfaces – 4.3. Pyrough implementation

is moved along the  $r$ -axis by its corresponding displacement vector on the generated rough surface.

- **Faceted-wire**

The *fWire* object allows for the design of a second type of wire made of faceted surfaces which is commonly observed at the nanoscale [Hanrath and Korgel 2005; Bernal et al. 2011; Roos et al. 2014]. In this case, the initial regular mesh of length *length* along the  $z$  direction is constructed with the *extrude* function of *gmsh*. But in this case the base is formed of a  $(0,0)$  centered regular polygon with  $n_f$  sides inscribed in a circle of radius *radius* in the  $xy$ -plane. Then the same rolling approach as for a wire with circular cross-section is used to build the rough wire except that the surface nodes are here translated along the outward facet normal  $\vec{n}$  they belong to. An additional step is required to identify nodes on surface edges. These latter are displaced along  $\vec{n}=\vec{n}_1+\vec{n}_2$  where  $\vec{n}_1$  and  $\vec{n}_2$  are the normal directions of the two facets the node belongs to. This process is described in Figure 4.6c.

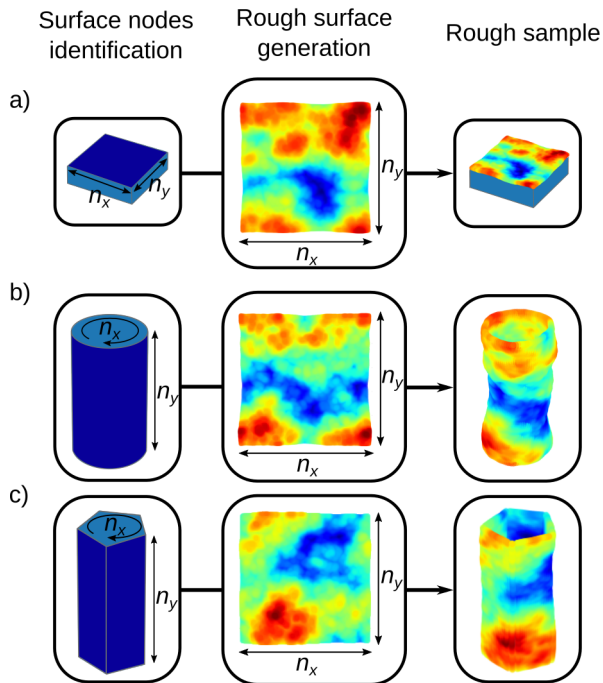


Figure 4.6.: Construction of various rough samples, a) film, b) wire with circular cross-section and c) faceted wire. For each sample, the surface nodes are colored in dark blue and  $n_x$  and  $n_y$  correspond to the number of points along  $x$  and  $y$ -axis respectively in the original 3D mesh. A jet color map is used for the representation of height distributions, red is the maximum value whereas blue is the minimum one.

- **Faceted particles and cube**

As described in Figure 4.7, fully-rough 3D faceted shapes (cube or Wulff-like) can also be designed using *Pyrough*. In these cases, one rough surface per facet is generated as illustrated in Figure 4.7. A specific process for the identification of each facet nodes is used in the *node\_surface* function of the *src/Func\_pyrough.py* file. Here, a node  $M$  is labelled as belonging to a given surface described by points  $A, B$  and  $C$  if  $\det(\vec{AB}, \vec{AC}, \vec{AM}) = 0$ . Once the list of nodes for each facet is generated, each flat surface is rotated around  $\vec{v} = \vec{n} \wedge \vec{u}_z$  by the angle  $\theta = \arccos\left(\frac{\vec{n} \cdot \vec{u}_z}{\|\vec{n}\| \|\vec{u}_z\|}\right)$  formed between the facet outward normal  $\vec{n}$  and  $\vec{u}_z$  the  $z$ -direction, to align the isolated surface with the  $xy$ -plane. Then coordinates are normalized on the  $[0, 1]$  interval in line with the periodicity of Equation 4.13 along the  $x$  and  $y$ -axis. Finally, each node is translated along its facet normal  $\vec{n}$  using  $h(x, y)$  to build the rough surface. The process is repeated for each facet of the sample. Using this method, all facets are generated independently but with the same roughness parameter set ( $\eta, C_1, A, B, etc.$ ). As for the faceted wires, nodes localized on surface edges and corners are treated using facets-associated averaged displacements.

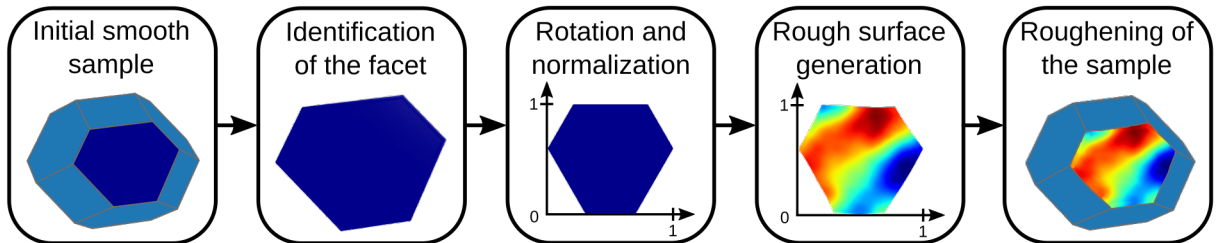


Figure 4.7.: Construction of Wulff-faceted samples including the identification of one facet and relative nodes before the use of Equation 4.13. The process is repeated for each facet of the sample using the same roughness parameter set.

- **Sphere**

*Pyrough* allows for the generation of spherical objects of radius  $radius$ , centered in  $(0,0,0)$ , with roughened surfaces using the *addSphere* function of *gmsh*. In this case, roughness is applied to each surface node of the sphere by summing spherical harmonics based on Equation 4.14. A maximum harmonic degree of 15 is used to correctly represent the sphere morphology as suggested by Wang *et al.* [Wang et al. 2021] but it can be easily modified according to the user's requirements. The power law is integrated through the auto-correlation function  $l^{-2(2\eta+1)}$  (Equation 4.18) so that the user can easily monitor the roughness degree.

#### 4. Pyrough : a tool to build 3D samples with rough surfaces – 4.3. Pyrough implementation

Note that for any shape generated by *Pyrough*, the minimum value of  $h(x, y)$  is added to every node-associated displacement while translations are performed along the outward normals of the sample, both in order to prevent element interpenetration issues. Figure 4.8 shows how edge and corner-associated nodes are treated for the construction of the *fWire* and *Wulff* objects. Only the normal  $\vec{n}$  is computed in the *fWire* case since the displacement is directly given by the generated rough surface. In the *Wulff* case, each  $h_{i,j} \vec{n}_i$  vector is averaged according to the facet normal the node belongs to, where  $h_{i,j}$  is the imposed displacement of node  $j$  on facet  $i$ .

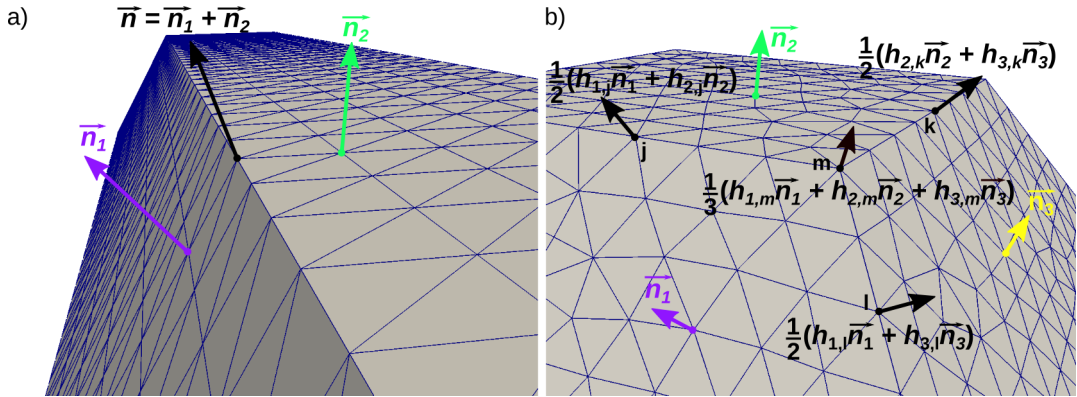


Figure 4.8.: Computation of normal direction and displacement in the case of edge and corner-associated nodes. a) *fWire* case b) *Wulff* case for  $j$ ,  $k$  and  $l$  edge-associated and  $m$  corner-associated nodes. Purple, green and yellow vectors are facet normals and black vectors are the resulting displacement vectors.

#### 4.3.4. Refinement and volumetric 3D mesh

Surface roughening can induce significant element distortions into the sample. Thus, mesh refinement is used to mitigate this aspect using the *gmsh* library and applying a mathematical field that maps the element size throughout the sample. *Pyrough* relies on a linear scaling of the element size that ranges from maximum  $n_S$  to minimum  $\alpha \cdot n_S$ , the latter characterizing the element size right under the rough surface. Also, a specific field is defined for each *Pyrough* shape object as follow,

- Film :  $n_S + n_S(\alpha - 1) \frac{z - z_{min}}{z_{max} - z_{min}}$  with  $z_{min}$  and  $z_{max}$  respectively the node minimum and maximum  $z$ -coordinate from the film mesh.
- Wire with circular or faceted cross-section :  $n_S + n_S(\alpha - 1) \frac{\sqrt{x^2 + y^2}}{r_{max}}$  with  $r_{max}$  the maximum radial coordinate.

#### 4. Pyrough : a tool to build 3D samples with rough surfaces – 4.3. Pyrough implementation

- Sphere, Wulff shape, Cube :  $n_S + n_S(\alpha - 1) \frac{\sqrt{x^2+y^2+z^2}}{r_{max}}$  with  $r_{max}$  the maximum radial coordinate.

Then, a 3D volumic mesh is derived using the *gmsh* classical procedure and first-order tetrahedron elements. Examples for the mesh refinement process are shown in Figure 4.9

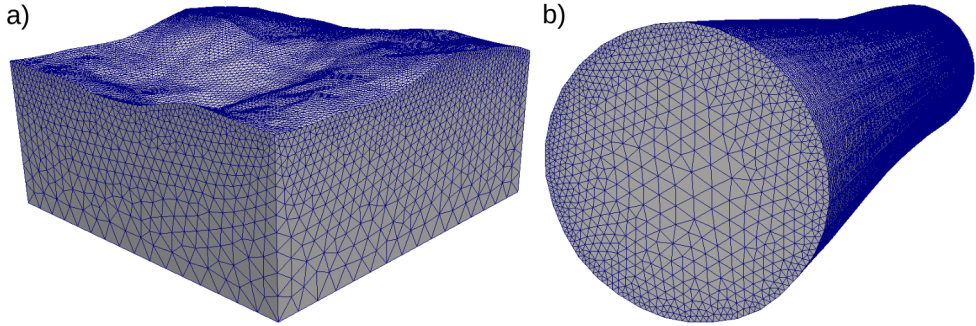


Figure 4.9.: *Pyrough* refined mesh process using element size fields, a) application to a *Box* type object where the size of the elements is reduced getting closer to the surface, b) application to a circular wire with a radial decrease of the mesh size.

#### 4.3.5. Atomic position file generation

For the generation of atomic position files, *Pyrough* is coupled to ATOMSK. An initial atomic block of the target material and crystallography is generated. The rough sample is carved out of the initial block using the *.stl* mesh as a mask, as shown in Figure 4.10b. To avoid *ATOMSK* automatic reshaping of the mesh to the size of the box, the initial block is generated with maximum dimensions along *x*, *y* and *z*-axis being equal to those from the input mesh. Atoms positioned outside the 3D mesh are selected and deleted from the box. This process leads to rough sample inside a box that preserves the initial dimensions. A final reboxing process is performed via the *rebox* function of *ATOMSK* to fit the box with sample dimensions. Additionally, all atom are translated so that *x*, *y* and *z* minimum coordinates are 0.

#### 4.3.6. Outputs

The name of each output file generated by *Pyrough* relies on the prefix of the *.json* input file. Thus, considering the *object.json* input file, *Pyrough* systematically generates an *object.stl* file for the rough and refined 3D mesh and an *object\_stat.txt* file for its corresponding ID-card. In addition, all the mesh files corresponding to the *FEM* list variable are generated *e.g.*, *object.msh*, *object.vtk*, *etc.* Atomic positions can be generated as well using formats specified in the *ATOM* list variable *e.g.*, *object.lmp*,

#### 4. Pyrough : a tool to build 3D samples with rough surfaces – 4.3. Pyrough implementation

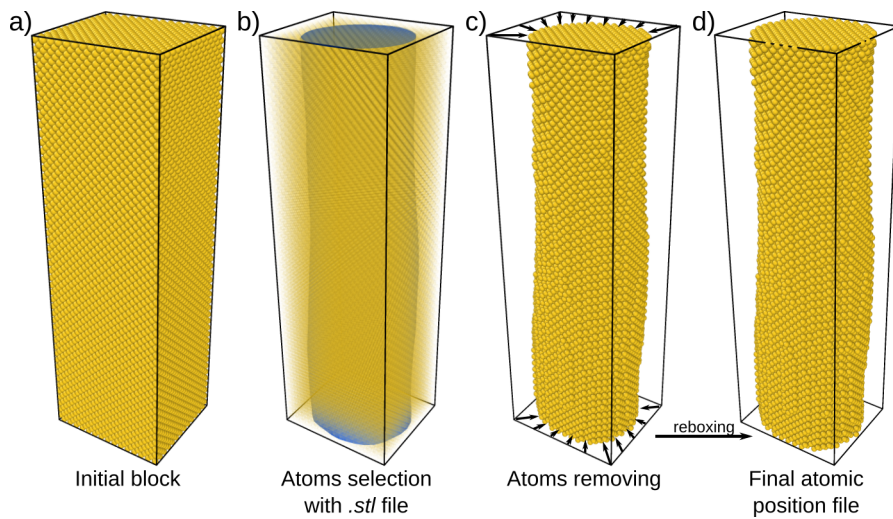


Figure 4.10.: Atomic position file generation for the design of a Au wire. a) Initial block with the dimensions of the input mesh, b) selection of atoms from the 3D mesh, c) rough sample, d) reboxed simulation cell.

*object.xyz, etc.* Additional examples about currently available shapes in *Pyrough* are shown in Figure 4.11 using a one-to-one comparison between mesh and atomistic representations.

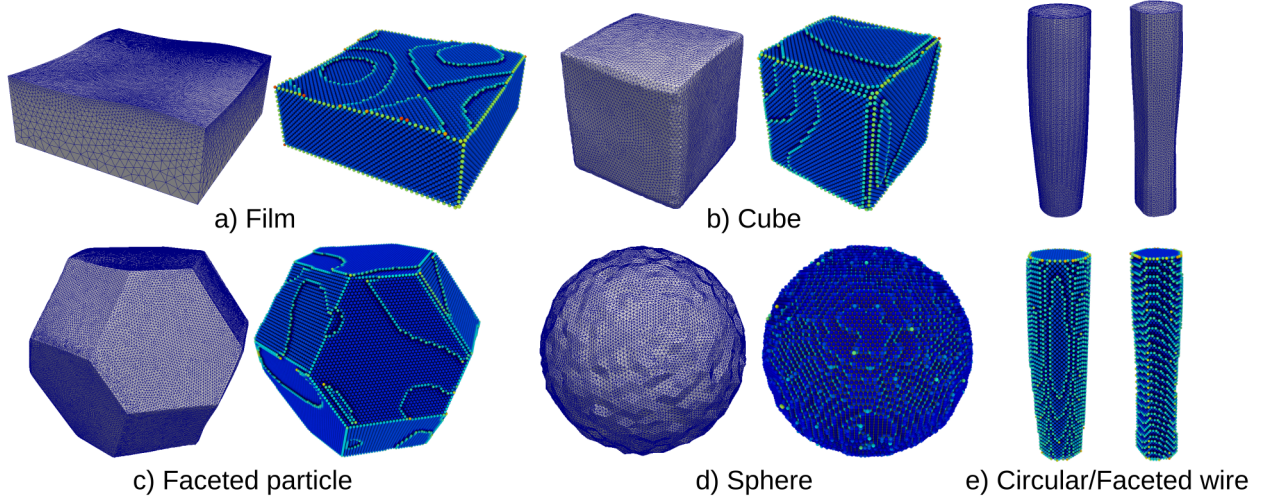


Figure 4.11.: Examples of objects that can currently be generated using *Pyrough*. Each single shape is represented using its corresponding FEM mesh and atomistic representation.

## 4.4. Other examples of application

In addition to classical shape generation, additional functionalities were integrated into *Pyrough*. In the following, the most important ones are described.

### 4.4.1. Statistically-equivalent surface construction

The *-surface* option was added in *Pyrough* as an extension to generate virtual surfaces with roughness properties similar to those measured in real-life experiments using e.g., an AFM image, via a reverse processing approach. It is called using the following command line,

```
python Pyrough.py -surface image.png size zmin zmax
```

where *-surface* is the keyword to call for the experimental image processing, *image.png* is the imaged surface to analyze, *size* is the lateral dimension of the surface in nm and *zmin* and *zmax* are, respectively, the surface minimum and maximum heights in nm.

When analyzing a finite-length portion of an aperiodic rough surface, the abrupt truncation at the boundaries introduces high-frequency leakage that distorts the true spectral representation. To remove this effect, window functions are applied to the surface tapering it towards zero at the window edges [Elson and Bennett 1995; Prabhu 2014]. For this specific application, we rely on the radially symmetric Hann window as described in the work of Jacobs *et al.* [Jacobs et al. 2017],

$$w_{Hann}^{2D}(x, y) = \left( \frac{3\pi}{8} - \frac{2}{\pi} \right)^{-\frac{1}{2}} \times \left( 1 + \cos \left( \frac{2\pi\sqrt{X^2 + Y^2}}{\min(L_x, L_y)} \right) \right) \quad (4.19)$$

for  $X^2 + Y^2 < \left( \frac{\min(L_x, L_y)}{2} \right)^2$

where  $L_x$  and  $L_y$  are the original dimensions of the image,  $X = x - L_x/2$  and  $Y = y - L_y/2$ . One can note that  $w_{Hann}^{2D}=0$  if the condition on  $X^2 + Y^2$  is not fulfilled.

In this context, the PSD of the real surface is computed using a fast Fourier transform (FFT) of the provided experimental dataset after the application of the window function  $w_{Hann}^{2D}(x, y) \cdot h(x, y)$ .

The amplitudes of the FFT are computed using the *fftn* function of *numpy.fft* library denoted as *np.fft*,

```
fourier_image = np.fft.fftn(image)
fourier_amplitudes = fourier_image**2
```

The norms of the wave vectors, denoted as *qnm*, are generated in the correct order for the previous call. This is achieved using the *fftfreq* function with *N* corresponding to the size of the image in pixels.

```
q = np.fft.freq(N) * N
```

#### 4. Pyrough : a tool to build 3D samples with rough surfaces – 4.4. Other examples of application

```

q2D = np.meshgrid(q, q)
qnrm = np.sqrt(q2D[0]**2 + q2D[1]**2)
qnrm = qnrm.flatten()
fourier_amplitudes = fourier_amplitudes.flatten()

```

As the PSD is centered in the middle of the image, the relevant wavelengths fall in the interval  $[1; N/2]$ . Indeed, sub-pixel wavelengths would make no sense and wavelengths greater than  $N/2$  would induce a sampling bias linked with vectors exiting the image. Then, wave vectors bins are defined such that the associated  $q$  values represent the midpoints of these bins. The average Fourier amplitude within each bin is computed using the *binned\_statistic* function from the *scipy.stats* library. To obtain the PSD, the average Fourier amplitude is multiplied by the surface within each bin.

```

qbins = np.arange(0.5, N//2+1, 1)
qvals = 0.5 * (qbins[1:] + qbins[:-1])
Abins, _, _ = stats.binned_statistic(qnrm, fourier_amplitudes,
                                      statistic = "mean",
                                      bins = qbins)
PSD = Abins * np.pi * (qbins[1:]**2 - qbins[:-1]**2)

```

The resulting PSD  $C^{2D}(q)$  is plotted as a function of wave vectors *qvals* on a double logarithmic scale, and  $\eta$  is deducted from a linear fit. Finally, *RMS* value is derived directly from the grey-scaled image and maximum/minimum height values using Equation 4.6.

The efficiency of this approach was tested on a self-affine rough surface with an *a priori* known value of the Hurst exponent as shown in Figure 4.12a. The image has a size of  $820 \times 820$  pixels corresponding to a  $1.5 \text{ cm} \times 1.5 \text{ cm}$  area. *Pyrough*'s evaluation  $\eta=-0.11$ , which corresponds to  $H=0.78$ , is in good agreement with Persson's value ( $H=0.80$ ) and confirms the robustness of the method. An example of application for an image with unknown  $\eta$  is shown in Figure 4.12b using the *-surface* option. It shows the  $200 \times 200 \text{ nm}^2$  top surface of a polystyrene particle [Yamamoto et al. 2005] for which we mapped local heights using gray-scale analyses (*imread* function, *cv2* Python package) that range between -4.5 nm and 4.5 nm. The resolution of the image is  $800 \times 800$  pixels. Associated statistical parameters are presented in Table 4.2.

Results give  $\eta = -0.20$  and  $RMS = 4.62 \text{ nm}$ . They are used as *Pyrough* inputs to model several numerical rough surfaces with a similar statistical description. One ends up with a random rough surface as shown in Figure 4.12b with a roughness exponent and a statistical distribution similar to the experimental data set (see Table 4.2). Such approach can be used to perform statistical analyses on a wide variety of samples with similar surface roughness properties compared to experimental observations.

#### 4. Pyrough : a tool to build 3D samples with rough surfaces – 4.4. Other examples of application

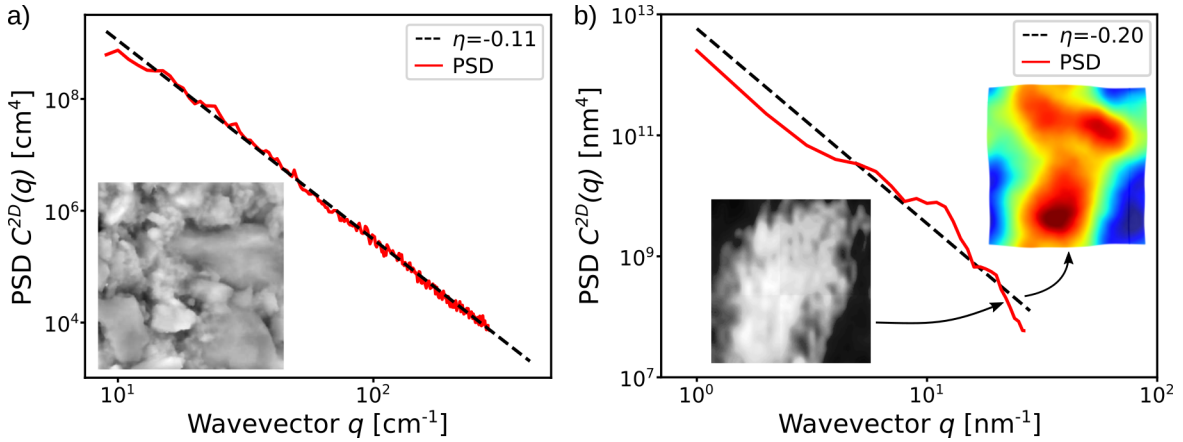


Figure 4.12.: Computation of  $C^{2D}(q)$  of a) known surface where computed  $\eta$  is equal to the value calculated from data in ref. [Persson et al. 2005] and b) comparison of PSDs as extracted from an experimental polystyrene particle surface [Yamamoto et al. 2005] and a *Pyrough*-generated surface with measured roughness parameters ( $\eta$  and RMS) as inputs.

Table 4.2.: Statistical analysis of a roughened surface obtained in (i) the experiment, the analysis of the top surface of a polystyrene particle [Yamamoto et al. 2005], and (ii) using *Pyrough* -surface module. The experimental measured parameters are used as *Pyrough* inputs to generate a surface characterized by similar statistical parameters.

Parameter	Experiment	<i>Pyrough</i>
$\sigma$	4.62	4.65
RMS	4.65	4.65
sk	-0.24	-0.20
K	2.27	2.40

#### 4.4.2. Nanoindentation with a roughened spherical tip

When performing nanoindentation, both the sample and the indenter tip surface roughness are supposed to have a severe impact on the local stress distribution in the sample subsurface [Kim and Oliver 1998; Pastewka and Robbins 2014; Zhang et al. 2022]. Figure 4.13 illustrates how the roughness of a spherical indenter designed using *Pyrough* influences the local stress state during nanoindentation using FEM. Three simulations are performed including one with a perfectly smooth indenter and two with roughened tips characterized by  $\eta = 0.50$  and  $0.75$ , respectively. The FEM simulations are performed using the COMSOL Multiphysics™ software [Multiphysics 1998]. The indenter is modeled as a 15 nm diameter diamond sphere characterized by a Young's modulus  $E=1050$  GPa, a Poisson's ratio  $\nu = 0.1$  and a density  $\rho = 3515$  kg.m<sup>-3</sup>.

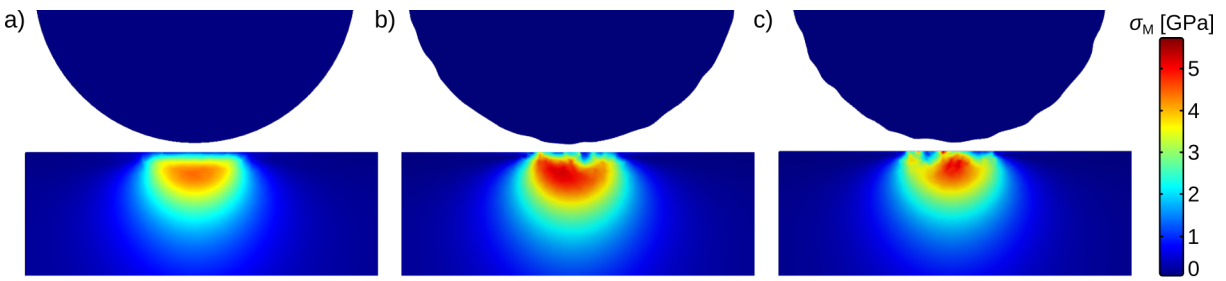


Figure 4.13.: Von Mises stress distribution during the nanoindentation of a gold sample with a roughened spherical tip, a) perfect sphere, b)  $\eta = 0.75$ , c)  $\eta = 0.50$ . The von Mises stress  $\sigma_M$  is recorded for an indentation depth of 0.6 nm but the tip is moved back on the illustration for the sake of visibility.

The indented sample is made of gold with  $E = 70$  GPa,  $\nu = 0.44$ ,  $\rho = 19300$  kg.m<sup>-3</sup> and dimensions  $30 \times 30 \times 7.5$  nm<sup>3</sup>. Mesh size is equal to 2.5 Å for the slab and the tips, with a refine factor set equal to 0.5 for the rough tips. The probe is loaded at the center of the sample top surface with a displacement of the indenter along the  $z$ -axis defined as  $\delta l_z(t) = -\dot{\delta l} \times t$  where  $t$  is the time and  $\dot{\delta l}$  is the indenter displacement rate. The displacements of the indenter along the  $x$  and  $y$  axis are set to zero. The side and bottom surfaces of the sample are kept fixed during the simulation whereas the top surface is unconstrained but associated in a contact pair with the indenter. The contact is solved using the Penalty method with the offset null penalty function [Perić and Owen 1992]. Figure 4.13 shows the distribution of the von Mises stress  $\sigma_M$  inside the gold surface after a displacement of the indenter of 0.6 nm. For the perfectly spherical indenter,  $\sigma_M$  is homogeneously distributed due to the spherical symmetry of the contact with a maximum value of 4.6 GPa  $z$ -axis aligned and located 5.0 Å below the sample surface. In contrast,  $\sigma_M$  is asymmetrically distributed for the two cases relying on roughened indenters. The two simulations are characterized by a maximum stress of 5.9 GPa ( $\eta=0.50$ , Figure 4.13b) and 5.7 GPa ( $\eta=0.75$ , Figure 4.13c), respectively. The impact of roughness is particularly significant here where small asperities on the indenter surface behave like smaller indenters that induce stress localization within the sample. The indenter's roughness also breaks the contact symmetry as the contact zone is not continuous anymore.

#### 4.4.3. Groovy grain boundary and interface

Accounting for the detailed shape of interfaces such as grain boundaries (GBs) is crucial to understand thermal [Merabia and Termentzidis 2014], electrical [Foy et al. 2020], magnetic [Fleischmann et al. 2010] or mechanical [Zhang et al. 2016] properties evolution near interfaces [Rost et al. 2003; Prakash et al. 2015]. Here we rely on the *Grain* object in *Pyrough* that enables for the construction of a rough interface between two different materials and/or crystallographic orientations. The *Grain* object is built sticking together two *Film* objects characterized by  $h$  and its opposite  $-h$  roughness

functions, respectively. This process is illustrated in Figure 4.14 where it is applied to a coherent  $<001>$  Ag/Au interface.

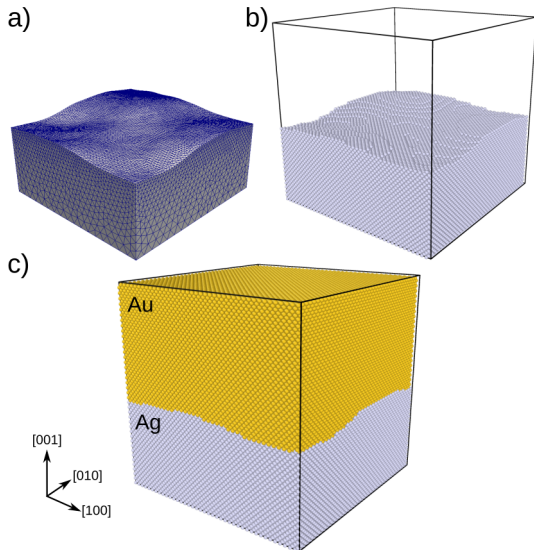


Figure 4.14.: Generation of a wavy grain boundary using *Pyrough* and the *Grain* object, a) single-grain FEM mesh with a rough surface characterized by  $h$ , b) same single grain filled with Ag atoms, c) Coupling of the complementary Au grain characterized by  $-h$  leading to an Ag/Au  $<001>$  coherent interface.

#### 4.4.4. Nanowire with rough surface

The mechanical properties of nanocrystals strongly depend on their shape [Amodeo and Lizoul 2017; Kilymis et al. 2018]. In order to generate more realistic virtual objects in MD simulations, one can apply roughness to their surfaces. Here we use *Pyrough* to generate 5000 Au NWs with 3 nm radius pseudo-circular cross-section (object *cWire*) and 20 nm length with various  $\eta$  and normalization factors  $C_1$ . Three categories of cross-section geometries are defined to classify the NW shapes including high amplitude (HA), low amplitude (LA) and quasi-circular (QC). Rougher geometries (HA) lead to unrealistic designs, whereas LA and QC geometries produce credible roughness comparable to that observed experimentally [Uesawa et al. 2010; Kim et al. 2011; Narayanan et al. 2015]. The QC geometry shows small variations of the external radius distribution with a cross-section shape that is close to the perfect circle. Cross-sections geometries rely on the *RMS* of the sample with an increasing value corresponding to a HA-shape tendency. The ranking of the *RMS* depending on  $\eta$  and  $C_1$  is presented in Figure 4.15. Based on the data set, one can find where to get the required geometry. For an identical value of  $C_1$ , the shapes are always displayed in the same order with increasing  $\eta$ : HA, LA and QC. It is in accordance with the roughness exponent's definition since it controls the bandwidth of the low-pass filter applied

#### 4. Pyrough : a tool to build 3D samples with rough surfaces – 4.5. Conclusion

to the surface roughening process. This confirms that *Pyrough* is adequate for the construction of different rough 3D object topologies.

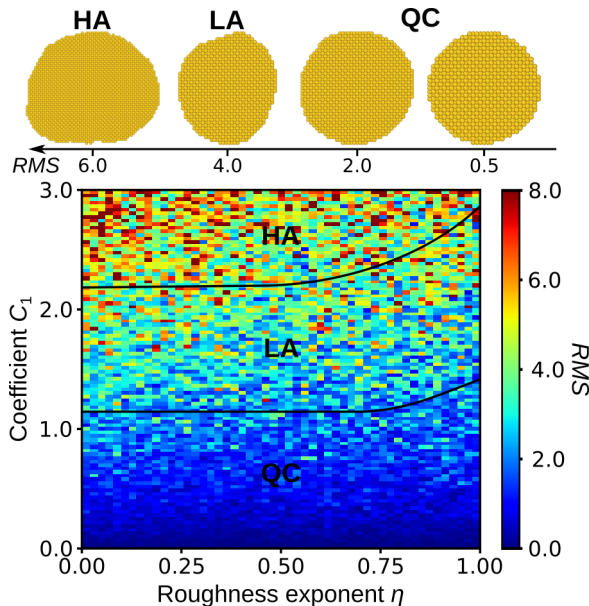


Figure 4.15.: Nanowire cross-section geometry classification according to  $RMS$  values and  $RMS$  distribution map of Au nanowires as a function of  $\eta$  and  $C_1$ . In order of highest to lowest  $RMS$ : HA, LA and QC.

## 4.5. Conclusion

This chapter relies on the development of *Pyrough*, a Python tool that enables the design of 3D virtual samples with roughened surfaces for application to atomistic and FEM simulations. The object-oriented aspect of *Pyrough* makes it user-friendly and its usage consists in few simple command lines. The objects catalog of *Pyrough* allows to construct simple 3D shapes (particles, wires, GBs, etc.) and can easily be upgraded by the user thanks to a free access via GitHub. The aim of *Pyrough* is to provide a better representation of 3D virtual objects when compared to the experiment by considering surface roughness and providing the user ways to manage it. The multi-scale diversity of outputs from atomistic to macroscopic FEM simulations makes *Pyrough* extremely versatile and useful for a large range of applications improving the accuracy of material property calculations.

Repository link : <https://github.com/jamodeo12/Pyrough>

The program documentation is available at : <https://jamodeo12.github.io/Pyrough/>

**Chapter IV summary :**

This chapter focuses on the development of *Pyrough*, a new tool to design 3D samples with rough surfaces. First, we have introduced the classical roughness theory that enables the construction of rough surfaces in the direct space and to tailor the degree of roughness with the roughness exponent. Then, the code implementation is presented including its workflow, the surface nodes management and available outputs. Finally, a non-exhaustive list of potential applications is presented. *Pyrough* is used as the main tool in the next chapters to generate samples for MD simulations.

# 5

## Influence of surface roughness on the deformation of gold nanoparticles in compression

This chapter refers to the study of the influence of surface roughness on the strength of Au NPs in compression, using *Pyrough* as the tool for the generation of virtual samples. First, we investigate the differences in the force-displacement behavior when compared to a reference sample with flat facets. Then, differences in term of deformation mechanisms are studied and compared to experimental findings. Finally, a theoretical model is proposed, based on the ideal strength of NPs with perfectly flat facets and surface topology, to predict the strength distribution of rough NPs.

## 5.1. Introduction

While it is well known that surfaces play a key role at the nanoscale for functional property applications (*e.g.*, catalysis, adhesion), it becomes obvious that rigorous characterization and optimization of NO surfaces is at the heart of nanomechanics and defect engineering. Nevertheless, the smaller the sample, the more difficult it is to test it mechanically. Among others, the studies of Mordehai and collaborators appear as pioneering works when applying such mechanical tests to micro- and NPs using SEM, atomistic and FEM simulations [Mordehai et al. 2011a; Mordehai et al. 2011b]. A similar approach was used by Issa and collaborators to investigate the mechanical response of MgO ceramic NPs [Issa et al. 2015; Issa et al. 2021]. In particular, the latter study is characterized by quantitative strength discrepancies when comparing experiments and simulations that could be attributed to experimental biases, as recently shown in ref.[Chen et al. 2022]. Overall, a direct consequence of downsizing is a more and more scattered mechanical response due to both intrinsic and extrinsic experimental biases. Indeed, the yield strength of NOs can vary by more than one order of magnitude at constant size as shown *e.g.*, in refs. [Sharma et al. 2018; Shahbeyk et al. 2019; Zimmerman et al. 2021]. In this context, we consider surface roughness as a potentially major source for data scattering when considering the measurement of NO strength. While Coupeau and collaborators recently highlighted contact reactions between surface steps and dislocation using *in situ* ultra-high vacuum STM in large-scale sample [Coupeau et al. 2020; Khoroshilov et al. 2022], the surfaces of NOs are often rough with surface-ledge height ranging from a single atomic layer to several nanometers (see *e.g.*, refs. [Iijima 1985; Zhang et al. 2001b; Mordehai et al. 2011b; Kim et al. 2018]) and it is well-known that contact singularities gradually act as stress concentrators with decreasing size. However, despite its possible influence on the SDN process and overall strength, this issue has not been addressed comprehensively neither experimentally nor in the simulation of small-scale objects. This is in contrast with the numerous studies performed by tribologists and contact mechanics researchers, at larger scales. In this chapter, it is illustrated how surface roughness plays a key role on the strength and elementary deformation processes of metal NPs and a model is proposed relying on the surface topology to predict the strength dispersion of NPs under compression accounting for contact roughness.

## 5.2. Methods

### 5.2.1. Design of nanoparticle with rough surfaces

NPs with rough surfaces are designed using *Pyrough*, the open-source Python tool I developed during this PhD project (see Chapter 4 for technical details). In this study, we use the *Wulff* module of *Pyrough* with low-index surface energies  $\gamma_{\{100\}}=1296.5$  mJ/m<sup>2</sup>,  $\gamma_{\{110\}}=1531.2$  mJ/m<sup>2</sup> and  $\gamma_{\{111\}}=1196.4$  mJ/m<sup>2</sup> (see Appendix A for surface

5. Influence of surface roughness on the deformation of gold nanoparticles in compression – 5.2. Methods

energy calculation details) as inputs to build faceted-Au NPs. Indeed, faceted-Au micro- and NPs have been the subject of a great deal of research recently (see e.g., ref. [Mordehai et al. 2011a; Mordehai et al. 2011b; Wang et al. 2012; Kovalenko et al. 2017; Roy et al. 2019; Lauraux et al. 2022]). Experimentally, they can be fabricated by dewetting a thin film on a substrate, resulting in NPs with surfaces having a varying degree of roughness, without any sign of surface oxidation which makes them the ideal samples for the study of the surface roughness impact on the mechanics of NPs under compression. Au NPs with height  $l_0=20$  nm are built for  $\eta$  ranging from 0 to 1 and  $C_1=0.5$  and 1.2. Note that the generated rough surfaces in this context are not self-affine ( $\eta \notin [-0.5, 0]$ ), as our primary objective is to model one or few steps on the external facets of the samples, which necessitates even smoother surfaces. This approach aligns with experimental observations at these scales [Iijima 1985; Henry 2005]. Additionally,  $C_1=0.5$  leads to NPs characterized by surface roughness of a single atomic layer depth, while  $C_1=1.2$  produces coarser surfaces. Examples of Au NPs for various  $\eta$  and  $C_1=0.5$  are illustrated in Figure 5.1a-d. Twenty samples characterized by surfaces with statistically-identical roughness are generated for each  $(\eta, C_1)$  pair. Note that even if several samples have same  $\eta$  and  $C_1$  values, each of them has a unique topography due to the randomness induced by  $G_{a,b}$  and  $U_{a,b}$ . Twenty additional samples with flat surfaces are also produced for comparison.

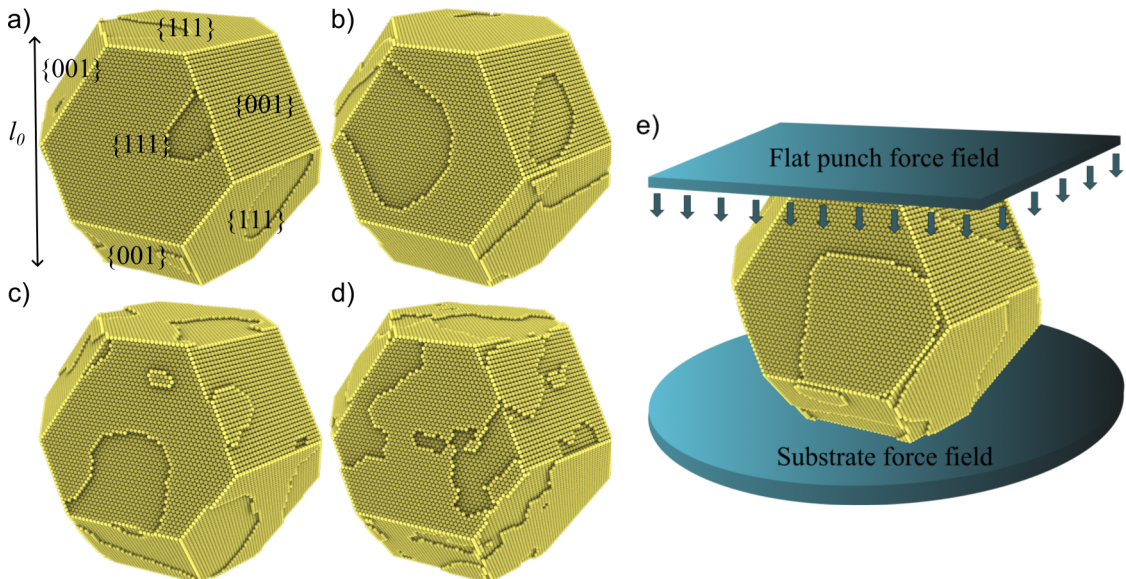


Figure 5.1.: Wulff-shaped Au nanoparticles with (unrelaxed) rough surfaces as generated using *Pyrough* and MD compression protocol, a)  $\eta=0.95$ , b)  $\eta=0.75$ , c)  $\eta=0.25$ , and d)  $\eta=0.0$ , e) the nanocompression simulation setup is made of two axis-aligned and infinite force fields that behave respectively as indenter and substrate, similarly to the one described in chapter 3.

### 5.2.2. Molecular dynamics simulation

In the following, MD simulations are carried out to investigate the influence of surface roughness on the mechanical behavior of Wulff-shaped Au NPs with rough surfaces under displacement-controlled compression. The EAM interatomic potential developed by Grochola *et al.* [Grochola et al. 2005] is used to describe atomic interactions in Au. The transferability of the Grochola potential to nanomechanics was addressed in several studies in which lattice, surface and dislocation properties are shown to accurately reproduce both experiments and DFT results [Deng and Sansoz 2009; Zheng et al. 2010; Mordehai et al. 2011a; Dupraz et al. 2015; Roy et al. 2022; Iteney et al. 2023]. A timestep of 2 fs is used for all MD simulations.

Designing samples with *Pyrough* leads to a mathematically-defined surface roughness that does not necessarily correspond to the thermodynamical equilibrium. To optimize sample surfaces, the potential energy is initially minimized following the protocol described in Chapter 2. Then, special attention is paid to the thermal equilibration procedure using non-periodic SWBC. The sample is first subjected to an initial 10 ps run in the NVE ensemble to initialize atom velocities and temperature (10 K target temperature). Then a temperature ramp is ran over 20 ps in the NVT ensemble up to *ca.* 810 K corresponding to 70% of the theoretical melting temperature of Au, which is followed by a high-temperature equilibration run during 1 ns at constant temperature. The sample is finally quenched down to room temperature (for later compression purpose) where a final equilibration run is performed during 0.5 ns. The mean square displacement (MSD) of the atoms is computed to monitor the reconstruction of rough surfaces during the whole equilibration process. The MSD tracks the deviation of atomic positions  $\mathbf{r}_i(t)$  over time with respect to a reference  $\mathbf{r}_i(0)$ .

$$\langle r^2(t) \rangle = \frac{1}{N} \sum_i^N |\mathbf{r}_i(t) - \mathbf{r}_i(0)|^2 \quad (5.1)$$

where  $N$  is the total number of atoms.

Nanocompression MD simulations along the [111]-direction *i.e.*, perpendicular to the NP top surface, are performed at room temperature using the Nosé–Hoover thermostat and non-periodic SWBC following the methodology previously introduced in Chapter 2 and in refs. [Issa et al. 2015; Amodeo and Lizoul 2017] (see Figure 5.1e). Additional simulations are also performed at  $T=10$  K to reduce the thermal noise while characterizing deformation processes.

## 5.3. Results

### 5.3.1. Nanoparticle equilibration

Figure 5.2a illustrates an example of MSD evolution during sample equilibration for a gold NP characterised by  $\eta=0.00$  and  $C_1=0.5$  (one-layer depth surface roughness). Results show a typical first-order system evolution with the MSD increasing up to a steady-state. In the high-temperature equilibration regime, such a behaviour can be modeled using a first-order approach  $\langle r^2(t) \rangle = K(1 - e^{-\frac{t}{\tau}})$ , where  $K$  and  $\tau$  are the system gain and time constants, respectively. The equilibration time  $t_{equi}=3\tau$  is defined as the time to reach 95% of the MSD final value.  $t_{equi}$  for  $\eta$  ranging from 0 to 1 as well as for NPs with flat surfaces are illustrated in Figure 5.2b. Each  $t_{equi}$  probability density function (PDF) is calculated from the mean ( $\mu_t$ ) and standard deviation ( $s_t$ ) of each dataset using the equation  $PDF(t_{equi}) = \frac{1}{s_t\sqrt{2\pi}}e^{-\frac{1}{2}\left(\frac{t_{equi}-\mu_t}{s_t}\right)^2}$ . This formulation is also employed for the distribution of critical stresses, as depicted in Figures 5.12 and 5.13. While each NP is characterised by a unique ( $K$ ,  $\tau$ ,  $t_{equi}$ ) triplet, a clear trend emerges for  $t_{equi}$ : the rougher the NP, the longer  $t_{equi}$ . Such a tendency relies on the topography of the surface height distribution  $h(x, y)$ . Rougher surfaces (low  $\eta$ ) are characterized by a larger contribution of high-frequency components of  $h(x, y)$  that induce energetically unfavorable configurations such as zig-zag surface terraces or small atomic islets, as shown in Figure 5.1c and d. During equilibration, terraces become more regular and originally-isolated islets either merge with adjacent surface steps or undergo reshaping in preferred directions, which requires a longer equilibration time. For less rough samples (larger  $\eta$ ), surfaces primarily feature extended and steadier atomic terraces, as shown in Figure 5.1a. Thus, the equilibration process essentially involves the smooth and quick reorientation of surface steps. For NPs with originally perfectly flat surfaces,  $t_{equi}$  is almost zero as Wulff-shaped NPs are already close to their equilibrium shape before the simulation.

Surface atoms reorganization during thermal equilibration induces a variation of the NP surface topology. Figure 5.3 shows the variation of the apparent roughness exponent before and after equilibration, respectively  $\eta_0$  and  $\eta_{eq}$ , for the whole ( $\eta, C_1=0.5$ ) samples collection, both computed using *Pyrough*-surface option applied to the atomic configuration image. More details on the -surface option can be found in Chapter 4. Note that  $\eta_0$  might slightly differ from *Pyrough*'s input  $\eta$  as it is computed from the sample's top surface that is restricted by a discrete set of atomic positions while  $\eta$  relies on the numerical surface  $h(x, y)$  defined by Equation 4.13. Finally, results show that  $\eta_{eq}/\eta_0$  is slightly larger than 1 in most of the cases meaning that the sample equilibration smooths the height distribution  $h(x, y)$  without completely cancelling the surface roughness. Also, the spread of the  $\eta_{eq}/\eta_0$  distribution increases as  $\eta$  decreases in agreement with our prior observations wherein a significantly larger number of atoms is displaced (larger MSD) when increasing the surface roughness.

5. Influence of surface roughness on the deformation of gold nanoparticles in compression – 5.3. Results

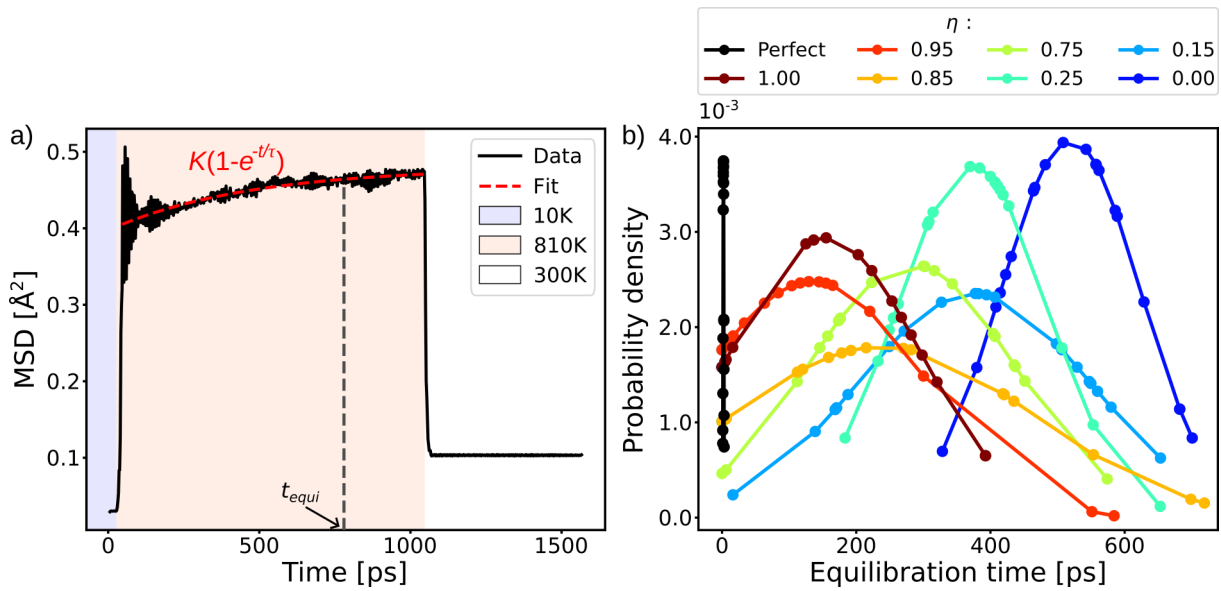


Figure 5.2.: Thermal equilibration of Au-faceted nanoparticles with rough surfaces, a) Evolution of the MSD during sample equilibration for a nanoparticle characterised by ( $\eta=0.00$ ,  $C_1=0.5$ ), b) Equilibration time  $t_{equi}$  distribution as a function of the roughness exponent  $\eta$ , for  $C_1=0.5$ . 20 samples (symbols) are tested for each  $\eta$  and curves are guides for the eyes. For the perfect case (nanoparticle with flat surfaces), the probability density function is reduced by a factor of 190 to scale with the other distributions.

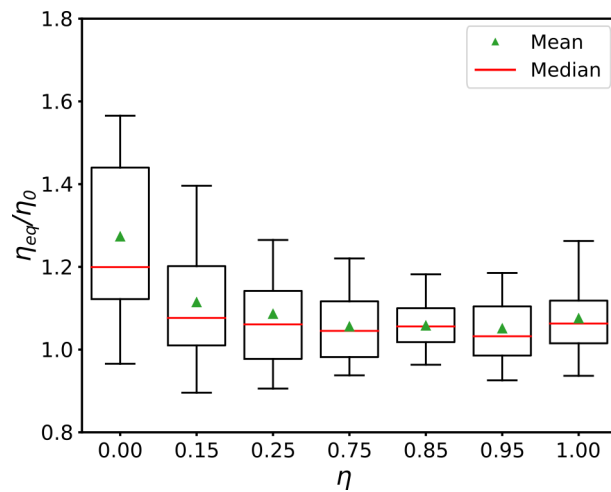


Figure 5.3.: Evolution of top surface roughness exponent  $\eta_{eq}/\eta_0$  after/before sample thermal equilibration as function of input  $\eta$ . The box plot relies on the central 50% of the sampling while bars show the scatter of the last 50%.

5. Influence of surface roughness on the deformation of gold nanoparticles in compression – 5.3. Results

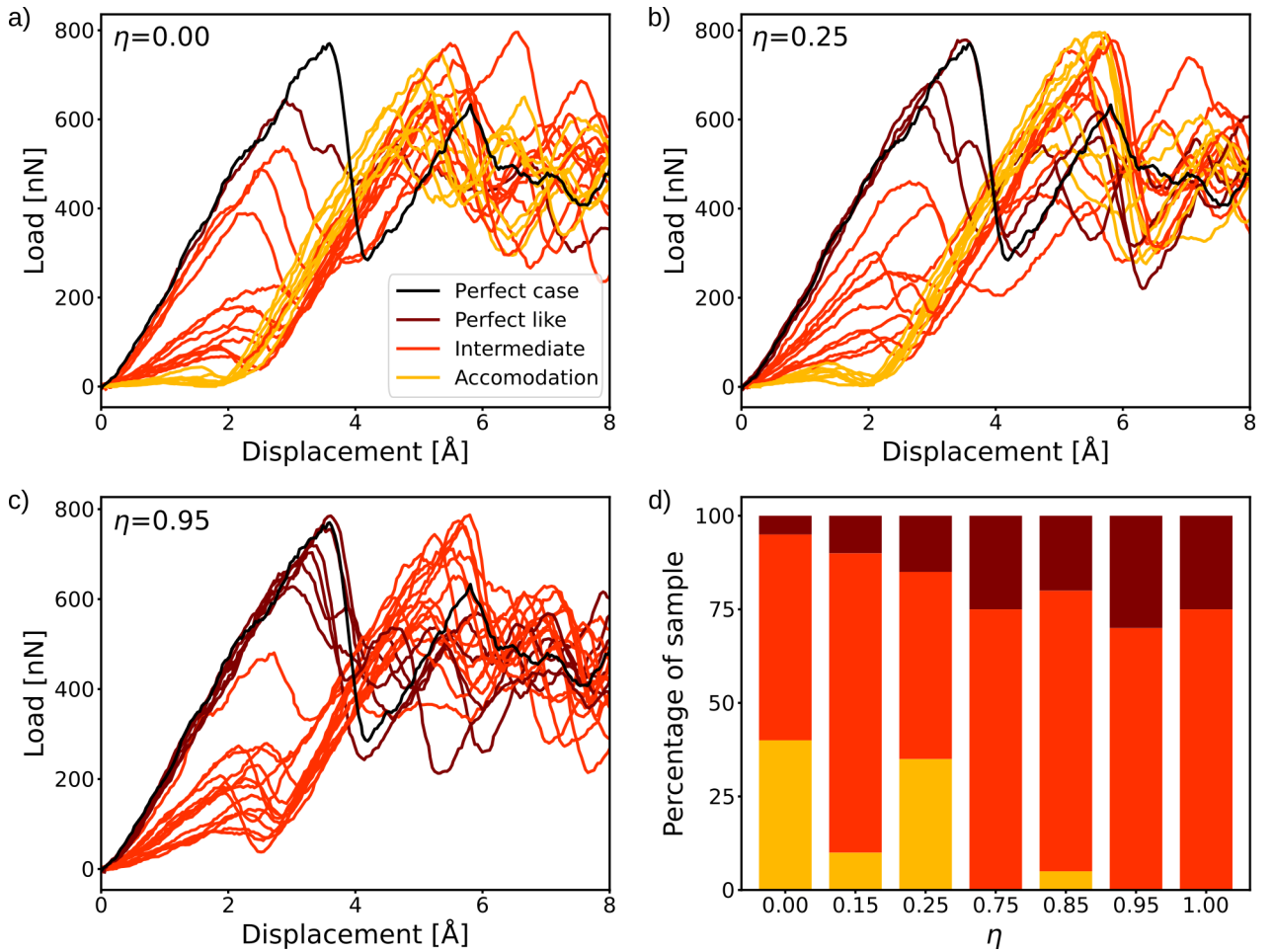


Figure 5.4.: Load-displacement for  $<111>$ -oriented Au-faceted nanoparticles with rough surfaces compressed at  $T=300$  K, a)  $\eta = 0.00$ , b)  $\eta = 0.25$ , and c)  $\eta = 0.95$ . 20 samples are tested for each  $(\eta, C_1=0.5)$  configuration. *Perfect-like*, *intermediate* and *accommodation* cases are illustrated in brown, red and orange respectively while the *perfect* case (nanoparticle with flat surfaces) is shown in black, d) Sample fraction distribution among the *Perfect-like*, *intermediate* and *accommodation* cases as a function of  $\eta$ .

### 5.3.2. Mechanical response

Figure 5.4 illustrates the mechanical response of the faceted-Au NPs compressed along [111] using MD at  $T=300$  K for various level of surface roughness as compared to one of the perfect case. For the sake of clarity, data are filtered using the Savitzky-Golay method (filter window  $f_w=7$ , polynomial order  $n=1$ ) that allows to get rid of temperature-induced fluctuations [Press and Teukolsky 1990]. The two usual elastic and plastic regimes of deformation are easily recognizable in the case of the NP with perfectly flat surfaces (*perfect* case). They are delimited by a yield force of  $F_y^P=779$  nN, where a load drop marks the beginning of the plastic deformation regime. Afterwards,

## 5. Influence of surface roughness on the deformation of gold nanoparticles in compression – 5.3. Results

the mechanical test consists in a succession of quasi-linear elastic reloads followed by force drops that highlight each plastic event. The mechanical response of NPs with rough surfaces is significantly different from the one of the *perfect* case. In the following, these differences are rationalized into three categories, *i.e.* the *perfect-like*, the *intermediate* and the *accommodation* cases, that progressively emphasize the impact of surface roughness. The *perfect-like* behavior is characterized by a load response particularly close to the one of the *perfect* case in the elastic regime. However, the first load drops occur at slightly lower critical displacement  $\delta_y$  and force  $F_y$ , the latter ranging from  $0.8F_y^p$  up to  $F_y^p$ . In this regime, secondary force peaks are of lower amplitude when compared to the *perfect* case. Also, the *intermediate* trend is characterized by various load-displacement slopes in the elastic regime all below the one of the *perfect* case including  $F_y$  in the  $[0.2F_y^p : 0.8F_y^p]$  range. While first force drops are of lower amplitude and occur for lower  $\delta_y$ , secondary elastic reloads can reach maximum forces as high as in the *perfect* case, in the  $[0.8F_y^p : F_y^p]$  range. Finally, *accommodation* cases are characterized by an initial pseudo-contact with almost zero force recorded until the displacement reaches  $\sim 2 \text{ \AA}$ , where the force starts to increase. This particular trend is observed when the top surface of the NP is characterized by one or several small atomic islets (made of a few atoms each) that are pushed by the indenter below the surface of the NP with little effort. The critical displacement of about  $\sim 2 \text{ \AA}$  does not depend on  $\eta$  but is rather imposed by the displacement at which the indenter starts to deform subsurface atomic layers. This distance can be approximated by the  $\{111\}$  interplanar distance  $d_{\{111\}} = a_0 / \sqrt{3} = 2.36 \text{ \AA}$ . One can note that in this case there is no clear evidence of elastic deformation of the subsurface layers during the pushing of the surface atomic islets within the NP subsurface region. This entire process that leaves the surface perfectly clean and flat (comparable to the one of the *perfect* case) is illustrated in Figure 5.5. Atoms are displaced from their original positions against the top surface, pushing locally underneath atomic layers within the NP. This changes the usual FCC stacking sequence for the next subsequent crystallographic planes generating stacking-faults (atoms in red in Figure 5.5). At  $\delta=1.91 \text{ \AA}$ , the top surface is perfectly flat as the islet is fully integrated into the sample that is now characterized by stacking defects. One can notice that the misalignment is accommodated by the external facets if the islet is initially positioned near a top surface's border. As a consequence, the rest of the load-displacement curve of *accommodation* cases is very similar to the one of the *perfect* case including secondary elastic reloads reaching the  $[0.8F_y^p : F_y^p]$  force range. The fraction of *perfect-like*, *intermediate* and *accommodation* cases for  $\eta$  ranging from 0 to 1 are depicted in Figure 5.4d. *Intermediate* cases are the most observed on the whole  $\eta$  range. *Accommodation* cases are more prevalent for lower  $\eta$  values (as more roughness favours surface islets) but fully disappear for  $\eta > 0.85$  where *intermediate* cases are mostly present, followed by *perfect-like* cases, the proportion of which increases while decreasing the surface roughness.

5. Influence of surface roughness on the deformation of gold nanoparticles in compression – 5.3. Results

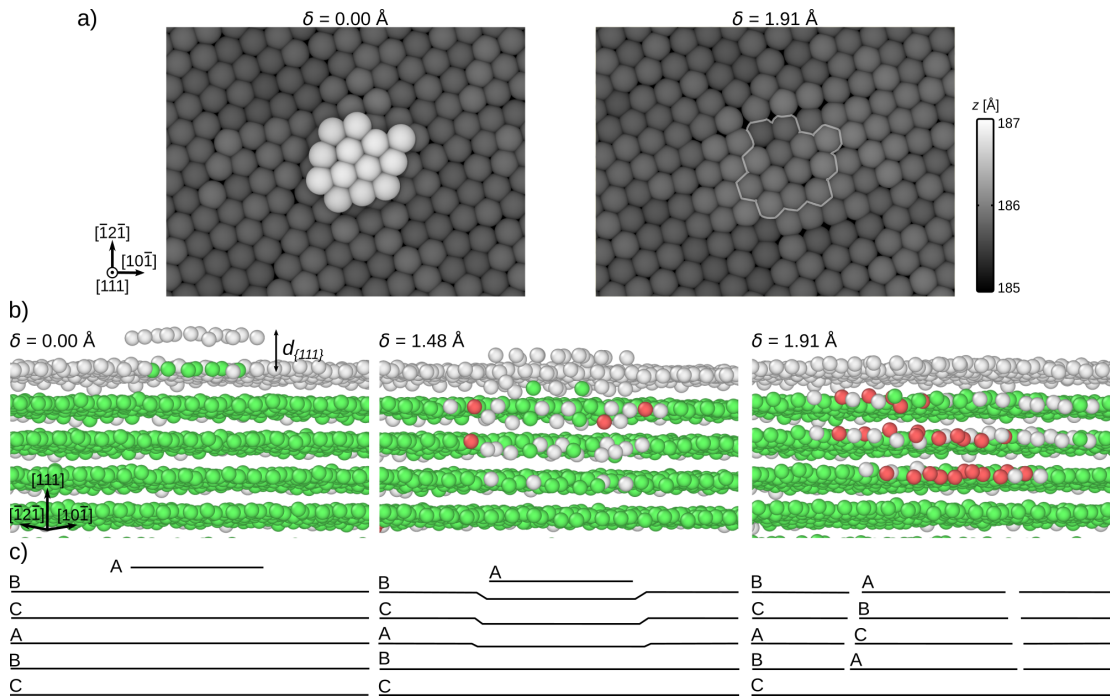


Figure 5.5.: Surface-islet penetration within the nanoparticle during compression, a) top surface view (atoms colored by height), b) cross-section. Atoms colored in green corresponds to FCC local environment, stacking-fault atoms are in red (HCP local environment) and atoms colored in light-grey corresponds to surfaces and other point defects, c) stacking sequence.

### 5.3.3. Deformation processes

As previously shown, surface roughness can drastically reduce the critical force at which metallic NPs yield. Indeed, surface terraces act as stress concentrators from which dislocation nucleate when the yield force is reached. This process is illustrated in Figure 5.6 where the von Mises stress per atom  $\sigma_M^i$  is emphasized just before the first plastic event happening in (i) a NP with flat surfaces and (ii) a ( $\eta=0.85$ ,  $C_1=0.5$ ) NP characterized by a load-displacement curve with the *intermediate* trend. For the flat-surface NP,  $\sigma_M^i$  spatial distribution is characterized by a lens-shaped symmetrical pattern right beneath the (111) top facet (similar to those shown in refs. [Mordehai et al. 2011a; Kiliyis et al. 2018; Amodeo and Pizzagalli 2021]) and a maximum value of about 8.64 GPa is measured close to an external vertex, at 8.5 Å under the top surface. For the NP with rough surfaces, the stress pattern is more asymmetric as following the rough surface topography and is localized right beneath a surface step. Also, the stress maximum (~8.56 GPa) is close but slightly lower than the one measured in the flat NP. Figure 5.6 also emphasizes the lack of stress concentration in the vicinity of lateral facets (besides the lateral surface steps) leading to an incipient plasticization process mainly confined below the contacting surface, where the external load is applied.

5. Influence of surface roughness on the deformation of gold nanoparticles in compression – 5.3. Results

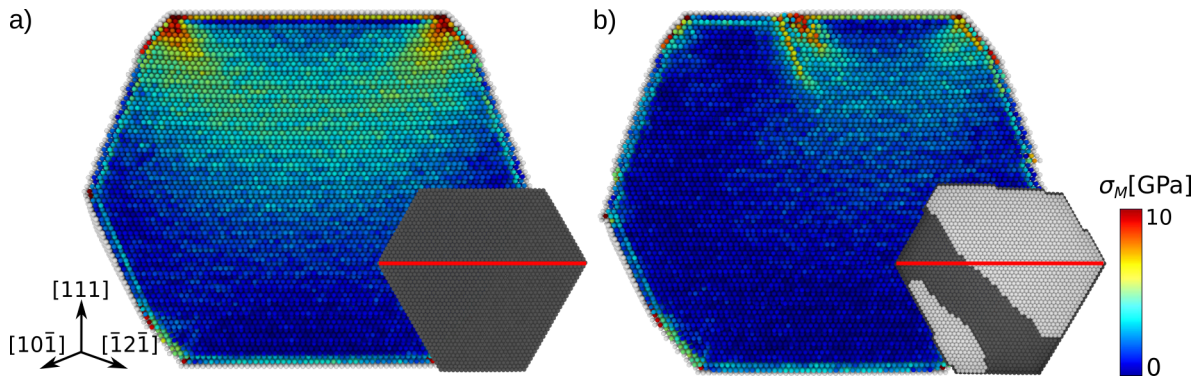


Figure 5.6.: Per atom von Mises stress stress  $\sigma_M^i$  in faceted-Au nanoparticles under compression at  $T=10$  K, cross-section view. Snapshots were taken ahead of the the first dislocation nucleation event in a) a nanoparticle with flat surfaces (*perfect* case) and b) a nanoparticle with rough surfaces ( $\eta=0.85$ ,  $C_1=0.5$ ), *intermediate* case. Insets illustrate the nanoparticle top surface where first-layer atoms are colored lighter than those below. Red lines illustrate main figure cross-section.

The Figure 5.7 illustrates an example of a first plastic event characterized in a ( $\eta=0.25$ ,  $C_1=0.5$ ) NP, *intermediate* load-displacement trend. In this case, a dislocation dissociated in the  $(\bar{1}\bar{1}1)$  plane nucleates at a critical displacement  $\delta_y=1.93$  Å from a one-layer depth atomic terrace that emerges at the edges of lateral facets (Figure 5.7a, c① and c②). The dislocation is made of a leading  $\frac{1}{6}[\bar{1}\bar{2}1](\bar{1}\bar{1}1)$  and a trailing  $\frac{1}{6}[\bar{1}\bar{1}2](\bar{1}\bar{1}1)$  Shockley partial dislocations separated by an intrinsic stacking-fault. After nucleation, the dislocation starts gliding through the NP while its emerging screw components shear the NP surface by zipping the surface steps (Figure 5.7 insets). This process contributes to the reduction of the NP's height and, consequently, to the load decrease, conditioned by the displacement-controlled character of the simulation, shown in Figure 5.7b up to a displacement of about 3.34 Å. Concurrently, a significant increase of the NP top surface area  $S$  from  $47.6$  nm $^2$  up to  $132.4$  nm $^2$  is noticed. At this stage,  $S$  closely approaches the area of a perfectly-flat NP top facet of about  $S^p=133.6$  nm $^2$ , which confirms that first plastic events mostly cancel one-layer surface steps resulting in a configuration akin to the *perfect* case. This justifies the particularly-high amplitude of the second force peaks shown in Figure 5.7b, close to the *perfect* case yield force ( $F_y=703$  nN, *c.a.*  $0.9F_y^p$ ). One notes that the emerging components of the dislocation strictly follow the surface step during the shearing process which implies the cross-slip of a portion of the dislocation into the  $(\bar{1}\bar{1}1)$  plane, as shown in Figure 5.7c③.

However, cross-slip is not the sole original dislocation process influenced by surface roughness. Figure 5.8 depicts the first dislocation nucleation process in a ( $\eta=0.75$ ,  $C_1=0.5$ ) NP (*intermediate* load-displacement trend). Here, we look at the dislocation nucleation process from the inside of the NP from where surface steps oriented along the  $[0\bar{1}1]$ ,  $[10\bar{1}]$ ,  $[1\bar{1}0]$  and  $[2\bar{1}\bar{1}]$  directions are identified. While the yield of the NP

5. Influence of surface roughness on the deformation of gold nanoparticles in compression – 5.3. Results

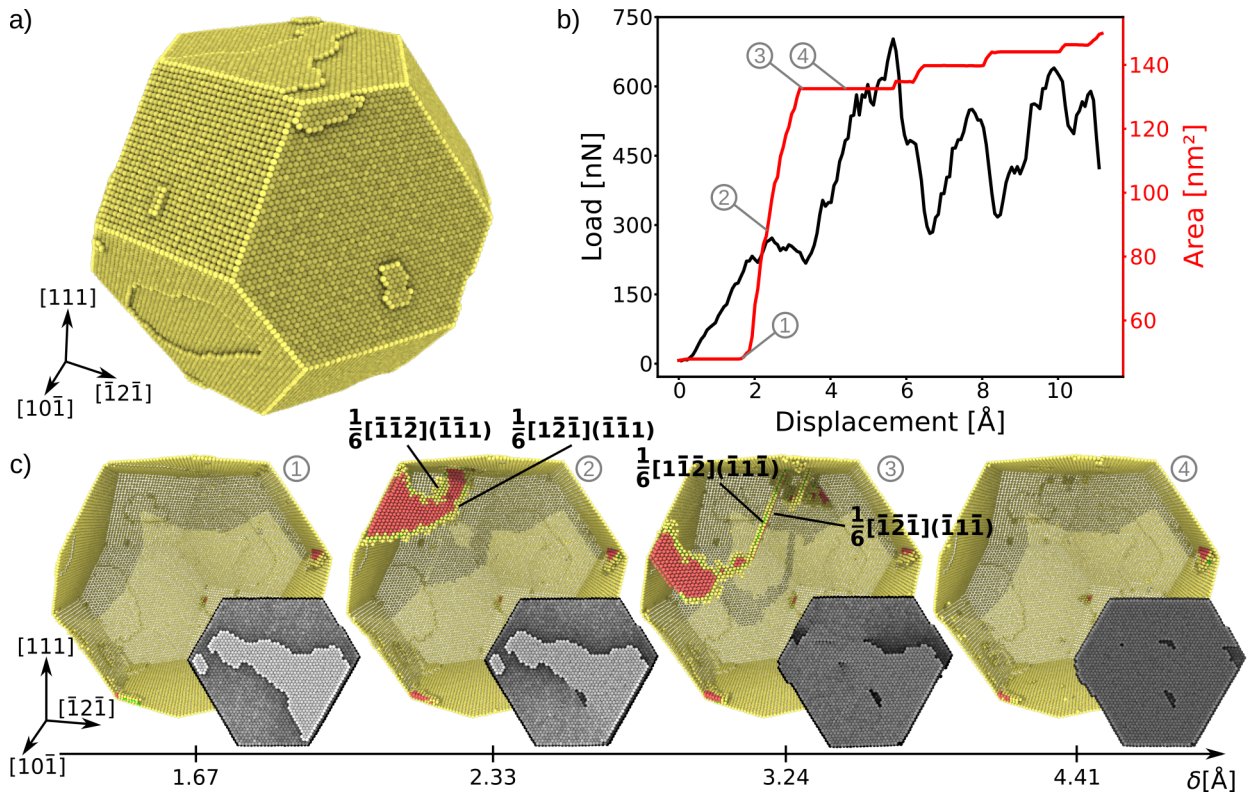


Figure 5.7.: Dislocation nucleation in a faceted-Au NP with rough surfaces ( $\eta=0.25$ ,  $C_1=0.5$ ) under compression at  $T=300$  K. a) initial sample (after equilibration), b) load-displacement curve and top surface area evolution, c) dislocation nucleation process for displacements between 1.67 and 4.41 Å. Surface and partial dislocation core atoms are colored in yellow, atoms in the stacking-fault are colored in red. Perfect crystal atoms are removed for the sake of clarity. Insets show the evolution of the top surface ledge during the dislocation nucleation/propagation process.

is characterized by the nucleation of regular  $1/2<110>\{111\}$  dislocations (colored in green), one can also identify the nucleation of dislocation in the  $\{001\}$  crystallographic planes (colored in blue). This is for example the case in Figures 5.8e,f where a  $1/2[\bar{1}0\bar{1}](0\bar{1}\bar{0})$  dislocation nucleates after a short period during which two  $1/2<110>\{111\}$  dislocations were pinned at the ends of a  $[2\bar{1}\bar{1}]$ -oriented surface step. These new dislocations have  $1/2<110>$  Burgers vectors and are only observed in the cases of rough surface NPs accommodating both particular ledge directions and stress field. Finally, one can notice that, again in this case, the nucleation of the various dislocations allows the withdrawal of the original one-layer surface steps, at the top of the NP.

5. Influence of surface roughness on the deformation of gold nanoparticles in compression – 5.4. Discussion

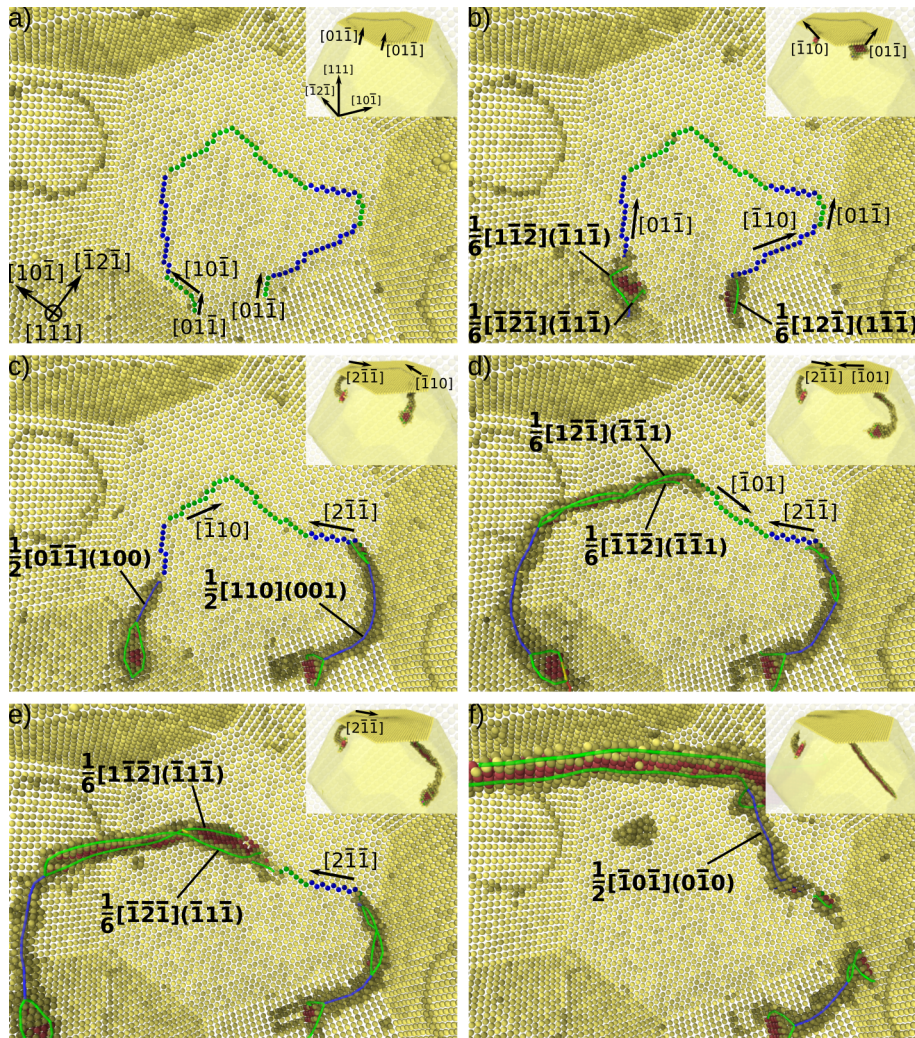


Figure 5.8.: Dislocation nucleation in a faceted-Au NP with rough surfaces ( $\eta=0.75$ ,  $C_1=0.5$ ) under compression at  $T=300$  K, a)  $\delta=3.63$  Å, b)  $\delta=4.18$  Å, c)  $\delta=4.74$  Å, d)  $\delta=5.19$  Å, e)  $\delta=5.58$  Å and f)  $\delta=6.97$  Å. View from the inside of the nanoparticle from which perfect crystal atoms are removed for the sake of clarity. Dislocations in  $\{110\}$  and  $\{001\}$  slip planes are colored in green and blue, respectively. Same colors are used to identify corresponding surface steps.

## 5.4. Discussion

### 5.4.1. Effect of roughness on the strength

Surface roughness influences both the mechanical response of nanocrystals and their relative elementary deformation processes. As shown in Figure 5.7, single-layer surface steps drastically reduce the yield force  $F_y$  of faceted-Au NPs while changing dislocation nucleation centre locations from NP top surface edges to ledges. It is

5. Influence of surface roughness on the deformation of gold nanoparticles in compression – 5.4. Discussion

well-known that dislocation plasticity is a dissipative process and, here, the energy drop computed during the first dislocation nucleation event is lower in amplitude in case of NPs with rough surfaces when compared to the perfect case. Figure 5.9 shows the boxplot distribution of potential energy drop  $\Delta E_p$  normalized by the number of atoms for every rough sample, at the onset of the initial plastic event. These results are compared to values obtained in the *perfect* case. A significant decrease of the required  $\Delta E_p$  to initiate plastic deformation is observed at any  $\eta$ . We believe that the relative difference in energy dissipation is due to the surface ledge correction in case of rough surface NPs as compared to the creation of fresh surface steps in originally pristine NPs. These observations corroborate previous results on the influence of surface steps on the dislocation nucleation process for which various models can be found in refs. [Brochard et al. 2000a; Hirel et al. 2007; Hara et al. 2009; Lu et al. 2012].

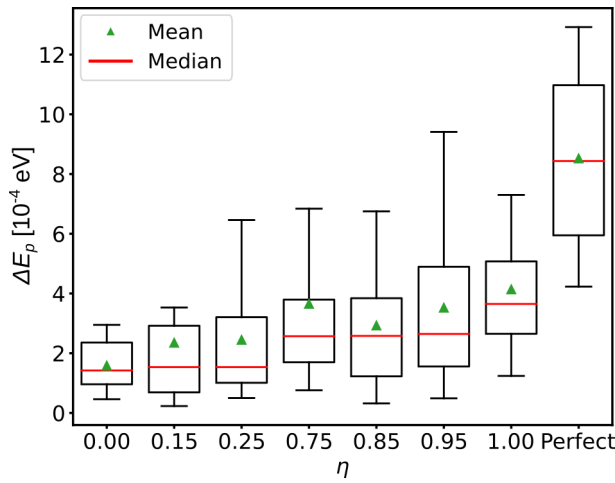


Figure 5.9.: Per atom potential energy drop at the first dislocation nucleation event, as a function of  $\eta$  (20 simulations for each  $\eta$ ), as compared to the *Perfect* cases.

The gradual disappearance of surface steps while dislocations nucleate and the topology of the first dislocations are closely related, with the top surface height morphology driving the original type of defect that nucleates and its motion. Indeed, we observed that dislocations can change their original glide direction and slip plane to follow the surface topography via the cross-slip of screw dislocation portions, below the surface. This process can lead to anomalous slip as, *e.g.* in uncommon  $1/2<110>\{001\}$  slip systems (see Figure 5.8), in a similar manner to what was recently observed in Bragg coherent X-ray diffraction imaging experiments performed on platinum NPs [Richard et al. 2023]. While such a peculiar behaviour is the result of a complex combination of surface step direction, primary *vs.* cross-slip planes, Burgers vectors and local stress, one can note that a simple Schmid factor analysis also corroborates the results. A particularly high Schmid factor ( $m=0.47$ ) exists in the  $1/2[0\bar{1}\bar{1}](100)$  slip system (see Figure 5.8c) while the maximum Schmid factor for a  $1/6<112>\{111\}$  dislocation under compression along [111] is  $m=0.31$ , even though in

5. Influence of surface roughness on the deformation of gold nanoparticles in compression – 5.4. Discussion

our case the stress field is heterogeneously distributed within the sample.

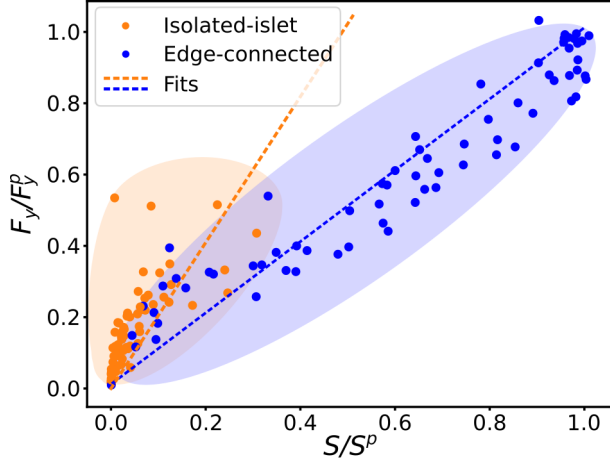


Figure 5.10.: Rough surface nanoparticle yield force  $F_y$  vs. (initial) top surface area  $S$ , both respectively normalized by mean  $F_y^p$  and  $S^p$  associated to flat-surface NPs. Blue symbols: edge-connected top surface cases, orange symbols: isolated-islet cases. Colored dashed-lines aim for linear regressions within the two domains with  $F_y/F_y^p=0.95S/S^p$  and  $F_y/F_y^p=2.08S/S^p$ , respectively.

The main objective of this chapter is to quantify the impact of surface roughness on the critical strength of metal NPs. Figure 5.10 illustrates the variations of the yield force  $F_y$  of NPs with rough surfaces as a function of the initial contact surface  $S$ , both respectively normalized by  $F_y^p$  and  $S^p$ , mean data derived from the NP with flat surface (*perfect* case). One can easily identify two regimes from the data set: 1) for larger  $S/S^p$ ,  $F_y/F_y^p$  follows a linear trend with fairly low dispersion and a slope near to 1 and 2) for  $S/S^p$  lower than about 1/3, the dispersion increases decreasing the normalized contact surface until  $F_y/F_y^p$  resumes again a linear dependence with a larger slope than in the aforementioned regime. A more detailed analysis of the contact surfaces shows that the two regimes are due to the propensity of the surface top layer to be connected (or not) to a lateral edge. Thus, two cases are identified and illustrated in Figure 5.11a and b. On the one hand, the top layer is fully disconnected from the lateral surface (Figure 5.11a) leading to the formation of one or few *isolated-islets* of atoms. On the other hand, the top layer is connected to a lateral facet via an edge (Figure 5.11b) which will be called *edge-connected* in the following. Note that samples characterized by top surface isolated-islets and edge-connected surfaces are plotted in orange and blue, respectively, in the Figure 5.10. Adjusting the corresponding data using a least squares fitting procedure [Vugrin et al. 2007], a linear dependency of the edge-connected dataset with a slope of 0.95 is confirmed while the isolated-islet dataset is characterized by a slope of 2.08, slightly more than doubled. In both regimes, the linear dependency between  $F_y/F_y^p$  and  $S/S^p$  shows that the critical force  $F_y$  to nucleate a dislocation scales with the evolution of the contact surface area  $S$  (imposed

## 5. Influence of surface roughness on the deformation of gold nanoparticles in compression – 5.4. Discussion

by the first-top layer and computed using the protocol described in section 2.2.2) and  $\eta$ , without changes in the critical compressive stress ( $\sigma_y=F_y/S$ ) or shear stress. Nevertheless, the slope variation emphasizes an evolution of the dislocation nucleation process. On the one hand, the dislocation nucleus has a half-loop shape when nucleating from an isolated islet, for low  $S/S^P$ , as illustrated in Figure 5.11a,c. Otherwise, in case of edge-connected (large  $S/S^P$ ), the nucleation areas are always located nearby a lateral edge. Consequently, dislocation nuclei in this case have one tip lying on a lateral facet while the second one is attached to the top rough surface. Such a configuration leads to the nucleation of a quarter-loop dislocation as shown e.g., Figure 5.11b,d. This process is particularly similar to the one occurring in flat-surface NPs. No significant differences in terms of dislocation radii were noticed with e.g.,  $r_{1/4}=9.18$  Å and  $r_{1/2}=9.24$  Å for the two dislocations illustrated in Figure 5.11, respectively. Also, maximum shear stresses are particularly close in the both cases amounting to 6.18 GPa (isolated-islet case) and 6.09 GPa (connected-edge case).

Several studies focusing on the nanocompression of faceted-Au NPs with perfectly flat surfaces illustrate the nucleation of dislocation quarter-loops that further extend during compression [Mordehai et al. 2011b; Feruz and Mordehai 2016; Iteney et al. 2023]. Owing the dislocation shape (quarter- vs. half-loop) observed here, the linear-dependency of the dislocation energy and the force increase of about a factor of 2 between the two regimes while showing particularly close critical dislocation radii, we believe that the yield-force increase computed in the isolated-islet regime is purely a dislocation size-effect that does not rely on a possible variation of the stress state associated to the surface step topology.

### 5.4.2. Nucleation model in case of rough surfaces

$\eta$  impacts dramatically the yield force  $F_y$  but only weakly the critical compressive stress  $\sigma_y$  as soon as it is defined using the detailed contact surface  $S$  i.e., the one that accounts for isolated-islets and connected-edge domains. Nevertheless, such a detailed description of  $S$  is generally not accounted in nanomechanical experiments that usually rely on effective flat surfaces (that we can approximate here to  $S^P$ ), due to insufficient resolution or 2D projections. In these conditions, the effective critical compressive stress measured in the experiment  $\sigma_y^*=F_y/S^P$  is directly impacted by the surface roughness. To propose a predictive model of  $\sigma_y^*$ , one can define the contact surface fraction  $\phi=S/S^P$ . Whereas  $\phi$  can be retrieved using atomic force microscopy in the experiment, it is computed using  $h(x, y)$  definition as,

$$\phi = \frac{1}{S^P} \iint h(x, y) \cdot \theta[h(x, y) - (h_{max} - h_{cut})] dx dy \quad (5.2)$$

where  $h_{max}$  is the maximum of the height distribution,  $h_{cut}$  is a cut-off distance set here as half the {111} interplanar distance ( $h_{cut}=1.18$  Å) and  $\theta$  is the Heaviside step function defined as  $\theta(\lambda) = 0$  if  $\lambda < 0$  and  $\theta(\lambda) = 1$  if  $\lambda \geq 0$ . Owing to the sole

5. Influence of surface roughness on the deformation of gold nanoparticles in compression – 5.4. Discussion

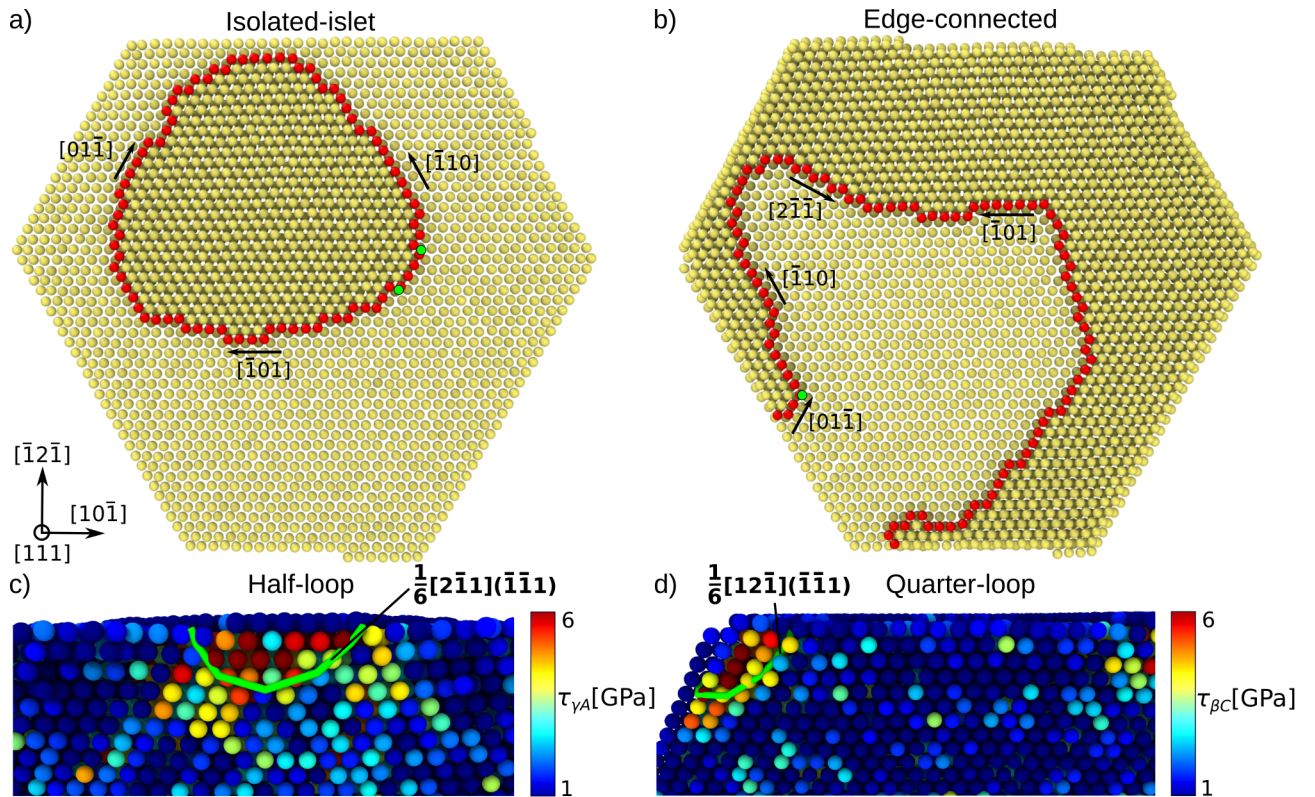


Figure 5.11.: Influence of the contact surface configuration (isolated-islet or edge-connected) on the dislocation nucleation process, a,b) contact surface: a) isolated-islet and b) edge-connected configurations, top view. Surface step atoms are highlighted in red and green dots emphasize dislocation nucleation emerging segment locations, c,d) shear stress per atom computed in the partial slip system in which the first Shockley partial dislocation nucleates. Cross-section view normal to the slip plane identified using the Thomson tetrahedron notation. The atomic configuration is captured few steps before the first plastic event, while the latter critical dislocation configuration (colored in green) that corresponds respectively to c) an half- and d) a quarter-loop, is superimposed for the sake of clarity.

critical compressive stress  $\sigma_y^p$  in the case of a perfectly flat NPs, the effective critical compressive stress is defined as,

$$\sigma_y^* = \chi \cdot \phi \cdot \sigma_y^p \quad (5.3)$$

with  $\chi$  being a contact shape factor equal to 1 (edge-connected case) or 2 (isolated-islet case) and  $\sigma_y^p = 6.20$  GPa is averaged over the 20 compression tests modeled using a perfectly-flat NP. Note that this latter can also be retrieved from nanocompression experiments or from theory.

5. Influence of surface roughness on the deformation of gold nanoparticles in compression – 5.4. Discussion

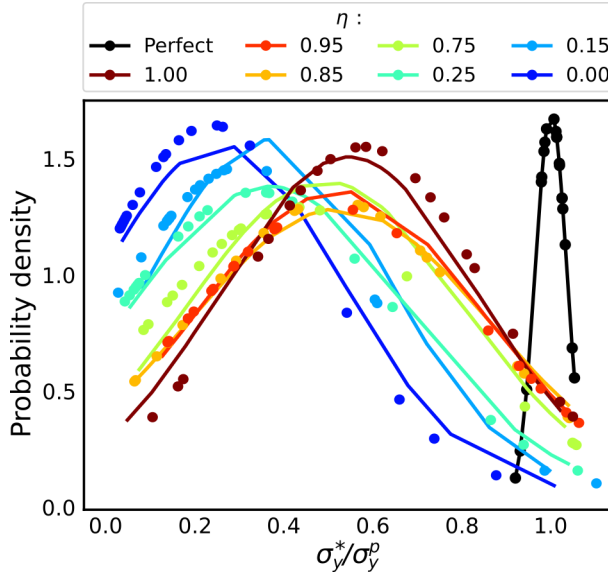


Figure 5.12.: Effective critical compressive stress  $\sigma_y^*$  distribution normalized by the perfect case yield strength  $\sigma_y^p$  as a function of  $\eta$ . Symbols: MD simulations, curves: model (Equation 5.3). For the sake of visibility, the probability density function of the *perfect* case is reduced by a factor of 6.67.

In Figure 5.12, the  $\sigma_y^*$  model relies on the whole set of height distribution  $h(x, y)$  used in the MD nanocompression simulations described in the previous section. Results show that model  $\sigma_y^*/\sigma_y^p$  compares with a satisfactory agreement with data extracted from MD nanocompression simulations and both are characterized by the similar tendency, *i.e.* the rougher, the weaker. Note that minor discrepancies still exist. We believe that they could be related to surface topological details, such as the surface step orientation and density, and temperature-induced stochastic effects. Mean  $\mu$  and standard deviation  $s$  of  $\sigma_y^*/\sigma_y^p$  distribution for simulation and model are presented in Table 5.1 as a function of the roughness exponent. While the *perfect* case is characterized by a particularly narrow distribution centered around  $\sigma_y^*/\sigma_y^p=1$ , samples with rough surfaces show wider distributions shifted towards lower  $\sigma_y^*/\sigma_y^p$ . Extreme cases  $\eta=0.00$  and  $\eta=0.25$  show distributions centered around extreme low  $\sigma_y^*/\sigma_y^p$  of 0.22 and 0.32, respectively. One notes that a significant decrease of NP strength is still noticed in the smoothest cases (see *e.g.*,  $\eta=0.95$  and  $\eta=1.00$ ), with statistical distributions centered around  $\sigma_y^*/\sigma_y^p \sim 0.50$ . This confirms that even fairly-low surface roughness induces large critical stress variations when compared to the perfect case, with a decrease that can reach up to 90% of  $\sigma_y^p$ . Finally, the abrupt transition from a narrow to a broad critical strength distribution confirms that roughness is the source of significant data scattering (well beyond temperature fluctuations) whatever its level.

Table 5.1.: Mean  $\mu$  and standard deviation  $s$  of  $\sigma_y^*/\sigma_y^p$  distributions obtained by MD simulations ( $\mu_S$  and  $s_S$ ) and model Equation 5.3 ( $\mu_M$  and  $s_M$ ).

		$\eta$						
		0.00	0.15	0.25	0.75	0.85	0.95	1.00
$C_1 = 0.5$	$\mu_S$	0.22	0.29	0.32	0.41	0.49	0.49	0.56
	$\mu_M$	0.24	0.34	0.34	0.47	0.50	0.50	0.52
	$s_S$	0.25	0.29	0.31	0.33	0.32	0.33	0.27
	$s_M$	0.27	0.27	0.31	0.31	0.34	0.32	0.28
$C_1 = 1.2$	$\mu_S$	0.10	0.12	0.12	0.19	0.17	0.24	0.22
	$\mu_M$	0.11	0.13	0.13	0.20	0.18	0.27	0.21
	$s_S$	0.09	0.11	0.12	0.15	0.16	0.21	0.16
	$s_M$	0.08	0.11	0.12	0.15	0.15	0.20	0.17

### 5.4.3. Towards multi-layer roughness

While investigating the mechanical response of rough surface NPs (Figure 5.4), we observed that secondary force peaks were in the same range as the *perfect* case primary's. This result was attributed to a resorption process of the single-layer surface step induced by the nucleation and propagation of the first dislocations which made the NP pristine again. To investigate further the influence of surface roughness, additional simulations involving larger height distributions (see Figure 5.13a) are presented in the following with NPs population characterized by  $C_1=1.2$  and same  $\eta$  range. Figure 5.13 summarizes the simulation results where *intermediate* and *accommodation* cases can still be observed (as in the single-layer surface step case) at variance with the *perfect-like* regime. This behaviour is due to the larger amplitude of  $h(x, y)$  which favors smaller contact surface areas and thus, an even more pronounced effect of roughness on the mechanical response as confirmed by the shift of  $\sigma_y^*/\sigma_y^p$  distributions towards lower values (Figure 5.13c, Table 5.1). In this case, the cut-off distance from Equation 5.2 is set equal to 1.18 Å, similar to the  $C_1 = 0.5$  corresponding study, to account for the contact surface area. This demonstrates that atomic steps from subsequent rough layers do not impact the strength of NPs. However, this assertion might no longer hold true for larger size structures, necessitating further investigation. Also, secondary load peaks illustrated in Figure 5.13b are of lower amplitude, *i.e.* they mostly reach intermediate values below primary force peaks, as another consequence of  $C_1$  variation. The evolution of the dislocation behavior under the indenter is also influenced by the presence of numerous surface steps and terraces at various heights.

As for the  $C_1=0.5$  case, dislocations nucleate from a surface step, however, they interact here with subsequent steps in the underlying atomic layers. As illustrated in Figure 5.14, several scenarios emerge including: i) neighboring atomic steps serving as anchor points for dislocations that impede locally the dislocation microstructure growth during compression while promoting the nucleation of dislocation from other

5. Influence of surface roughness on the deformation of gold nanoparticles in compression – 5.4. Discussion

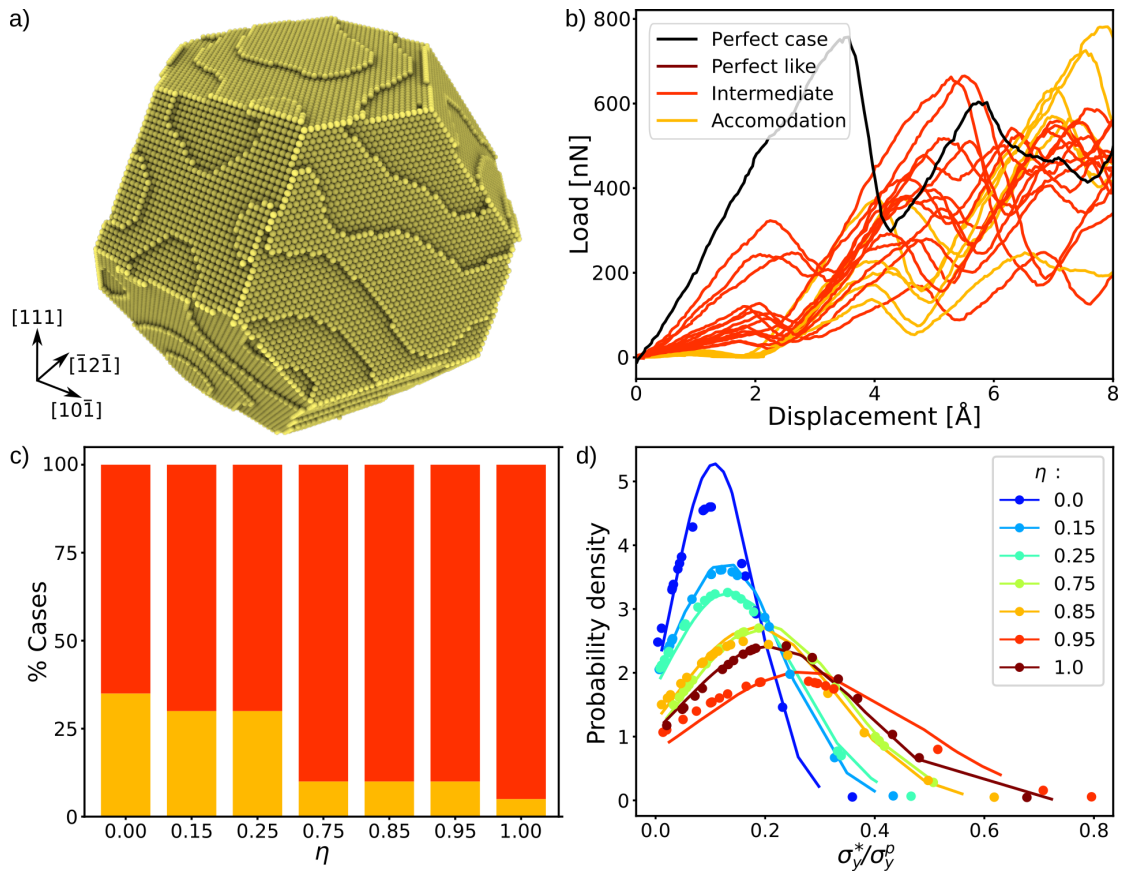


Figure 5.13.: MD nanocompression of Au-faceted nanoparticles with wide surface roughness ( $C_1=1.2$ ), a) example of nanoparticle ( $\eta=0.75$ ), b) examples of load *vs.* displacement curves for  $\eta=0.25$ . The *perfect case*, *perfect-like*, *intermediate* and *accommodation* trends are illustrated in black, brown, red and yellow, respectively, c) Sample fraction distribution among *intermediate* and *accommodation* cases as a function of  $\eta$  (no *Perfect-like* case), d) normalized effective critical compressive stress  $\sigma_y^*$  distributions as a function of  $\eta$ . Symbols: MD simulations, curves: model (Equation 5.3).

locations (Figure 5.14a), ii) surface-step reconstruction induced by dislocation shearing (Figure 5.14b) or iii) a combination of both processes, *i.e.* part of the dislocation configuration under the indenter being blocked by a surface ledge while the other develops and shears a nearby surface ledge (Figure 5.14c). In this last case, the moving dislocation exerts a driving force on the rest of the emerging dislocation microstructure which unpins and concurrently gets absorbed by the closest lateral facet. Note that the case where a dislocation nucleates and moves out of the sample without contact reaction with nearby surface steps (typical of  $C_1=0.5$ ) is also observed for  $C_1=1.2$ .

5. Influence of surface roughness on the deformation of gold nanoparticles in compression – 5.5. Conclusion

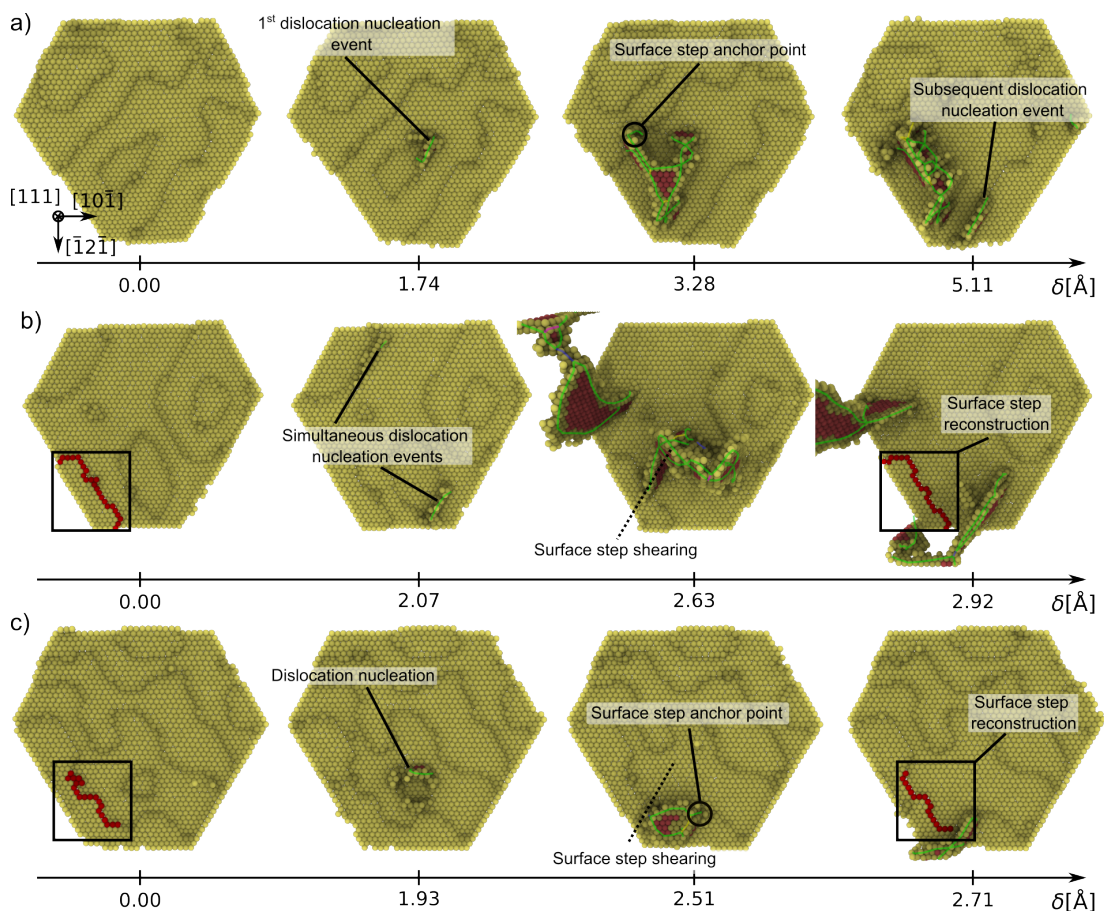


Figure 5.14.: Examples of emerging dislocation microstructure evolution during MD nanocompression of Au-faceted nanoparticles with wide surface roughness ( $C_1=1.2$ ), a) surface step acting as an anchor point that impedes the further growth of the first dislocation promoting new nucleation event elsewhere on the surface, b) surface reconstruction induced by a dislocation shearing the surface ledge. One can note in this case the simultaneous nucleation of at least two dislocations, c) combination of both processes. View from below the top surface of the nanoparticle. Atoms colored in red denote zones of interest in case of surface ledge reconstruction induced by dislocation shearing.

## 5.5. Conclusion

MD mechanics simulations of NOs are often based on simplistic designs made of flat facets and sharp edges or corners without considering the impact of these approximations on the sample strength and elementary deformation processes. In line with the recent studies that emphasized the role of NPs shape on the mechanical properties [Amodeo and Lizoul 2017; Kilymis et al. 2018; Sharma et al. 2018], we design here *in silico* NPs with rough surfaces that more rigorously describe the surface topology

## 5. Influence of surface roughness on the deformation of gold nanoparticles in compression – 5.5. Conclusion

of metal or semi-conductor NPs used in experiments. Here we show that even the smallest roughness (associated with a large roughness exponent) dramatically impacts the sample critical strength that can decrease by almost 90% for the roughest systems, when compared to the mean strength of flat-surface samples. This result provides some clues to explain the data scattering regularly observed in nanoscale experiments, which can vary by one order of magnitude for critical stresses. Also, the numerous simulations performed allow to confirm that the yield force perfectly scales with the contact surface topography *i.e.*, the fraction of atoms in contact with an indenter, bearing in mind a scaling factor transition from 1 to 2 for smaller contact regions where the shape of the first dislocation nucleated transits from a half- (isolated-islet regime) to a quarter-loop (edge-connected regime). Our statistical approach allowed to design a model for strength dispersion predictions in case of a sample with rough surfaces which only relies on two ingredients as main inputs *i.e.*, 1) the characterisation of the top surface and 2) the ideal strength of the system, both of which can be deduced from experiment or theory. In addition, surface roughness has been shown to be at the roots of exotic deformation processes in Au FCC metal NPs including dislocation nucleation and glide in uncommon slip systems which may explain the recent experimental observations. In the future, more of these phenomena might be identified using *e.g.*, machine learning approaches, and new ideas based on surface topology characterization at the nanoscale are currently under investigation in order to better describe the mechanical properties of NOs in the experiments.

### **Chapter V summary:**

**This chapter focuses on the study of the influence of surface roughness on the strength of Au NPs in compression. First, we have introduced the sample preparation and simulation protocol, using *Pyrough* as the main tool for the generation of atomic position files. Then, the mechanical properties of NPs with rough surfaces as compared to perfect samples are discussed. Finally, a model for the prediction of strength distributions at given ( $\eta, C_1$ ) is proposed. It takes the initial contact surface fraction into account as an input, as well as the ideal strength of the NP.**

# 6

## **Surface oxide layer : growth dynamics and influence on nanoindentation**

This chapter focuses on the influence of the presence of a thin oxide layer on the mechanical properties of metal NOs. With a combination of experimental and numerical studies, first insights into the reduction and oxidation conditions for metal samples are given, with the aim of conducting mechanical tests on both oxidized and non-oxidized NOs. Furthermore, we study the impact of surface roughness on the oxide growth kinetics. Additionally, a study to assess the influence of an oxide layer on the mechanical response of NOs under indentation is performed, providing initial insights into the deformation processes involved, as compared to non-oxidized samples.

## 6.1. Introduction

The oxidation of metal alloy surfaces has been studied for a long time [Cabrera and Mott 1949; Atkinson 1985] and is crucial for various applications spanning from micro-electronics and heterogeneous catalysis to wear and corrosion protection. Numerous experimental studies have focused on understanding the processes involved in metal oxidation. Some research groups have investigated the mechanism and kinetics of metal oxide growth [Atkinson et al. 1982; Jeurgens et al. 1999], while others have explored the reaction of O<sub>2</sub> molecules with metal surfaces [Yamazoe et al. 1979; Kulkarni et al. 1995; Benka and Steinbatz 2003], as well as the initial adsorption and diffusion of oxygen atoms [Narusawa et al. 1981; Matsumoto et al. 2001; Chevalier et al. 2005]. While numerous experimental studies have characterized the formation mechanism and microstructure of oxide films, many questions regarding the elementary processes at the atomic scale remain open. From a mechanical perspective, although it is well-established that surfaces play a key role in elementary deformation processes at the nanoscale, only a limited number of studies have addressed the potential influence of an oxide layer on the strength of NOs. Thin film nanoindentation experiments have shown, for instance, that an oxide layer on top of a pure metal substrate significantly affects its mechanical properties [Chechenin et al. 1995; Pang and Bahr 2001; Li et al. 2016b]. Additionally, due to the heterogeneous growth processes, the mechanical behavior and strength might depend on the location of the solicitation [Morasch and Bahr 2005]. However, no experimental study has specifically investigated this potential bias and its effect on the strength of metal NOs such as NPs or NWs. This represents a clear gap, especially when considering recent findings in mechanical tests that show or mention the presence of an oxide layer around most of reactive metal NPs [Han et al. 2015; Kositski et al. 2016; Sharma et al. 2018; Sharma et al. 2020]. Thus, how does oxide surface layer influences the mechanical properties and elementary processes of reactive metal NPs under compression ? With advancements in computer modeling, it is now possible to consider interactions between metals and oxygen using methods like ReaxFF interatomic potentials, thereby enabling a wide range of numerical investigations. MD or DFT algorithms have significantly advanced our understanding of primary oxide growth mechanisms in metals [Zhang et al. 2001a; Balbuena et al. 2004; Garruchet et al. 2010; Gattinoni and Michaelides 2015]. Furthermore, samples featuring surface oxide overlayers have been subjected to tensile or nanoindentation tests, and results show the impact on the strength and deformation mechanisms [Sen et al. 2014; Aral et al. 2016; Aral et al. 2019; Luu et al. 2022]. In the context of this PhD, it is worth noting that the influence of surface oxide layer on the mechanical properties of metal NPs remains unexplored, which presents a field for potential new investigations. In this chapter, we first present an experimental study that focuses on the oxidation and reduction of Ni NPs. This exploration aims to establish preliminary insights into the experimental conditions required for mechanical tests and the study of the impact of an oxide layer on the strength of NOs. Then, we conduct a MD simulation campaign to compare and discuss the experiments. Finally, MD virtual nanoindentation tests are carried out to provide initial insights into the influence of an oxide layer on the

strength of metal samples.

## 6.2. Experimental observations of metal nanoparticle oxidation

Here we investigate the oxidation and reduction of metallic NPs using the Titan ETEM of the INSA-Lyon CLYM laboratory. This set of experiments is a first step towards the mechanical characterization of oxidized or non-oxidized metallic NPs. The goal is to quantify how much a reactive metallic nanocrystal can be reduced or oxidized or under which conditions it can be assumed as non-oxidized before it is affecting the nanomechanical response. Ni NPs fabricated via solid-state dewetting are used as oxidation-sensitive model nanostructure.

### 6.2.1. Sample preparation and preliminary characterization

Ni NPs were prepared by Pr. Eugen Rabkin and his group from Technion Institute, Israël, using the solid-state dewetting method [Gentili et al. 2012; Leroy et al. 2016; Preston et al. 2019]. Every protochips were first plasma cleaned (2 min, 100 W, 200 mTorr Oxygen) before the deposition of a 4.1-4.4 nm Ni layer. Then, samples were dewetted using a rapid thermal anneal process: 1h at 1000°C (heating rate of 1°C/s) in reducing atmosphere (Ar-10%H 5N). Unfortunately, for some of the protochips, electrical connections were missing after annealing and some others were damaged during manipulations, preventing from further heating often required to conduct oxido-reduction experiments.

For the remaining samples, preliminary TEM observations were performed. Figure 6.1 shows a widespread distribution of NP sizes including NPs with diameter of 30-40 nm and a lot of sub-nanometric particles or atoms agglomerates. Additionally, two different shapes of NPs were identified, including spherical and faceted. Several NPs with planar defects (stacking-faults and twins) and/or with a 3-4 nm crystalline shell, identified as a native NiO oxide, were observed. Moreover, many NPs were embedded in an amorphous agglomerate that could not be easily removed. Neither plasma cleaning nor oxidation worked but an irradiation under e-beam seemed to remove the amorphous shell. We believe this agglomerate was related to the carbon contamination of the furnace during the preparation phase as it was mentioned by Pr. Eugen Rabkin before the sample delivery.

### 6.2.2. Environmental microscope oxido-reduction of Ni nanoparticles

After preliminary characterization, an initial heating phase up to 300°C by step of 100°C with 5 min constant temperature plateau was performed. The oxygen pressure

6. Surface oxide layer : growth dynamics and influence on nanoindentation – 6.2.  
Experimental observations of metal nanoparticle oxidation

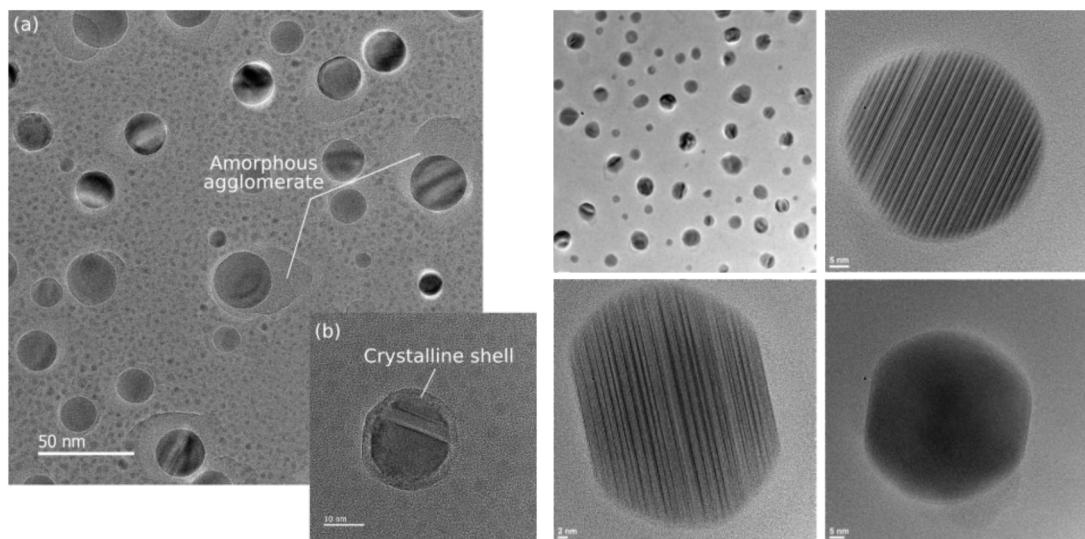


Figure 6.1.: Preliminary TEM imaging of Ni NPs processed by the dewetting method. Various sizes and shapes are observed and parts of them are encapsulated in an amorphous or crystalline shell.

was set as  $P_{O_2} = 10^{-3}$  mbar during the entire phase. As shown in Figure 6.2a-b, no further oxidation of the native oxide was observed. At this point, the oxygen pressure was increased at  $P_{O_2} = 0.5$  mbar. Here, pre-oxidized NPs start to oxidize further, as shown in Figure 6.2c. The effect becomes particularly noticeable after several tens of minutes, where the additional oxide layer appears rougher and amorphous, compared to the native oxide. Thus, re-oxidizing NPs with native oxide shell does not lead to homogeneous oxide growth but rather to an irregular thickening of the pre-existing layer. At this stage, the temperature was then returned to room temperature.

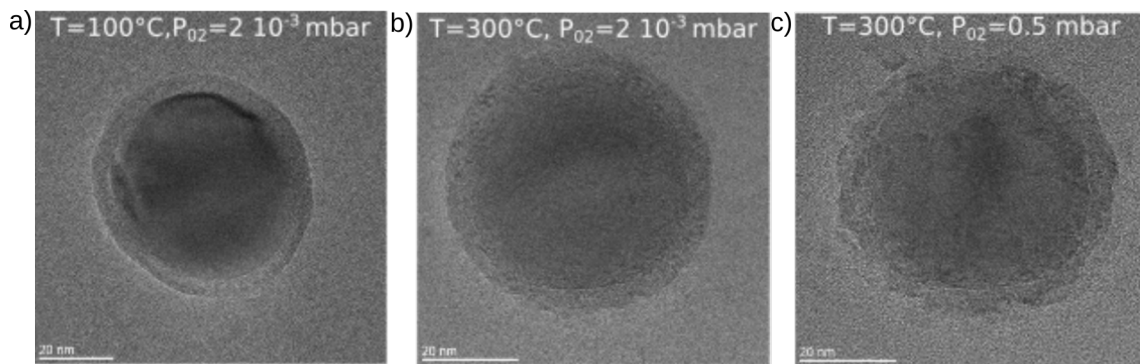


Figure 6.2.: Oxidation of an Ni NP with native oxide. a) Original NP with native oxide at a)  $100^\circ\text{C}$  and b)  $300^\circ\text{C}$ . c) Growth of a rough secondary oxide shell at  $300^\circ\text{C}$  when  $P_{O_2}$  is increased to 0.5 mbar.

The reduction phase of the oxide shell was performed by injecting  $\text{H}_2$  at  $P_{H_2} = 1.3$  mbar. The temperature was increased by successive  $50^\circ\text{C}$  plateaus that were main-

## 6. Surface oxide layer : growth dynamics and influence on nanoindentation – 6.2. Experimental observations of metal nanoparticle oxidation

tained for 2 min. Nothing happened up to 200°C where the smaller NPs started to reduce. All of the NPs were reduced at 350 °C which led to the end of the reduction phase. An example of a reduced Ni NP is shown in Figure 6.3a. These conditions can be selected for a quick reduction mode assuming the size of the NPs we have here.

Draining the hydrogen, setting a low pressure of oxygen of  $P_{O_2} = 2.10^{-4}$  mbar, and cooling the sample to room temperature leads to the instantaneous reoxidation of the NPs characterized by a similar 3-4 nm NiO crystalline shell (see Figure 6.3b).

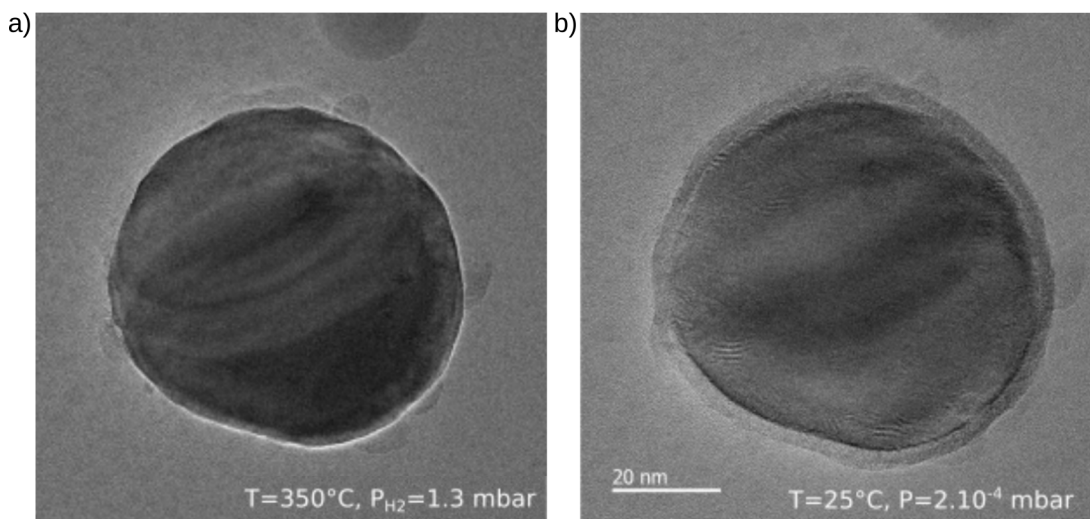


Figure 6.3.: Flash reduction and re-oxidation of a Ni NP. a) Some residues of the native oxide are still observable and b) the native oxide is fully rebuilt in high vacuum.

### 6.2.3. Main experimental outcomes

With the use of ETEM, the experimental campaign lead to various outcomes in terms of Ni oxidation and reduction conditions.

- Ni NPs are systematically covered by a crystalline native NiO layer. In the case of 30-40 nm NPs, its thickness is about 3-4 nm.
- Reduction of the crystalline 3-4 nm Ni shell at  $P_{H_2} = 1.2$  mbar occurs at a temperature in the range 200-400 °C depending on the size of the NPs. This process leads to oxide-free NPs.
- Reduced Ni NPs oxidize instantaneously even in the residual vacuum of the microscope. Similarly, the NPs fully re-oxidize in air, for instance during lunch breaks when dismounted from the ETEM, resulting in the same 3-4 nm layer thickness. Hence, no quantitative analysis of the oxide growth kinetics was conducted due to the rapid pace of the process.

## 6. Surface oxide layer : growth dynamics and influence on nanoindentation – 6.3. Numerical study of oxide growth on metal at the nanoscale

- Oxidized NPs can be further oxidized using  $P_{O_2} = 0.5$  mbar at 300°C. The outcome is less homogeneous than the native oxide.

Results show that reduction can easily be performed and environmental conditions are proposed. However, outside these conditions, Ni NPs are systematically covered by a crystalline native NiO layer. Thus, one can assess that, without an environmental setup, mechanical tests may only be performed on pre-oxidized NPs, hampering the quantitative campaign between non-oxidized and oxidized NOs mechanical properties.

Following the conclusion of this experimental campaign, we aimed at finding new candidates with better reduction and oxidation properties, among which Cu might be a better candidate according to experts. In the following, we run an MD study on the oxidation of Ni and Cu thin films to compare both oxidation kinetics and confirm that Cu might be better suited for experimental investigations.

### 6.3. Numerical study of oxide growth on metal at the nanoscale

In this section, we conduct an original study of metal oxidation by O<sub>2</sub> gas. This is particularly noteworthy due to the samples being designed for subsequent nanoindentation tests, what distinguishes them as significantly larger in size compared to previous investigations primarily focused on smaller atom clusters.

#### 6.3.1. Methods

To study the oxide growth kinetics using MD, [111]-Ni and [111]-Cu samples of dimensions  $l_x = 100$  Å,  $l_y = 86$  Å,  $l_z = 61$  Å are generated using ATOMSK. This geometry was chosen to be comparable to the {111} top facets of metal FCC NPs investigated in previous chapters. PBC along  $x$  and  $y$ -directions and Free-BC along the  $z$ -axis are used. The ReaxFF potentials developed by Assowe *et al.* [Assowe et al. 2012] and Zhu *et al.* [Zhu et al. 2020] are used to describe the charged interactions between Ni and Cu, respectively, and O. The MD simulation time step is set at 0.5 fs for every calculation. An initial sample preparation phase is conducted according to the protocol described in Chapter 2. Simulations are run in the NVT thermodynamic ensemble. Temperature activation phase is performed at 10 K and is followed by a temperature ramp at a rate of  $6 \cdot 10^{13}$  K.s<sup>-1</sup>. Note that during this phase, box dimensions along  $x$  and  $y$  directions are dilated to account for the thermal expansion using the *fix deform* command from LAMMPS. Thermal expansion coefficients percentages  $\% \alpha_{Ni}$  and  $\% \alpha_{Cu}$  for Ni and Cu, respectively, have been computed following the protocol presented in Appendix C, and values are summarized in Table 6.1. Then, four distinct equilibration phases are conducted for both Ni and Cu at constant temperatures of 300K, 600K, 900K and

Table 6.1.: Simulation parameters for each temperature runs.

	300K	600K	900K	1200K
$\% \alpha_{Ni}$	0.318	0.647	1.031	1.468
$\% \alpha_{Cu}$	0.321	0.635	1.054	1.578
$v_{O_2}$ [m.s <sup>-1</sup> ]	967	1368	1675	1934
$P_{O_2}$ [atm]	213	427	641	855

1200K during 20 ps. This is performed to investigate the influence of the temperature on the oxide growth kinetics.

During oxidation, O<sub>2</sub> molecules are injected above the sample with a velocity  $v_{O_2}$  that corresponds to the imposed temperature and oriented downwards along the z-direction (see Table 6.1). The constant molar concentration of O<sub>2</sub> in the gas volume  $C_{O_2}$  is set at  $2 \cdot 10^3$  mol.m<sup>-3</sup>. According to equation 2.36, this corresponds to constant O<sub>2</sub> pressures of 213 atm, 427 atm, 641 atm and 855 atm at each temperature. Table 6.1 summarizes physical parameters that correspond to each simulation run. Charge equilibration is performed at every MD step and the oxidation phase duration is 700 ps.

### 6.3.2. Oxidation rate and processes

As a first investigation, we focus on the rate of growth of Ni and Cu. Figure 6.4 illustrates the oxidation kinetics observed on the surfaces of Ni and Cu at temperatures of 300 K, 600 K, 900 K, and 1200 K. The data presented here depict the number of O atoms that have reacted with the metal atoms, *i.e.* those O atoms that exhibit a charge lower than  $-0.2e$ , where  $e$  is the elementary charge of a proton ( $e = 1.60 \cdot 10^{-19}$  C). Additionally, the inset graph for Cu is a zoom on the number of O atoms adsorbed at temperatures of 300 K, 600 K, and 900 K. Each curve shows a trend characterized by logarithmic growth, consistent with prior investigations into the formation of thin oxide layers on metal surfaces [Cabreria and Mott 1949; Lawless 1974; Xu et al. 2012]. However, a notable disparity emerges between the two materials. In the case of Ni, saturation occurs at 1500, 3750, and 6200 bonded O atoms at 300 K, 600 K, and 900 K, respectively. Moreover, even after 700 ps at 1200 K, the oxidation process remains incomplete, with 11700 bonded O atoms observed. In contrast, the number of O atoms bonding to the surface of Cu is significantly lower. Only 420, 490, and 440 O atoms are counted at temperatures of 300 K, 600 K, and 900 K, respectively, and at 1200 K, the kinetic results in the bonding of 1620 O atoms to the Cu surface.

These results clearly depict the slow kinetics for Cu as compared to Ni. Indeed, even at MD time scales, Ni instantly oxidizes, which is consistent with previous experimental observations, what makes it unsuited for the study of oxide growth kinetics and its influence on the strength of NOs. This result confirms that Cu might be a better candidate in the experiments as this process can be easily monitored and suggests that it might be possible to obtain non-oxidized Cu nanostructures under less extreme

6. Surface oxide layer : growth dynamics and influence on nanoindentation – 6.3.  
Numerical study of oxide growth on metal at the nanoscale

conditions as compared to Ni.

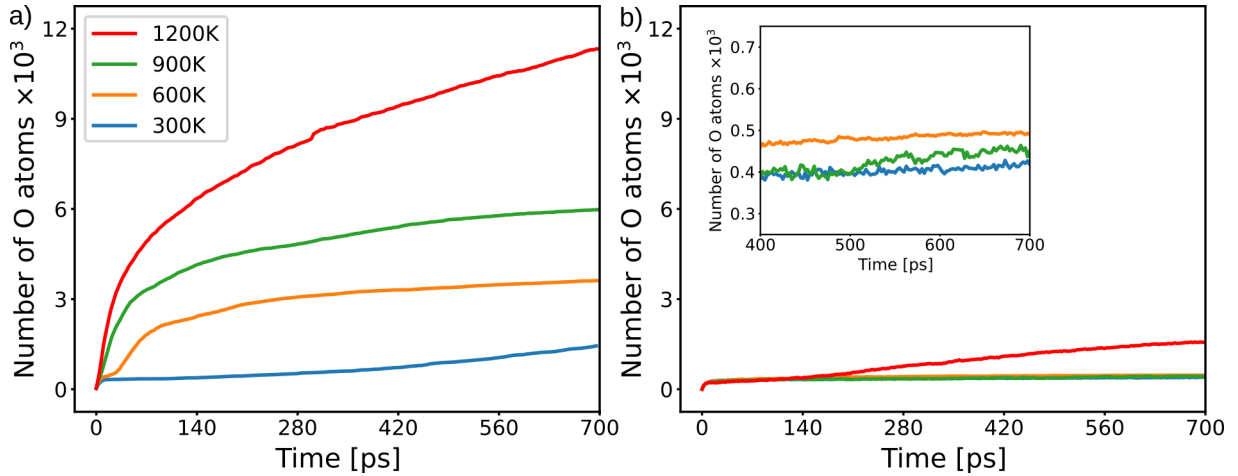


Figure 6.4.: Evolution of the number of reacted O atoms as a function of time and temperature for a) Ni and b) Cu.

Furthermore, it is observed that the oxidation process unfolds in four distinct stages. Initially, no  $O_2$  molecules are incorporated within the sample, but they are adsorbed on the surface. Subsequently, O atoms dissociate, and the surface metal atoms adjacent to the adsorbed O atoms tend to migrate outward and react. The vacancies created as a result further make the surrounding metal atoms less bonded. These weakened atoms are more akin to oxidation, particularly due to the strong binding effect between oxygen and vacancies [Zou et al. 2015], which leads to the formation of islet-like oxide clusters on the surface. These islets then serve as preferential sites for additional O atoms to bond and initiate the lateral expansion on the metal surface. Finally, once the surface is entirely covered by a thin oxide film, an in-depth growth phase ensues and results in an increase of the oxide layer thickness. For a deeper understanding of these four stages, a snapshot of the simulation box's top view for each step and both materials is provided in Figure 6.5, where non-reacted O atoms are hidden. Each snapshots for Ni and Cu are captured with a similar amount of bonded O atoms to illustrate the diverse oxidation mechanisms. While both Ni and Cu exhibit an islet growth mode, in line with previous numerical and experimental investigations [Holloway and Hudson 1974; Mitchell et al. 1976; Zhou and Yang 2005; Garruchet et al. 2010; Devine et al. 2011; Jeon et al. 2011; Lu et al. 2015], the initial adsorption processes differ. In the case of Ni, an organized configuration emerges at 350 bonded O atoms, characterized by well-defined fixation sites for  $O_2$  molecules. Analyzing the nearest Ni fixation site for each adsorbed O atom in this snapshot (*i.e.*, the minimum in-plane distance from each O atom to any Ni atom within the three topmost layers), a distribution of 47.4% bottom, 49.7% mid, and 2.9% top Ni atoms is observed. This distribution corresponds to  $O_2$  molecules positioned on parallel top-bound fixation sites on FCC Ni, which represent the configuration with the mini-

## 6. Surface oxide layer : growth dynamics and influence on nanoindentation – 6.3. Numerical study of oxide growth on metal at the nanoscale

mum binding energy as reported in ref. [Assowe et al. 2012; Yatsymyrskyi et al. 2020]. After dissociation, O atoms are positioned above the FCC threefold hollow sites [Haase et al. 1992; Garruchet et al. 2010]. In contrast, Cu exhibits lower reactivity towards O<sub>2</sub> compared to Ni. Here, the sticking probability is nearly zero, and O<sub>2</sub> molecules predominantly rebound off the surface. Furthermore, no specific configuration is observed for the adsorbed O atoms. Applying the same analysis protocol reveals a distribution of 45.8% bottom, 32.7% mid, and 21.5% top Cu atoms for the nearest fixation sites, which does not align with any well-defined configuration. Previous studies suggest parallel top-bound fixation sites on FCC Cu for O<sub>2</sub> towards FCC threefold hollow sites for O as the energetically slightly more favorable sites [Toomes et al. 2000; Xu and Mavrikakis 2001; Gattinoni and Michaelides 2015]. However, our observations diverge towards a trend that corresponds to a direct random penetration and dissociation of O atoms within the Cu thin film, as observed experimentally and in DFT studies for the Cu(111) surface [Besenbacher and Nørskov 1993; Soon et al. 2006; Soon et al. 2007].

Moreover, increasing the temperature accelerates the initiation of the oxidation process but does not significantly alter the subsequent kinetics (see Figure 6.4). The sole stage affected by temperature elevation is the initial phase associated with adsorption and dissociative chemisorption, wherein its duration decreases owing to thermal agitation, which induces a quicker nucleation of surface islets.

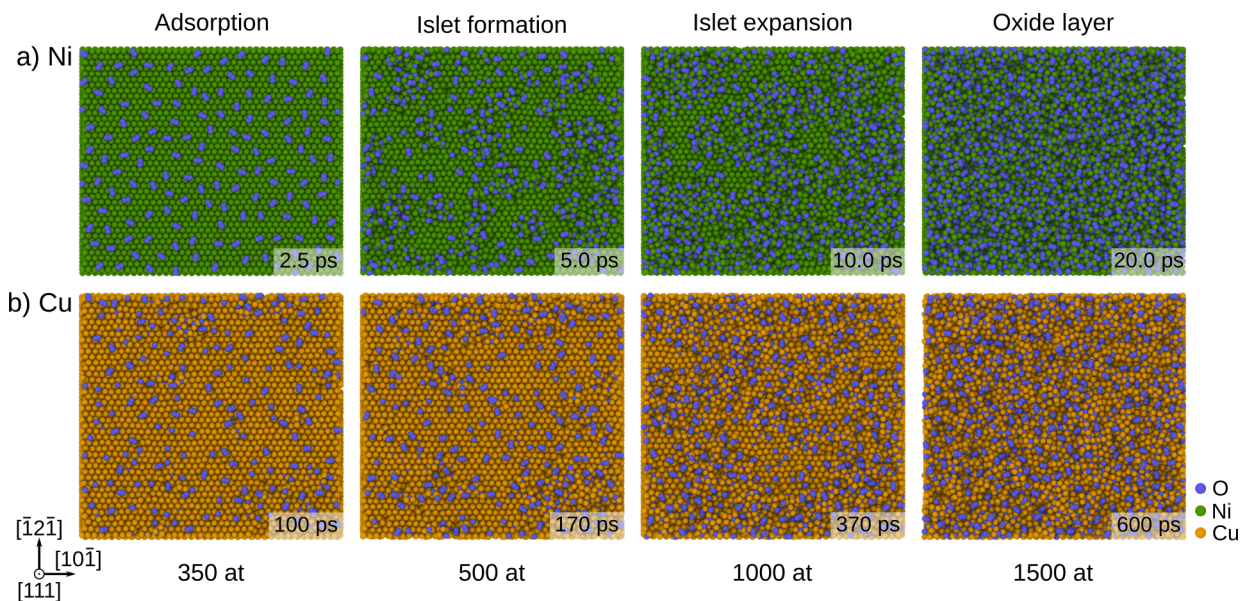


Figure 6.5.: Oxidation mechanisms for metal samples. Sample top view during the oxidation phase as a function of the number of reacted O atoms for a) Ni and b) Cu.

It is crucial to note that, due to the heterogeneous nature of this process and the incomplete coverage of the surface until the final stage of oxidation, it is challenging to

## 6. Surface oxide layer : growth dynamics and influence on nanoindentation – 6.3. Numerical study of oxide growth on metal at the nanoscale

define a precise "oxide layer thickness" throughout the entire oxidation phase. This is why we define the number of bonded O atoms as the parameter to follow the kinetics of oxide growth (see Figure 6.4). Therefore, when referring to oxide layer thickness in subsequent discussions, it is implicitly assumed that the surface is fully covered by an oxide layer. This thickness is defined by the difference in heights between the topmost metal atom and the bottommost O atom. Figure 6.6 presents a side view of the simulation boxes at the end of the oxidation phase (*i.e.* after 700 ps), where non-reacted O atoms are hidden. In the case of Ni, an oxide layer fully covers the surface for simulations conducted at 600 K, 900 K, and 1200 K. Conversely, kinetics are slower at 300 K, and oxide islets have not completely covered the entire surface. The process of in-depth growth is evident, with O atoms that penetrate the samples, but also Ni atoms that diffuse outward. This results in an increase in oxide layer thickness along both positive and negative  $z$ -directions. The final thickness, measuring a few nanometers, aligns with our previous experimental observations of Ni NPs (see Figures 6.2 and 6.3), where similar values were recorded. For Cu, no oxide layer is observed for simulations conducted at 300 K, 600 K and 900 K where only a small number of  $O_2$  molecules are adsorbed at the surface (see Figure 6.4). However, at 1200 K, O atoms manage to penetrate within the surface. The growth of oxide is observed along both positive and negative  $z$ -directions and results in a final layer thickness of 1.30 nm.

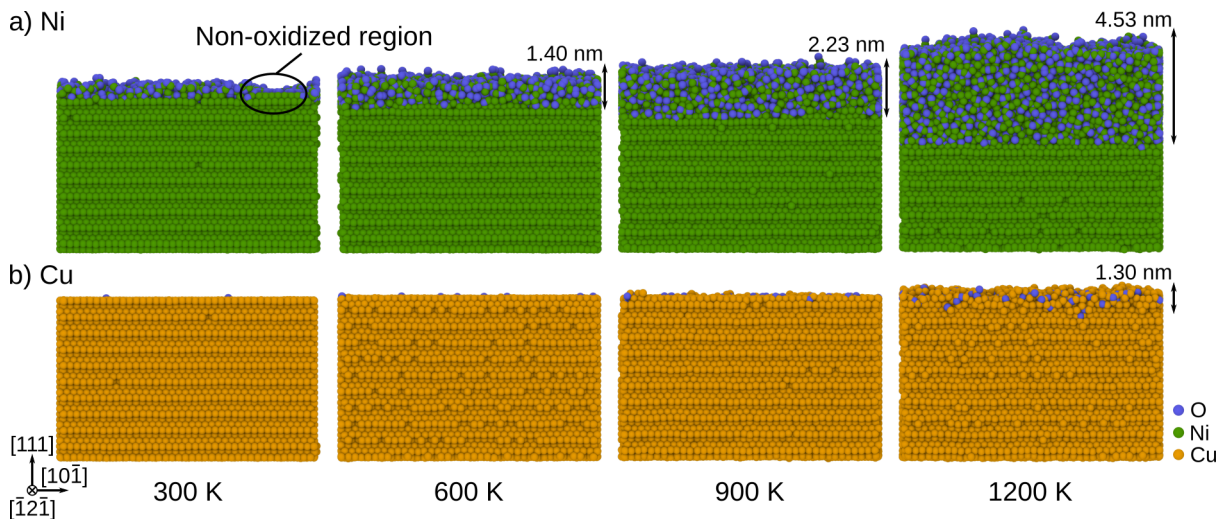


Figure 6.6.: Final sample state at the end of the oxidation phase as a function of temperature. Side views of a) Ni and b) Cu samples.

### 6.3.3. Oxide structure and re-crystallisation attempts

The atomic charge distribution  $q$  for both Ni and Cu substrates is shown in Figure 6.7, as a function of  $z$ -coordinate along the oxidation direction after 700 ps at 1200 K. It is noteworthy that the atomic charges for the metal substrates and  $O_2$  gas remain zero in both cases. Within the oxide layer, positive charges are attributed to Ni and Cu atoms,

6. Surface oxide layer : growth dynamics and influence on nanoindentation – 6.3.  
Numerical study of oxide growth on metal at the nanoscale

while negative charges state from O atoms. Close to the oxide-gas interface, O atoms exhibit weak charges, that gradually increase to more negative values within the oxide depth. Specifically, the maximum negative charge is observed at approximately 1.3 nm and 0.7 nm from the oxide-gas interface for Ni/O and Cu/O systems, respectively. The reduction in oxygen charge magnitude near the oxide-gas interface is attributed to insufficient cation concentrations to ionize O in the oxygen-rich surface region. Consequently, the charge distribution within the metal oxide film is non-uniform and is strongly correlated with the coordination number, in terms of neighboring O atoms of the metal atoms. The average coordination number  $Z$  for Ni and Cu within the oxide layer, relative to the  $z$ -coordinate, is depicted by the grey curves in Figure 6.7. This evolution is determined from atomic positions using the same protocol as in ref. [Sankaranarayanan and Ramanathan 2008] with a spherical radius  $R = 1.2r_0$  where  $r_0$  is the first-nearest-neighbor distance obtained in the partial radial distribution functions (PRDF) curves for Ni-O and Cu-O (see Figure 6.8), measured at 1.82 Å and 1.88 Å respectively. Notably, the charges of Ni and Cu atoms increase with their coordination numbers.

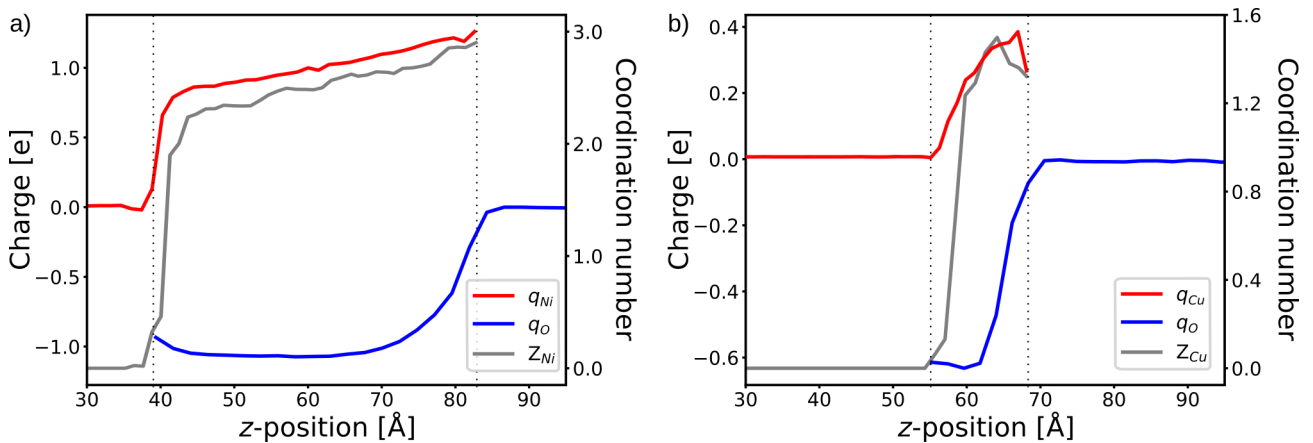


Figure 6.7.: Average charge distribution (in blue and red) and coordination number (in grey) along  $z$ -axis at the end of oxidation phase at 1200 K for O, a) Ni and b) Cu samples. The average charge density and coordination number profiles are computed with bins of size 1.0  $\text{\AA}$ . Oxide layer zones are delimited by thin black dotted lines.

In the following, the local structural properties of the oxide layer through the coordination of Ni and Cu with O atoms and the PRDF are investigated. The PRDF, noted  $g(r)$ , provides information on the short-range atomic arrangement structure, especially for the average Ni-O, Cu-O, O-O, Ni-Ni and Cu-Cu bond lengths. Figures 6.8a and c show the PRDF in the case of oxidized Ni and Cu thin films after the oxidation phase performed at 1200 K, measured within the oxide layer (4.53 nm thickness for Ni and 1.30 nm for Cu). In both cases, the PRDF for O-O exhibits a sharp and well defined peak at 1.35  $\text{\AA}$  which corresponds to un-dissociated  $\text{O}_2$  molecules at the outer surface

## 6. Surface oxide layer : growth dynamics and influence on nanoindentation – 6.3. Numerical study of oxide growth on metal at the nanoscale

of oxide layer. The position of the first peak, named as the first-nearest-neighbor distance, indicates that the Ni-O bond length is 1.82 Å and Cu-O bond length is 1.88 Å. The value for Ni-O bond is slightly lower than the theoretical length of crystalline B1 NiO (2.21 Å) given by the interatomic potential, which is supposed to be the lowest energy configuration [Assowe et al. 2012]. This shortening of the Ni–O bond length indicates an increased oxide density and the presence of mixed and non-stoichiometric  $\text{Ni}_x\text{O}_y$ . Thus, the oxide film is clearly amorphous, as confirmed by PRDF at higher  $r$  which does not reach zero nor exhibits sharp peaks. Results are the same for the Ni-Ni bond length with a peak at 2.69 Å followed by a region that encompasses a wide range of lengths without approaching 0. In the case of Cu-O bond,  $\text{Cu}_2\text{O}$  and  $\text{CuO}$  crystalline species are theoretically the most commonly observed. However, the bond length is consistent with previous investigations that denote the presence of different mixtures of  $\text{Cu}_x\text{O}_y$  compositions [Jeon et al. 2011; Ahmed et al. 2015; Ma et al. 2021]. In addition, for higher length values, non-zero  $g(r)$  also demonstrates the amorphous state of the Cu oxide layer.

Thus, we did not succeed in growing a crystalline oxide layer. This is clearly due to extreme environmental conditions (high pressures and  $\text{O}_2$  flux, as shown in Table 6.1), and the restricted time and size scales. However, these results, at least for Ni, echo the previous experimental observations. Indeed, as shown in Figure 6.2, extreme experimental conditions lead to the formation of an amorphous oxide shell above the pre-existing native oxide layer. We believe that these simulations might describe qualitatively the growth process of oxide layers under extreme conditions.

To further investigate the possibility for MD to grow crystalline oxides, we performed a temperature quench at a relatively slow temperature rate (for MD) of  $2.4 \cdot 10^{11} \text{ K.s}^{-1}$ , from 1200 K to 10 K in the NPT ensemble. Figure 6.8b and d show the PRDF at the end of the quenching phase as compared to the previous ones. No clear evidence of re-crystallisation are observed from data, with  $g(r)$  that still describes amorphous  $\text{Ni}_x\text{O}_y$  and  $\text{Cu}_x\text{O}_y$  structures. However, a small peak for Ni-O bonds seems to emerge at  $\sim 2.38$  Å. This value, much closer to the theoretical crystalline NiO bond length in B1 structure, gives a first sign of a potential re-crystallisation of the oxide layer. Longer MD simulations might be needed to confirm that re-crystallisation is indeed occurring and to study the dominant mechanisms during the process of crystalline oxide layer formation.

To sum up, the kinetics in this approach are too fast to allow for the collective atomic rearrangements necessary to obtain the formation of a crystalline oxide, even after a temperature quench phase. The native Ni crystalline oxide observed experimentally does indeed appear after a few seconds, however, these timescales are still far too long for MD simulations and systems are found to be in a metastable configuration.

6. Surface oxide layer : growth dynamics and influence on nanoindentation – 6.3.  
Numerical study of oxide growth on metal at the nanoscale

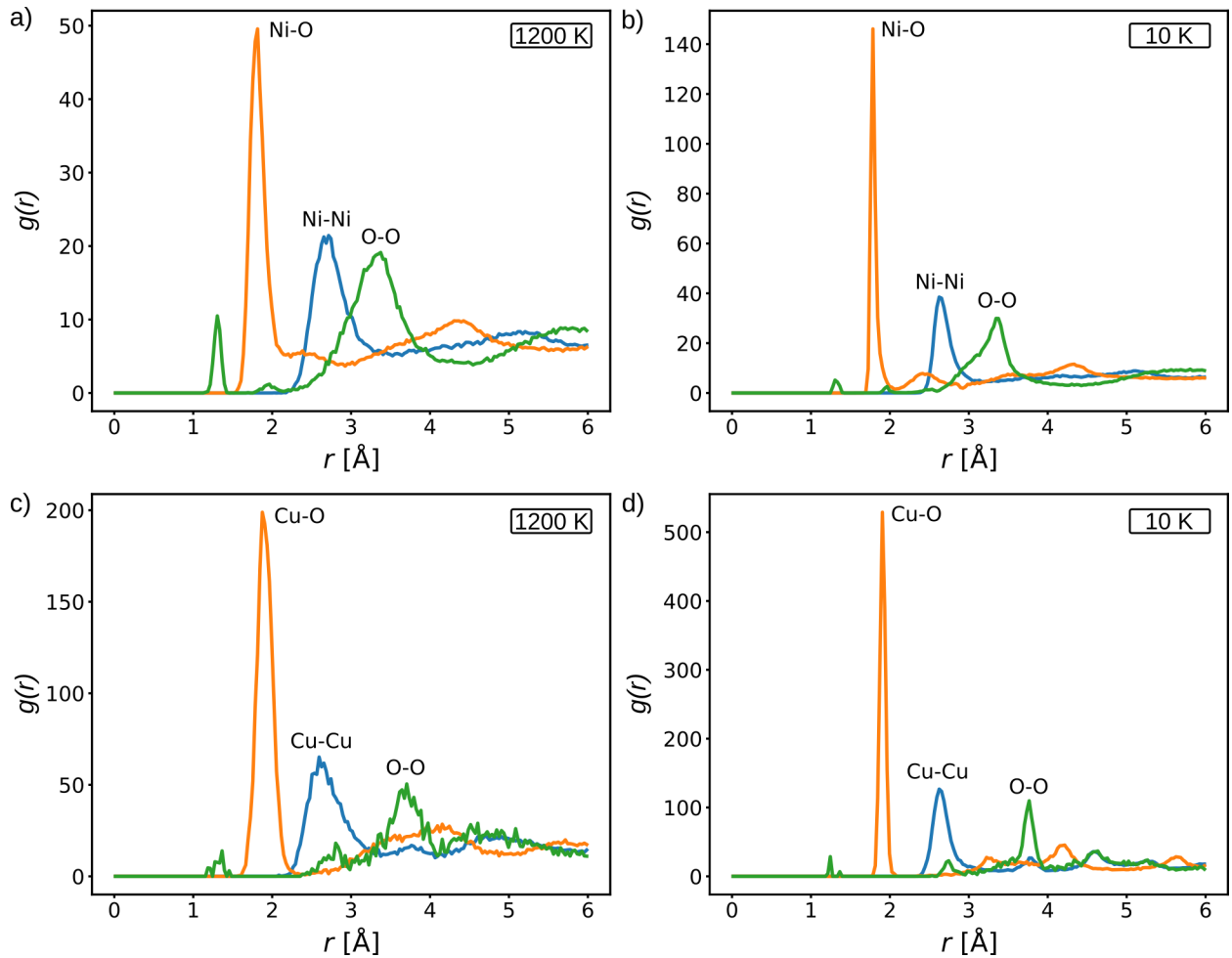


Figure 6.8.: Partial radial distribution functions within the oxide layers before and after quenching. a,b) Ni and c,d) Cu, both at 1200 K and 10 K, respectively.

### 6.3.4. Effect of surface roughness

To investigate the influence of surface roughness on the kinetics of oxide growth, two rough thin film meshes are generated using *Pyrough*. The roughness exponent  $\eta$  is set to 0.9 for both meshes, with differing *RMS* values of 1 and 3. The initial height topography can be visualized in Figures 6.10 and 6.11. To ensure consistency in height topography between Ni and Cu, considering the mesh filling with crystals of different lattice parameters, the atomic position file of Ni serves as a reference. Then, Ni atoms are substituted with Cu, and the sample is expanded along every direction using the ATOMSK *-deform* command by a factor corresponding to the ratio between both lattice parameters. Following the standard protocol for sample energy minimization, temperature activation and equilibration (see Chapter 2), the oxidation phase is conducted at 1200 K for 400 ps, with  $C_{O_2}=2 \cdot 10^3 \text{ mol.m}^{-3}$ .

A comparison of oxide growth kinetics for each rough sample as compared to

6. Surface oxide layer : growth dynamics and influence on nanoindentation – 6.3.  
Numerical study of oxide growth on metal at the nanoscale

flat surfaces is presented in Figure 6.9. No clear differences seem to emerge from the comparison of Ni thin films oxide growth kinetics, with a final amount of 9500 bounded O atoms. However, kinetics appear to be strongly influenced by surface roughness in the case of Cu. We believe differences are more notable for Cu due to the low reaction rate with  $O_2$  that allows for a more detailed study of the initial stages of oxidation. In contrast, Ni oxidation process is too quick to discern any variations. The shapes of the curves differ for rough surfaces and exhibit a logarithmic increase, whereas for the flat surface, a saturation phase precedes a linear increase. The total number of bounded O atoms after 400 ps is 1500 and 1450 for  $RMS=3$  and  $RMS=1$ , respectively, whereas only 1000 O atoms bounded to the flat surface at the same timestep.

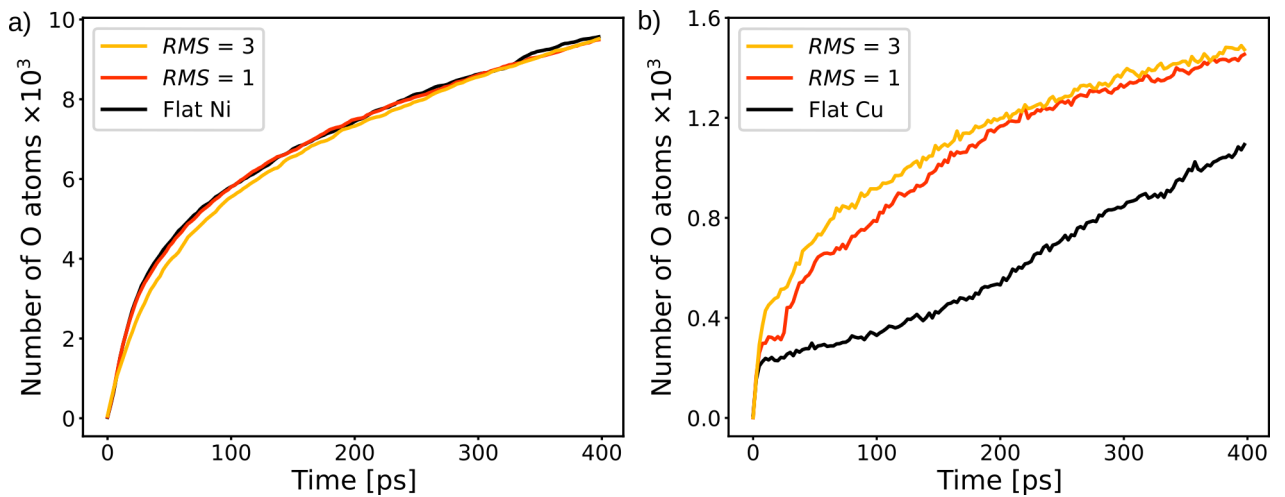


Figure 6.9.: Oxide growth kinetics on rough metal surfaces. Evolution of adsorbed O atoms on a) Ni and b) Cu rough surfaces as compared to flat thin films. Two different roughness profiles are tested and are characterized by  $RMS$  equal to 1 or 3.

The differences in curve profiles suggest potential variations in adsorption mechanisms compared to those observed on a flat surface. To investigate the mechanisms involved in the initial stages of surface oxidation, atomic configurations are presented in Figure 6.10 for the  $RMS=1$  surface and in Figure 6.11 for the  $RMS=3$  case. In the case of Ni, surface oxidation occurs instantaneously, and the initial rough pattern disappears after 300 ps. Consequently, the samples are covered by an amorphous  $\sim 3$  nm oxide layer, independent of the initial surface roughness. Conversely, Cu surfaces, which oxidize at a slower rate, exhibit a lateral oxide growth process from atomic steps that act as preferential fixation sites for O atoms. Previous research has shown that in the presence of surface steps, oxidation proceeds via an adatom process, where the oxide phase grows laterally on the surface terrace due to surface diffusion of adsorbed O atoms and Cu atoms detaching from step edges [Zhou et al. 2012; Li et al. 2014; Zhu et al. 2016; Luo et al. 2016]. This process diverges from the typical reaction sequence that involves O adsorption and subsurface O incorporation, owing to the absence of

## 6. Surface oxide layer : growth dynamics and influence on nanoindentation – 6.4. Nanoindentation of oxidized nanocrystals

mobile metal atoms at the surface. Consequently, the initial stage of oxidation entails a lateral oxide growth, followed by the initiation of in-depth growth once every site near surface steps is filled. Additionally, Figures 6.10d and 6.11d illustrate that the

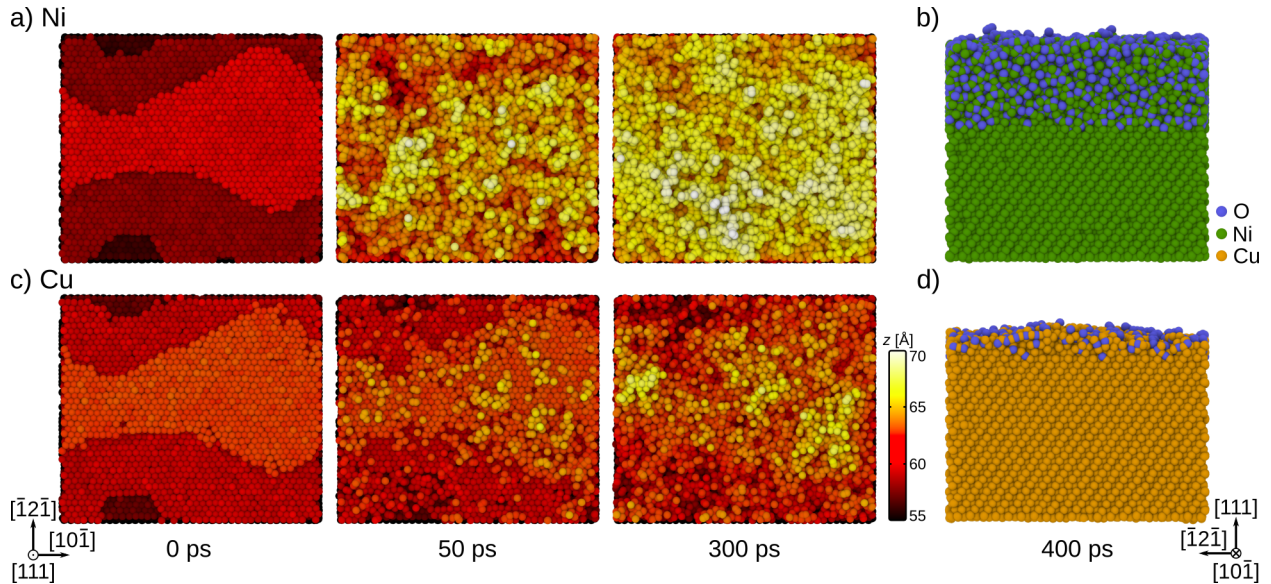


Figure 6.10.: Top surface oxidation of Ni and Cu rough surfaces characterized by  $\eta=0.9$  and  $RMS=1$  at different times. a) Top and b) side view for Ni, and c) top and d) size view for Cu oxidation process. Atoms are colored as a function of  $z$ -coordinate in top views.

final oxide layer thickness is uniform on the rough surface, which allows the initial height topography to remain observable through the oxide layer. Nevertheless, akin to the situation with Ni, the ongoing growth of the oxide layer could potentially erase the height discrepancies and lead to the formation of a comparatively uniform amorphous layer. However, achieving this would require longer computational simulations.

## 6.4. Nanoindentation of oxidized nanocrystals

In this section, we investigate the influence of the presence of an oxide layer on the mechanical behavior of metal nanosamples. Three oxidized Ni thin films obtained from prior oxidation and quench phases (see Figure 6.6) are used as inputs, with oxide thicknesses of 1.40 nm, 2.23 nm, and 4.53 nm. An oxidized Cu sample with an oxide thickness of 1.30 nm is also included as input. Furthermore, pure Ni and Cu flat thin films are subjected to nanoindentation tests to provide comparison data. Displacement-controlled nanoindentation is conducted at 10 K, in the NPT ensemble. A spherical indenter of radius  $R_{ind}=25 \text{ \AA}$  is moved along  $z$ -direction towards the surface at a displacement rate  $\dot{\Delta}l=0.01 \text{ \AA.ps}^{-1}$ . Bottom atoms are held fixed (see chapter 2 for more details).

6. Surface oxide layer : growth dynamics and influence on nanoindentation – 6.4.  
Nanoindentation of oxidized nanocrystals

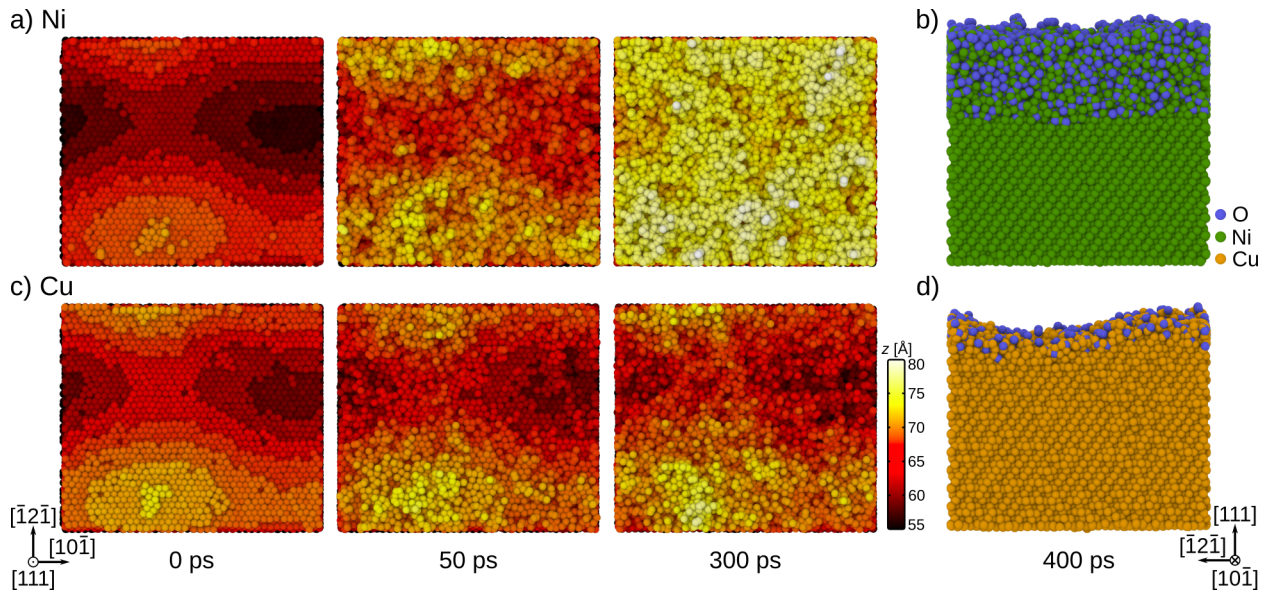


Figure 6.11.: Top surface oxidation of Ni and Cu rough surfaces characterized by  $\eta=0.9$  and  $RMS=3$  at different times. a) Top and b) side view for Ni, and c) top and d) size view for Cu oxidation process. Atoms are colored as a function of  $z$ -coordinate in top views.

Figure 6.12 shows the force *vs.* displacement response of every thin film tested under nanoindentation. For the pure metal flat surfaces, three distinct regimes are observed. The initial stage corresponds to the quasi-elastic regime and extends up to  $\delta=4.20$  Å for Ni and  $\delta=4.59$  Å for Cu. During this phase, the load increases with increasing indentation depth by following the Hertzian elastic law ( $F = \frac{4}{3}E^* R_{ind}^{1/2}\delta^{3/2}$ , where  $E^*$  is the effective Young's modulus), until the force suddenly drops at a critical force  $F_y=190$  nN and  $F_y=187$  nN for Ni and Cu, respectively. At this stage, dislocations are nucleated and propagate beneath the indenter. In the third stage, the nucleated dislocations pile-up and interact with other dislocations of adjacent slip planes which results in the formation of prismatic dislocation loops. Subsequent load drops and fluctuations indicate dislocation slip and propagation. The nucleation of the first dislocations in pure Ni and Cu thin films is illustrated in Figures 6.13a and 6.14a.

While the variations in the force *vs.* displacement curves of pure metal are typical of MD nanoindentation, those of oxidized thin films exhibit a significantly different behavior, characterized by a distinct mechanical response. These systems display a lower effective Young's modulus  $E^*$  (see Table 6.2), characteristic of amorphous materials, and a softer elasto-plastic transition, consistent with previous research on surface indentation [Shi and Falk 2007; Qiu et al. 2014; Avila et al. 2021; Luu et al. 2022] and mechanical testing of NOs covered by an amorphous layer [Sen et al. 2014; Aral et al. 2016; Goryaeva et al. 2019; Aral and Islam 2023]. The yield values at which the first dislocations nucleate in the metal are compared in Table 6.2 and are illustrated by the dashed vertical lines in Figure 6.12. The yield forces are higher for oxidized Ni compared to the pure crystal, but this discrepancy pales in comparison to the

6. Surface oxide layer : growth dynamics and influence on nanoindentation – 6.4.  
Nanoindentation of oxidized nanocrystals

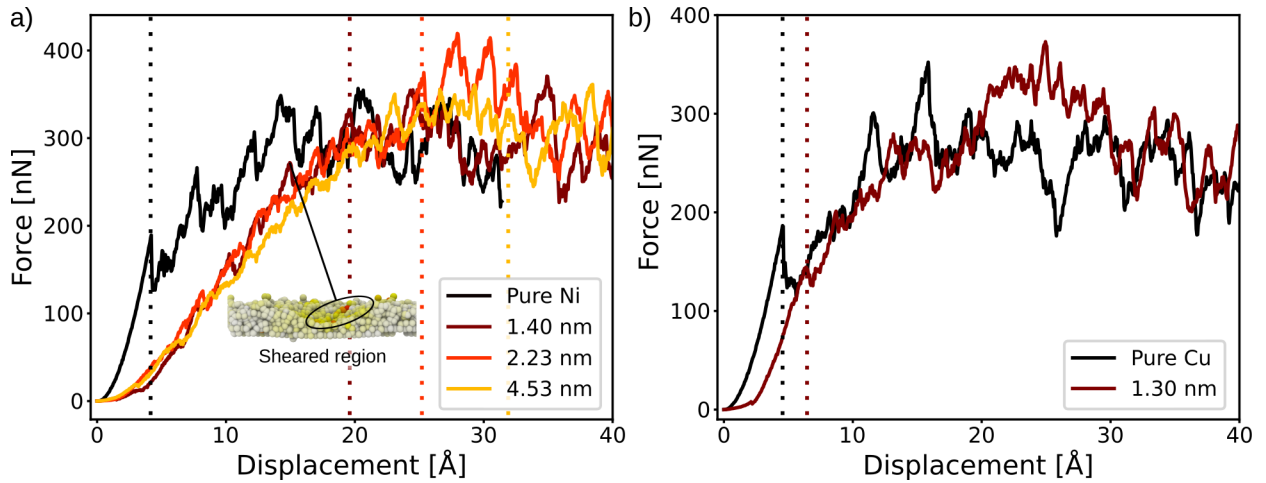


Figure 6.12.: Nanoindentation of oxidized a) Ni and b) Cu samples, as compared to non-oxidized metal flat surface (black curves). Vertical dotted lines refer to the nucleation of the first dislocations in every cases.

Table 6.2.: Yield values corresponding to the nucleation of the first dislocations during nanoindentation tests.

	Oxide thickness	$E^*$ [GPa]	$F_y$ [nN]	$\delta$ [\AA]
Ni	Pure	299.47	190	4.20
	1.40 nm	53.77	332	19.55
	2.23 nm	59.18	376	25.36
	4.53 nm	59.81	332	32.05
Cu	Pure	270.23	187	4.59
	1.30 nm	119.67	145	6.39

significantly longer critical displacement. Conversely, the oxidized Cu sample yields at a lower force than that observed in the pure crystal, with a slightly higher critical displacement. However, one cannot clearly distinguish the elastic regime from the plastic deformation domain which suggests a complex deformation process where small irreversible plastic events occur within the elastic regime, followed by a smooth transition into a more effective plastic regime. Such behavior is commonly observed in amorphous systems [Tanguy et al. 2006; Fusco et al. 2010]. To study the spatial distribution and time evolution of the plastic deformation during indentation, we compute the non-affine squared displacement  $D_{min}^2$  to determine the local plastic shear strain of each atom [Falk and Langer 1998]. In the inset of Figure 6.12, we show  $D_{min}^2$  at  $\delta=15$  Å, with the configuration at  $\delta=14.5$  Å serving as the reference. Plastic shear occurs in the amorphous oxide region above metal thin film, which is responsible for the minor drop in the force vs. displacement curve and explains the fluctuations in the elastic regime. Across all systems, the shear activity is correlated with the load drops. Figures 6.13 and 6.14 show the distribution of  $D_{min}^2$  in the Ni and Cu samples when

6. Surface oxide layer : growth dynamics and influence on nanoindentation – 6.4.  
Nanoindentation of oxidized nanocrystals

the first dislocations nucleate, with the initial configurations serving as the references. As indentation depth increases, the shear strain rapidly expands outward from the contact region between the indenter and substrate to the far-field region.

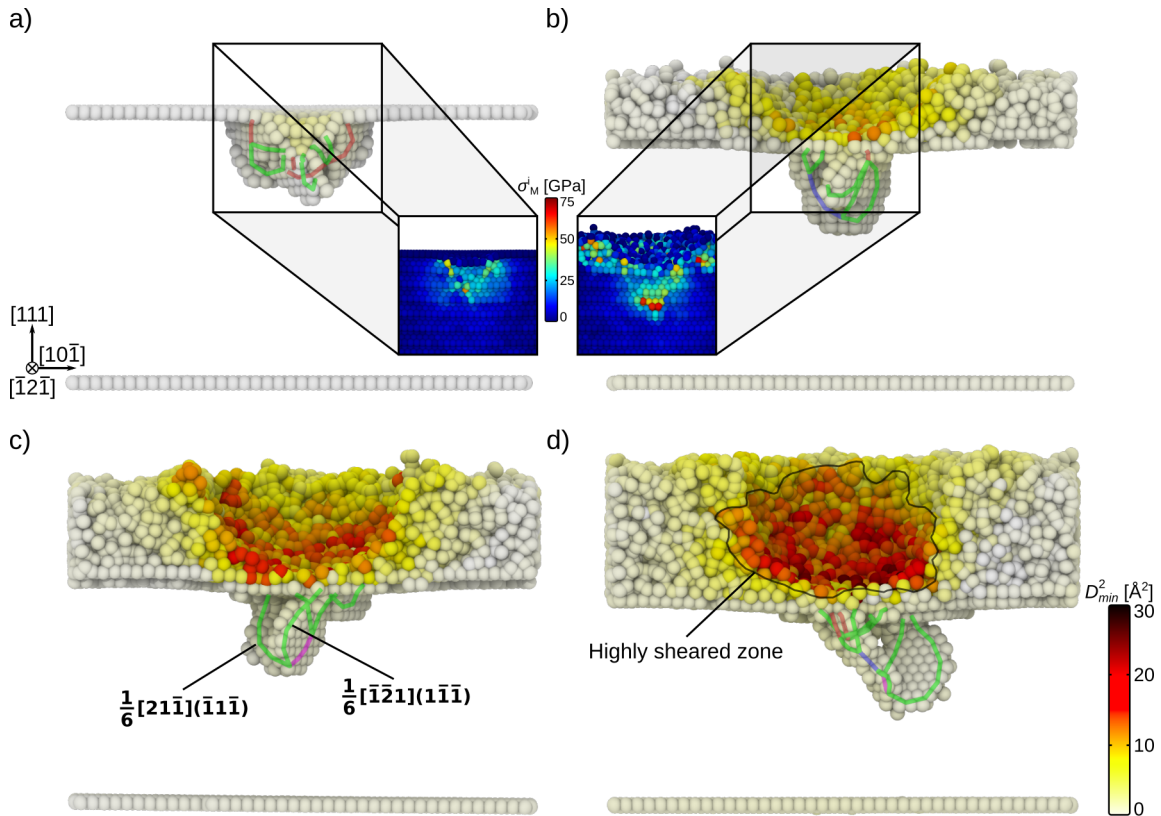


Figure 6.13.: Nucleation of the first dislocations during the nanoindentation of Ni thin films. a) Non-oxidized surface, b) 1.40 nm, c) 2.23 nm and d) 4.53 nm oxide layer thickness. Color code denotes the non-affine squared displacement. The atoms in a non-FCC configuration are shown. Insets show the von Mises stress  $\sigma_M^i$  distribution right before the nucleation of the dislocations.

The inset of Figure 6.13 shows the distribution of von Mises stress  $\sigma_M^i$  before dislocation nucleation in the crystal, comparing the cases of Ni non-oxidized and 1.40 nm oxide layer thickness samples. Higher stress values are observed in the oxidized surface case, with a distribution that extends into the amorphous region. Combined with the interpretation of non-affine squared displacements, this proves that the indenter does not push on an amorphous oxide film covered metal surface but rather pushes material to the sides before stressing the metal sub-surface.

In summary, our simulation results suggest that the presence of an oxide layer significantly influences the strength of metal thin films. While the primary deformation mechanisms in crystalline metals typically involve dislocation nucleation and slip,

6. Surface oxide layer : growth dynamics and influence on nanoindentation – 6.5.  
Conclusion

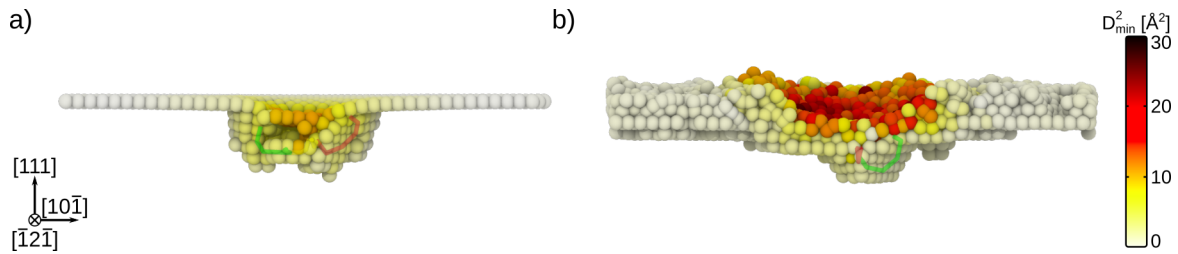


Figure 6.14.: Nucleation of the first dislocations during the nanoindentation of Cu thin films. a) Non-oxidized surface and b) 1.30 nm oxide layer thickness. Color code denotes the non-affine squared displacement and the atoms in a non-FCC configuration are shown.

amorphous oxidized surfaces display an initial elasto-plastic transition regime. This regime is characterized by highly sheared zones that tend to move atoms towards the sides of the spherical indenter, thereby delaying the dislocation nucleation process. Eventually, as the indenter approaches the metal layer and stress reaches a critical level, dislocations nucleate and propagate through the crystal.

## 6.5. Conclusion

Initial investigations into monitoring surface oxidation using an ETEM revealed exceptionally fast kinetics for Ni. This rapid oxidation rate impedes detailed studies on the influence of the presence or absence of an oxide layer on the strength of Ni NPs, as it is assumed that all samples are covered by a 3-4 nm crystalline native oxide layer in air. Consequently, Cu was identified as another candidate for such studies. MD simulations demonstrate significantly slower kinetics of oxide growth in the case of Cu, which suggests the improved feasibility of mechanical tests on possibly reduced Cu NPs. However, particular attention should be paid on NPs surface state as both surface roughness and oxidation were shown to impact the mechanical properties of nanosamples. Further investigations revealed the amorphous nature of the grown oxide layers, which might be expected considering the simulation conditions in MD compared to real-life scenarios. The initial step towards the study of oxidized metal samples involved the indentation of thin films to explore the impact of such an oxide layer. Results indicate distinct deformation mechanisms that lead to sample softening, consistent with previous findings. However, questions may arise regarding the accuracy of these tests, as the initial deformation process involves cleaning the amorphous phase beneath the indenter before further indenting the metal substrate. One potential approach to fully consider the role of the oxide layer could be to use a flat indenter, which would ensure that mechanical solicitation is solely oriented along the compression axis and would prevent the movement of the amorphous phase to the sides.

**Chapter VI summary:**

This chapter focuses on the study of the growth of an oxide layer on metal samples and its influence on the mechanical properties. First, experimental investigations were made in order to define the reduction and oxidation conditions of Ni NPs. Results show that Ni instantly oxidizes, even at low O<sub>2</sub> pressures. Then, MD simulations were performed to compare the oxide growth dynamics and its crystallography on Ni and Cu surfaces, as well as the effect of surface roughness. Cu oxidation is much slower than Ni one at the nanoscale which confirms its suitability for the experimental study of the influence of oxidation on the mechanical behavior of NOs. Finally, nanoindentation tests were performed on non-oxidized and oxidized Ni and Cu surfaces with different layer thicknesses. Results show that deformation mechanisms significantly differ between both materials. Finally, Cu nanocrystals have shown to be more akin for the study of nanomechanical properties with and without surface oxide in the experiment.

## **Conclusion and perspectives**

The present PhD work relies on the development and the application of original methods to allow for a more accurate representation of nanomechanical testing in simulations. Despite the well-observed experimental data scattering in relation to the "smaller is stronger" trend, distinguishing between intrinsic and extrinsic experimental biases remains challenging and hinders predictive evaluations of NPs mechanical properties. This limitation was not adequately addressed by existing modeling approaches, which often overlook the influence of sample geometry and testing conditions and end up with a disparity between simulation results and experimental findings. Our work tried to address this gap by considering the experimental biases in the simulations, thereby paving the way for more realistic numerical studies.

To gain deeper insights into the deformation mechanisms, we used atomistic simulation techniques. These methods enabled us to explore the mechanical behavior of NPs through the development of original simulation protocols or the use of more realistic sample design frameworks. These might open new routes in the future to enhance the fidelity of virtual systems and simulation conditions, thereby striving to bridge the gap between numerical simulations and experimental observations. Still, several ideas for further exploration warrant attention.

We first developed an original algorithm to model load-controlled nanocompression in MD. Unlike experimental setups, which allow for the control of indenters via imposed load or displacement rates, MD simulations typically only provide the displacement control of the indenter. Our algorithm mimics experimental setups by employing a feedback loop to ensure the strict control of the force. Implemented as a Python script, this feedback control loop can be easily tailored to model various mechanical solicitations and indenter shapes, including flat punch compression or indentation with a sphere. When applied to the compression of NPs, we revealed large strain bursts during plastic deformation, indicative of rapid sample collapse into a final pancake shape. Similarly, during indentation, we observed pop-ins that denote instantaneous penetration of the indenter into the sample surface. These findings closely mirror experimental observations and underscore the distinct deformation processes underlying both control modes. In addition, we proved that the actual theoretical models do not allow to describe precisely the mechanical response of NPs under load-controlled solicitation, which denotes the importance of modeling this control mode. This study provides the missing link in simulations to model mechanical testing in all its forms concerning the control modes, as compared to the experiments.

Additional developments can be foreseen for the load-controlled MD method. Indeed, to date, it is only suited for the use of an analytical force-field, but other definitions exist such as the modeling of indenters with frozen atoms, as it has been done in reference studies. Moreover, our first exchanges with research groups interested by the load-controlled nanoindentation showed that many nanoindentation tests are performed using a quasi-static routine while the algorithm is developed in the context of dynamic simulations. Thus, the development of a similar method suited for quasi-static simulations might be of interest. Another perspective would be to adapt

the method for integration within the LAMMPS code to provide a way for the users to select the mechanical solicitation control mode in MD simulations using the *fix indent* command.

Then, we developed *Pyrough*, a tool for the construction of virtual samples presenting surface roughness for FEM and atomistic simulations. Based on the classical roughness theory, rough surfaces are constructed and implemented on basic 3D shapes, including thin films, faceted and spherical particles or cylindrical and faceted wires. *Pyrough* allows for the monitoring of the statistical roughness parameters to generate 3D virtual objects, from the smoothest to the roughest. Its object-oriented structure allows for the easy implementation of additional shapes and methods, according to any user's needs. First applications of *Pyrough* were made, which even led to code improvements. Additional options were implemented in the code, including the construction of rough interfaces and GBs, or the virtual reproduction of experimental surfaces based on the computation of their statistical roughness parameters. This new tool represents a first step towards the accurate representation of virtual samples and paves the way for further investigations by considering roughness at small-scales. The perspectives for *Pyrough* include code maintenance and the communication and promotion of the tool within the scientific community.

Moreover, *Pyrough* served as the primary tool for the construction of rough samples to run a comparative and statistical MD study on the impact of surface roughness on the strength of Au faceted NPs. Our results revealed a significant influence of surface irregularities within the contact zone between NPs and the indenter on the strength, with variations of up to 80% compared to samples featuring flat facets, traditionally employed in MD simulations to date. Thus, this study demonstrates that surface roughness is one of the reasons for the experimentally observed data scattering around the global trend, where NOs strength can vary by one order of magnitude at constant size. Furthermore, we observed that the top surface morphology played a crucial role in promoting cross-slip of screw dislocation junctions at the NPs surfaces, which results in the emergence of unusual slip systems within the FCC crystal structure. This observation aligns with recent experimental evidences that demonstrate such slip systems in FCC NPs. Subsequently, we proposed a model to predict the strength distribution of rough NPs by considering both the theoretical strength of samples with perfectly flat external surfaces and the morphological features of the top surface. This study led to a large amount of new questionings. In the end of the chapter, we briefly investigate the effect of several rough layers and find that our model predicts well the strength distribution while taking only the top layer into account for the contact surface area. Thus, at these scales, systems are found to be very rigid regarding the successive atomic steps, *i.e.* the first layer indents the second, and so on. It might be interesting to increase the system size and see if a more collective role of atomic steps comes into play in the deformation mechanisms of NOs. One way would be to increase the samples size in the input file of *Pyrough*. Moreover, a first study could be conducted on this subject thanks to the recent acquisition of electronic tomography

data files from the observation of experimental Au faceted NPs. These *.stl* meshes could be filled with atoms following the same protocol as implemented in *Pyrough* and studied in MD. The size of the NPs are here of ~100 nm and dozens of rough atomic layers are observable on the external surfaces. This would require longer calculation times and an optimization phase to select meaningful outputs.

In addition, the investigation of different shapes can be performed, particularly, the study of rough NWs is of interest. Literature review and recent discussions from conferences suggest to better represent virtual NWs, as the ones seen in experiments present surface irregularities. Notably, I had the opportunity to discuss with Dr. Gunther Richter during the 2022 MMM Conference in Baltimore, USA, and during online meetings, who confirmed that surface irregularities were observed on the metal NWs. Furthermore, the degree of roughness varies depending on the synthesis conditions. Thus, a quantitative comparative study of the characterization of surface roughness and its influence on the strength of metal NWs using both experimental and MD outputs should be performed.

An initial MD simulation campaign was also conducted on rough Cu nanospheres during my PhD. Similar to our study on Au faceted NPs, 140 atomic samples were generated using *Pyrough*, the same simulation conditions, as well as the same ( $H, C_1$ ) values. The first results show a strong dependence of the strength with surface roughness where, similar to Au NPs, values can decrease by up to 80% compared to the perfect case. The comparison of contact surface areas with yield forces tend to converge towards the model we constructed in this thesis. However deeper analyses are needed to confirm this hypothesis. Also, this might confirm that samples at these size scales are strongly rigid as the deformation consists in successive atomic planes being indented by the upper ones. Moreover, the asymmetry of the systems was shown to be responsible for the nucleation of unusual dislocation microstructures as compared to previous work made on perfect nanospheres under compression.

The measurement of statistical roughness parameters at the surface of NOs is also a route to explore from an experimental point of view. During my PhD, we tried to observe surface irregularities on Pt NPs using an AFM at room temperature. Atomic steps were indeed observed but a more rigorous protocol would be needed to fully characterize the top surface height distribution of NOs. The STM was proposed as the best suited equipment for these tests, but it would require the fabrication of new samples on conductive substrates. Then, once this phase is overcome, a comparative MD study could be performed on NPs sharing the same roughness statistical parameters as the observed samples in the experiment, via *Pyrough*, to investigate the deformation mechanisms under compression.

Finally, an initial investigation into the growth process and the influence of oxide layers on the mechanical properties of metal samples was proposed. Experimental studies conducted using an ETEM provided insights into the feasibility of controlling the oxidation or reduction state of Ni NPs for subsequent mechanical testing. However, it was determined that Ni may not be the most suitable material for such experiments. Thus, using MD, we conducted a comparative analysis of the oxidation processes

of Ni and Cu. Our findings suggested that Cu may be a more suitable candidate for the monitoring of the surface oxide layer due to its slower growth kinetics under similar environmental conditions, even when subjected to surface roughness, which was observed to accelerate the oxidation process. However, it should be noted that MD simulations do not facilitate the growth of crystalline oxides. Following these simulations, samples were subjected to nanoindentation tests that revealed distinct deformation mechanisms, consistent with prior research on the deformation of amorphous materials. But further analysis should be made at this point, notably on the accuracy for the ReaxFF potentials to describe mechanics as these are primarily designed for charged interactions. This aspect should be borne in mind when comparing mechanical properties of NOs using these kinds of interatomic potentials.

Several avenues of exploration emerge from this study. New experiments should be performed, this time with Cu NPs. Now that the first tests were conducted on Ni NPs, a rigorous protocol should be proposed to investigate the reduction and oxidation conditions of Cu NPs. This should be performed to find experimental conditions that allow for the mechanical testing of oxidized and non-oxidized NPs. This would enable the quantification of the effect of an oxide overlayer on the strength of NPs under compression. In addition, from a numerical simulation point of view, crystallization attempts failed during my PhD. One should try to investigate further the feasibility of crystallization in MD and if not possible, oxide crystalline overlayer could be constructed *by-hand*. This would involve the study of the interface between metal and metal oxide crystals, and a special focus on the energy minimization phase. Also, similar mechanical tests as in the end of this thesis, including the indentation of metal samples covered by an oxide layer, should be performed but with a flat punch indenter. This in order to study the effect of the oxide layer under uniaxial mechanical solicitation, without pushing atoms to the sides. Finally, once all these phases are performed, a comparative MD study could be performed on the influence of an oxide layer on the mechanical behavior of NPs under compression. The role of an oxide layer covering a rough NP as constructed using *Pyrough* is also of final interest concerning the strength disparities.

## Bibliography

- Adams, D. J. and I. R. McDonald (1974). "Rigid-Ion Models of the Interionic Potential in the Alkali Halides". *Journal of Physics C: Solid State Physics* 7.16, p. 2761 (cit. on p. 42).
- Ahmed, A., P. Elvati, and A. Violi (2015). "Size-and Phase-Dependent Structure of Copper(II) Oxide Nanoparticles". *RSC Advances* 5.44, pp. 35033–35041 (cit. on p. 140).
- Akulut, M. (2012). "Nanoparticle-Based Lubrication Systems". *Journal of Powder Metallurgy and Mining* 01.01, pp. 1–3 (cit. on p. 8).
- Altay, R., A. K. Sadaghiani, M. I. Sevgan, A. Şışman, and A. Koşar (2020). "Numerical and Experimental Studies on the Effect of Surface Roughness and Ultrasonic Frequency on Bubble Dynamics in Acoustic Cavitation". *Energies* 13.5, p. 1126 (cit. on p. 59).
- Amodeo, J., C. Begau, and E. Bitzek (2014). "Atomistic Simulations of Compression Tests on Ni<sub>3</sub>Al Nanocubes". *Materials Research Letters* 2.3, pp. 140–145 (cit. on p. 34).
- Amodeo, J. and K. Lizoul (2017). "Mechanical Properties and Dislocation Nucleation in Nanocrystals with Blunt Edges". *Materials & Design* 135, pp. 223–231 (cit. on pp. XI, 34, 35, 54, 65, 82, 105, 111, 127).
- Amodeo, J., E. Maras, and D. Rodney (2021). "Site Dependence of Surface Dislocation Nucleation in Ceramic Nanoparticles". *npj Computational Materials* 7.1, p. 60 (cit. on p. 31).
- Amodeo, J. and L. Pizzagalli (2021). "Modeling the Mechanical Properties of Nanoparticles: A Review". *Comptes Rendus. Physique* 22.S3, pp. 1–32 (cit. on pp. X, 9, 31, 34, 63, 116).
- Andersen, H. C. (1980). "Molecular Dynamics Simulations at Constant Pressure and/or Temperature". *The Journal of Chemical Physics* 72.4, pp. 2384–2393 (cit. on p. 52).
- Angelo, J. E., N. R. Moody, and I. Baskes (1995). "Trapping of Hydrogen to Lattice Defects in Nickel". *Modelling and Simulation in Materials Science and Engineering* 3.3, p. 289 (cit. on pp. 43, 76).
- Aral, G. and M. M. Islam (2023). "Effect of Oxidation on Mechanical Properties of Copper Nanowire: A ReaxFF (Reactive Force Field) Molecular Dynamics Study". *Journal of Applied Physics* 133.9 (cit. on pp. 39, 144).

## Bibliography

- Aral, G., M. M. Islam, and A. C. T. Van Duin (2018). “Role of Surface Oxidation on the Size Dependent Mechanical Properties of Nickel Nanowires: A ReaxFF Molecular Dynamics Study”. *Physical Chemistry Chemical Physics* 20.1, pp. 284–298 (cit. on p. 39).
- Aral, G., M. M. Islam, Y.-J. Wang, S. Ogata, and A. C. T. Van Duin (2019). “Atomistic Insights on the Influence of Pre-Oxide Shell Layer and Size on the Compressive Mechanical Properties of Nickel Nanowires”. *Journal of Applied Physics* 125.16 (cit. on pp. 39, 130).
- Aral, G., Y.-J. Wang, S. Ogata, and A. C. T. Van Duin (2016). “Effects of Oxidation on Tensile Deformation of Iron Nanowires: Insights from Reactive Molecular Dynamics Simulations”. *Journal of Applied Physics* 120.13 (cit. on pp. 39, 130, 144).
- Arthur, J. R. (2002). “Molecular Beam Epitaxy”. *Surface Science* 500.1-3, pp. 189–217 (cit. on pp. 26, 28).
- Assowe, O., O. Politano, V. Vignal, P. Arnoux, B. Diawara, O. Verners, and A. C. T. Van Duin (2012). “Reactive Molecular Dynamics of the Initial Oxidation Stages of Ni(111) in Pure Water: Effect of an Applied Electric Field”. *The Journal of Physical Chemistry A* 116.48, pp. 11796–11805 (cit. on pp. 48, 134, 137, 140, 193).
- Atkinson, A. (1985). “Transport Processes during the Growth of Oxide Films at Elevated Temperature”. *Reviews of Modern Physics* 57.2, pp. 437–470 (cit. on pp. XIII, 130).
- Atkinson, A., R. I. Taylor, and A. E. Hughes (1982). “A Quantitative Demonstration of the Grain Boundary Diffusion Mechanism for the Oxidation of Metals”. *Philosophical Magazine A* 45.5, pp. 823–833 (cit. on pp. XIII, 130).
- Avila, K. E., V. H. Vardanyan, S. Küchermann, and H. M. Urbassek (2021). “Response of an Amorphous/Crystalline Interface to Nanoindentation: An Atomistic Study”. *Applied Surface Science* 551, p. 149285 (cit. on p. 144).
- El-Awady, J. A., M. Wen, and N. M. Ghoniem (2009). “The Role of the Weakest-Link Mechanism in Controlling the Plasticity of Micropillars”. *Journal of the Mechanics and Physics of Solids* 57.1, pp. 32–50 (cit. on p. 14).
- Ayachit, U. (2015). *The Paraview Guide: A Parallel Visualization Application*. Kitware, Inc. (cit. on p. 59).
- Azadehhranjbar, S., R. Ding, I. M. Padilla Espinosa, A. Martini, and T. D. B. Jacobs (2023). “Size-Dependent Role of Surfaces in the Deformation of Platinum Nanoparticles”. *ACS Nano* 17.9, pp. 8133–8140 (cit. on p. 21).
- Bagri, A., C. Mattevi, M. Acik, Y. J. Chabal, M. Chhowalla, and V. B. Shenoy (2010). “Structural Evolution during the Reduction of Chemically Derived Graphene Oxide”. *Nature Chemistry* 2.7, pp. 581–587 (cit. on p. 44).
- Bahr, D., D. Kramer, and W. Gerberich (1998). “Non-Linear Deformation Mechanisms during Nanoindentation”. *Acta Materialia* 46.10, pp. 3605–3617 (cit. on p. 20).

## Bibliography

- Bakolas, V. (2003). "Numerical Generation of Arbitrarily Oriented Non-Gaussian Three-Dimensional Rough Surfaces". *Wear* 254.5-6, pp. 546–554 (cit. on p. [85](#)).
- Balbuena, P. B., D. Altomare, N. Vadlamani, S. Bingi, L. A. Agapito, and J. M. Seminario (2004). "Adsorption of O, OH, and H<sub>2</sub>O on Pt-Based Bimetallic Clusters Alloyed with Co, Cr, and Ni". *The Journal of Physical Chemistry A* 108.30, pp. 6378–6384 (cit. on p. [130](#)).
- Bancaud, A., C. Lavelle, S. Huet, and J. Ellenberg (2012). "A Fractal Model for Nuclear Organization: Current Evidence and Biological Implications". *Nucleic Acids Research* 40.18, pp. 8783–8792 (cit. on p. [83](#)).
- Barabási, A.-L. and H. E. Stanley (1995). *Fractal concepts in surface growth*. Cambridge university press (cit. on p. [85](#)).
- Barber, C. B., D. P. Dobkin, and H. Huhdanpaa (1996). "The Quickhull Algorithm for Convex Hulls". *ACM Transactions on Mathematical Software* 22.4, pp. 469–483 (cit. on p. [56](#)).
- Barmparis, G. D., Z. Lodziana, N. Lopez, and I. N. Remediakis (2015). "Nanoparticle Shapes by Using Wulff Constructions and First-Principles Calculations". *Beilstein Journal of Nanotechnology* 6, pp. 361–368 (cit. on pp. [60, 94](#)).
- Barnsley, M. F., R. L. Devaney, B. B. Mandelbrot, H.-O. Peitgen, D. Saupe, R. F. Voss, Y. Fisher, and M. McGuire (1988). *The Science of Fractal Images*. Vol. 1. Springer (cit. on p. [89](#)).
- Baskes, M. I. (1992). "Modified Embedded-Atom Potentials for Cubic Materials and Impurities". *Physical Review B* 46.5, pp. 2727–2742 (cit. on p. [42](#)).
- Begau, C., A. Hartmaier, E. George, and G. Pharr (2011). "Atomistic Processes of Dislocation Generation and Plastic Deformation during Nanoindentation". *Acta Materialia* 59.3, pp. 934–942 (cit. on p. [29](#)).
- Bel Haj Salah, S., C. Gerard, and L. Pizzagalli (2017). "Influence of Surface Atomic Structure on the Mechanical Response of Aluminum Nanospheres under Compression". *Computational Materials Science* 129, pp. 273–278 (cit. on pp. [XI, 82](#)).
- Benka, O. and M. Steinbatz (2003). "Oxidation of Aluminum Studied by Secondary Electron Emission". *Surface Science* 525.1-3, pp. 207–214 (cit. on pp. [XIII, 130](#)).
- Berendsen, H. J. C., J. P. M. Postma, W. F. Van Gunsteren, A. DiNola, and J. R. Haak (1984). "Molecular Dynamics with Coupling to an External Bath". *The Journal of Chemical Physics* 81.8, pp. 3684–3690 (cit. on p. [52](#)).
- Bernal, R. A., R. Agrawal, B. Peng, K. A. Bertness, N. A. Sanford, A. V. Davydov, and H. D. Espinosa (2011). "Effect of Growth Orientation and Diameter on the Elasticity of GaN Nanowires. A Combined in Situ TEM and Atomistic Modeling Investigation". *Nano Letters* 11.2, pp. 548–555 (cit. on p. [96](#)).

## Bibliography

- Berre, I., F. Doster, and E. Keilegavlen (2019). “Flow in Fractured Porous Media: A Review of Conceptual Models and Discretization Approaches”. *Transport in Porous Media* 130.1, pp. 215–236 (cit. on p. 59).
- Besenbacher, F. and J. K. Nørskov (1993). “Oxygen Chemisorption on Metal Surfaces: General Trends for Cu, Ni and Ag”. *Progress in Surface Science* 44.1, pp. 5–66 (cit. on p. 137).
- Bian, J. J., L. Yang, X. R. Niu, and G. F. Wang (2018). “Orientation-Dependent Deformation Mechanisms of Bcc Niobium Nanoparticles”. *Philosophical Magazine* 98.20, pp. 1848–1864 (cit. on p. 33).
- Bian, J.-J. and G.-F. Wang (2013). “Atomistic Deformation Mechanisms in Copper Nanoparticles”. *Journal of Computational and Theoretical Nanoscience* 10.9, pp. 2299–2303 (cit. on pp. 32, 34).
- Bitzek, E., P. Koskinen, F. Gähler, M. Moseler, and P. Gumbsch (2006). “Structural Relaxation Made Simple”. *Physical Review Letters* 97.17, p. 170201 (cit. on p. 48).
- Bonyár, A. (2016). “AFM Characterization of the Shape of Surface Structures with Localization Factor”. *Micron* 87, pp. 1–9 (cit. on p. 85).
- Brinckmann, S., J.-Y. Kim, and J. R. Greer (2008). “Fundamental Differences in Mechanical Behavior between Two Types of Crystals at the Nanoscale”. *Physical Review Letters* 100.15, p. 155502 (cit. on pp. 15, 16).
- Brochard, S., P. Beauchamp, and J. Grilhé (2000a). “Dislocation Nucleation from Surface Steps: Atomistic Simulation in Aluminium”. *Philosophical Magazine A* 80.3, pp. 503–524 (cit. on pp. 35, 120).
- Brochard, S., P. Beauchamp, and J. Grilhé (2000b). “Stress Concentration near a Surface Step and Shear Localization”. *Physical Review B* 61.13, pp. 8707–8713 (cit. on pp. XI, 82).
- Brochard, S., P. Beauchamp, and J. Grilhé (2001). “Simulations of Dislocation Nucleation from Atomic Size Surface Steps and Grooves”. *Materials Science and Engineering: A* 309–310, pp. 456–462 (cit. on p. 35).
- Brochard, S., P. Hirel, L. Pizzagalli, and J. Godet (2010). “Elastic Limit for Surface Step Dislocation Nucleation in Face-Centered Cubic Metals: Temperature and Step Height Dependence”. *Acta Materialia* 58.12, pp. 4182–4190 (cit. on pp. XI, 36, 82).
- Brown, S. R. and C. H. Scholz (1985). “Broad Bandwidth Study of the Topography of Natural Rock Surfaces”. *Journal of Geophysical Research* 90.B14, p. 12575 (cit. on p. 83).
- Bryukhanov, I. (2020). “Dynamics of Edge Dislocation in Cu–Ni Solid Solution Alloys at Atomic Scale”. *International Journal of Plasticity* 135, p. 102834 (cit. on p. 69).
- Bush, A., R. Gibson, and T. Thomas (1975). “The Elastic Contact of a Rough Surface”. *Wear* 35.1, pp. 87–111 (cit. on p. 86).

## Bibliography

- Byggmästar, J., F. Granberg, A. Kuronen, K. Nordlund, and K. O. E. Henriksson (2015). “Tensile Testing of Fe and FeCr Nanowires Using Molecular Dynamics Simulations”. *Journal of Applied Physics* 117.1 (cit. on p. 95).
- Byggmästar, J., G. Nikoulis, A. Fellman, F. Granberg, F. Djurabekova, and K. Nordlund (2022). “Multiscale Machine-Learning Interatomic Potentials for Ferromagnetic and Liquid Iron”. *Journal of Physics: Condensed Matter* 34.30, p. 305402 (cit. on p. 42).
- Cabrera, N. and N. F. Mott (1949). “Theory of the Oxidation of Metals”. *Reports on Progress in Physics* 12.1, pp. 163–184 (cit. on pp. XIII, 130, 135).
- Campana, C. and M. H. Muser (2007). “Contact Mechanics of Real versus Randomly Rough Surfaces: A Green’s Function Molecular Dynamics Study”. *Europhysics Letters* 77.3, p. 38005 (cit. on p. 87).
- Camposilvan, E. and M. Anglada (2016). “Size and Plasticity Effects in Zirconia Micropillars Compression”. *Acta Materialia* 103, pp. 882–892 (cit. on p. 15).
- Candela, T., F. Renard, Y. Klinger, K. Mair, J. Schmittbuhl, and E. E. Brodsky (2012). “Roughness of Fault Surfaces over Nine Decades of Length Scales: FAULT ROUGHNESS”. *Journal of Geophysical Research: Solid Earth* 117.B8 (cit. on p. 83).
- Cao, K., Y. Han, H. Zhang, L. Gao, H. Yang, J. Chen, Y. Li, and Y. Lu (2018). “Size-Dependent Fracture Behavior of Silver Nanowires”. *Nanotechnology* 29.29, p. 295703 (cit. on p. 17).
- Casillas, G., A. Ponce, J. J. Velázquez-Salazar, and M. José-Yacamán (2013). “Direct Observation of Liquid-like Behavior of a Single Au Grain Boundary”. *Nanoscale* 5.14, p. 6333 (cit. on p. 21).
- Catlow, C. R. A. (1977). “Point Defect and Electronic Properties of Uranium Dioxide”. *Proceedings of the Royal Society of London. A. Mathematical and Physical Sciences* 353.1675, pp. 533–561 (cit. on p. 42).
- Chang, H.-J., M. Fivel, D. Rodney, and M. Verdier (2010). “Multiscale Modelling of Indentation in FCC Metals: From Atomic to Continuum”. *Comptes Rendus Physique* 11.3-4, pp. 285–292 (cit. on pp. 29, 76–78).
- Chechenin, N., J. Böttiger, and J. Krog (1995). “Nanoindentation of Amorphous Aluminum Oxide Films I. The Influence of the Substrate on the Plastic Properties”. *Thin Solid Films* 261.1-2, pp. 219–227 (cit. on p. 130).
- Chen, S., F. Liu, B. Liu, X. Chen, X. Ke, M. Zhang, X. Tang, P. Guan, Z. Zhang, Z. Shan, and Q. Yu (2022). “Reaching Near-Theoretical Strength by Achieving Quasi-Homogenous Surface Dislocation Nucleation in MgO Particles”. *Materials Today* 55, pp. 37–45 (cit. on pp. 27, 109).
- Cheng, G., S. Yin, T.-H. Chang, G. Richter, H. Gao, and Y. Zhu (2017). “Anomalous Tensile Detwinning in Twinned Nanowires”. *Physical Review Letters* 119.25, p. 256101 (cit. on p. 17).

## Bibliography

- Cheng, G., S. Yin, C. Li, T.-H. Chang, G. Richter, H. Gao, and Y. Zhu (2020). “In-Situ TEM Study of Dislocation Interaction with Twin Boundary and Retraction in Twinned Metallic Nanowires”. *Acta Materialia* 196, pp. 304–312 (cit. on p. 17).
- Cherian, R., C. Gerard, P. Mahadevan, N. T. Cuong, and R. Maezono (2010). “Size Dependence of the Bulk Modulus of Semiconductor Nanocrystals from First-Principles Calculations”. *Physical Review B* 82.23, p. 235321 (cit. on p. 28).
- Chevalier, S., F. Desserrey, and J. P. Larpin (2005). “Oxygen Transport during the High Temperature Oxidation of Pure Nickel”. *Oxidation of Metals* 64.3-4, pp. 219–234 (cit. on pp. XIII, 24, 130).
- Clark, B. G., D. S. Gianola, O. Kraft, and C. P. Frick (2010). “Size Independent Shape Memory Behavior of Nickel-Titanium”. *Advanced Engineering Materials* 12.8, pp. 808–815 (cit. on p. 15).
- Cococcioni, M., F. Mauri, G. Ceder, and N. Marzari (2005). “Electronic-Enthalpy Functional for Finite Systems under Pressure”. *Physical Review Letters* 94.14, p. 145501 (cit. on p. 28).
- Conesa-Boj, S., F. Boioli, E. Russo-Averchi, S. Dunand, M. Heiss, D. Rüffer, N. Wyrsch, C. Ballif, L. Miglio, and A. F. I. Morral (2014). “Plastic and Elastic Strain Fields in GaAs/Si Core–Shell Nanowires”. *Nano Letters* 14.4, pp. 1859–1864 (cit. on p. 19).
- Corcoran, S. G., R. J. Colton, E. T. Lilleodden, and W. W. Gerberich (1997). “Anomalous Plastic Deformation at Surfaces: Nanoindentation of Gold Single Crystals”. *Physical Review B* 55.24, R16057 (cit. on p. 20).
- Cordero, N. M., S. Forest, and E. P. Busso (2016). “Second Strain Gradient Elasticity of Nano-Objects”. *Journal of the Mechanics and Physics of Solids* 97, pp. 92–124 (cit. on p. 9).
- Coupeau, C., J. Michel, J. Bonneville, and M. Drouet (2020). “An Atomic-Scale Insight into Ni<sub>3</sub>Al Slip Traces”. *Materialia* 9, p. 100563 (cit. on pp. 26–28, 109).
- Cui, Y., M. Ding, T. Sui, W. Zheng, G. Qiao, S. Yan, and X. Liu (2020). “Role of Nanoparticle Materials as Water-Based Lubricant Additives for Ceramics”. *Tribology International* 142, p. 105978 (cit. on p. 8).
- Dalvi, S., A. Gujrati, S. R. Khanal, L. Pastewka, A. Dhinojwala, and T. D. Jacobs (2019). “Linking energy loss in soft adhesion to surface roughness”. *Proceedings of the National Academy of Sciences* 116.51, pp. 25484–25490 (cit. on p. 88).
- Davydok, A., B. N. Jaya, O. Robach, O. Ulrich, J.-S. Micha, and C. Kirchlechner (2016). “Analysis of the Full Stress Tensor in a Micropillar: Ability of and Difficulties Arising during Synchrotron Based Laue Diffraction”. *Materials & Design* 108, pp. 68–75 (cit. on p. 24).
- Daw, M. S. and M. I. Baskes (1984). “Embedded-Atom Method: Derivation and Application to Impurities, Surfaces, and Other Defects in Metals”. *Physical Review B* 29.12, pp. 6443–6453 (cit. on p. 42).

## Bibliography

- De Vos Burchart, E., V. Verheij, H. Van Bekkum, and B. Van De Graaf (1992). “A Consistent Molecular Mechanics Force Field for All-Silica Zeolites”. *Zeolites* 12.2, pp. 183–189 (cit. on p. 46).
- Deb Nath, S. (2014). “Elastic, Elastic–Plastic Properties of Ag, Cu and Ni Nanowires by the Bending Test Using Molecular Dynamics Simulations”. *Computational Materials Science* 87, pp. 138–144 (cit. on p. 95).
- DeCarlo, L. T. (1997). “On the Meaning and Use of Kurtosis”. *Psychological methods* 2.3, p. 292 (cit. on p. 86).
- Dehm, G., B. Jaya, R. Raghavan, and C. Kirchlechner (2018). “Overview on Micro- and Nanomechanical Testing: New Insights in Interface Plasticity and Fracture at Small Length Scales”. *Acta Materialia* 142, pp. 248–282 (cit. on pp. IX, 23–25, 63, 71).
- Dehm, G. (2009). “Miniaturized Single-Crystalline Fcc Metals Deformed in Tension: New Insights in Size-Dependent Plasticity”. *Progress in Materials Science* 54.6, pp. 664–688 (cit. on p. 15).
- Deng, C. and F. Sansoz (2009). “Near-Ideal Strength in Gold Nanowires Achieved through Microstructural Design”. *ACS Nano* 3.10, pp. 3001–3008 (cit. on p. 111).
- Devine, B., T.-R. Shan, Y.-T. Cheng, A. J. H. McGaughey, M. Lee, S. R. Phillpot, and S. B. Sinnott (2011). “Atomistic Simulations of Copper Oxidation and Cu/Cu<sub>2</sub>O Interfaces Using Charge-Optimized Many-Body Potentials”. *Physical Review B* 84.12, p. 125308 (cit. on p. 136).
- Diao, J., K. Gall, M. L. Dunn, and J. A. Zimmerman (2006). “Atomistic Simulations of the Yielding of Gold Nanowires”. *Acta Materialia* 54.3, pp. 643–653 (cit. on p. 30).
- Dimiduk, D., M. Uchic, and T. Parthasarathy (2005). “Size-Affected Single-Slip Behavior of Pure Nickel Microcrystals”. *Acta Materialia* 53.15, pp. 4065–4077 (cit. on pp. 13–15).
- Dimiduk, D. M., C. Woodward, R. LeSar, and M. D. Uchic (2006). “Scale-Free Intermittent Flow in Crystal Plasticity”. *Science* 312.5777, pp. 1188–1190 (cit. on p. 15).
- Doane, D. P. and L. E. Seward (2011). “Measuring Skewness: A Forgotten Statistic?” *Journal of Statistics Education* 19.2, p. 3 (cit. on p. 86).
- Duesbery, M. S. (1998). “Dislocation Motion, Constriction and Cross-Slip in Fcc Metals”. *Modelling and Simulation in Materials Science and Engineering* 6.1, pp. 35–49 (cit. on p. 16).
- Duparré, A., J. Ferre-Borrull, S. Gleich, G. Notni, J. Steinert, and J. M. Bennett (2002). “Surface Characterization Techniques for Determining the Root-Mean-Square Roughness and Power Spectral Densities of Optical Components”. *Applied Optics* 41.1, p. 154 (cit. on p. 85).
- Dupraz, M., G. Beutier, D. Rodney, D. Mordehai, and M. Verdier (2015). “Signature of Dislocations and Stacking Faults of Face-Centred Cubic Nanocrystals in Coherent

## Bibliography

- X-ray Diffraction Patterns: A Numerical Study". *Journal of Applied Crystallography* 48.3, pp. 621–644 (cit. on p. 111).
- Elson, J. M. and J. M. Bennett (1995). "Calculation of the Power Spectral Density from Surface Profile Data". *Applied Optics* 34.1, p. 201 (cit. on p. 101).
- Elssfah, E., C. Tang, J. Zhang, H. Song, X. Ding, and S. Qi (2007). "Low-Temperature Performance of Al<sub>4</sub>B<sub>2</sub>O<sub>9</sub> Nanowires". *Materials Research Bulletin* 42.3, pp. 482–486 (cit. on p. 8).
- Emami, A., S. Khaleghian, and S. Taheri (2021). "Asperity-Based Modification on Theory of Contact Mechanics and Rubber Friction for Self-Affine Fractal Surfaces". *Friction* 9.6, pp. 1707–1725 (cit. on p. 88).
- Erbi, M., H. Amara, and R. Gatti (2023). *Tuning Elastic Properties of Metallic Nanoparticles by Shape Controlling: From Atomistic to Continuous Models*. preprint (cit. on p. 34).
- Eslami, H. and F. Müller-Plathe (2007). "Molecular Dynamics Simulation in the Grand Canonical Ensemble". *Journal of Computational Chemistry* 28.10, pp. 1763–1773 (cit. on p. 52).
- Falk, M. L. and J. S. Langer (1998). "Dynamics of Viscoplastic Deformation in Amorphous Solids". *Physical Review E* 57.6, pp. 7192–7205 (cit. on p. 145).
- Feinauer, J., A. Spettl, I. Manke, S. Strege, A. Kwade, A. Pott, and V. Schmidt (2015). "Structural Characterization of Particle Systems Using Spherical Harmonics". *Materials Characterization* 106, pp. 123–133 (cit. on p. 89).
- Feruz, Y. and D. Mordehai (2016). "Towards a Universal Size-Dependent Strength of Face-Centered Cubic Nanoparticles". *Acta Materialia* 103, pp. 433–441 (cit. on pp. 31, 63, 70, 122).
- Fleischmann, C., F. Almeida, J. Demeter, K. Paredis, A. Teichert, R. Steitz, S. Brems, B. Opperdoes, C. Van Haesendonck, A. Vantomme, and K. Temst (2010). "The Influence of Interface Roughness on the Magnetic Properties of Exchange Biased CoO/Fe Thin Films". *Journal of Applied Physics* 107.11, p. 113907 (cit. on p. 104).
- Fleming, R. A. and M. Zou (2017). "The Effects of Confined Core Volume on the Mechanical Behavior of Al/a-Si Core-Shell Nanostructures". *Acta Materialia* 128, pp. 149–159 (cit. on p. 20).
- Foiles, S. M., M. I. Baskes, and M. S. Daw (1986). "Embedded-Atom-Method Functions for the Fcc Metals Cu, Ag, Au, Ni, Pd, Pt, and Their Alloys". *Physical Review B* 33.12, pp. 7983–7991 (cit. on p. 42).
- Foy, N., E. Chevallier, H. Zerari, D. Zehouani, and D. Favry (2020). "Electrical Probing of a Steel Rough Interface under Shear Stress". *Tribology International* 151, p. 106432 (cit. on p. 104).

## Bibliography

- Frank, F. C. and B. R. Lawn (1967). "On the Theory of Hertzian Fracture". *Proceedings of the Royal Society of London. Series A. Mathematical and Physical Sciences* 299.1458, pp. 291–306 (cit. on p. [76](#)).
- Frick, C., B. Clark, S. Orso, A. Schneider, and E. Arzt (2008). "Size Effect on Strength and Strain Hardening of Small-Scale [111] Nickel Compression Pillars". *Materials Science and Engineering: A* 489.1-2, pp. 319–329 (cit. on p. [15](#)).
- Fu, T., X. Peng, C. Huang, S. Weng, Y. Zhao, Z. Wang, and N. Hu (2017). "Strain Rate Dependence of Tension and Compression Behavior in Nano-Polycrystalline Vanadium Nitride". *Ceramics International* 43.15, pp. 11635–11641 (cit. on p. [72](#)).
- Fusco, C., T. Albaret, and A. Tanguy (2010). "Role of Local Order in the Small-Scale Plasticity of Model Amorphous Materials". *Physical Review E* 82.6, p. 066116 (cit. on p. [145](#)).
- Gao, J., W. D. Luedtke, D. Gourdon, M. Ruths, J. N. Israelachvili, and U. Landman (2004). "Frictional Forces and Amontons' Law: From the Molecular to the Macroscopic Scale". *The Journal of Physical Chemistry B* 108.11, pp. 3410–3425 (cit. on p. [88](#)).
- Gao, Y., W. Wang, S. Chang, and W. Huang (2013). "Morphology Effect of CeO<sub>2</sub> Support in the Preparation, Metal-Support Interaction, and Catalytic Performance of Pt/CeO<sub>2</sub> Catalysts". *ChemCatChem* 5.12, pp. 3610–3620 (cit. on p. [82](#)).
- Garruchet, S., O. Politano, P. Arnoux, and V. Vignal (2010). "A Variable Charge Molecular Dynamics Study of the Initial Stage of Nickel Oxidation". *Applied Surface Science* 256.20, pp. 5968–5972 (cit. on pp. [38](#), [130](#), [136](#), [137](#)).
- Gattinoni, C. and A. Michaelides (2015). "Atomistic Details of Oxide Surfaces and Surface Oxidation: The Example of Copper and Its Oxides". *Surface Science Reports* 70.3, pp. 424–447 (cit. on pp. [38](#), [130](#), [137](#)).
- Gentili, D., G. Foschi, F. Valle, M. Cavallini, and F. Biscarini (2012). "Applications of Dewetting in Micro and Nanotechnology". *Chemical Society Reviews* 41.12, p. 4430 (cit. on p. [131](#)).
- Gerberich, W., E. B. Tadmor, J. Kysar, J. A. Zimmerman, A. M. Minor, I. Szlufarska, J. Amodeo, B. Devincre, E. Hintsala, and R. Ballarini (2017). "Review Article: Case Studies in Future Trends of Computational and Experimental Nanomechanics". *Journal of Vacuum Science & Technology A: Vacuum, Surfaces, and Films* 35.6, p. 060801 (cit. on pp. [IX](#), [22](#), [23](#)).
- Geuzaine, C. and J.-F. Remacle (2009). "Gmsh: A 3-D Finite Element Mesh Generator with Built-in Pre- and Post-Processing Facilities: THE GMSH PAPER". *International Journal for Numerical Methods in Engineering* 79.11, pp. 1309–1331 (cit. on pp. [59](#), [91](#)).
- GNU (2007). *GNU General Public License, Version 3* (cit. on p. [91](#)).

## Bibliography

- Goryaeva, A. M., C. Fusco, M. Bugnet, and J. Amodeo (2019). “Influence of an Amorphous Surface Layer on the Mechanical Properties of Metallic Nanoparticles under Compression”. *Physical Review Materials* 3.3, p. 033606 (cit. on pp. 31, 56, 144).
- Gouldstone, A., N. Chollacoop, M. Dao, J. Li, A. Minor, and Y. Shen (2007). “Indentation across Size Scales and Disciplines: Recent Developments in Experimentation and Modeling”. *Acta Materialia* 55.12, pp. 4015–4039 (cit. on pp. 73, 79).
- Gouldstone, A., H.-J. Koh, K.-Y. Zeng, A. Giannakopoulos, and S. Suresh (2000). “Discrete and Continuous Deformation during Nanoindentation of Thin Films”. *Acta Materialia* 48.9, pp. 2277–2295 (cit. on pp. 73, 77, 79).
- Gouldstone, A., K. J. Van Vliet, and S. Suresh (2001). “Simulation of Defect Nucleation in a Crystal”. *Nature* 411.6838, pp. 656–656 (cit. on pp. XI, 82).
- Greenwood, J. (1966). “Fundamentals of Friction, Macroscopic and Microscopic Processes, edited by IL Singer and HM Polack Kluwer, Dordrecht, 1992; JA Greenwood and JBP Williamson”. *Proc. R. Soc. London, Ser. A* 295, p. 300 (cit. on p. 87).
- Greenwood, J. A. and J. P. Williamson (1966). “Contact of Nominally Flat Surfaces”. *Proceedings of the Royal Society of London. Series A. Mathematical and Physical Sciences* 295.1442, pp. 300–319 (cit. on p. 86).
- Greer, A., Y. Cheng, and E. Ma (2013). “Shear Bands in Metallic Glasses”. *Materials Science and Engineering: R: Reports* 74.4, pp. 71–132 (cit. on p. 8).
- Greer, J. R. and J. T. De Hosson (2011). “Plasticity in Small-Sized Metallic Systems: Intrinsic versus Extrinsic Size Effect”. *Progress in Materials Science* 56.6, pp. 654–724 (cit. on pp. VII, IX, 8, 16, 22, 23).
- Greer, J. R. and W. D. Nix (2006). “Nanoscale Gold Pillars Strengthened through Dislocation Starvation”. *Physical Review B* 73.24, p. 245410 (cit. on p. 15).
- Greer, J. R., W. C. Oliver, and W. D. Nix (2005). “Size Dependence of Mechanical Properties of Gold at the Micron Scale in the Absence of Strain Gradients”. *Acta Materialia* 53.6, pp. 1821–1830 (cit. on pp. 13, 15, 79).
- Greer, J. R., C. R. Weinberger, and W. Cai (2008). “Comparing the Strength of f.c.c. and b.c.c. Sub-Micrometer Pillars: Compression Experiments and Dislocation Dynamics Simulations”. *Materials Science and Engineering: A* 493.1-2, pp. 21–25 (cit. on p. 15).
- Grochola, G., S. P. Russo, and I. K. Snook (2005). “On Fitting a Gold Embedded Atom Method Potential Using the Force Matching Method”. *The Journal of Chemical Physics* 123.20, p. 204719 (cit. on pp. 43, 65, 111).
- Grosch, K. A. (1963). “The Relation between the Friction and Visco-Elastic Properties of Rubber”. *Proceedings of the Royal Society of London. Series A. Mathematical and Physical Sciences* 274.1356, pp. 21–39 (cit. on p. 87).
- Guénolé, J., W. G. Nöhring, A. Vaid, F. Houllé, Z. Xie, A. Prakash, and E. Bitzek (2020). “Assessment and Optimization of the Fast Inertial Relaxation Engine (Fire) for En-

## Bibliography

- ergy Minimization in Atomistic Simulations and Its Implementation in Lammps". *Computational Materials Science* 175, p. 109584 (cit. on p. [48](#)).
- Gumir, F. J., K. Al-Farhany, W. Jamshed, E. S. M. Tag El Din, and A. Abd-Elmonem (2022). "Natural Convection in a Porous Cavity Filled (35%MWCNT-65% Fe<sub>3</sub>O<sub>4</sub>)/Water Hybrid Nanofluid with a Solid Wavy Wall via Galerkin Finite-Element Process". *Scientific Reports* 12.1, p. 17794 (cit. on p. [59](#)).
- Gurrutxaga-Lerma, B., J. Verschueren, A. P. Sutton, and D. Dini (2021). "The Mechanics and Physics of High-Speed Dislocations: A Critical Review". *International Materials Reviews* 66.4, pp. 215–255 (cit. on p. [69](#)).
- Haase, J., B. Hillert, L. Becker, and M. Pedio (1992). "A SEXAFS Study of the p(2 × 2)-O/Ni(111) System". *Surface Science* 262.1-2, pp. 8–14 (cit. on p. [137](#)).
- Hallil, A., R. Tétot, F. Berthier, I. Braems, and J. Creuze (2006). "Use of a Variable-Charge Interatomic Potential for Atomistic Simulations of Bulk, Oxygen Vacancies, and Surfaces of Rutile TiO<sub>2</sub>". *Physical Review B* 73.16, p. 165406 (cit. on p. [42](#)).
- Han, S. M., T. Bozorg-Grayeli, J. R. Groves, and W. D. Nix (2010). "Size Effects on Strength and Plasticity of Vanadium Nanopillars". *Scripta Materialia* 63.12, pp. 1153–1156 (cit. on p. [15](#)).
- Han, W.-Z., L. Huang, S. Ogata, H. Kimizuka, Z.-C. Yang, C. Weinberger, Q.-J. Li, B.-Y. Liu, X.-X. Zhang, J. Li, E. Ma, and Z.-W. Shan (2015). "From "Smaller Is Stronger" to "Size-Independent Strength Plateau": Towards Measuring the Ideal Strength of Iron". *Advanced Materials* 27.22, pp. 3385–3390 (cit. on pp. [X](#), [XIII](#), [18](#), [25](#), [26](#), [63](#), [67](#), [130](#)).
- Hanrath, T. and B. A. Korgel (2005). "Crystallography and Surface Faceting of Germanium Nanowires". *Small* 1.7, pp. 717–721 (cit. on p. [96](#)).
- Hara, S., S. Izumi, and S. Sakai (2009). "Reaction Pathway Analysis for Dislocation Nucleation from a Ni Surface Step". *Journal of Applied Physics* 106.9, p. 093507 (cit. on pp. [36](#), [120](#)).
- Hasegawa, M., J. Liu, K. Okuda, and M. Nunobiki (1996). "Calculation of the Fractal Dimensions of Machined Surface Profiles". *Wear* 192.1-2, pp. 40–45 (cit. on p. [83](#)).
- Hatzell, M. C., M. Raju, V. J. Watson, A. G. Stack, A. C. T. Van Duin, and B. E. Logan (2014). "Effect of Strong Acid Functional Groups on Electrode Rise Potential in Capacitive Mixing by Double Layer Expansion". *Environmental Science & Technology* 48.23, pp. 14041–14048 (cit. on p. [44](#)).
- Hay, J., P. Agee, and E. Herbert (2010). "Continuous Stiffness Measurement during Instrumented Indentation Testing". *Experimental Techniques* 34.3, pp. 86–94 (cit. on p. [24](#)).
- Heinrich, G., M. Klüppel, and T. Vilgis (2000). "Evaluation of Self-Affine Surfaces and Their Implication for Frictional Dynamics as Illustrated with a Rouse Material". *Computational and Theoretical Polymer Science* 10.1-2, pp. 53–61 (cit. on p. [87](#)).

## Bibliography

- Hemker, K. and W. Sharpe (2007). "Microscale Characterization of Mechanical Properties". *Annual Review of Materials Research* 37.1, pp. 93–126 (cit. on pp. [IX](#), [63](#)).
- Henry, C. R. (2005). "Morphology of Supported Nanoparticles". *Progress in Surface Science* 80.3-4, pp. 92–116 (cit. on p. [110](#)).
- Herre, P., J. Will, M. Dierner, D. Wang, T. Yokosawa, T. Zech, M. Wu, T. Przybilla, S. Romeis, T. Unruh, W. Peukert, and E. Specker (2021). "Rapid Fabrication and Interface Structure of Highly Faceted Epitaxial Ni-Au Solid Solution Nanoparticles on Sapphire". *Acta Materialia* 220, p. 117318 (cit. on p. [26](#)).
- Hertz, H. (1896). *Hertz's Miscellaneous Papers, chapters 5 and 6*. ed: Macmillan, London, UK (cit. on p. [86](#)).
- Hirel, P. (2015). "Atomsk: A Tool for Manipulating and Converting Atomic Data Files". *Computer Physics Communications* 197, pp. 212–219 (cit. on pp. [53](#), [60](#), [91](#)).
- Hirel, P., S. Brochard, L. Pizzagalli, and P. Beauchamp (2007). "Effects of Temperature and Surface Step on the Incipient Plasticity in Strained Aluminium Studied by Atomistic Simulations". *Scripta Materialia* 57.12, pp. 1141–1144 (cit. on pp. [36](#), [120](#)).
- Hjorth Larsen, A., J. Jørgen Mortensen, J. Blomqvist, I. E. Castelli, R. Christensen, M. Dułak, J. Friis, M. N. Groves, B. Hammer, C. Hargus, E. D. Hermes, P. C. Jennings, P. Bjerre Jensen, J. Kermode, J. R. Kitchin, E. Leonhard Kolsbjerg, J. Kubal, K. Kaasbjerg, S. Lysgaard, J. Bergmann Maronsson, T. Maxson, T. Olsen, L. Pastewka, A. Peterson, C. Rostgaard, J. Schiøtz, O. Schütt, M. Strange, K. S. Thygesen, T. Vegge, L. Vilhelmsen, M. Walter, Z. Zeng, and K. W. Jacobsen (2017). "The Atomic Simulation Environment—a Python Library for Working with Atoms". *Journal of Physics: Condensed Matter* 29.27, p. 273002 (cit. on p. [94](#)).
- Holloway, P. and J. Hudson (1974). "Kinetics of the Reaction of Oxygen with Clean Nickel Single Crystal Surfaces". *Surface Science* 43.1, pp. 123–140 (cit. on p. [136](#)).
- Hoover, W. G. and B. L. Holian (1996). "Kinetic Moments Method for the Canonical Ensemble Distribution". *Physics Letters A* 211.5, pp. 253–257 (cit. on p. [51](#)).
- Hu, T. Y., B. L. Zheng, M. Y. Hu, P. F. He, and Z. F. Yue (2015). "Molecular Dynamics Simulation of Incipient Plasticity of Nickel Substrates of Different Surface Orientations during Nanoindentation". *Materials Science and Technology* 31.3, pp. 325–331 (cit. on p. [29](#)).
- Hu, Y. and K. Tonder (1992). "Simulation of 3-D Random Rough Surface by 2-D Digital Filter and Fourier Analysis". *International Journal of Machine Tools and Manufacture* 32.1-2, pp. 83–90 (cit. on p. [82](#)).
- Hudson, J. B. (1998). *Surface science: an introduction*. John Wiley & Sons (cit. on p. [59](#)).
- Hyde, B., H. D. Espinosa, and D. Farkas (2005). "An Atomistic Investigation of Elastic and Plastic Properties of Au Nanowires". *JOM* 57.9, pp. 62–66 (cit. on p. [30](#)).

## Bibliography

- Hyun, S., L. Pei, J.-F. Molinari, and M. O. Robbins (2004). “Finite-Element Analysis of Contact between Elastic Self-Affine Surfaces”. *Physical Review E* 70.2, p. 026117 (cit. on p. 87).
- Hyun, S. and M. O. Robbins (2007). “Elastic Contact between Rough Surfaces: Effect of Roughness at Large and Small Wavelengths”. *Tribology International* 40.10-12, pp. 1413–1422 (cit. on p. 87).
- Iijima, S. (1985). “Electron Microscopy of Small Particles”. *Journal of Electron Microscopy* 34.4, pp. 249–265 (cit. on pp. XII, 26–28, 109, 110).
- Issa, I., J. Amodeo, J. Réthoré, L. Joly-Pottuz, C. Esnouf, J. Morthomas, M. Perez, J. Chevalier, and K. Masenelli-Varlot (2015). “In Situ Investigation of MgO Nanocube Deformation at Room Temperature”. *Acta Materialia* 86, pp. 295–304 (cit. on pp. X, 19, 20, 54, 63, 65, 67, 109, 111).
- Issa, I., L. Joly-Pottuz, J. Amodeo, D. J. Dunstan, C. Esnouf, J. Réthoré, V. Garnier, J. Chevalier, and K. Masenelli-Varlot (2021). “From Dislocation Nucleation to Dislocation Multiplication in Ceramic Nanoparticle”. *Materials Research Letters* 9.6, pp. 278–283 (cit. on pp. X, 19, 22, 63, 67, 109).
- Iteney, H., T. W. Cornelius, O. Thomas, and J. Amodeo (2023). “Load versus Displacement-Controlled Nanocompression: Insights from Atomistic Simulations”. *Scripta Materialia* 226, p. 115245 (cit. on pp. 62, 111, 122).
- Iteney, H., J. A. Gonzalez Joa, C. Le Bourlot, T. W. Cornelius, O. Thomas, and J. Amodeo (2024). “Pyrough: A Tool to Build 3D Samples with Rough Surfaces for Atomistic and Finite-Element Simulations”. *Computer Physics Communications* 295, p. 108958 (cit. on pp. 60, 81).
- Jacobs, T. D. B., T. Junge, and L. Pastewka (2017). “Quantitative Characterization of Surface Topography Using Spectral Analysis”. *Surface Topography: Metrology and Properties* 5.1, p. 013001 (cit. on pp. XI, 82, 84, 88, 101).
- Jacobs, T. D. B. and A. Martini (2017). “Measuring and Understanding Contact Area at the Nanoscale: A Review”. *Applied Mechanics Reviews* 69.6, p. 060802 (cit. on pp. 56, 88).
- Jacobs, T. D. B., K. E. Ryan, P. L. Keating, D. S. Grierson, J. A. Lefever, K. T. Turner, J. A. Harrison, and R. W. Carpick (2013). “The Effect of Atomic-Scale Roughness on the Adhesion of Nanoscale Asperities: A Combined Simulation and Experimental Investigation”. *Tribology Letters* 50.1, pp. 81–93 (cit. on pp. 37, 88).
- Jeng, Y.-R. (1990). “Experimental Study of the Effects of Surface Roughness on Friction”. *Tribology Transactions* 33.3, pp. 402–410 (cit. on p. 82).
- Jennings, A. T., M. J. Burek, and J. R. Greer (2010). “Microstructure versus Size: Mechanical Properties of Electroplated Single Crystalline Cu Nanopillars”. *Physical Review Letters* 104.13, p. 135503 (cit. on pp. 15, 17, 27).

## Bibliography

- Jeon, B., S. K. Sankaranarayanan, A. C. van Duin, and S. Ramanathan (2011). “Influence of Surface Orientation and Defects on Early-Stage Oxidation and Ultrathin Oxide Growth on Pure Copper”. *Philosophical Magazine* 91.32, pp. 4073–4088 (cit. on pp. 38, 136, 140).
- Jeurgens, L., W. Sloof, F. Tichelaar, C. Borsboom, and E. Mittemeijer (1999). “Determination of Thickness and Composition of Aluminium-Oxide Overlayers on Aluminium Substrates”. *Applied Surface Science* 144–145, pp. 11–15 (cit. on pp. XIII, 130).
- Johnson, K. L. (1987). *Contact Mechanics*. Cambridge university press (cit. on p. 76).
- Kanafi, M. M. (2023). *Surface Generator: Artificial Randomly Rough Surfaces*. MATLAB Central File Exchange (cit. on pp. XI, 82).
- Khorasani, A. M., M. R. S. Yazdi, and M. S. Safizadeh (2012). “Analysis of Machining Parameters Effects on Surface Roughness: A Review”. *International Journal of Computational Materials Science and Surface Engineering* 5.1, p. 68 (cit. on p. 82).
- Khoroshilov, V. S., D. M. Kazantsev, V. L. Alperovich, C. Coupeau, and M. Drouet (2022). “Asymmetry of Anticrossing between Atomic Steps on Metal and Semiconductor Surfaces”. *Journal of Physics: Conference Series* 2227.1, p. 012008 (cit. on pp. 26, 109).
- Kiani, M. T., R. P. Patil, and X. W. Gu (2019). “Dislocation Surface Nucleation in Surfactant-Passivated Metallic Nanocubes”. *MRS Communications* 9.3, pp. 1029–1033 (cit. on p. 27).
- Kiener, D., W. Grosinger, G. Dehm, and R. Pippan (2008). “A Further Step towards an Understanding of Size-Dependent Crystal Plasticity: In Situ Tension Experiments of Miniaturized Single-Crystal Copper Samples”. *Acta Materialia* 56.3, pp. 580–592 (cit. on p. 15).
- Kiener, D., C. Motz, M. Rester, M. Jenko, and G. Dehm (2007). “FIB Damage of Cu and Possible Consequences for Miniaturized Mechanical Tests”. *Materials Science and Engineering: A* 459.1-2, pp. 262–272 (cit. on p. 23).
- Kiener, D., C. Motz, T. Schöberl, M. Jenko, and G. Dehm (2006). “Determination of Mechanical Properties of Copper at the Micron Scale”. *Advanced Engineering Materials* 8.11, pp. 1119–1125 (cit. on pp. 13, 15).
- Kilymis, D., C. Gérard, J. Amodeo, U. Waghmare, and L. Pizzagalli (2018). “Uniaxial Compression of Silicon Nanoparticles: An Atomistic Study on the Shape and Size Effects”. *Acta Materialia* 158, pp. 155–166 (cit. on pp. XI, 20, 34, 35, 82, 105, 116, 127).
- Kim, H., Y.-H. Park, I. Kim, J. Kim, H.-J. Choi, and W. Kim (2011). “Effect of Surface Roughness on Thermal Conductivity of VLS-grown Rough Si<sub>1-x</sub>Ge<sub>x</sub> Nanowires”. *Applied Physics A* 104.1, pp. 23–28 (cit. on p. 105).
- Kim, S.-H., H.-K. Kim, J.-H. Seo, D.-M. Whang, J.-P. Ahn, and J.-C. Lee (2018). “Deformation Twinning of Ultrahigh Strength Aluminum Nanowire”. *Acta Materialia* 160, pp. 14–21 (cit. on pp. XII, 17, 109).

## Bibliography

- Kim, T. and A. Olver (1998). "Stress History in Rolling–Sliding Contact of Rough Surfaces". *Tribology International* 31.12, pp. 727–736 (cit. on p. [103](#)).
- Kim, J.-Y. and J. R. Greer (2008). "Size-Dependent Mechanical Properties of Molybdenum Nanopillars". *Applied Physics Letters* 93.10, p. 101916 (cit. on pp. [13](#), [16](#), [17](#)).
- Kim, J.-Y. and J. R. Greer (2009). "Tensile and Compressive Behavior of Gold and Molybdenum Single Crystals at the Nano-Scale". *Acta Materialia* 57.17, pp. 5245–5253 (cit. on p. [15](#)).
- Kim, J.-Y., D. Jang, and J. R. Greer (2009). "Insight into the Deformation Behavior of Niobium Single Crystals under Uniaxial Compression and Tension at the Nanoscale". *Scripta Materialia* 61.3, pp. 300–303 (cit. on p. [15](#)).
- Kim, Y. and J. Choi (2021). "Oxide Growth Characteristics on Al (100), (110), and (111) Surfaces: A Chemo-Mechanical Evaluation". *Materials Today Communications* 26, p. 102006 (cit. on p. [38](#)).
- Kirchlechner, C., J. Keckes, C. Motz, W. Grosinger, M. Kapp, J. Micha, O. Ulrich, and G. Dehm (2011). "Impact of Instrumental Constraints and Imperfections on the Dislocation Structure in Micron-Sized Cu Compression Pillars". *Acta Materialia* 59.14, pp. 5618–5626 (cit. on pp. [24](#), [25](#)).
- Komanduri, R., N. Chandrasekaran, and L. Raff (2001). "Molecular Dynamics (MD) Simulation of Uniaxial Tension of Some Single-Crystal Cubic Metals at Nanolevel". *International Journal of Mechanical Sciences* 43.10, pp. 2237–2260 (cit. on p. [9](#)).
- Korte, S. and W. Clegg (2009). "Micropillar Compression of Ceramics at Elevated Temperatures". *Scripta Materialia* 60.9, pp. 807–810 (cit. on p. [15](#)).
- Kositski, R., O. Kovalenko, S.-W. Lee, J. R. Greer, E. Rabkin, and D. Mordehai (2016). "Cross-Split of Dislocations: An Athermal and Rapid Plasticity Mechanism". *Scientific Reports* 6.1, p. 25966 (cit. on pp. [XIII](#), [63](#), [130](#)).
- Kovalenko, O., C. Brandl, L. Klinger, and E. Rabkin (2017). "Self-Healing and Shape Memory Effects in Gold Microparticles through the Defects-Mediated Diffusion". *Advanced Science* 4.8, p. 1700159 (cit. on p. [110](#)).
- Kraft, O., P. A. Gruber, R. Mönig, and D. Weygand (2010). "Plasticity in Confined Dimensions". *Annual Review of Materials Research* 40, pp. 293–317 (cit. on pp. [22](#), [23](#)).
- Kulkarni, G. U., C. N. R. Rao, and M. W. Roberts (1995). "Nature of the Oxygen Species at Ni(110) and Ni(100) Surfaces Revealed by Exposure to Oxygen and Oxygen-Ammonia Mixtures: Evidence for the Surface Reactivity of O- Type Species". *The Journal of Physical Chemistry* 99.10, pp. 3310–3316 (cit. on pp. [XIII](#), [130](#)).
- Lai, Y., C. Lee, Y. Cheng, H. Chou, H. Chen, X. Du, C. Chang, J. Huang, S. Jian, J. Jang, and T. Nieh (2008). "Bulk and Microscale Compressive Behavior of a Zr-based Metallic Glass". *Scripta Materialia* 58.10, pp. 890–893 (cit. on p. [15](#)).

## Bibliography

- Lam, T.-N., S. Y. Lee, N.-T. Tsou, H.-S. Chou, B.-H. Lai, Y.-J. Chang, R. Feng, T. Kawasaki, S. Harjo, P. K. Liaw, A.-C. Yeh, M.-J. Li, R.-F. Cai, S.-C. Lo, and E.-W. Huang (2020). “Enhancement of Fatigue Resistance by Overload-Induced Deformation Twinning in a CoCrFeMnNi High-Entropy Alloy”. *Acta Materialia* 201, pp. 412–424 (cit. on p. 17).
- Landefeld, A., W. M. Mook, J. Rösler, and J. Michler (2012). “Compression Experiments on -Nanoparticles”. *ISRN Nanomaterials* 2012, pp. 1–4 (cit. on pp. 27, 28).
- Lao, J., M. Naghdi Tam, D. Pinisetty, and N. Gupta (2013). “Molecular Dynamics Simulation of FCC Metallic Nanowires: A Review”. *JOM* 65.2, pp. 175–184 (cit. on pp. 30, 34).
- Larsen, P. M., S. Schmidt, and J. Schiøtz (2016). “Robust Structural Identification via Polyhedral Template Matching”. *Modelling and Simulation in Materials Science and Engineering* 24.5, p. 055007 (cit. on p. 61).
- Lauraux, F., S. Labat, M.-I. Richard, S. J. Leake, T. Zhou, O. Kovalenko, E. Rabkin, T. U. Schülli, O. Thomas, and T. W. Cornelius (2022). “In Situ Nano-Indentation of a Gold Sub-Micrometric Particle Imaged by Multi-Wavelength Bragg Coherent X-ray Diffraction”. *Materials* 15.18, p. 6195 (cit. on p. 110).
- Lawless, K. R. (1974). “The Oxidation of Metals”. *Reports on Progress in Physics* 37.2, pp. 231–316 (cit. on p. 135).
- Lee, C. J., J. C. Huang, and T. G. Nieh (2007). “Sample Size Effect and Microcompression of Mg<sub>65</sub>Cu<sub>25</sub>Gd<sub>10</sub> Metallic Glass”. *Applied Physics Letters* 91.16, p. 161913 (cit. on p. 15).
- Lee, S., J. Im, Y. Yoo, E. Bitzek, D. Kiener, G. Richter, B. Kim, and S. H. Oh (2014). “Reversible Cyclic Deformation Mechanism of Gold Nanowires by Twinning–Detwinning Transition Evidenced from in Situ TEM”. *Nature Communications* 5.1, p. 3033 (cit. on p. 18).
- Legros, M. (2014). “In Situ Mechanical TEM: Seeing and Measuring under Stress with Electrons”. *Comptes Rendus Physique* 15.2-3, pp. 224–240 (cit. on pp. IX, 63).
- Leroy, F., Ł. Borowik, F. Cheynis, Y. Almadori, S. Curiotto, M. Trautmann, J. Barbé, and P. Müller (2016). “How to Control Solid State Dewetting: A Short Review”. *Surface Science Reports* 71.2, pp. 391–409 (cit. on p. 131).
- Li, C., G. Cheng, H. Wang, and Y. Zhu (2020a). “Microelectromechanical Systems for Nanomechanical Testing: Displacement- and Force-Controlled Tensile Testing with Feedback Control”. *Experimental Mechanics* 60.7, pp. 1005–1015 (cit. on p. 24).
- Li, J., G. Vizkelethy, P. Revesz, J. W. Mayer, and K. N. Tu (1991). “Oxidation and Reduction of Copper Oxide Thin Films”. *Journal of Applied Physics* 69.2, pp. 1020–1029 (cit. on p. 24).

## Bibliography

- Li, J., X. Lu, C. G. Farquharson, and X. Hu (2018). “A Finite-Element Time-Domain Forward Solver for Electromagnetic Methods with Complex-Shaped Loop Sources”. *Geophysics* 83.3, E117–E132 (cit. on p. 60).
- Li, L., L. Luo, J. Ciston, W. A. Saidi, E. A. Stach, J. C. Yang, and G. Zhou (2014). “Surface-Step-Induced Oscillatory Oxide Growth”. *Physical Review Letters* 113.13, p. 136104 (cit. on p. 142).
- Li, X., T. Huang, D. E. Heath, N. M. O’Brien-Simpson, and A. J. O’Connor (2020b). “Antimicrobial nanoparticle coatings for medical implants: Design challenges and prospects”. *Biointerphases* 15.6 (cit. on p. 8).
- Li, Y., A. J. Bushby, and D. J. Dunstan (2016a). “The Hall–Petch Effect as a Manifestation of the General Size Effect”. *Proceedings of the Royal Society A: Mathematical, Physical and Engineering Sciences* 472.2190, p. 20150890 (cit. on p. 22).
- Li, Y., X. Fang, S. Lu, Q. Yu, G. Hou, and X. Feng (2016b). “Effects of Creep and Oxidation on Reduced Modulus in High-Temperature Nanoindentation”. *Materials Science and Engineering: A* 678, pp. 65–71 (cit. on p. 130).
- Liang, W. and M. Zhou (2006). “Atomistic Simulations Reveal Shape Memory of Fcc Metal Nanowires”. *Physical Review B* 73.11, p. 115409 (cit. on p. 30).
- Lilleodden, E. (2010). “Microcompression Study of Mg (0001) Single Crystal”. *Scripta Materialia* 62.8, pp. 532–535 (cit. on p. 15).
- Lim, Y. (2023). *Generating Rough Surface for Abaqus Using MATLAB*. MATLAB Central File Exchange (cit. on pp. XI, 82).
- Lin, B., Y. Liu, L. Heng, X. Wang, J. Ni, J. Lin, and L. Jiang (2018). “Morphology Effect of Ceria on the Catalytic Performances of Ru/CeO<sub>2</sub> Catalysts for Ammonia Synthesis”. *Industrial & Engineering Chemistry Research* 57.28, pp. 9127–9135 (cit. on p. 82).
- Long, X., W. Tang, Y. Feng, C. Chang, L. M. Keer, and Y. Yao (2018). “Strain Rate Sensitivity of Sintered Silver Nanoparticles Using Rate-Jump Indentation”. *International Journal of Mechanical Sciences* 140, pp. 60–67 (cit. on p. 72).
- López-Beltrán, A. and A. Mendoza-Galván (2006). “The Oxidation Kinetics of Nickel Thin Films Studied by Spectroscopic Ellipsometry”. *Thin Solid Films* 503.1-2, pp. 40–44 (cit. on p. 24).
- Lorenz, B., Y. R. Oh, S. K. Nam, S. H. Jeon, and B. N. J. Persson (2015). “Rubber Friction on Road Surfaces: Experiment and Theory for Low Sliding Speeds”. *The Journal of Chemical Physics* 142.19, p. 194701 (cit. on p. 87).
- Lu, H., Y. Ni, J. Mei, J. Li, and H. Wang (2012). “Anisotropic Plastic Deformation beneath Surface Step during Nanoindentation of FCC Al by Multiscale Analysis”. *Computational Materials Science* 58, pp. 192–200 (cit. on p. 120).
- Lu, A.-H., E. L. Salabas, and F. Schüth (2007). “Magnetic Nanoparticles: Synthesis, Protection, Functionalization, and Application”. *Angewandte Chemie International Edition* 46.8, pp. 1222–1244 (cit. on p. 8).

## Bibliography

- Lu, X., T. Ma, M. Zeng, Y. Chen, and Q. W. Wang (2015). "Study on Physicochemical Mechanism of Nickel Surface Oxidation Behavior under High Temperature Condition by Using Molecular Dynamic Method". *International Conference on Heat Exchanger Fouling and Cleaning* (cit. on pp. 38, 136).
- Luan, B. and M. O. Robbins (2005). "The Breakdown of Continuum Models for Mechanical Contacts". *Nature* 435.7044, pp. 929–932 (cit. on p. 37).
- Luan, B. and M. O. Robbins (2006). "Contact of Single Asperities with Varying Adhesion: Comparing Continuum Mechanics to Atomistic Simulations". *Physical Review E* 74.2, p. 026111 (cit. on p. 37).
- Luo, L., L. Zou, D. K. Schreiber, M. J. Olszta, D. R. Baer, S. M. Bruemmer, G. Zhou, and C.-M. Wang (2016). "In Situ Atomic Scale Visualization of Surface Kinetics Driven Dynamics of Oxide Growth on a Ni–Cr Surface". *Chemical Communications* 52.16, pp. 3300–3303 (cit. on p. 142).
- Luu, H.-T., S. Raumel, F. Dencker, M. Wurz, and N. Merkert (2022). "Nanoindentation in Alumina Coated Al: Molecular Dynamics Simulations and Experiments". *Surface and Coatings Technology* 437, p. 128342 (cit. on pp. 130, 144).
- Ma, Y., X. Zhang, P. Zheng, E. Ni, Y. Wang, Y. Jiang, and H. Li (2021). "Structural Transformation from Low-Coordinated Oxides to High-Coordinated Oxides during the Oxidation of Cu Nanoparticles". *The Journal of Physical Chemistry C* 125.16, pp. 8759–8766 (cit. on p. 140).
- Maioli, P., T. Stoll, H. E. Sauceda, I. Valencia, A. Demessence, F. Bertorelle, A. Crut, F. Vallée, I. L. Garzón, G. Cerullo, and N. Del Fatti (2018). "Mechanical Vibrations of Atomically Defined Metal Clusters: From Nano- to Molecular-Size Oscillators". *Nano Letters* 18.11, pp. 6842–6849 (cit. on p. 28).
- Mandelbrot, B. B. (1985). "Self-Affine Fractals and Fractal Dimension". *Physica Scripta* 32.4, pp. 257–260 (cit. on pp. XI, 60, 82, 84).
- Mandelbrot, B. B. (1967). "How Long Is the Coast of Britain? Statistical Self-Similarity and Fractional Dimension". *Science* 156.3775, pp. 636–638 (cit. on p. 83).
- Mandelbrot, B. B. (1982). *The fractal geometry of nature*. Vol. 1. WH freeman New York (cit. on p. 83).
- Mandelbrot, B. B., Dann. E. Passoja, and A. J. Paullay (1984). "Fractal Character of Fracture Surfaces of Metals". *Nature* 308.5961, pp. 721–722 (cit. on pp. 83, 84).
- Mandelbrot, B. B. and J. W. Van Ness (1968). "Fractional Brownian Motions, Fractional Noises and Applications". *SIAM Review* 10.4, pp. 422–437 (cit. on p. 84).
- Mareschal, J.-C. (1989). "Fractal Reconstruction of Sea-Floor Topography". *Fractals in Geophysics* 131.1-2, pp. 197–210 (cit. on p. 83).
- Marian, J. and A. Caro (2006). "Moving Dislocations in Disordered Alloys: Connecting Continuum and Discrete Models with Atomistic Simulations". *Physical Review B* 74.2, p. 024113 (cit. on p. 69).

## Bibliography

- Marshak, A., A. Davis, W. Wiscombe, and R. Cahalan (1995). “Radiative Smoothing in Fractal Clouds”. *Journal of Geophysical Research* 100.D12, p. 26247 (cit. on p. 83).
- Martens, J. (2010). “Deep Learning via Hessian-free Optimization”. *ICML* 27, pp. 735–742 (cit. on p. 48).
- Matsumoto, T., R. Bennett, P. Stone, T. Yamada, K. Domen, and M. Bowker (2001). “Scanning Tunneling Microscopy Studies of Oxygen Adsorption on Cu(111)”. *Surface Science* 471.1-3, pp. 225–245 (cit. on pp. XIII, 130).
- Mavriplis, D. J. (1995). “An Advancing Front Delaunay Triangulation Algorithm Designed for Robustness”. *Journal of Computational Physics* 117.1, pp. 90–101 (cit. on p. 59).
- Menezes, P. and S. Kailas (2016). “Role of Surface Texture and Roughness Parameters on Friction and Transfer Film Formation When UHMWPE Sliding against Steel”. *Biosurface and Biotribology* 2.1, pp. 1–10 (cit. on p. 82).
- Merabia, S. and K. Termentzidis (2014). “Thermal Boundary Conductance across Rough Interfaces Probed by Molecular Dynamics”. *Physical Review B* 89.5, p. 054309 (cit. on p. 104).
- Miller, R. (2004). “A Stress-Gradient Based Criterion for Dislocation Nucleation in Crystals”. *Journal of the Mechanics and Physics of Solids* 52.7, pp. 1507–1525 (cit. on p. 77).
- Miller, R. and D. Rodney (2008). “On the Nonlocal Nature of Dislocation Nucleation during Nanoindentation”. *Journal of the Mechanics and Physics of Solids* 56.4, pp. 1203–1223 (cit. on p. 77).
- Mishin, Y. (2021). “Machine-Learning Interatomic Potentials for Materials Science”. *Acta Materialia* 214, p. 116980 (cit. on p. 42).
- Mishin, Y., M. J. Mehl, D. A. Papaconstantopoulos, A. F. Voter, and J. D. Kress (2001). “Structural Stability and Lattice Defects in Copper: *Ab Initio*, Tight-Binding, and Embedded-Atom Calculations”. *Physical Review B* 63.22, p. 224106 (cit. on p. 43).
- Mitchell, D., P. Sewell, and M. Cohen (1976). “A Kinetic Study of the Initial Oxidation of the Ni(001) Surface by RHEED and x-Ray Emission”. *Surface Science* 61.2, pp. 355–376 (cit. on pp. 24, 136).
- Mitlin, D., A. Misra, T. E. Mitchell, J. P. Hirth, and R. G. Hoagland (2005). “Interface Dislocation Structures at the Onset of Coherency Loss in Nanoscale Ni–Cu Bilayer Films”. *Philosophical Magazine* 85.28, pp. 3379–3392 (cit. on pp. XI, 82).
- Mo, Y., K. T. Turner, and I. Szlufarska (2009). “Friction Laws at the Nanoscale”. *Nature* 457.7233, pp. 1116–1119 (cit. on p. 56).
- Mohanraj, V. J. and Y. Chen (2007). “Nanoparticles - A Review”. *Tropical Journal of Pharmaceutical Research* 5.1, pp. 561–573 (cit. on p. 8).

## Bibliography

- Mojumder, S., M. Mahboob, and M. Motalab (2020). “Atomistic and Finite Element Study of Nanoindentation in Pure Aluminum”. *Materials Today Communications* 23, p. 100798 (cit. on p. 29).
- Monk, J. and D. Farkas (2007). “Tension–Compression Asymmetry and Size Effects in Nanocrystalline Ni Nanowires”. *Philosophical Magazine* 87.14–15, pp. 2233–2244 (cit. on p. 30).
- Mook, W. M., J. D. Nowak, C. R. Perrey, C. B. Carter, R. Mukherjee, S. L. Girshick, P. H. McMurry, and W. W. Gerberich (2007). “Compressive Stress Effects on Nanoparticle Modulus and Fracture”. *Physical Review B* 75.21, p. 214112 (cit. on p. 18).
- Morasch, K. and D. Bahr (2005). “Nanomechanical Testing for Fracture of Oxide Films”. *Journal of Materials Research* 20.6, pp. 1490–1497 (cit. on pp. 25, 26, 130).
- Mordehai, D., O. David, and R. Kositski (2018). “Nucleation-Controlled Plasticity of Metallic Nanowires and Nanoparticles”. *Advanced Materials* 30.41, p. 1706710 (cit. on pp. X, 30, 31, 34, 63).
- Mordehai, D., M. Kazakevich, D. J. Srolovitz, and E. Rabkin (2011a). “Nanoindentation Size Effect in Single-Crystal Nanoparticles and Thin Films: A Comparative Experimental and Simulation Study”. *Acta Materialia* 59.6, pp. 2309–2321 (cit. on pp. X, 18, 27, 63, 70, 109–111, 116).
- Mordehai, D., S.-W. Lee, B. Backes, D. J. Srolovitz, W. D. Nix, and E. Rabkin (2011b). “Size Effect in Compression of Single-Crystal Gold Microparticles”. *Acta Materialia* 59.13, pp. 5202–5215 (cit. on pp. XII, 18, 19, 22, 23, 31, 32, 34, 43, 67, 79, 109, 110, 122).
- Mortier, W. J., S. K. Ghosh, and S. Shankar (1986). “Electronegativity-Equalization Method for the Calculation of Atomic Charges in Molecules”. *Journal of the American Chemical Society* 108.15, pp. 4315–4320 (cit. on pp. 43, 46).
- Moser, B., K. Wasmer, L. Barbieri, and J. Michler (2007). “Strength and Fracture of Si Micropillars: A New Scanning Electron Microscopy-Based Micro-Compression Test”. *Journal of Materials Research* 22.4, pp. 1004–1011 (cit. on p. 15).
- Mousa, M.-H., R. Chaine, S. Akkouche, and E. Galin (2007). “Efficient Spherical Harmonics Representation of 3D Objects”. In: IEEE, pp. 248–255 (cit. on p. 89).
- Mulligan, J. A., X. Feng, and S. G. Adie (2019). “Quantitative Reconstruction of Time-Varying 3D Cell Forces with Traction Force Optical Coherence Microscopy”. *Scientific Reports* 9.1, p. 4086 (cit. on p. 59).
- Multiphysics, C. (1998). “Introduction to COMSOL Multiphysics”. *COMSOL Multiphysics, Burlington, MA* (cit. on pp. XI, 59, 82, 103).
- Nahas, Y., F. Berneau, J. Bonneville, C. Coupeau, M. Drouet, B. Lamongie, M. Marteau, J. Michel, P. Tanguy, and C. Tromas (2013). “An Experimental UHV AFM-STM Device for Characterizing Surface Nanostructures under Stress/Strain at Variable Temperature”. *Review of Scientific Instruments* 84.10, p. 105117 (cit. on p. 26).

## Bibliography

- Narayanan, S., G. Cheng, Z. Zeng, Y. Zhu, and T. Zhu (2015). “Strain Hardening and Size Effect in Five-fold Twinned Ag Nanowires”. *Nano Letters* 15.6, pp. 4037–4044 (cit. on p. 105).
- Narusawa, T., W. M. Gibson, and E. Törnqvist (1981). “Relaxation of Ni(111) Surface by Oxygen Adsorption”. *Physical Review Letters* 47.6, pp. 417–420 (cit. on pp. XIII, 130).
- Nash, S. G. (1985). “Preconditioning of Truncated-Newton Methods”. *SIAM Journal on Scientific and Statistical Computing* 6.3, pp. 599–616 (cit. on p. 48).
- Navarro, V., O. R. de la Fuente, A. Mascaraque, and J. M. Rojo (2008). “Uncommon Dislocation Processes at the Incipient Plasticity of Stepped Gold Surfaces”. *Physical Review Letters* 100.10, p. 105504 (cit. on pp. XI, 25, 27, 82).
- Nayak, P. R. (1971). “Random Process Model of Rough Surfaces”. *Journal of Lubrication Technology* 93.3, pp. 398–407 (cit. on pp. 84, 85).
- Neyts, E. C., K. Ostrikov, Z. J. Han, S. Kumar, A. C. T. Van Duin, and A. Bogaerts (2013). “Defect Healing and Enhanced Nucleation of Carbon Nanotubes by Low-Energy Ion Bombardment”. *Physical Review Letters* 110.6, p. 065501 (cit. on p. 44).
- Ng, K. and A. Ngan (2008). “Breakdown of Schmid’s Law in Micropillars”. *Scripta Materialia* 59.7, pp. 796–799 (cit. on p. 15).
- Ng, K. and A. Ngan (2009). “Effects of Trapping Dislocations within Small Crystals on Their Deformation Behavior”. *Acta Materialia* 57.16, pp. 4902–4910 (cit. on p. 15).
- Ngan, A. and K. Ng (2010). “Transition from Deterministic to Stochastic Deformation”. *Philosophical Magazine* 90.14, pp. 1937–1954 (cit. on p. 15).
- Nilius, N. (2009). “Properties of Oxide Thin Films and Their Adsorption Behavior Studied by Scanning Tunneling Microscopy and Conductance Spectroscopy”. *Surface Science Reports* 64.12, pp. 595–659 (cit. on p. 24).
- Nisany, S. and D. Mordehai (2022). “A Multiple Site Type Nucleation Model and Its Application to the Probabilistic Strength of Pd Nanowires”. *Metals* 12.2, p. 280 (cit. on p. 30).
- Nomura, K.-i., R. K. Kalia, A. Nakano, and P. Vashishta (2008). “A Scalable Parallel Algorithm for Large-Scale Reactive Force-Field Molecular Dynamics Simulations”. *Computer Physics Communications* 178.2, pp. 73–87 (cit. on pp. 43, 47).
- Norfleet, D., D. Dimiduk, S. Polasik, M. Uchic, and M. Mills (2008). “Dislocation Structures and Their Relationship to Strength in Deformed Nickel Microcrystals”. *Acta Materialia* 56.13, pp. 2988–3001 (cit. on p. 14).
- Nosé, S. (1984). “A Unified Formulation of the Constant Temperature Molecular Dynamics Methods”. *The Journal of Chemical Physics* 81.1, pp. 511–519 (cit. on pp. 51, 52).

## Bibliography

- O'Reilly, M., X. Jiang, J. Beechinor, S. Lynch, C. NíDheasuna, J. Patterson, and G. Crean (1995). "Investigation of the Oxidation Behaviour of Thin Film and Bulk Copper". *Applied Surface Science* 91.1-4, pp. 152–156 (cit. on p. 24).
- Ohmura, T., S. Matsuoka, K. Tanaka, and T. Yoshida (2001). "Nanoindentation Load–Displacement Behavior of Pure Face Centered Cubic Metal Thin Films on a Hard Substrate". *Thin Solid Films* 385.1-2, pp. 198–204 (cit. on pp. 73, 77, 79).
- Onofrio, N., D. Guzman, and A. Strachan (2015). "Atomic Origin of Ultrafast Resistance Switching in Nanoscale Electrometallization Cells". *Nature Materials* 14.4, pp. 440–446 (cit. on p. 44).
- Ouyang, G., W. G. Zhu, C. Q. Sun, Z. M. Zhu, and S. Z. Liao (2010). "Atomistic Origin of Lattice Strain on Stiffness of Nanoparticles". *Physical Chemistry Chemical Physics* 12.7, p. 1543 (cit. on p. 9).
- Özgünaltay, G., A. R. Yazici, and J. Görücü (2003). "Effect of Finishing and Polishing Procedures on the Surface Roughness of New Tooth-Coloured Restoratives: Finishing/Polishing Effects on Surface Roughness". *Journal of Oral Rehabilitation* 30.2, pp. 218–224 (cit. on p. 82).
- Palasantzas, G. (2003). "Influence of Self-Affine Surface Roughness on the Friction Coefficient for Rubbers". *Journal of Applied Physics* 94.9, pp. 5652–5655 (cit. on p. 87).
- Pang, M. and D. F. Bahr (2001). "Thin-Film Fracture during Nanoindentation of a Titanium Oxide Film–Titanium System". *Journal of Materials Research* 16.9, pp. 2634–2643 (cit. on p. 130).
- Paranjpe, M. and C. Müller-Goymann (2014). "Nanoparticle-Mediated Pulmonary Drug Delivery: A Review". *International Journal of Molecular Sciences* 15.4, pp. 5852–5873 (cit. on p. 8).
- Parthasarathy, T. A., S. I. Rao, D. M. Dimiduk, M. D. Uchic, and D. R. Trinkle (2007). "Contribution to Size Effect of Yield Strength from the Stochastics of Dislocation Source Lengths in Finite Samples". *Scripta Materialia* 56.4, pp. 313–316 (cit. on p. 14).
- Pastewka, L. and M. O. Robbins (2014). "Contact between Rough Surfaces and a Criterion for Macroscopic Adhesion". *Proceedings of the National Academy of Sciences* 111.9, pp. 3298–3303 (cit. on pp. 82, 103).
- Patir, N. (1978). "A Numerical Procedure for Random Generation of Rough Surfaces". *Wear* 47.2, pp. 263–277 (cit. on p. 82).
- Peng, C., Y. Zhan, and J. Lou (2012). "Size-Dependent Fracture Mode Transition in Copper Nanowires". *Small* 8.12, pp. 1889–1894 (cit. on p. 17).
- Perić, D. and D. R. J. Owen (1992). "Computational Model for 3-D Contact Problems with Friction Based on the Penalty Method". *International Journal for Numerical Methods in Engineering* 35.6, pp. 1289–1309 (cit. on p. 104).

## Bibliography

- Persson, B. N. J. (2001). "Theory of Rubber Friction and Contact Mechanics". *The Journal of Chemical Physics* 115.8, pp. 3840–3861 (cit. on pp. [86](#), [87](#)).
- Persson, B. N. J. (2002). "Adhesion between Elastic Bodies with Randomly Rough Surfaces". *Physical Review Letters* 89.24, p. 245502 (cit. on p. [86](#)).
- Persson, B. N. J., O. Albohr, U. Tartaglino, A. I. Volokitin, and E. Tosatti (2005). "On the Nature of Surface Roughness with Application to Contact Mechanics, Sealing, Rubber Friction and Adhesion". *Journal of Physics: Condensed Matter* 17.1, R1–R62 (cit. on pp. [84](#), [103](#)).
- Persson, B. N. J., F. Bucher, and B. Chiaia (2002). "Elastic Contact between Randomly Rough Surfaces: Comparison of Theory with Numerical Results". *Physical Review B* 65.18, p. 184106 (cit. on p. [86](#)).
- Persson, B. N. J. (2006). "Contact Mechanics for Randomly Rough Surfaces". *Surface Science Reports* 61.4, pp. 201–227 (cit. on p. [84](#)).
- Persson, B. N. (2013). *Sliding friction: physical principles and applications*. Springer Science & Business Media (cit. on p. [87](#)).
- Pharr, G. M., E. G. Herbert, and Y. Gao (2010). "The Indentation Size Effect: A Critical Examination of Experimental Observations and Mechanistic Interpretations". *Annual Review of Materials Research* 40.1, pp. 271–292 (cit. on p. [22](#)).
- Pizzagalli, L. (2020). "Finite-Temperature Mechanical Properties of Nanostructures with First-Principles Accuracy". *Physical Review B* 102.9, p. 094102 (cit. on p. [28](#)).
- Plimpton, S. (1995). "Fast Parallel Algorithms for Short-Range Molecular Dynamics". *Journal of Computational Physics* 117.1, pp. 1–19 (cit. on p. [42](#)).
- Plimpton, S. J. and B. A. Hendrickson (1992). "Parallel Molecular Dynamics With the Embedded Atom Method". *MRS Proceedings* 291, p. 37 (cit. on p. [78](#)).
- Polak, E. and G. Ribiere (1969). "Note sur la convergence de méthodes de directions conjuguées". *Revue française d'informatique et de recherche opérationnelle. Série rouge* 3.16, pp. 35–43 (cit. on p. [48](#)).
- Prabhu, K. M. M. (2014). *Window Functions and Their Applications in Signal Processing*. Boca Raton, Fla. [u.a]: CRC Press. 382 pp. (cit. on p. [101](#)).
- Prakash, A., J. Guénolé, J. Wang, J. Müller, E. Spiecker, M. Mills, I. Povstugar, P. Choi, D. Raabe, and E. Bitzek (2015). "Atom Probe Informed Simulations of Dislocation–Precipitate Interactions Reveal the Importance of Local Interface Curvature". *Acta Materialia* 92, pp. 33–45 (cit. on p. [104](#)).
- Press, W. H. and S. A. Teukolsky (1990). "Savitzky-Golay Smoothing Filters". *Computers in Physics* 4.6, pp. 669–672 (cit. on p. [114](#)).
- Preston, A. S., R. A. Hughes, T. B. Demille, V. M. Rey Davila, and S. Neretina (2019). "Dewetted Nanostructures of Gold, Silver, Copper, and Palladium with Enhanced Faceting". *Acta Materialia* 165, pp. 15–25 (cit. on p. [131](#)).

## Bibliography

- Qin, Q., S. Yin, G. Cheng, X. Li, T.-H. Chang, G. Richter, Y. Zhu, and H. Gao (2015). “Recoverable Plasticity in Penta-Twinned Metallic Nanowires Governed by Dislocation Nucleation and Retraction”. *Nature Communications* 6.1, p. 5983 (cit. on p. 17).
- Qiu, C., P. Zhu, F. Fang, D. Yuan, and X. Shen (2014). “Study of Nanoindentation Behavior of Amorphous Alloy Using Molecular Dynamics”. *Applied Surface Science* 305, pp. 101–110 (cit. on p. 144).
- Rahm, J. and P. Erhart (2020). “WulffPack: A Python Package for Wulff Constructions”. *Journal of Open Source Software* 5.45, p. 1944 (cit. on pp. 60, 65, 94).
- Raju, M., A. C. T. Van Duin, and K. A. Fichthorn (2014). “Mechanisms of Oriented Attachment of TiO<sub>2</sub> Nanocrystals in Vacuum and Humid Environments: Reactive Molecular Dynamics”. *Nano Letters* 14.4, pp. 1836–1842 (cit. on p. 44).
- Rao, R. A., Q. Gan, and C. B. Eom (1997). “Growth Mechanisms of Epitaxial Metallic Oxide SrRuO<sub>3</sub> Thin Films Studied by Scanning Tunneling Microscopy”. *Applied Physics Letters* 71.9, pp. 1171–1173 (cit. on pp. 25, 26).
- Rao, S. I., D. M. Dimiduk, M. Tang, M. D. Uchic, T. A. Parthasarathy, and C. Woodward (2007). “Estimating the Strength of Single-Ended Dislocation Sources in Micron-Sized Single Crystals”. *Philosophical Magazine* 87.30, pp. 4777–4794 (cit. on p. 14).
- Rao, S., D. Dimiduk, T. Parthasarathy, M. Uchic, M. Tang, and C. Woodward (2008). “Athermal Mechanisms of Size-Dependent Crystal Flow Gleaned from Three-Dimensional Discrete Dislocation Simulations”. *Acta Materialia* 56.13, pp. 3245–3259 (cit. on p. 14).
- Rassoulinejad-Mousavi, S. M., Y. Mao, and Y. Zhang (2016). “Evaluation of Copper, Aluminum, and Nickel Interatomic Potentials on Predicting the Elastic Properties”. *Journal of Applied Physics* 119.24, p. 244304 (cit. on p. 43).
- Richard, M.-I., S. Labat, M. Dupraz, J. Carnis, L. Gao, M. Texier, N. Li, L. Wu, J. P. Hofmann, M. Levi, S. J. Leake, S. Lazarev, M. Sprung, E. J. Hensen, E. Rabkin, and O. Thomas (2023). “Anomalous Glide Plane in Platinum Nano- and Microcrystals”. *ACS Nano* 17.6, pp. 6113–6120 (cit. on pp. XII, 120).
- Richter, G., K. Hillerich, D. S. Gianola, R. Mönig, O. Kraft, and C. A. Volkert (2009). “Ultrahigh Strength Single Crystalline Nanowiskers Grown by Physical Vapor Deposition”. *Nano Letters* 9.8, pp. 3048–3052 (cit. on pp. 15, 17).
- Ringe, E., R. P. Van Duyne, and L. D. Marks (2011). “Wulff Construction for Alloy Nanoparticles”. *Nano Letters* 11.8, pp. 3399–3403 (cit. on p. 60).
- Roos, B., B. Kapelle, G. Richter, and C. A. Volkert (2014). “Surface Dislocation Nucleation Controlled Deformation of Au Nanowires”. *Applied Physics Letters* 105.20, p. 201908 (cit. on pp. 17, 96).
- Rost, M. J., D. A. Quist, and J. W. M. Frenken (2003). “Grains, Growth, and Grooving”. *Physical Review Letters* 91.2, p. 026101 (cit. on p. 104).

## Bibliography

- Röttger, M. C., A. Sanner, L. A. Thimons, T. Junge, A. Gujrati, J. M. Monti, W. G. Nöhring, T. D. B. Jacobs, and L. Pastewka (2022). “Contact.Engineering—Create, Analyze and Publish Digital Surface Twins from Topography Measurements across Many Scales”. *Surface Topography: Metrology and Properties* 10.3, p. 035032 (cit. on pp. XI, 82, 86).
- Roy, S., R. Gatti, B. Devincre, and D. Mordehai (2019). “A Multiscale Study of the Size-Effect in Nanoindentation of Au Nanoparticles”. *Computational Materials Science* 162, pp. 47–59 (cit. on pp. 9, 110).
- Roy, S., S. Wille, D. Mordehai, and C. A. Volkert (2022). “Investigating Nanoscale Contact Using AFM-Based Indentation and Molecular Dynamics Simulations”. *Metals* 12.3, p. 489 (cit. on p. 111).
- Rubio, G., N. Agrait, and S. Vieira (1996). “Atomic-Sized Metallic Contacts: Mechanical Properties and Electronic Transport”. *Physical Review Letters* 76.13, pp. 2302–2305 (cit. on p. 88).
- Ruiz de Miras, J., G. Martínez-Lledó, W. Orwig, and J. Sepulcre (2020). “A MATLAB Tool for Computing the Spherical Harmonic Fractal Dimension of the Cerebral Cortex”. *Computer Physics Communications* 254, p. 107381 (cit. on p. 89).
- Ruppert, D. (1987). “What Is Kurtosis? An Influence Function Approach”. *The American Statistician* 41.1, pp. 1–5 (cit. on p. 86).
- Rycroft, C. (2009). *Voro++: A Three-Dimensional Voronoi Cell Library in C++*, LBNL-1432E, 946741 (cit. on p. 56).
- Rys, F. S. and A. Waldvogel (1986). “Fractal Shape of Hail Clouds”. *Physical Review Letters* 56.7, pp. 784–787 (cit. on p. 83).
- Sankaranarayanan, S. K. R. S. and S. Ramanathan (2008). “Molecular Dynamics Simulation Study of Nanoscale Passive Oxide Growth on Ni-Al Alloy Surfaces at Low Temperatures”. *Physical Review B* 78.8, p. 085420 (cit. on p. 139).
- Sankaranarayanan, S. K. R. S. and S. Ramanathan (2010). “Electric Field Control of Surface Oxygen Dynamics and Its Effect on the Atomic Scale Structure and Morphology of a Growing Ultrathin Oxide Film”. *The Journal of Physical Chemistry C* 114.14, pp. 6631–6639 (cit. on p. 38).
- Schmutzler, H. J., H. Viefhaus, and H. J. Grabke (1992). “The Influence of the Oxide/Metal Interface Composition on the Adherence of Oxide Layers on Metal Substrates”. *Surface and Interface Analysis* 18.8, pp. 581–584 (cit. on p. 25).
- Schneider, A. S., D. Kaufmann, B. G. Clark, C. P. Frick, P. A. Gruber, R. Möning, O. Kraft, and E. Arzt (2009a). “Correlation between Critical Temperature and Strength of Small-Scale Bcc Pillars”. *Physical Review Letters* 103.10, p. 105501 (cit. on pp. 15, 22).
- Schneider, A., B. Clark, C. Frick, P. Gruber, and E. Arzt (2009b). “Effect of Orientation and Loading Rate on Compression Behavior of Small-Scale Mo Pillars”. *Materials Science and Engineering: A* 508.1-2, pp. 241–246 (cit. on p. 13).

## Bibliography

- Schuster, B. E., Q. Wei, H. Zhang, and K. T. Ramesh (2006). "Microcompression of Nanocrystalline Nickel". *Applied Physics Letters* 88.10, p. 103112 (cit. on p. 13).
- Schuster, B., Q. Wei, T. Hufnagel, and K. Ramesh (2008). "Size-Independent Strength and Deformation Mode in Compression of a Pd-based Metallic Glass". *Acta Materialia* 56.18, pp. 5091–5100 (cit. on p. 13).
- Sedlaček, M., B. Podgornik, and J. Vižintin (2009). "Influence of Surface Preparation on Roughness Parameters, Friction and Wear". *Wear* 266.3-4, pp. 482–487 (cit. on p. 82).
- Sen, F. G., A. T. Alpas, A. C. T. Van Duin, and Y. Qi (2014). "Oxidation-Assisted Ductility of Aluminium Nanowires". *Nature Communications* 5.1, p. 3959 (cit. on pp. 130, 144).
- Senftle, T., S. Hong, M. M. Islam, S. B. Kylasa, Y. Zheng, Y. K. Shin, C. Junkermeier, R. Engel-Herbert, M. J. Janik, H. M. Aktulga, T. Verstraelen, A. Grama, and A. C. T. van Duin (2016). "The ReaxFF Reactive Force-Field: Development, Applications and Future Directions". *npj Computational Materials* 2.1, p. 15011 (cit. on pp. 43, 44).
- Senftle, T. P., R. J. Meyer, M. J. Janik, and A. C. T. Van Duin (2013). "Development of a ReaxFF Potential for Pd/O and Application to Palladium Oxide Formation". *The Journal of Chemical Physics* 139.4, p. 044109 (cit. on p. 44).
- Setoodeh, A., H. Attariani, and M. Khosronejad (2008). "Nickel Nanowires under Uniaxial Loads: A Molecular Dynamics Simulation Study". *Computational Materials Science* 44.2, pp. 378–384 (cit. on p. 30).
- Shahbeyk, Voyiadjis, Habibi, Astaneh, and Yaghoobi (2019). "Review of Size Effects during Micropillar Compression Test: Experiments and Atomistic Simulations". *Crystals* 9.11, p. 591 (cit. on pp. XII, 23, 109).
- Shan, Z. W., R. K. Mishra, S. A. Syed Asif, O. L. Warren, and A. M. Minor (2008). "Mechanical Annealing and Source-Limited Deformation in Submicrometre-Diameter Ni Crystals". *Nature Materials* 7.2, pp. 115–119 (cit. on p. 15).
- Sharma, A., J. Hickman, N. Gazit, E. Rabkin, and Y. Mishin (2018). "Nickel Nanoparticles Set a New Record of Strength". *Nature Communications* 9.1, p. 4102 (cit. on pp. XII, XIII, 18, 109, 127, 130).
- Sharma, A., J. Amodeo, N. Gazit, Y. Qi, O. Thomas, and E. Rabkin (2021). "When More Is Less: Plastic Weakening of Single Crystalline Ag Nanoparticles by the Polycrystalline Au Shell". *ACS Nano* 15, p. 14061 (cit. on pp. 18, 20, 21, 43, 63, 72).
- Sharma, A., N. Gazit, L. Klinger, and E. Rabkin (2020). "Pseudoelasticity of Metal Nanoparticles Is Caused by Their Ultrahigh Strength". *Advanced Functional Materials* 30.18, p. 1807554 (cit. on pp. XIII, 130).
- Shen, Q., Q. Song, H. Li, C. Xiao, T. Wang, H. Lin, and W. Li (2019). "Fatigue Strengthening of Carbon/Carbon Composites Modified with Carbon Nanotubes and Silicon Carbide Nanowires". *International Journal of Fatigue* 124, pp. 411–421 (cit. on p. 8).

## Bibliography

- Shewchuk, J. R. (1994). "An Introduction to the Conjugate Gradient Method without the Agonizing Pain". *Carnegie-Mellon University. Department of Computer Science Pittsburgh* (cit. on p. 48).
- Shi, Y. and M. L. Falk (2007). "Simulations of Nanoindentation in a Thin Amorphous Metal Film". *Thin Solid Films* 515.6, pp. 3179–3182 (cit. on p. 144).
- Shim, S., H. Bei, M. Miller, G. Pharr, and E. George (2009). "Effects of Focused Ion Beam Milling on the Compressive Behavior of Directionally Solidified Micropillars and the Nanoindentation Response of an Electropolished Surface". *Acta Materialia* 57.2, pp. 503–510 (cit. on pp. 23, 25).
- Shin, J., L. Y. Chen, U. T. Sanli, G. Richter, S. Labat, M.-I. Richard, T. Cornelius, O. Thomas, and D. S. Gianola (2019). "Controlling Dislocation Nucleation-Mediated Plasticity in Nanostructures via Surface Modification". *Acta Materialia* 166, pp. 572–586 (cit. on pp. 20, 39).
- Shinoda, W., M. Shiga, and M. Mikami (2004). "Rapid Estimation of Elastic Constants by Molecular Dynamics Simulation under Constant Stress". *Physical Review B* 69.13, p. 134103 (cit. on p. 43).
- Shreiber, K. and D. Mordehai (2015). "Dislocation-Nucleation-Controlled Deformation of Ni<sub>3</sub>Al Nanocubes in Molecular Dynamics Simulations". *Modelling and Simulation in Materials Science and Engineering* 23.8, p. 085004 (cit. on p. 31).
- Skarlinski, M. D. and D. J. Quesnel (2015). "Effect of Native Oxide Layers on Copper Thin-Film Tensile Properties: A Reactive Molecular Dynamics Study". *Journal of Applied Physics* 118.23, p. 235306 (cit. on p. 39).
- Slezak, J., B. Zion, and S. Sibener (1999). "Enhanced Oxidation Rate of Ni(111) by Atomic Oxygen". *Surface Science* 442.1, pp. L983–L988 (cit. on p. 24).
- Somadder, S. and M. S. Islam (2018). "Stress Analysis of a Cylinder Subjected to Thermo-mechanical Loads by Using FEM". *IOP Conference Series: Materials Science and Engineering* 438, p. 012036 (cit. on p. 95).
- Soon, A., M. Todorova, B. Delley, and C. Stampfl (2006). "Oxygen Adsorption and Stability of Surface Oxides on Cu (111) : A First-Principles Investigation". *Physical Review B* 73.16, p. 165424 (cit. on p. 137).
- Soon, A., M. Todorova, B. Delley, and C. Stampfl (2007). "Surface Oxides of the Oxygen–Copper System: Precursors to the Bulk Oxide Phase?" *Surface Science* 601.24, pp. 5809–5813 (cit. on p. 137).
- Sparks, G. (2017). "Spatiotemporal Slip Dynamics during Deformation of Gold Micro-Crystals". *Acta Materialia* 122, pp. 109–119 (cit. on p. 24).
- Stangebye, S., Y. Zhang, S. Gupta, T. Zhu, O. Pierron, and J. Kacher (2022). "Understanding and Quantifying Electron Beam Effects during in Situ TEM Nanomechanical Tensile Testing on Metal Thin Films". *Acta Materialia* 222, p. 117441 (cit. on p. 24).

## Bibliography

- Stauffer, D. D., A. Beaber, A. Wagner, O. Ugurlu, J. Nowak, K. Andre Mkhoyan, S. Girshick, and W. Gerberich (2012). “Strain-Hardening in Submicron Silicon Pillars and Spheres”. *Acta Materialia* 60.6-7, pp. 2471–2478 (cit. on p. 34).
- Stone, T. W. and M. F. Horstemeyer (2012). “Length Scale Effects of Friction in Particle Compaction Using Atomistic Simulations and a Friction Scaling Model”. *Journal of Nanoparticle Research* 14.9, p. 1121 (cit. on p. 34).
- Stukowski, A. (2010). “Visualization and Analysis of Atomistic Simulation Data with OVITO—the Open Visualization Tool”. *Modelling and Simulation in Materials Science and Engineering* 18.1, p. 015012 (cit. on p. 61).
- Stukowski, A. (2018). “Dislocation Analysis Tool for Atomistic Simulations”. In: *Handbook of Materials Modeling*. Ed. by W. Andreoni and S. Yip. Cham: Springer International Publishing, pp. 1–14 (cit. on p. 61).
- Sun, J., L. He, Y.-C. Lo, T. Xu, H. Bi, L. Sun, Z. Zhang, S. X. Mao, and J. Li (2014). “Liquid-like Pseudoelasticity of Sub-10-Nm Crystalline Silver Particles”. *Nature Materials* 13.11, pp. 1007–1012 (cit. on p. 21).
- Svolos, L., C. A. Bronkhorst, and H. Waisman (2020). “Thermal-Conductivity Degradation across Cracks in Coupled Thermo-Mechanical Systems Modeled by the Phase-Field Fracture Method”. *Journal of the Mechanics and Physics of Solids* 137, p. 103861 (cit. on p. 60).
- Swope, W. C., H. C. Andersen, P. H. Berens, and K. R. Wilson (1982). “A Computer Simulation Method for the Calculation of Equilibrium Constants for the Formation of Physical Clusters of Molecules: Application to Small Water Clusters”. *The Journal of chemical physics* 76.1, pp. 637–649 (cit. on p. 49).
- Syed Asif, S. A., K. J. Wahl, and R. J. Colton (2000). “The Influence of Oxide and Adsorbates on the Nanomechanical Response of Silicon Surfaces”. *Journal of Materials Research* 15.2, pp. 546–553 (cit. on p. 25).
- Tamagnini, C., R. Castellanza, and R. Nova (2002). “A Generalized Backward Euler Algorithm for the Numerical Integration of an Isotropic Hardening Elastoplastic Model for Mechanical and Chemical Degradation of Bonded Geomaterials”. *International Journal for Numerical and Analytical Methods in Geomechanics* 26.10, pp. 963–1004 (cit. on p. 48).
- Tanguy, A., F. Leonforte, and J.-L. Barrat (2006). “Plastic Response of a 2D Lennard-Jones Amorphous Solid: Detailed Analysis of the Local Rearrangements at Very Slow Strain-Rate”. *The European Physical Journal E* 20.3, pp. 355–364 (cit. on p. 145).
- Tersoff, J. (1986). “New Empirical Model for the Structural Properties of Silicon”. *Physical Review Letters* 56.6, pp. 632–635 (cit. on p. 42).
- Tersoff, J. (1988). “New Empirical Approach for the Structure and Energy of Covalent Systems”. *Physical Review B* 37.12, pp. 6991–7000 (cit. on p. 42).

## Bibliography

- Thompson, A. P., H. M. Aktulga, R. Berger, D. S. Bolintineanu, W. M. Brown, P. S. Crozier, P. J. In 'T Veld, A. Kohlmeyer, S. G. Moore, T. D. Nguyen, R. Shan, M. J. Stevens, J. Tranchida, C. Trott, and S. J. Plimpton (2022). "LAMMPS - a Flexible Simulation Tool for Particle-Based Materials Modeling at the Atomic, Meso, and Continuum Scales". *Computer Physics Communications* 271, p. 108171 (cit. on p. [42](#)).
- Toomes, R., D. Woodruff, M. Polcik, S. Bao, Ph. Hofmann, and K.-M. Schindler (2000). "Is PEXAFS Really PhD?" *Surface Science* 445.2-3, pp. 300–308 (cit. on p. [137](#)).
- Trybula, M. E. and P. A. Korzhavyi (2019). "Atomistic Simulations of Al(100) and Al(111) Surface Oxidation: Chemical and Topological Aspects of the Oxide Structure". *The Journal of Physical Chemistry C* 123.1, pp. 334–346 (cit. on p. [38](#)).
- Tsuzuki, H., P. S. Branicio, and J. P. Rino (2009). "Molecular Dynamics Simulation of Fast Dislocations in Copper". *Acta Materialia* 57.6, pp. 1843–1855 (cit. on p. [69](#)).
- Turcotte, D. L. (1997). *Fractals and chaos in geology and geophysics*. Cambridge university press (cit. on p. [83](#)).
- Uchic, M. D., D. M. Dimiduk, J. N. Florando, and W. D. Nix (2004). "Sample Dimensions Influence Strength and Crystal Plasticity". *Science* 305.5686, pp. 986–989 (cit. on pp. [13](#), [14](#)).
- Uchic, M. D. and D. M. Dimiduk (2005). "A Methodology to Investigate Size Scale Effects in Crystalline Plasticity Using Uniaxial Compression Testing". *Materials Science and Engineering: A* 400–401, pp. 268–278 (cit. on p. [13](#)).
- Uchic, M. D., P. A. Shade, and D. M. Dimiduk (2009). "Plasticity of Micrometer-Scale Single Crystals in Compression". *Annual Review of Materials Research* 39.1, pp. 361–386 (cit. on pp. [VII](#), [8](#)).
- Uesawa, N., S. Inasawa, Y. Tsuji, and Y. Yamaguchi (2010). "Gas-Phase Synthesis of Rough Silicon Nanowires via the Zinc Reduction of Silicon Tetrachloride". *The Journal of Physical Chemistry C* 114.10, pp. 4291–4296 (cit. on p. [105](#)).
- Undisz, A., F. Schrempel, W. Wesch, and M. Rettenmayr (2009). "*In Situ* Observation of Surface Oxide Layers on Medical Grade Ni-Ti Alloy during Straining". *Journal of Biomedical Materials Research Part A* 88A.4, pp. 1000–1009 (cit. on p. [25](#)).
- Valentini, P., W. W. Gerberich, and T. Dumitrică (2007). "Phase-Transition Plasticity Response in Uniaxially Compressed Silicon Nanospheres". *Physical Review Letters* 99.17, p. 175701 (cit. on p. [34](#)).
- Van Duin, A. C. T., S. Dasgupta, F. Lorant, and W. A. Goddard (2001). "ReaxFF: A Reactive Force Field for Hydrocarbons". *The Journal of Physical Chemistry A* 105.41, pp. 9396–9409 (cit. on pp. [42](#), [43](#)).
- Vannice, M. A. (2005). *Kinetics of Catalytic Reactions*. New York: Springer. 240 pp. (cit. on p. [59](#)).

## Bibliography

- Verkhovtsev, A. V., A. V. Yakubovich, G. B. Sushko, M. Hanuske, and A. V. Solov'yov (2013). "Molecular Dynamics Simulations of the Nanoindentation Process of Titanium Crystal". *Computational Materials Science* 76, pp. 20–26 (cit. on p. 29).
- Verlet, L. (1967). "Computer "Experiments" on Classical Fluids. I. Thermodynamical Properties of Lennard-Jones Molecules". *Physical Review* 159.1, pp. 98–103 (cit. on p. 49).
- Volkert, C. A. and E. T. Lilleodden (2006). "Size Effects in the Deformation of Sub-Micron Au Columns". *Philosophical Magazine* 86.33-35, pp. 5567–5579 (cit. on pp. 13, 15).
- Volkert, C. A., A. Donohue, and F. Spaepen (2008). "Effect of sample size on deformation in amorphous metals". *Journal of applied physics* 103.8 (cit. on p. 13).
- Vugrin, K. W., L. P. Swiler, R. M. Roberts, N. J. Stucky-Mack, and S. P. Sullivan (2007). "Confidence Region Estimation Techniques for Nonlinear Regression in Groundwater Flow: Three Case Studies". *Water Resources Research* 43.3 (cit. on pp. 121, 193).
- Wagner, A. J., E. D. Hintsala, P. Kumar, W. W. Gerberich, and K. A. Mkhoyan (2015). "Mechanisms of Plasticity in Near-Theoretical Strength Sub-100 Nm Si Nanocubes". *Acta Materialia* 100, pp. 256–265 (cit. on p. 34).
- Wang, G., J. Bian, J. Feng, and X. Feng (2014). "Compressive Behavior of Crystalline Nanoparticles with Atomic-Scale Surface Steps". *Materials Research Express* 2.1, p. 015006 (cit. on p. 31).
- Wang, X., Z.-Y. Yin, H. Xiong, D. Su, and Y.-T. Feng (2021). "A Spherical-harmonic-based Approach to Discrete Element Modeling of 3D Irregular Particles". *International Journal for Numerical Methods in Engineering* 122.20, pp. 5626–5655 (cit. on p. 97).
- Wang, Z.-J., Z.-W. Shan, J. Li, J. Sun, and E. Ma (2012). "Pristine-to-Pristine Regime of Plastic Deformation in Submicron-Sized Single Crystal Gold Particles". *Acta Materialia* 60.3, pp. 1368–1377 (cit. on p. 110).
- Warren, O. L., S. A. Downs, and T. J. Wyrobek (2004). "Challenges and Interesting Observations Associated with Feedback-Controlled Nanoindentation". *Zeitschrift für Metallkunde* 95.5, pp. 287–296 (cit. on p. 63).
- Watson, W., T. King, T. Spedding, and K. Stout (1979). "The Machined Surface — Time Series Modelling". *Wear* 57.1, pp. 195–205 (cit. on p. 82).
- Weber, B., T. Suhina, T. Junge, L. Pastewka, A. M. Brouwer, and D. Bonn (2018). "Molecular Probes Reveal Deviations from Amontons' Law in Multi-Asperity Frictional Contacts". *Nature Communications* 9.1, p. 888 (cit. on p. 82).
- Wei, D., J. Wang, J. Nie, and B. Zhou (2018). "Generation of Realistic Sand Particles with Fractal Nature Using an Improved Spherical Harmonic Analysis". *Computers and Geotechnics* 104, pp. 1–12 (cit. on pp. 89, 91).

## Bibliography

- Weinberger, C. R. and W. Cai (2008). "Surface-Controlled Dislocation Multiplication in Metal Micropillars". *Proceedings of the National Academy of Sciences* 105.38, pp. 14304–14307 (cit. on p. 15).
- Weinberger, C. R. and W. Cai (2012). "Plasticity of Metal Nanowires". *Journal of Materials Chemistry* 22.8, p. 3277 (cit. on pp. 17, 30, 95).
- Weinberger, C. R., A. T. Jennings, K. Kang, and J. R. Greer (2012). "Atomistic Simulations and Continuum Modeling of Dislocation Nucleation and Strength in Gold Nanowires". *Journal of the Mechanics and Physics of Solids* 60.1, pp. 84–103 (cit. on pp. 30, 34).
- Weishaupt, K., V. Joekar-Niasar, and R. Helmig (2019). "An Efficient Coupling of Free Flow and Porous Media Flow Using the Pore-Network Modeling Approach". *Journal of Computational Physics: X* 1, p. 100011 (cit. on p. 60).
- Weiss, J., W. B. Rhouma, T. Richeton, S. Dechanel, F. Louchet, and L. Truskinovsky (2015). "From Mild to Wild Fluctuations in Crystal Plasticity". *Physical Review Letters* 114.10, p. 105504 (cit. on p. 22).
- West, G. B., J. H. Brown, and B. J. Enquist (1997). "A General Model for the Origin of Allometric Scaling Laws in Biology". *Science* 276.5309, pp. 122–126 (cit. on p. 83).
- Williams, D. B. and C. B. Carter (1996). "The Transmission Electron Microscope". In: *Transmission Electron Microscopy*. Boston, MA: Springer US, pp. 3–17 (cit. on pp. VII, 8).
- Williamson, J., J. Pullen, R. Hunt, and D. Leonard (1969). "The shape of solid surfaces". *Surface Mechanics, ASME, New York*, pp. 24–35 (cit. on p. 85).
- Wong, P.-z., J. Howard, and J.-S. Lin (1986). "Surface Roughening and the Fractal Nature of Rocks". *Physical Review Letters* 57.5, pp. 637–640 (cit. on p. 83).
- Wu, H. (2006). "Molecular Dynamics Study on Mechanics of Metal Nanowire". *Mechanics Research Communications* 33.1, pp. 9–16 (cit. on p. 30).
- Wu, J.-Y. (2017). "A Unified Phase-Field Theory for the Mechanics of Damage and Quasi-Brittle Failure". *Journal of the Mechanics and Physics of Solids* 103, pp. 72–99 (cit. on p. 59).
- Wu, X., Y. Guo, Q. Wei, and W. Wang (2009). "Prevalence of Shear Banding in Compression of Zr41Ti14Cu12.5Ni10Be22.5 Pillars as Small as 150nm in Diameter". *Acta Materialia* 57.12, pp. 3562–3571 (cit. on p. 24).
- Wulff, G. (1901). "XXV. Zur Frage Der Geschwindigkeit Des Wachstums Und Der Auflösung Der Krystallflächen". *Zeitschrift für Kristallographie - Crystalline Materials* 34.1-6, pp. 449–530 (cit. on pp. 60, 94).
- Xu, Q., N. Salles, J. Chevalier, and J. Amodeo (2022). "Atomistic Simulation and Interatomic Potential Comparison in -Al<sub>2</sub>O<sub>3</sub> : Lattice, Surface and Extended-Defects Properties". *Modelling and Simulation in Materials Science and Engineering* 30.3, p. 035008 (cit. on p. 190).

## Bibliography

- Xu, Y. and M. Mavrikakis (2001). "Adsorption and Dissociation of O<sub>2</sub> on Cu(1 1 1): Thermochemistry, Reaction Barrier and the Effect of Strain". *Surface Science* 494.2, pp. 131–144 (cit. on p. [137](#)).
- Xu, Z., K. M. Rosso, and S. Bruemmer (2012). "Metal Oxidation Kinetics and the Transition from Thin to Thick Films". *Physical Chemistry Chemical Physics* 14.42, p. 14534 (cit. on p. [135](#)).
- Yaghoobi, M. and G. Z. Voyiadjis (2014). "Effect of Boundary Conditions on the MD Simulation of Nanoindentation". *Computational Materials Science* 95, pp. 626–636 (cit. on p. [78](#)).
- Yaghoobi, M. and G. Z. Voyiadjis (2016). "Atomistic Simulation of Size Effects in Single-Crystalline Metals of Confined Volumes during Nanoindentation". *Computational Materials Science* 111, pp. 64–73 (cit. on pp. [29](#), [78](#)).
- Yamamoto, T., T. Fukushima, Y. Kanda, and K. Higashitani (2005). "Molecular-Scale Observation of the Surface of Polystyrene Particles by AFM". *Journal of Colloid and Interface Science* 292.2, pp. 392–396 (cit. on pp. [102](#), [103](#)).
- Yamazoe, N., J. Fuchigami, M. Kishikawa, and T. Seiyama (1979). "Interactions of Tin Oxide Surface with O<sub>2</sub>, H<sub>2</sub>O and H<sub>2</sub>". *Surface Science* 86, pp. 335–344 (cit. on pp. [XIII](#), [130](#)).
- Yang, L., J.-J. Bian, and G.-F. Wang (2017). "Impact of Atomic-Scale Surface Morphology on the Size-Dependent Yield Stress of Gold Nanoparticles". *Journal of Physics D: Applied Physics* 50.24, p. 245302 (cit. on p. [31](#)).
- Yang, Z., Z. Lu, and Y.-P. Zhao (2009). "Atomistic Simulation on Size-Dependent Yield Strength and Defects Evolution of Metal Nanowires". *Computational Materials Science* 46.1, pp. 142–150 (cit. on p. [30](#)).
- Yastrebov, V. A., G. Anciaux, and J.-F. Molinari (2017). "The Role of the Roughness Spectral Breadth in Elastic Contact of Rough Surfaces". *Journal of the Mechanics and Physics of Solids* 107, pp. 469–493 (cit. on p. [88](#)).
- Yastrebov, V. A., G. Anciaux, and J.-F. Molinari (2012). "Contact between Representative Rough Surfaces". *Physical Review E* 86.3, p. 035601 (cit. on p. [87](#)).
- Yatsymyrskyi, A., E. Ischenko, S. Gaidai, A. Dyachenko, T. Zakharova, and V. Lisnyak (2020). "DFT Study of H<sub>2</sub>, H<sub>2</sub>O, and O<sub>2</sub> Adsorption on Ni(111) Surface". *2020 IEEE 40th International Conference on Electronics and Nanotechnology (ELNANO)* (cit. on p. [137](#)).
- Ye, J. C., J. P. Chu, Y. C. Chen, Q. Wang, and Y. Yang (2012). "Hardness, Yield Strength, and Plastic Flow in Thin Film Metallic-Glass". *Journal of Applied Physics* 112.5, p. 053516 (cit. on p. [15](#)).
- Yin, S., G. Cheng, G. Richter, H. Gao, and Y. Zhu (2019). "Transition of Deformation Mechanisms in Single-Crystalline Metallic Nanowires". *ACS Nano* 13.8, pp. 9082–9090 (cit. on p. [34](#)).

## Bibliography

- Youngworth, R. N., B. B. Gallagher, and B. L. Stamper (2005). "An Overview of Power Spectral Density (PSD) Calculations". In: Optics & Photonics 2005. Ed. by H. P. Stahl. San Diego, California, USA, 58690U (cit. on p. 84).
- Ypma, T. J. (1995). "Historical Development of the Newton–Raphson Method". *SIAM Review* 37.4, pp. 531–551 (cit. on p. 73).
- Yu, Q., Z.-W. Shan, J. Li, X. Huang, L. Xiao, J. Sun, and E. Ma (2010). "Strong Crystal Size Effect on Deformation Twinning". *Nature* 463.7279, pp. 335–338 (cit. on p. 15).
- Zaefferer, S. (2011). "A critical review of orientation microscopy in SEM and TEM". *Crystal Research and Technology* 46.6, pp. 607–628 (cit. on pp. VII, 8).
- Zahoor, F., T. Z. Azni Zulkifli, and F. A. Khanday (2020). "Resistive Random Access Memory (RRAM): An Overview of Materials, Switching Mechanism, Performance, Multilevel Cell (Mlc) Storage, Modeling, and Applications". *Nanoscale Research Letters* 15.1, p. 90 (cit. on p. 59).
- Zhang, C. J., R. J. Baxter, P. Hu, A. Alavi, and M.-H. Lee (2001a). "A Density Functional Theory Study of Carbon Monoxide Oxidation on the Cu3Pt(111) Alloy Surface: Comparison with the Reactions on Pt(111) and Cu(111)". *The Journal of Chemical Physics* 115.11, pp. 5272–5277 (cit. on p. 130).
- Zhang, C., D. G. Kvashnin, L. Bourgeois, J. F. S. Fernando, K. Firestein, P. B. Sorokin, N. Fukata, and D. Golberg (2018). "Mechanical, Electrical, and Crystallographic Property Dynamics of Bent and Strained Ge/Si Core–Shell Nanowires As Revealed by *in Situ* Transmission Electron Microscopy". *Nano Letters* 18.11, pp. 7238–7246 (cit. on p. 20).
- Zhang, D., W. Drissen, J.-M. Breguet, R. Clavel, and J. Michler (2009). "A High-Sensitivity and Quasi-Linear Capacitive Sensor for Nanomechanical Testing Applications". *Journal of Micromechanics and Microengineering* 19.7, p. 075003 (cit. on p. 71).
- Zhang, H., B. Schuster, Q. Wei, and K. Ramesh (2006). "The Design of Accurate Micro-Compression Experiments". *Scripta Materialia* 54.2, pp. 181–186 (cit. on p. 24).
- Zhang, H.-w., Y. Liu, and S.-h. Sun (2010). "Synthesis and assembly of magnetic nanoparticles for information and energy storage applications". *Frontiers of Physics in China* 5, pp. 347–356 (cit. on p. 8).
- Zhang, L., C. Lu, and K. Tieu (2016). "A Review on Atomistic Simulation of Grain Boundary Behaviors in Face-Centered Cubic Metals". *Computational Materials Science* 118, pp. 180–191 (cit. on p. 104).
- Zhang, P., O. U. Salman, J.-Y. Zhang, G. Liu, J. Weiss, L. Truskinovsky, and J. Sun (2017). "Taming Intermittent Plasticity at Small Scales". *Acta Materialia* 128, pp. 351–364 (cit. on p. 22).

## Bibliography

- Zhang, S., D. Li, and Y. Liu (2022). “Friction Behavior of Rough Surfaces on the Basis of Contact Mechanics: A Review and Prospects”. *Micromachines* 13.11, p. 1907 (cit. on p. 103).
- Zhang, X. Y., L. D. Zhang, Y. Lei, L. X. Zhao, and Y. Q. Mao (2001b). “Fabrication and Characterization of Highly Ordered Au Nanowire Arrays”. *Journal of Materials Chemistry* 11.6, pp. 1732–1734 (cit. on pp. XII, 26–28, 109).
- Zheng, H., A. Cao, C. R. Weinberger, J. Y. Huang, K. Du, J. Wang, Y. Ma, Y. Xia, and S. X. Mao (2010). “Discrete Plasticity in Sub-10-Nm-Sized Gold Crystals”. *Nature Communications* 1.1, p. 144 (cit. on p. 111).
- Zhou, G., L. Luo, L. Li, J. Ciston, E. A. Stach, and J. C. Yang (2012). “Step-Edge-Induced Oxide Growth During the Oxidation of Cu Surfaces”. *Physical Review Letters* 109.23, p. 235502 (cit. on p. 142).
- Zhou, G. and J. C. Yang (2005). “Initial Oxidation Kinetics of Cu(100), (110), and (111) Thin Films Investigated by in Situ Ultra-high-vacuum Transmission Electron Microscopy”. *Journal of Materials Research* 20.7, pp. 1684–1694 (cit. on p. 136).
- Zhou, X. W., R. A. Johnson, and H. N. G. Wadley (2004). “Misfit-Energy-Increasing Dislocations in Vapor-Deposited CoFe/NiFe Multilayers”. *Physical Review B* 69.14, p. 144113 (cit. on p. 43).
- Zhu, Q., L. Zou, G. Zhou, W. A. Saidi, and J. C. Yang (2016). “Early and Transient Stages of Cu Oxidation: Atomistic Insights from Theoretical Simulations and in Situ Experiments”. *Surface Science* 652, pp. 98–113 (cit. on p. 142).
- Zhu, T., J. Li, A. Samanta, A. Leach, and K. Gall (2008). “Temperature and Strain-Rate Dependence of Surface Dislocation Nucleation”. *Physical Review Letters* 100.2, p. 025502 (cit. on p. 72).
- Zhu, W., H. Gong, Y. Han, M. Zhang, and A. C. T. Van Duin (2020). “Development of a Reactive Force Field for Simulations on the Catalytic Conversion of C/H/O Molecules on Cu-Metal and Cu-Oxide Surfaces and Application to Cu/CuO-Based Chemical Looping”. *The Journal of Physical Chemistry C* 124.23, pp. 12512–12520 (cit. on pp. 48, 134, 193).
- Zimmerman, J., A. Bisht, Y. Mishin, and E. Rabkin (2021). “Size and Shape Effects on the Strength of Platinum Nanoparticles”. *Journal of Materials Science* 56.32, pp. 18300–18312 (cit. on pp. XI, XII, 35, 82, 109).
- Zimmerman, J. A., C. L. Kelchner, P. A. Klein, J. C. Hamilton, and S. M. Foiles (2001). “Surface Step Effects on Nanoindentation”. *Physical Review Letters* 87.16, p. 165507 (cit. on p. 36).
- Zou, C., Y. K. Shin, A. C. van Duin, H. Fang, and Z.-K. Liu (2015). “Molecular Dynamics Simulations of the Effects of Vacancies on Nickel Self-Diffusion, Oxygen Diffusion and Oxidation Initiation in Nickel, Using the ReaxFF Reactive Force Field”. *Acta Materialia* 83, pp. 102–112 (cit. on p. 136).

## Bibliography

Zuo, Y., C. Chen, X. Li, Z. Deng, Y. Chen, J. Behler, G. Csányi, A. V. Shapeev, A. P. Thompson, M. A. Wood, and S. P. Ong (2020). “A Performance and Cost Assessment of Machine Learning Interatomic Potentials”. *The Journal of Physical Chemistry A* 124.4, pp. 731–745 (cit. on p. 42).

## **Appendix**

## A. Surface energy calculation

$\gamma_{\{hkl\}}$  is computed using a classical method for surface energy calculation already used in *e.g.*, Ref. [Xu et al. 2022]. For this purpose, a simulation cell of size about  $3 \times 3 \times 3 \text{ nm}^3$  is designed for each targeted  $\{hkl\}$  surface. The energy of the system is minimized using periodic BCs and the CG method down to a net force norm of  $10^{-8} \text{ eV}\text{\AA}^{-1}$  and 0 pressure. The minimized potential energy per atom (*i.e.*, the cohesive energy) is called  $E_{bulk}$ . As a second step, the simulation box is extended twice along the direction perpendicular to the target surface, without remapping atom positions, introducing empty space and, thus, creating a surface  $\{hkl\}$ . The energy of the system is then further minimized, without box relaxation, using the same convergence criterion. Due to presence of surfaces, the system is characterized by a larger potential energy here called  $E_{def}$ . Finally, the surface energy  $\gamma_{\{hkl\}}$  is computed using Equation A.1 where  $A$  is the 1-side surface area and  $n$  is the number of atoms.

$$\gamma_{\{hkl\}} = \frac{E_{def} - n \cdot E_{bulk}}{2A} \quad (\text{A.1})$$

## B. Example of Pyrough’s input files

### Thin film

```
{
  "Box": {
    "eta": 0.85,
    "C1": 1.5,
    "Height": 50,
    "Width": 151,
    "Length": 151,
    "N": 30,
    "M": 30,
    "Mesh_size": 5,
    "Refine_factor": 0.7,
    "Raw_stl": "na"
  },
  "Output": {
    {"ATOM": ["lmp", "xyz"]},
    {"FEM": ["stl", "msh"]}
  },
  "ATOM_Param": {
    "Lattice_parameter": 4.07,
    "Material": "Au",
    "Orien_x": [1, 0, 0],
    "Orien_y": [0, 1, 0],
    "Orien_z": [0, 0, 1],
    "Lattice_structure": "fcc"
  }
}
```

### Faceted wire

```
{
  "fWire": {
    "eta": 0.5,
    "RMS": 2.0,
    "Length": 200,
    "Radius": 30,
    "N_Faces": 6,
    "N": 30,
    "M": 30,
    "Mesh_size": 5,
    "Refine_factor": 0.5,
    "Raw_stl": "na"
  },
  "Output": {
    {"ATOM": ["lmp", "xyz"]},
    {"FEM": ["stl", "msh"]}
  },
  "ATOM_Param": {
    "Lattice_parameter": 4.09,
    "Material": "Ag",
    "Orien_z": [1, 1, 1],
    "Orien_y": [1, -2, 1]
  }
}
```

```
"Orien_x": [-1,0,1],  
"Lattice_structure": "fcc"}  
}
```

### **Wulff-shaped faceted nanoparticle**

```
{"Wulff":  
    {"eta": 0.75,  
     "RMS": 1,  
     "n_atoms": 27738,  
     "N": 30,  
     "M": 30,  
     "Surfaces": [[1,0,0], [1,1,0], [1,1,1]],  
     "Energies": [1296.53414304361, 1531.21487518984, 1196.  
                  42896317992],  
     "Mesh_size": 5,  
     "Refine_factor": 0.5,  
     "Raw_stl": "na"},  
  
"Output":  
    {"ATOM": ["lmp", "xyz"],  
     "FEM": ["stl", "msh"]},  
  
"ATOM_Param":  
    {"Lattice_parameter": 4.07,  
     "Material": "Au",  
     "Orien_x": [1,0,0],  
     "Orien_y": [0,1,0],  
     "Orien_z": [0,0,1],  
     "Lattice_structure": "fcc"}  
}
```

## C. Thermal expansion coefficient computation

The thermal expansion coefficients are computed from an MD minimization and temperature ramp routine using  $5 \times 5 \times 5$  replicated FCC Ni and Cu elementary cells. PBC are used and simulations are performed in the NPT ensemble. The ReaxFF interatomic potentials developed by Assowe *et al.* [Assowe et al. 2012] and Zhu *et al.* [Zhu et al. 2020] are used for Ni and Cu, respectively. The MD timestep is 0.2 fs. The energy of the system is first minimized at 1 K with a 0 pressure criterion along all directions. Then, a temperature ramp is performed at a rate of  $5 \cdot 10^{12}$  K.ps<sup>-1</sup>, still using a 0 pressure criterion. The dimensions of the box are recorded *on-the-fly* and the variations of the lattice parameter are represented as a function of the temperature in Figure 1. The configuration at 300 K serves as a reference point. Data are fitted by a second order polynomial using a least squares fitting procedure [Vugrin et al. 2007]. The values that are used in the corresponding MD simulations at 300 K, 600 K, 900 K and 1200 K are gathered in Table 6.1.

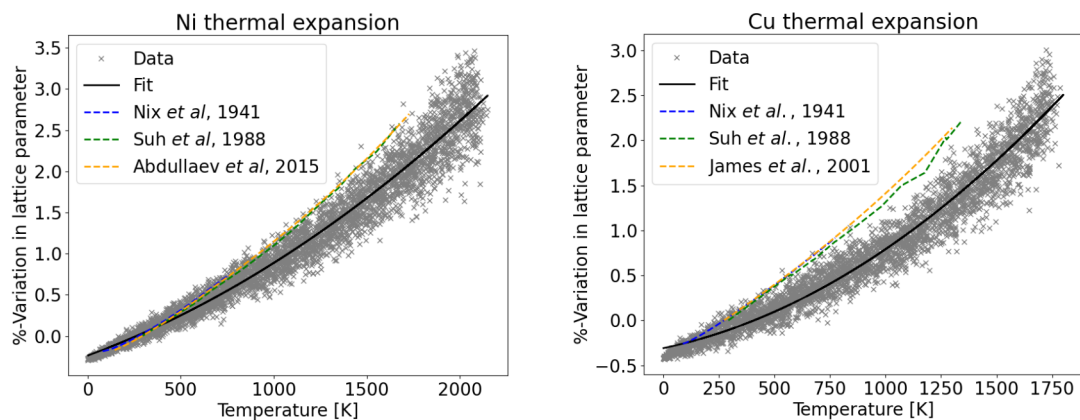


Figure 1.: Thermal expansion coefficients using ReaxFF potentials in the case of Ni and Cu. Simulation data are compared to previous experimental outcomes.

## List of Figures

1.1. Microcompression of a 5 $\mu\text{m}$ diameter pillar of pure Ni oriented for single slip. a) Schematic of the microcompression test setup. b) SEM image of the FIB-prepared sample. c) SEM image of the same sample after compression test. Adapted from [Dimiduk et al. 2005]. . . . .	13
1.2. Typical Stress-Strain curves obtained from microcompression testing experiments of pure Ni micropillars at room temperature, from [Uchic et al. 2004] . . . . .	14
1.3. Normalized shear flow stress <i>vs.</i> size of several FCC metallic samples, from [Greer and De Hosson 2011]. . . . .	16
1.4. Compression of FCC and BCC metal nanopillars. Stress-Strain curve for a) Cu and c) Mo nanopillars of different diameters showing the “ <i>smaller is stronger</i> ” trend. Yield stress <i>vs.</i> pillar diameter for b) Cu and d) Mo with slopes -0.63 and -0.44 respectively. From [Jennings et al. 2010] and [Kim and Greer 2008]. . . . .	17
1.5. Mechanical test of Au NWs using <i>in situ</i> TEM (scale bar of 100 nm). a-c) Images taken after the load drops in the compressive loading. The traces in the lateral surfaces of a dislocation slip mechanism are shown with blue arrows. d-f) Unloading the sample showing the nucleation and extension of nanotwins. g) Recorded force versus strain during the compressive (blue) and subsequent tensile (red) loading. Images from [Lee et al. 2014]. . . . .	18
1.6. Compression of Au faceted nanoparticles. a) Load-displacement curves and SEM images before/after compression of a b) 800 nm and c) 300 nm top diameter particle, from [Mordehai et al. 2011b]. . . . .	19

1.7. Stress–strain curves for two MgO nanocubes of 90 (red curve) and 120 (black curve) nm edge lengths deformed <i>in situ</i> inside the TEM. In the inset: TEM image of a 120 nm sample during compression, $\varepsilon = 7.3\%$ . The black arrow shows a contrast band corresponding to dislocations that emerge from the surface of the cube. Two numerical simulation snapshots of a 12.6 nm edge length nanocube are also represented. Reconstructed $1/2\langle 110 \rangle\{110\}$ dislocations are shown in green. From [Issa et al. 2015]. . . . .	20
1.8. SEM imaging of Ag-Au and Ag NPs compression tests and e) load-displacement curves. a, b) Ag-Au core-shell NPs before and after test. c, d) Single crystalline Ag NPs before and after test. From [Sharma et al. 2021]. . . . .	21
1.9. Strength <i>vs.</i> size master plot. Review of the nanopillar compressions of a) FCC from ref. [Shahbeyk et al. 2019] and b) BCC from ref. [Greer and De Hosson 2011] metals. Case of nanoparticles compression or whisker tension/compression such as c) Au from ref. [Mordehai et al. 2011b] or d) Cu from ref. [Kraft et al. 2010] (compression in blue and tension in orange), respectively. . . . .	23
1.10. Extrinsic biases affecting the mechanical response of nano-objects. a) Stress–strain curves for as-grown (directionally solidified) and FIB-milled Mo-pillars, from [Shim et al. 2009], b) comparison of load (Agilent G200) and displacement controlled (ASMEC UNAT2) compression tests of 5 $\mu\text{m}$ sized single crystalline Cu pillars, from [Dehm et al. 2018], c) compression of three differently misaligned Cu micro-pillars, from [Kirchlechner et al. 2011], and d) nanoindentation of a gold stepped film (in blue) compared to the case of a (111)-oriented (in red), from [Navarro et al. 2008]. . . . .	25
1.11. Oxide layer on nano-objects. a-c) Compression of a Fe nanosphere with an oxide overlayer, from [Han et al. 2015], d) STM image of SrRuO <sub>3</sub> thin film showing three-dimensional island growth on LaAlO <sub>3</sub> substrate, from [Rao et al. 1997], and e) histogram of the critical loads for the indentation of an Al substrate with a 54 nm thick oxide film, from [Morasch and Bahr 2005]. . . . .	26
1.12. Surface irregularities at small-scales. a) STM 110 nm square image of a Si(100) surface, from [Arthur 2002], b) dislocation interaction with a surface step of Ni <sub>3</sub> Al thin film, from [Coupeau et al. 2020], c) Al <sub>2</sub> O <sub>3</sub> faceted particle, from [Iijima 1985], d) SEM top view of a Ni <sub>3</sub> Al nanocube, from [Landefeld et al. 2012], and e) TEM image of single crystalline Au nanowire, from [Zhang et al. 2001b]. . . . .	28
1.13. Nanoindentation of a [111]-Ni thin film. a-e) Snapshots of atomic configuration during a plastic event and f) force <i>vs.</i> displacement curve. Only the atoms without local FCC environment are shown. From [Chang et al. 2010]. . . . .	29

1.14. Deformation mechanisms in mechanical testing of nanowires. a) Slip during the yielding of Au nanowire and b) Twinning during deformation of Ag nanowires. From [Lao et al. 2013]. . . . .	30
1.15. MD compression simulations of faceted Au nanoparticles. a) Simulation setup with frozen atoms for the indents, b-c) dislocation nucleation during the first plastic event, d) stress-strain curves of particles of various heights, terminated at the first dislocation nucleation event, and e) the compressive stress at the point of nucleation of the first dislocation <i>vs.</i> particle height. From [Mordehai et al. 2011b]. . . . .	32
1.16. Compression of Cu nanosphere. a) Simulation setup using the force-field approach, b) load-displacement curve with an inset of the particle microstructure at a compression depth of 38.8 Å, and c) the formation and expansion of the pyramid hillocks. From [Bian et al. 2018]. . . . .	33
1.17. Maximum compressive stress computed during uniaxial compressions, as a function of the size, modeled by MD. Markers and their colors represent the NP shape and materials. From [Amodeo and Pizzagalli 2021]. . . . .	34
1.18. Shape effect on strength. a) Stress-strain curves associated with the compression of Ni <sub>3</sub> Al cubic NPs, with the shape parameter $\alpha$ increasing from the bottom curve to the top one, from [Amodeo and Lizoul 2017] and b) comparison of yield stresses for spheres and faceted Si NPs of various sizes, from [Kilymis et al. 2018]. . . . .	35
1.19. Determination of the activation energy for the nucleation of a dislocation from a surface step. a) Sample subjected to biaxial tension and b) the calculated activation energy as a function of the applied strain for a stepped surface (blue circles) and for a flat surface (red circles). Adapted from [Hara et al. 2009] . . . . .	36
1.20. Indentation of diamond substrate with round (a-b) and roughened (c-d) tips. Data points from five tests performed with slightly different contact locations are shown overlapped. From [Jacobs et al. 2013]. . . . .	37
1.21. Early-stage of Ni oxidation. a) dissociative chemisorption stage, b) rapid nucleation of nickel oxide island, and c) lateral growth of the oxide island. Oxide thickness as a function of d) the crystallographic orientation and e) the temperature. Adapted from [Garruchet et al. 2010]. . . . .	38
1.22. Tensile testing of pre-oxidized Cu NWs. a) Initial structure (red spheres represent Cu atoms, and blue spheres denote O atoms) with b) the amorphous (purple) and FCC (green) lattice structures. Stress-strain curves comparison between the pristine NWs (in red) and their pre-oxidized counterparts (in blue) for the pristine NW radius c) 2.08, d) 3.10, and e) 5.20 nm, respectively. Adapted from [Aral and Islam 2023].	39

2.1. Example of applications of the ReaxFF method. a) Ni-catalysed Carbon nano-tubes growth [Neyts et al. 2013], b) electrometallisation cells [Onofrio et al. 2015], c) reduction of graphene oxide [Bagri et al. 2010], d) Pd surface oxidation [Senftle et al. 2013], e) oriented attachment mechanisms in TiO <sub>2</sub> nanocrystals [Raju et al. 2014], f) capacitive mixing by double layer expansion [Hatzell et al. 2014]. Adapted from [Senftle et al. 2016]. . . . .	44
2.2. Schematic representation of interatomic interactions including a) over-coordination of a C atom, b) torsion and angle energies, c) van der Waals and d) Coulomb interactions. . . . .	47
2.3. MD workflow including initial parameters such as system's structure and interatomic potential as well as Newton's equations of motion solving and atomic positions update. . . . .	51
2.4. Schematic example of thermodynamic ensembles. a) NVE, b) NVT and c) NPT . . . . .	52
2.5. Simulation protocol for MD a) nanocompression of a rough faceted particle and b) nanoindentation of an oxidized thin film. The height variation of the faceted nanoparticle is denoted by $l^{[111]}$ . . . . .	55
2.6. Surface area computation using a) a convex Hull envelope delineating the region enclosed by the blue boundary or b) the number of surface atoms $n_i$ times an elementary surface $s$ . . . . .	57
2.7. Oxidation simulation protocol. Bottom atoms are frozen while two NVT regions are defined for the thin film and the gas. Upper wall reflects atoms downwards when they come in contact. The 5 Å gap between gas and film corresponds to the high-range interaction cut-off. . . . .	58
3.1. MD load-controlled nanocompression workflow including the computation of group $R^N$ every $\Delta t$ , calculation of every atomic variables and the use of a Python feedback loop to solve Equation 3.3. . . . .	66
3.2. Mechanical response of a 14.57 nm height Au faceted NP under compression using load and displacement-controlled MD simulations. a) Load <i>vs.</i> time, b) engineering strain <i>vs.</i> time. Black dashed lines refer to time configurations illustrated in Figure 3.3. . . . .	67
3.3. Shape and dislocation microstructure evolution of a 14.57 nm height Au faceted NP under compression using load and displacement-controlled MD simulations. Atoms colored in gold and red, respectively, refer to surfaces and stacking-fault environments. Perfect crystal atoms are removed for the sake of clarity. Shockley partial dislocations are illustrated by green curves. . . . .	68
3.4. a) Dislocation density and b) average dislocation velocity in a 14.57 nm height Au faceted NP under compression using load- or displacement-controlled MD simulations . . . . .	69

3.5. Stress-strain curves for Au faceted NPs of various size $l_0^{[111]}$ under compression computed using load ( $\dot{F}=0.77 \text{ nN.ps}^{-1}$ , dark-colored curves) and displacement-controlled ( $\dot{\Delta l}=0.01 \text{ \AA.ps}^{-1}$ , light-colored curves) MD simulations. . . . .	70
3.6. Mechanical response of Au faceted NP under load-controlled MD compression as a function of a) the feedback-loop period $\Delta t$ in fs and b) the load rate $\dot{F}$ in $\text{nN.ps}^{-1}$ . . . . .	71
3.7. MD nanocompression simulation of a 20.1 nm Ag half-sphere using load and displacement-controlled MD. a) Force <i>vs.</i> displacement curves computed using load-controlled MD (Load MD), displacement-control (Disp. MD) and the envelope load model (Load model), b), c) evolution of the dislocation microstructure at displacement $\delta = 4.04 \text{ \AA}$ for the displacement and load-control cases, respectively. . . . .	72
3.8. Newton-Raphson iterative algorithm for the solving of non-linear equation and the computation of the indenter's position $z_{ind}(\dot{F}, t)$ at each time step. . . . .	74
3.9. MD Load-controlled nanoindentation workflow including the computation of group $R^N$ every $\Delta t$ , listing of every atom $i \in R^N$ coordinates and the parallel Newton-Raphson feedback loop to solve Equation 3.5. . . . .	75
3.10. Comparison between displacement-controlled and load-controlled nanoindentation. a) Force <i>vs.</i> displacement curves showing the pop-ins and a comparison with data from [Chang et al. 2010]. The inset shows the first pop-in. For better visualisation, markers size is reduced. b) Indenter's displacement <i>vs.</i> time denoting the penetration of the indenter inside the sample in the case of a load-controlled MD setup. . . . .	76
3.11. Evolution of the dislocation density as a function of indenter's displacement during Ni thin film nanoindentation by using both control modes. The inset shows the dislocation density burst that occurs at the critical displacement $\delta_y=11.10 \text{ \AA}$ . . . . .	77
3.12. Comparison of cumulative computation time as a function of the MD step for load and displacement-controlled nanoindentation tests. The step corresponding to the pop-in occurrence in the case of load control mode is denoted by the grey vertical dotted line . . . . .	79
4.1. Self-similarity and successive magnifications in the broccoli romanesco vegetable, from [Bancaud et al. 2012]. . . . .	83
4.2. Characterization of rough surfaces. a) PSD of self-affine surfaces characterized by different Hurst exponents $H_1$ and $H_2$ , b) STM image of a rough Au substrate, from [Barabási and Stanley 1995], c) AFM topography image of a Au thin film, from [Bonyár 2016], d) optical micrograph of a thick metal film, from [Barabási and Stanley 1995]. . . . .	85

4.3. Evolution of contact area fraction for rough surfaces with different $q_1 / q_L$ compared with the prediction of Persson's model (dashed curve) from Equation 4.10a. a) Zoom on microscopic contact and b) entire evolution of contact area fraction. Asymptotics of the BGW theory is given as an indication (black solid line). From [Yastrebov et al. 2017]. . . . .	88
4.4. Random rough surfaces modeled using Equation 4.13 for various roughness parameters. a) $\eta=0.00$ , b) $\eta=0.25$ , c) $\eta=0.50$ , d) $\eta=0.75$ , e) PSD of the various $h$ profiles computed as $C^{2D}(\mathbf{q})=\sum_{x,y} h_{\mathbf{q}}(x, y)^2$ with $h_{\mathbf{q}}(x, y)$ the height matrix corresponding to the wave vector $\mathbf{q}$ . For all calculations, $A=50$ , $B=50$ and $h(x, y)$ values are normalized between 1 and -1. . . . .	90
4.5. <i>Pyrough</i> default workflow categorized in four domains: <i>Input</i> , <i>Process</i> , <i>Output</i> and <i>External interface</i> . . . . .	92
4.6. Construction of various rough samples, a) film, b) wire with circular cross-section and c) faceted wire. For each sample, the surface nodes are colored in dark blue and $n_x$ and $n_y$ correspond to the number of points along $x$ and $y$ -axis respectively in the original 3D mesh. A jet color map is used for the representation of height distributions, red is the maximum value whereas blue is the minimum one. . . . .	96
4.7. Construction of Wulff-faceted samples including the identification of one facet and relative nodes before the use of Equation 4.13. The process is repeated for each facet of the sample using the same roughness parameter set. . . . .	97
4.8. Computation of normal direction and displacement in the case of edge and corner-associated nodes. a) <i>fWire</i> case b) <i>Wulff</i> case for $j$ , $k$ and $l$ edge-associated and $m$ corner-associated nodes. Purple, green and yellow vectors are facet normals and black vectors are the resulting displacement vectors. . . . .	98
4.9. <i>Pyrough</i> refined mesh process using element size fields, a) application to a <i>Box</i> type object where the size of the elements is reduced getting closer to the surface, b) application to a circular wire with a radial decrease of the mesh size. . . . .	99
4.10. Atomic position file generation for the design of a Au wire. a) Initial block with the dimensions of the input mesh, b) selection of atoms from the 3D mesh, c) rough sample, d) reboxed simulation cell. . . . .	100
4.11. Examples of objects that can currently be generated using <i>Pyrough</i> . Each single shape is represented using its corresponding FEM mesh and atomistic representation. . . . .	100
4.12. Computation of $C^{2D}(q)$ of a) known surface where computed $\eta$ is equal to the value calculated from data in ref. [Persson et al. 2005] and b) comparison of PSDs as extracted from an experimental polystyrene particle surface [Yamamoto et al. 2005] and a <i>Pyrough</i> -generated surface with measured roughness parameters ( $\eta$ and <i>RMS</i> ) as inputs. . . . .	103

4.13. Von Mises stress distribution during the nanoindentation of a gold sample with a roughened spherical tip, a) perfect sphere, b) $\eta = 0.75$ , c) $\eta = 0.50$ . The von Mises stress $\sigma_M$ is recorded for an indentation depth of 0.6 nm but the tip is moved back on the illustration for the sake of visibility.	104
4.14. Generation of a wavy grain boundary using <i>Pyrough</i> and the <i>Grain</i> object, a) single-grain FEM mesh with a rough surface characterized by $h$ , b) same single grain filled with Ag atoms, c) Coupling of the complementary Au grain characterized by $-h$ leading to an Ag/Au $<001>$ coherent interface. . . . .	105
4.15. Nanowire cross-section geometry classification according to <i>RMS</i> values and <i>RMS</i> distribution map of Au nanowires as a function of $\eta$ and $C_1$ . In order of highest to lowest <i>RMS</i> : HA, LA and QC. . . . .	106
 5.1. Wulff-shaped Au nanoparticles with (unrelaxed) rough surfaces as generated using <i>Pyrough</i> and MD compression protocol, a) $\eta=0.95$ , b) $\eta=0.75$ , c) $\eta=0.25$ , and d) $\eta=0.0$ , e) the nanocompression simulation setup is made of two axis-aligned and infinite force fields that behave respectively as indenter and substrate, similarly to the one described in chapter 3. . . . .	110
5.2. Thermal equilibration of Au-faceted nanoparticles with rough surfaces, a) Evolution of the MSD during sample equilibration for a nanoparticle characterised by ( $\eta=0.00$ , $C_1=0.5$ ), b) Equilibration time $t_{equi}$ distribution as a function of the roughness exponent $\eta$ , for $C_1= 0.5$ . 20 samples (symbols) are tested for each $\eta$ and curves are guides for the eyes. For the perfect case (nanoparticle with flat surfaces), the probability density function is reduced by a factor of 190 to scale with the other distributions.	113
5.3. Evolution of top surface roughness exponent $\eta_{eq}/\eta_0$ after/before sample thermal equilibration as function of input $\eta$ . The box plot relies on the central 50% of the sampling while bars show the scatter of the last 50%. . . . .	113
5.4. Load-displacement for $<111>$ -oriented Au-faceted nanoparticles with rough surfaces compressed at $T=300$ K, a) $\eta = 0.00$ , b) $\eta = 0.25$ , and c) $\eta = 0.95$ . 20 samples are tested for each ( $\eta$ , $C_1=0.5$ ) configuration. <i>Perfect-like</i> , <i>intermediate</i> and <i>accommodation</i> cases are illustrated in brown, red and orange respectively while the <i>perfect</i> case (nanoparticle with flat surfaces) is shown in black, d) Sample fraction distribution among the <i>Perfect-like</i> , <i>intermediate</i> and <i>accommodation</i> cases as a function of $\eta$ . . . . .	114
5.5. Surface-islet penetration within the nanoparticle during compression, a) top surface view (atoms colored by height), b) cross-section. Atoms colored in green corresponds to FCC local environment, stacking-fault atoms are in red (HCP local environment) and atoms colored in light-grey corresponds to surfaces and other point defects, c) stacking sequence. . . . .	116

5.6. Per atom von Mises stress stress $\sigma_M^i$ in faceted-Au nanoparticles under compression at $T=10$ K, cross-section view. Snapshots were taken ahead of the first dislocation nucleation event in a) a nanoparticle with flat surfaces ( <i>perfect</i> case) and b) a nanoparticle with rough surfaces ( $\eta=0.85$ , $C_1=0.5$ ), <i>intermediate</i> case. Insets illustrate the nanoparticle top surface where first-layer atoms are colored lighter than those below. Red lines illustrate main figure cross-section. . . . .	117
5.7. Dislocation nucleation in a faceted-Au NP with rough surfaces ( $\eta=0.25$ , $C_1=0.5$ ) under compression at $T=300$ K. a) initial sample (after equilibration), b) load-displacement curve and top surface area evolution, c) dislocation nucleation process for displacements between 1.67 and 4.41 Å. Surface and partial dislocation core atoms are colored in yellow, atoms in the stacking-fault are colored in red. Perfect crystal atoms are removed for the sake of clarity. Insets show the evolution of the top surface ledge during the dislocation nucleation/propagation process. . . . .	118
5.8. Dislocation nucleation in a faceted-Au NP with rough surfaces ( $\eta=0.75$ , $C_1=0.5$ ) under compression at $T=300$ K, a) $\delta=3.63$ Å, b) $\delta=4.18$ Å, c) $\delta=4.74$ Å, d) $\delta=5.19$ Å, e) $\delta=5.58$ Å and f) $\delta=6.97$ Å. View from the inside of the nanoparticle from which perfect crystal atoms are removed for the sake of clarity. Dislocations in {110} and {001} slip planes are colored in green and blue, respectively. Same colors are used to identify corresponding surface steps. . . . .	119
5.9. Per atom potential energy drop at the first dislocation nucleation event, as a function of $\eta$ (20 simulations for each $\eta$ ), as compared to the <i>Perfect</i> cases. . . . .	120
5.10. Rough surface nanoparticle yield force $F_y$ vs. (initial) top surface area $S$ , both respectively normalized by mean $F_y^p$ and $S^p$ associated to flat-surface NPs. Blue symbols: edge-connected top surface cases, orange symbols: isolated-islet cases. Colored dashed-lines aim for linear regressions within the two domains with $F_y/F_y^p=0.95S/S^p$ and $F_y/F_y^p=2.08S/S^p$ , respectively. . . . .	121
5.11. Influence of the contact surface configuration (isolated-islet or edge-connected) on the dislocation nucleation process, a,b) contact surface: a) isolated-islet and b) edge-connected configurations, top view. Surface step atoms are highlighted in red and green dots emphasize dislocation nucleation emerging segment locations, c,d) shear stress per atom computed in the partial slip system in which the first Shockley partial dislocation nucleates. Cross-section view normal to the slip plane identified using the Thomson tetrahedron notation. The atomic configuration is captured few steps before the first plastic event, while the latter critical dislocation configuration (colored in green) that corresponds respectively to c) an half- and d) a quarter-loop, is superimposed for the sake of clarity. . . . .	123

5.12. Effective critical compressive stress $\sigma_y^*$ distribution normalized by the perfect case yield strength $\sigma_y^p$ as a function of $\eta$ . Symbols: MD simulations, curves: model (Equation 5.3). For the sake of visibility, the probability density function of the <i>perfect</i> case is reduced by a factor of 6.67. . . . .	124
5.13. MD nanocompression of Au-faceted nanoparticles with wide surface roughness ( $C_1=1.2$ ), a) example of nanoparticle ( $\eta=0.75$ ), b) examples of load <i>vs.</i> displacement curves for $\eta=0.25$ . The <i>perfect</i> case, <i>perfect-like</i> , <i>intermediate</i> and <i>accommodation</i> trends are illustrated in black, brown, red and yellow, respectively, c) Sample fraction distribution among <i>intermediate</i> and <i>accommodation</i> cases as a function of $\eta$ (no <i>Perfect-like</i> case), d) normalized effective critical compressive stress $\sigma_y^*$ distributions as a function of $\eta$ . Symbols: MD simulations, curves: model (Equation 5.3). . . . .	126
5.14. Examples of emerging dislocation microstructure evolution during MD nanocompression of Au-faceted nanoparticles with wide surface roughness ( $C_1=1.2$ ), a) surface step acting as an anchor point that impedes the further growth of the first dislocation promoting new nucleation event elsewhere on the surface, b) surface reconstruction induced by a dislocation shearing the surface ledge. One can note in this case the simultaneous nucleation of at least two dislocations, c) combination of both processes. View from below the top surface of the nanoparticle. Atoms colored in red denote zones of interest in case of surface ledge reconstruction induced by dislocation shearing. . . . .	127
6.1. Preliminary TEM imaging of Ni NPs processed by the dewetting method. Various sizes and shapes are observed and parts of them are encapsulated in an amorphous or crystalline shell. . . . .	132
6.2. Oxidation of an Ni NP with native oxide. a) Original NP with native oxide at a) 100°C and b) 300°C. c) Growth of a rough secondary oxide shell at 300°C when $P_{O_2}$ is increased to 0.5 mbar. . . . .	132
6.3. Flash reduction and re-oxidation of a Ni NP. a) Some residues of the native oxide are still observable and b) the native oxide is fully rebuild in high vacuum. . . . .	133
6.4. Evolution of the number of reacted O atoms as a function of time and temperature for a) Ni and b) Cu. . . . .	136
6.5. Oxidation mechanisms for metal samples. Sample top view during the oxidation phase as a function of the number of reacted O atoms for a) Ni and b) Cu. . . . .	137
6.6. Final sample state at the end of the oxidation phase as a function of temperature. Side views of a) Ni and b) Cu samples. . . . .	138

6.7. Average charge distribution (in blue and red) and coordination number (in grey) along z-axis at the end of oxidation phase at 1200 K for O, a) Ni and b) Cu samples. The average charge density and coordination number profiles are computed with bins of size 1.0 Å. Oxide layer zones are delimited by thin black dotted lines. . . . .	139
6.8. Partial radial distribution functions within the oxide layers before and after quenching. a,b) Ni and c,d) Cu, both at 1200 K and 10 K, respectively. . . . .	141
6.9. Oxide growth kinetics on rough metal surfaces. Evolution of adsorbed O atoms on a) Ni and b) Cu rough surfaces as compared to flat thin films. Two different roughness profiles are tested and are characterized by RMS equal to 1 or 3. . . . .	142
6.10. Top surface oxidation of Ni and Cu rough surfaces characterized by $\eta=0.9$ and $RMS=1$ at different times. a) Top and b) side view for Ni, and c) top and d) size view for Cu oxidation process. Atoms are colored as a function of z-coordinate in top views. . . . .	143
6.11. Top surface oxidation of Ni and Cu rough surfaces characterized by $\eta=0.9$ and $RMS=3$ at different times. a) Top and b) side view for Ni, and c) top and d) size view for Cu oxidation process. Atoms are colored as a function of z-coordinate in top views. . . . .	144
6.12. Nanoindentation of oxidized a) Ni and b) Cu samples, as compared to non-oxidized metal flat surface (black curves). Vertical dotted lines refer to the nucleation of the first dislocations in every cases. . . . .	145
6.13. Nucleation of the first dislocations during the nanoindentation of Ni thin films. a) Non-oxidized surface, b) 1.40 nm, c) 2.23 nm and d) 4.53 oxide layer thickness. Color code denotes the non-affine squared displacement. The atoms in a non-FCC configuration are shown. Insets show the von Mises stress $\sigma_M^i$ distribution right before the nucleation of the dislocations. . . . .	146
6.14. Nucleation of the first dislocations during the nanoindentation of Cu thin films. a) Non-oxidized surface and b) 1.30 nm oxide layer thickness. Color code denotes the non-affine squared displacement and the atoms in a non-FCC configuration are shown. . . . .	147
1. Thermal expansion coefficients using ReaxFF potentials in the case of Ni and Cu. Simulation data are compared to previous experimental outcomes. . . . .	193

## List of Tables

3.1. Yield force $F_y$ , critical stress and time $\sigma_y$ and $t_y$ as well as adjusted elastic and plastic strains and load rates ( $\dot{\epsilon}_e$ , $\dot{\epsilon}_p$ , $\dot{F}_e$ and $\dot{F}_p$ ) computed during MD compression simulations of a 14.57 nm height Au faceted NP using load or displacement-control (respectively labelled $\dot{F}$ and $\dot{\Delta}l$ ). . . . .	68
4.1. Description of <i>Pyrough</i> 's input file. . . . .	94
4.2. Statistical analysis of a roughened surface obtained in (i) the experiment, the analysis of the top surface of a polystyrene particle [Yamamoto et al. 2005], and (ii) using <i>Pyrough</i> -surface module. The experimental measured parameters are used as <i>Pyrough</i> inputs to generate a surface characterized by similar statistical parameters. . . . .	103
5.1. Mean $\mu$ and standard deviation $s$ of $\sigma_y^*/\sigma_y^P$ distributions obtained by MD simulations ( $\mu_S$ and $s_S$ ) and model Equation 5.3 ( $\mu_M$ and $s_M$ ). . . . .	125
6.1. Simulation parameters for each temperature runs. . . . .	135
6.2. Yield values corresponding to the nucleation of the first dislocations during nanoindentation tests. . . . .	145